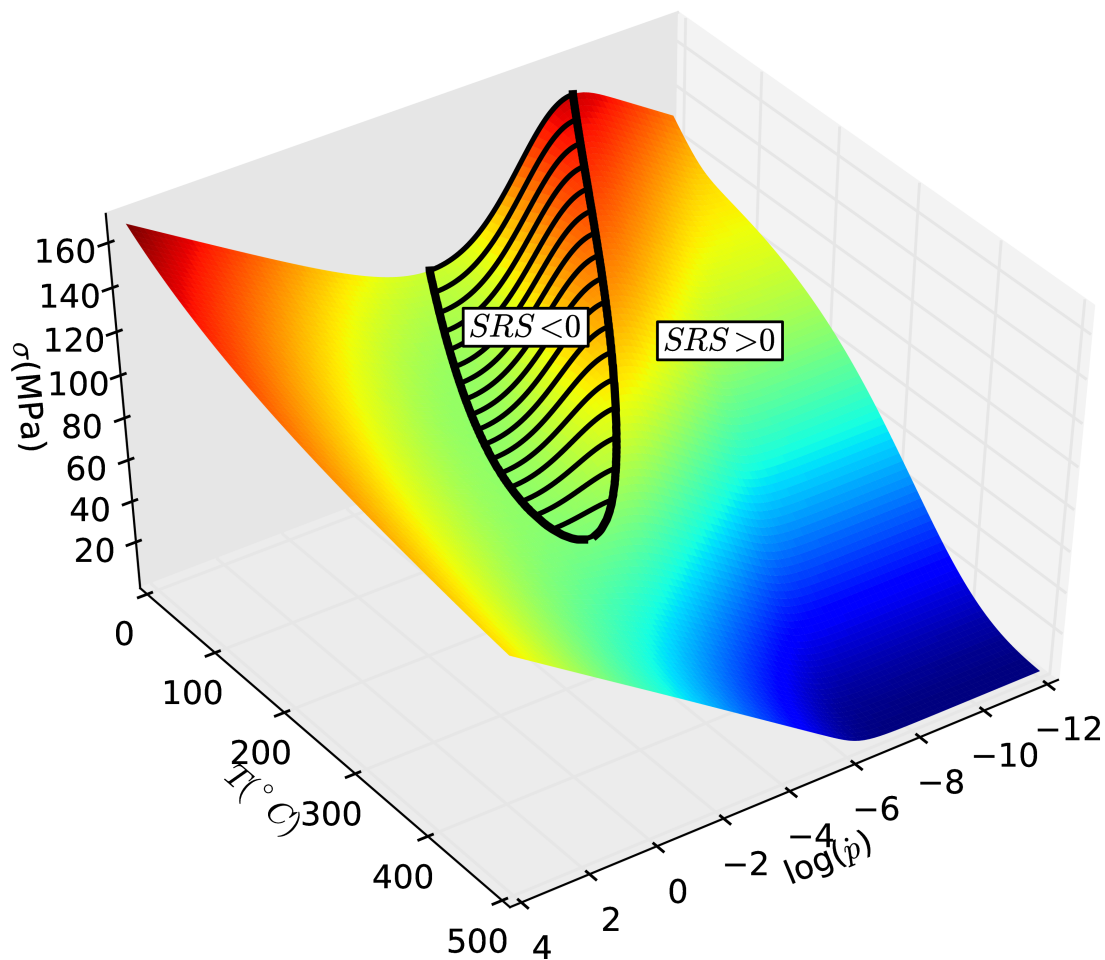MATTHIEU MAZIÈRE

Modelling the Portevin - Le Chatelier effect in metallic alloys

From physical mechanisms up to failure of components

Rapporteurs :

Ahmed Benallal

Mikhael Lebyodkin

Philippe Pilvin

Examinateurs :

Jean-Louis Chaboche

Samuel Forest

Djimedo Kondo

Jean-Loup Strudel

Note au lecteur :

Ce manuscrit d'habilitation à diriger les recherches est un document "tout en un".
Il contient ainsi :

— *Un curriculum vitae étendu incluant une liste de publications, ainsi que les stages et thèses que j'ai co-encadré, soutenus ou en cours.*
— *Un résumé en français de mes activités de recherche*
— *Un résumé en français de mes activités d'enseignement*
— *Un document original (à l'exception de 2 courts articles déjà publiés qui constituent le chapitre 5) d'une centaine de page en Anglais intitulé "Modeling the Portevin - Le Chatelier effect in metallic alloys" qui constitue le cœur du manuscrit.*

Il a été écrit principalement au court de l'année scolaire 2015-2016, au centre des matériaux, à l'école des Mines de Paris, et dans les bibliothèques et cafés Parisiens. Il est le résultats du travail de certains de mes doctorants (Huaidong, Julie, Anthony, Damien, Arina et Sicong) et stagiaires (Georges, Steffen, Carina et Quentin), et de collaborations fructueuses avec mes collègues du centre des matériaux (Samuel, Jacques, Anne-Françoise, Jean-Loup, ...), d'autres chercheurs académiques (Benoît, Claude, Clotilde, Jean-Louis,...) ou industriels (Hervé, François, Aurore, Patrick, Anaïs, Arnaud,...). [1] *Il n'aurait pas pu voir le jour sans l'aide de ma précieuse famille, Caroline, Manon et Joan, avec une mention spéciale aux deux derniers pour savoir me réveiller régulièrement vers 3h du matin, la meilleure heure pour prendre du recul sur les matériaux, la mécanique et le monde qui nous entoure...*

Matthieu

---

1. Certains doctorants et collègues (chercheurs, ingénieurs, techniciens, secrétaires, documentalistes, ...) avec lesquels j'ai travaillé sur d'autres sujets ne sont pas cité ici. Qu'ils ne s'offusquent pas, ils auront évidement leur place dans les remerciements qui viendront dans la version définitive de ce manuscrit.

CURRICULUM VITAE ÉTENDU

Matthieu MAZIERE
39, rue de l'Orillon
75011 Paris, FRANCE

Né le 22.12.1981 à Echirolles,
France
Nationalité : Française

Tel. : +33 6 64 99 15 68
E-Mail : maziere@mat.ensmp.fr

DOCTEUR EN SCIENCE ET GÉNIE DES MATÉRIAUX
AGRÉGÉ DE MÉCANIQUE, NORMALIEN

FORMATION

2004–2007	**Doctorat en Sciences et Génie des Matériaux** Mines ParisTech
2003–2004	**D.E.A. en Techniques Avancées en Calcul de Structure** E.N.S. Cachan / Ecole Polytechnique / Université Paris VI
2002–2003	**Agrégation de Mécanique** E.N.S. Cachan
2001–2002	**Maîtrise de Technologie Mécanique** E.N.S. Cachan
2000–2001	**Licence de Technologie Mécanique** E.N.S. Cachan
1998–2000	**Classe Préparatoire aux Grandes Ecoles Scientifiques** Lycée Lakanal Sceaux

RECHERCHE

2013–2016	**Maître Assistant** Centre des Matériaux - Mines ParisTech *Stabilité, Localisation de la déformation, Lois de comportement pour l'endommagement et la rupture*
2009–2013	**Chargé de Recherche** Centre des Matériaux - Mines ParisTech *Stabilité, Localisation de la déformation, Lois de comportement pour l'endommagement et la rupture*
2008–2009	**Chercheur Invité - Stage Post-Doctoral** Federal Institute for Materials Research and Testing (BAM) - Berlin - Allemagne *Propagation de fissure en fatigue*
2004–2007	**Thèse de doctorat : "Burst of turboengine disks"** Centre des Matériaux - Mines ParisTech *Calculs de structures en présence d'instabilités et de non-linéarités*
2004	**Mémoire de D.E.A. : "Fields' projection from a mesh to another"** C.E.A. - Saclay *Méthodes numériques pour le remaillage*
2002	**Mémoire de Maîtrise : "Finite element model of a guitar top plate"** U.N.S.W - Sydney - Australie *Acoustique musicale et vibrations*

ENSEIGNEMENT

2014–2016	**Matériaux avancés : les défis actuels** RESPONSABLE DE PARCOURS *Année pré-doctorale PSL-ITI (Mines ParisTech)*
2013–2016	**Mécanique des milieux continus** CHARGÉ DE COURS *Mastère spécialisé DMS (ex-CoMaDiS) (Mines ParisTech)*
2009–2016	**Mécanique des matériaux solides** RESPONSABLE DES PROJETS *Ecole d'ingénieur 1ère année (Mines ParisTech)*
2009–2016	**Mécanique des milieux continus** CHARGÉ DE TD (COURS DE SAMUEL FOREST) *Ecole d'ingénieur 1ère année (Mines ParisTech)*
2009–2016	**Semaine ATHENS Non Linear Computational Mechanics** CHARGÉ DE COURS ET RESPONSABLE DES PROJETS *Ecole d'ingénieur 2ème année (Mines ParisTech)*
2012–2016	**Modèles mécaniques pour la rupture ductile** CHARGÉ DE COURS *Master II MAGIS (ENS Cachan)*
2009–2016	**Approche multi-échelle de la plasticité des métaux** CHARGÉ DE COURS *Master DMSE (UPMC - ENPC ParisTech)*
2010–2011	**Modélisation Mécanique des Matériaux** CHARGÉ DE COURS *Master I Génie des Matériaux (Université d'Evry)*

ORGANISATION D'ÉVÉNEMENTS

2016	**Ecole thématique CNRS Métallurgie Mécanique** 23 - 29 Octobre, Porquerolles
2016	**Séminaire du département Mécanique et Matériaux de Mines ParisTech** 22 - 23 Septembre, Porquerolles
2015	**Séminaire du département Mécanique et Matériaux de Mines ParisTech** 10 - 11 Septembre, Fontainebleau
2014	**Séminaire du département Mécanique et Matériaux de Mines ParisTech** 18 - 19 Septembre, Porquerolles
2013	**11st CSMA Conference on Computational Mechanics** 13 - 17 Mai, Giens
2011	**2nd International Conference on Material Modeling** 31 Août - 2 Septembre, Paris
2011	**3ème Journée Nationale sur le Vieillissement Statique et Dynamique** 20 Avril, Paris

Séminaires invités et courts séjours

2014	**Institut de mécanique et d'ingénierie Bordeaux**
	Durabilité des Matériaux, des Assemblages et des Structures (DUMAS)
2012	**Universität Duisburg-Essen - Allemagne**
	Institut für Mechanik (Prof. Dr.-Ing. Jörg Schröder)
2011	**Karlsruhe Institute of Technology (KIT) - Allemagne**
	Institut für Technische Mechanik (Prof. Thomas Böhlke)
2010	**RWTH Aachen University - Allemagne**
	Material Simulation Group (Dr.-Ing. Ulrich Prahl)

Responsabilités

2015–2018	**Membre du Conseil d'Administration - Représentant des Enseignants-Chercheurs**
	Mines Paristech
2014–2017	**Membre du Conseil de Laboratoire CNRS UMR 7633**
	Centre des Matériaux - Mines ParisTech
2012–2018	**Membre du Comité Pédagogique**
	Mines ParisTech
2009–2012	**Membre du Comité de la Recherche**
	Mines ParisTech
2006–2007	**Membre du Conseil de l'Ecole Doctorale - Représentant des Doctorants**
	Mines and ENSAM ParisTech
2005–2007	**Membre du Conseil d'Administration - Représentant des Doctorants**
	Mines Paristech
2004–2006	**Membre du Conseil de Laboratoire CNRS UMR 7633**
	Centre des Matériaux - Mines ParisTech

Distinctions

Adolf Martens Fellowship in : Federal Institute for Materials Research and Testing (BAM) - 2008

Special Mention for oral presentation in : 6th EUROMECH Solid Mechanics Conference. Budapest, August 28th September 1st, 2006

Langues

Anglais : professionnel courant
Allemand : lu, écrit, parlé

Logiciels

Microsoft Windows et Environnement Linux
Abaqus, Castem, Zset, Catia, Solidworks
C++, Fortran, Python HTML, PHP

Doctorats - Thèses en Cours (5)

2015–2018   **Compétition entre localisation, instabilités et rupture ductile pour la ruine des structures aéronautiques**
MOUBINE AL KOTOB (DIR. S.FOREST)
Centre des Matériaux - Mines ParisTech / SAFRAN

2014–2017   **Interactions entre localisations et endommagement lors de la rupture ductile d'alliages métalliques par mesures 3D in-situ et calculs EF 3D régularisés**
SICONG REN (DIR. S.FOREST/G.ROUSSELIER)
Centre des Matériaux - Mines ParisTech

2014–2017   **Endommagement des aciers de troisième génération à structure duplex pour application automobile**
QUENTIN TONIZZO (DIR. A-F.GOURGUES)
Centre des Matériaux - Mines ParisTech / ANR MeMnAl

2014–2017   **Etude de la rupture ductile des acier pour l'aéronautique**
CLÉMENT DEFAISSE (DIR. J.BESSON)
Centre des Matériaux - Mines ParisTech / SAFRAN

2012–2016   **Modélisation de procédés de fabrication directe de pièces aéronautique et spatiale en TA6V par projection et fusion sélective d'un lit de poudre par laser : Approche thermique, métallurgique et mécanique**
GUILLAUME MARION (DIR. G.CAILLETAUD)
Centre des Matériaux - Mines ParisTech / FUI FALAFEL

Doctorats - Thèses Soutenues (7)

2011–2015   **Effets des bords découpés sur la ductilité des aciers avancés pour automobile : caractérisation par laminographie et modélisation**
Mouchine Kahziz (dir. T.Morgeneyer)
Centre des Matériaux - Mines ParisTech / Arcelor Mittal

2012–2015   **Multiscale investigation of room-temperature creep and sustained crack loading of Titanium. Influence of H and O content**
Arina Marchenko (dir. S.Forest)
Centre des Matériaux - Mines ParisTech / ANR FLUTI

2010–2013   **Fatigue à durée limitée du tantale : approche expérimentale et numérique multiéchelles**
Damien Colas (dir. Samuel Forest)
Centre des Matériaux - Mines ParisTech / CEA DAM

2009–2012   **Instabilités de Lüders et Transition ductile/fragile**
Anthony Marais (dir. Samuel Forest)
Centre des Matériaux - Mines ParisTech / EDF

2009–2012   **Simulation numérique de bifurcations de fissure dans les monocristaux de superalliage à base de nickel en mode mixte**
Prajwal Sabnis (dir. Samuel Forest)
Centre des Matériaux - Mines ParisTech / SAFRAN / ONERA

2008–2011   **Endommagement des aciers TWIP pour application automobile**
Julie Lorthios (dir. Anne-Françoise Gourgues)
Centre des Matériaux - Mines ParisTech / Arcelor Mittal

2007–2010   **Comportement mécanique et rupture des aciers au C-Mn en présence de vieillissement dynamique sous déformation**
Huaidong Wang (dir. Clotilde Berdin)
Centre des Matériaux - Mines ParisTech / MSSMAT - Ecole Centrale Paris / EDF

Masters & Stages (10)

2016	**Optimisation de contraintes résiduelles dans une pièce construite en fabrication additive**
	CHARLOTTE METTON
	Centre des Matériaux - Mines ParisTech / SAFRAN
2016	**Paramètres microstructuraux affectant la résilience des aciers trempes et revenus**
	FRANCK TIOGUEM
	Centre des Matériaux - Mines ParisTech / ASCO Metal
2014	**Compétition instabilité / rupture ductile pour la ruine des structures aéronautiques**
	PASCAL POMAREDE
	Centre des Matériaux - Mines ParisTech / SAFRAN
2013	**Modélisation thermomécanique du comportement d'un alliage de titane utilisé dans un compresseur de réacteur d'avion civil**
	EDOUARD PONCELIN DE RAUCOURT
	Centre des Matériaux - Mines ParisTech / SAFRAN
2012	**Modélisation du vieillissement dynamique du HA188 sous chargement complexe**
	QUENTIN PUJOL D'ANDRÉBO
	Centre des Matériaux - Mines ParisTech / SAFRAN
2012	**Identification of the necking and strain aging behavior of a C-Mn steel under tensile loading at different temperatures and strain rates**
	CARINA NISTERS,
	Centre des Matériaux - Mines ParisTech/ Universität Duisburg-Essen - Allemagne
2012	**Simulation of the Portevin - Le Chatelier effect in metal matrix composites**
	STEFFEN SPECHT
	Centre des Matériaux - Mines ParisTech / Universität Duisburg-Essen - Allemagne
2011	**Etude de l'effet Portevin - Le Chatelier dans un alliage d'aluminium**
	GEORGES PEYRE
	Centre des Matériaux
2010	**"Simulation des Einflusses von Uberlasten auf die Rissausbreitung in metallischen Werkstoffen unter zyklischer Beanspruchung"**
	BARBEL ZEISE
	Federal Institute for Materials Research and Testing (BAM) - Berlin - Allemagne
2008	**Caractérisation du comportement à rupture des alliages de zirconium de la gaine du crayon combustible des centrales nucléaires dans la phase post-trempe d'un APRP (Accident de Perte de Réfrigérant Primaire)**
	MI HE
	Centre des Matériaux - Mines ParisTech / EDF

Livres (1)

Book of abstracts : 2nd International Conference on Material Modelling. August 31st - September 2nd, 2011 Paris, France. Incorporating the 12th European Mechanics of Materials Conference
JACQUES BESSON, MATTHIEU MAZIÈRE
ISBN-13 : 978-2911256615 (2011)

Revues à comité de lecture (19)

The second Sandia fracture challenge : predictions of ductile failure under quasi-static and moderate-rate dynamic loading
BL BOYCE, SLB KRAMER, TR BOSILJEVAC, E CORONA, JA MOORE, K ELKHODARY, CHM SIMHA, BW WILLIAMS, AR CERRONE, A NONN, JD HOCHHALTER, GF BOMARITO, JE WARNER, BJ CARTER, DH WARNER, AR INGRAFFEA, T ZHANG, X FANG, J LUA, V CHIARUTTINI, M MAZIÈRE, S FELD-PAYET, VA YASTREBOV, J BESSON, J-L CHABOCHE, J LIAN, Y DI, B WU, D NOVOKSHANOV, N VAJRAGUPTA, P KUCHARCZYK, V BRINNEL, B DÖBEREINER, S MÜNSTERMANN, MK NEILSEN, K DION, KN KARLSON, JW FOULK III, AA BROWN, MG VEILLEUX, JL BIGNELL, SE SANBORN, CA JONES, PD MATTIE, K PACK, T WIERZBICKI, S-W CHI, S-P LIN, A MAHDAVI, J PREDAN, J ZADRAVEC, AJ GROSS, K RAVI-CHANDAR, L XUE
International Journal of Fracture, pp. 1-76 (2016)

In-situ 3-D synchrotron laminography assessment of edge fracture in Dual-Phase steels : Quantitative and numerical analysis
KAHZIZ, M., MORGENEYER, T., MAZIÈRE, M., HELFEN, L., BOUAZIZ, O., MAIRE, E.
Experimental Mechanics 56/2, 177-195 (2016)

Fracture behaviour of a Fe-22Mn-0.6C-0.2V austenitic TWIP steel
LORTHIOS, J., MAZIÈRE, M., LEMOINE, X., CUGY, P., BESSON, J., GOURGUES-LORENZON, A-F.
International Journal of Mechanical Sciences 101-102, pp. 99-113 (2015)

Portevin - Le Chatelier effect under cyclic loading : experimental and numerical investigations
MAZIÈRE, M., PUJOL D'ANDREBO, Q.
Philosophical Magazine 95/28-30, pp. 3257-3277 (2015)

Influence of static strain aging on the cleavage fracture of a C-Mn steel
MARAIS, A., MAZIÈRE, M., FOREST, S., PARROT, A., LE DELLIOU, P.
Engineering Fracture Mechanics 141, pp. 95-110 (2015)

A model for ductile damage prediction at low stress triaxialities incorporating void shape change and void rotation
CAO, T.S., MAZIÈRE, M., DANAS, K., BESSON, J.
International Journal of Solids and Structures 63, pp. 240-263 (2015)

Strain gradient plasticity modeling and finite element simulation of Lüders band formation and propagation
MAZIÈRE, M., FOREST, S.

Continuum Mechanics and Thermodynamics 27, pp. 83-104 (2015)

Investigation and modeling of the anomalous yield point phenomenon in pure tantalum
COLAS, D., FINOT, E., FLOURIOT, S., FOREST, S., MAZIÈRE, M., PARIS, T.
Materials Science and Engineering A 615, pp. 283-295 (2014)

Viscoplastic constitutive equations of combustion chamber materials including cyclic hardening and dynamic strain aging
CHABOCHE, J.-L., GAUBERT, A., KANOUTÉ, P., LONGUET, A., AZZOUZ, F., MAZIÈRE, M.
International Journal of Plasticity 46 , pp. 1-22 (2013)

Identification of a strain-aging model accounting for Lüders behavior in a C-Mn steel
MARAIS, A., MAZIÈRE, M., FOREST, S., PARROT, A., LE DELLIOU, P.
Philosophical Magazine 92 (28-30) , pp. 3589-3617 (2012)

Experimental and numerical study of dynamic strain ageing and its relation to ductile fracture of a C-Mn steel
WANG, H.D., BERDIN, C., MAZIÈRE, M., FOREST, S., PRIOUL, C., PARROT, A., LE-DELLIOU, P.
Materials Science and Engineering A 547 , pp. 19-31 (2012)

Investigations on the Portevin-Le Chatelier critical strain in an aluminum alloy
MAZIÈRE, M., DIERKE, H.
Computational Materials Science 52 (1) , pp. 68-72 (2012)

Effect of secondary orientation on notch-tip plasticity in superalloy single crystals
SABNIS, P.A., MAZIÈRE, M., FOREST, S., ARAKERE, N.K., EBRAHIMI, F.
International Journal of Plasticity 28 (1) , pp. 102-123 (2012)

Portevin-Le Chatelier (PLC) instabilities and slant fracture in C-Mn steel round tensile specimens
WANG, H., BERDIN, C., MAZIÈRE, M., FOREST, S., PRIOUL, C., PARROT, A., LE-DELLIOU, P.
Scripta Materialia 64 (5) , pp. 430-433 (2011)

Numerical simulation of the portevin - le chatelier effect in various material and at different scales
MAZIÈRE, M., FOREST, S., BESSON, J., WANG, H., BERDIN, C.
Materials Science Forum 638-642 , pp. 2670-2675 (2010)

Numerical aspects in the finite element simulation of the Portevin-Le Chatelier effect
MAZIÈRE, M., BESSON, J., FOREST, S., TANGUY, B., CHALONS, H., VOGEL, F.
Computer Methods in Applied Mechanics and Engineering 199 (9-12) , pp. 734-754 (2010)

Overspeed burst of elastoviscoplastic rotating disks : Part II - Burst of a superalloy turbine disk
MAZIÈRE, M., BESSON, J., FOREST, S., TANGUY, B., CHALONS, H., VOGEL, F.
European Journal of Mechanics, A/Solids 28 (3) , pp. 428-432 (2009)

Overspeed burst of elastoviscoplastic rotating disks - Part I : Analytical and numerical stability analyses
MAZIÈRE, M., BESSON, J., FOREST, S., TANGUY, B., CHALONS, H., VOGEL, F.
European Journal of Mechanics, A/Solids 28 (1) , pp. 36-44 (2009)

Numerical modelling of the Portevin-Le Chatelier effect
Mazière, M., Besson, J., Forest, S., Tanguy, B., Chalons, H., Vogel, F.
European Journal of Computational Mechanics, 17 (5-7) , pp. 761-772 (2008)

Actes de conférences (15)

La modélisation du vieillissement statique et dynamique dans le titane polycristallin non allié
Marchenko, A., Forest, S., Maziere, M.
Hydrogènematériaux, corrosion sous contrainte, fatigue corrosion, Journées jeunes chercheurs 2013, La Rochelle, 26-27 juin 2013, Presses des mines, 2013, p. 107-108 (2013)

Local approach applied to the fracture toughness of resistance spot welds
Krajcarz, F., Gourgues-Lorenzon, A.-F., Lucas, E., Maziere, M., Pineau, A.
13th international conference on fracture, 16-21 juin 2013, Beijing (2013)

3D synchrotron laminography assessment of damage evolution in blanked dual phase steels
Kahziz, M., Morgeneyer, T., Maziere, M., Helfen, L., Maire, E., Bouazziz, O.
13th international conference on fracture, 16-21 juin 2013, Beijing (2013)

Multi-scale approach of strain ageing in polycrystalline tantalum
Colas, D., Finot, E., Flouriot, S., Forest, S., Mazière, M., Paris, T.
ECCOMAS 2012 - European Congress on Computational Methods in Applied Sciences and Engineering, e-Book Full Papers , pp. 4175-4194 (2012)

Le calcul de structures en présence de vieillissement statique ou/et dynamique d'alliages métalliques
Maziere, M., Forest, S.
20ème congrès français de mécanique, Besancon, 29 aout-2 septembre 2011 (2011)

Influence of dynamic strain ageing on ductile fracture of a C-MN steel
Wang, H.D., Berdin, C., Mazière, M., Forest, S., Prioul, C., Parrot, A.
18th European Conference on Fracture : Fracture of Materials and Structures from Micro to Macro Scale (2010)

Simulation of fatigue crack growth by crack tip plastic blunting using cohesive zone elements
Mazière, M., Fedelich, B.
18th European Conference on Fracture (2010)

Simulation of fatigue crack growth by crack tip plastic blunting using cohesive zone elements
Mazière, M., Fedelich, B.
Procedia Engineering 2 (1) , pp. 2055-2064 (2010)

Simulation of the Portevin - Le Chatelier effect in metal matrix composites
Mazière, M., Mortensen, A., Mueller, R., Forest, S.
4th European Conference on Computational Mechanics, Paris. (2010)

Numerical modeling of ductile fracture in presence of Portevin Le-Chatelier effect in a C-Mn steel
Wang, H.D., Berdin, C., Mazière, M., Forest, S., Prioul, C., Parrot, A.
4th European Conference on Computational Mechanics, Paris. (2010)

Simulation par éléments finis de l'effet Portevin - Le Chatelier dans divers alliages métalliques et à différentes échelles
Mazière, M., Forest, S., Besson, J., Wang, H., Berdin, C.
9e Colloque National en Calcul de Structures, Giens. (2009)

Prévision de l'éclatement dans les disques de turbomachines
Mazière, M., Besson, J., Forest, S., Tanguy, B., Chalons, H., Vogel, F.
18ème Congrès Français de Mécanique, Grenoble. (2007)

Influence de la loi de comportement sur la prévision de l'éclatement d'un disque de turbomachine
Mazière, M., Besson, J., Forest, S., Tanguy, B., Chalons, H., Vogel, F.
Colloque National MECAMAT, Aussois. (2007)

Influence of spin-softening and nonlinear material behavior on the stability of rotating disks
Mazière, M., Besson, J., Forest, S., Tanguy, B., Chalons, H., Vogel, F.
6th EUROMECH Solid Mechanics Conference, Budapest. (2006)

Stabilité d'un disque de turbomachine en rotation
Mazière, M., Besson, J., Forest, S., Tanguy, B., Chalons, H., Vogel, F.
Colloque National MECAMAT, Aussois. (2006)

Résumé des activités de recherche

Instabilités visco-plastiques liées au vieillissement statique (bandes de Lüders) et dynamique (effet Portevin - Le Chatelier)

Le vieillissement par la déformation est un phénomène présent dans la plupart des alliages métalliques anciens (fers et aciers doux, alliages de cuivre et d'aluminium) ou plus récents (titanes, super-alliages base Cobalt ou Nickel) et qui apparaît souvent dans les gammes d'utilisation industrielles de ces alliages. Il se manifeste lors d'essais de traction par deux phénomènes bien connus des métallurgistes et des mécaniciens :

— Un pic de traction au niveau de la transition élastique/plastique durant laquelle cette dernière chute brutalement avant de rester constante le long d'un plateau pouvant atteindre plusieurs % de déformation. Durant ce plateau la déformation n'est pas homogène et s'accompagne de la propagation d'une ou plusieurs bandes de plasticité. Lorsque la bande a traversé toute l'éprouvette, la déformation redevient homogène et la courbe d'écrouissage reprend une forme habituelle. Ce phénomène est classiquement associé à W.Lüders [13] qui fut un des premiers à le mettre en évidence au 19ème siècle. Il est illustré sur la figure 1(a) par des essais de traction réalisés à basse température sur un acier C-Mn dans le cadre de la thèse d'A.Marais [198]

— L'apparition d'oscillations sur la courbe de traction durant la déformation plastique du matériau apparaissant en général un peu après la transition élastique/plastique et pouvant se poursuivre jusqu'à la rupture de l'éprouvette. En parallèle de ces oscillations on observe sur la surface des éprouvettes un certain nombre de bandes de localisation de la déformation se propageant de manière organisée ou chaotique. Ce phénomène est associé à A.Portevin et F.Le Chatelier (d'où le nom raccourci d'effet PLC) qui l'ont reporté parmi les premiers dans les alliages d'aluminium en 1923 [21]. Il est illustré sur la figure 1(b) par des essais de traction réalisés pour différentes vitesses de sollicitation à température ambiante sur un alliage d'aluminium dans le cadre d'une collaboration avec H.Dierke de T.U. Braunsweig [155, 199].
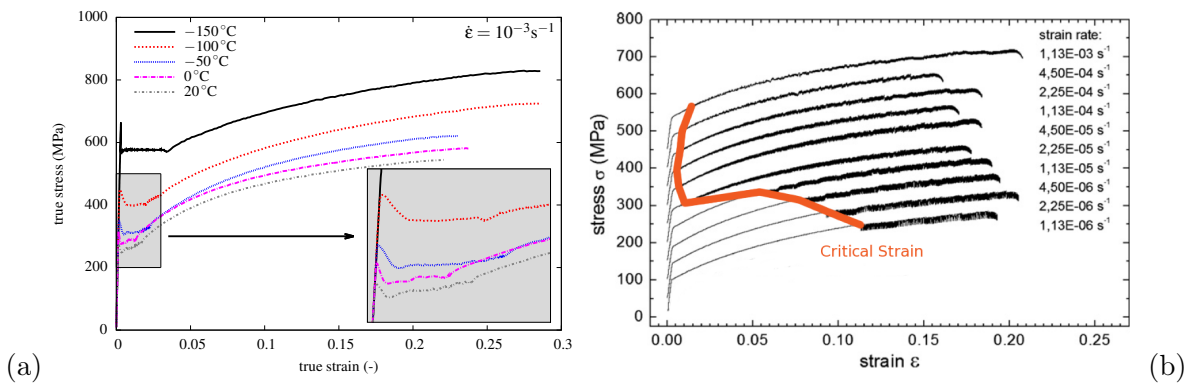

FIGURE 1 – (a) Pics de traction et plateaux de Lüders lors d'essais de traction sur des éprouvettes en acier C-Mn pour différentes températures [198] (b) Oscillations de type Portevin - Le Chatelier lors d'essais de traction à différentes vitesses et à température ambiante sur un alliage d'aluminium Al-Mg [199]

Le vieillissement par la déformation est défini comme l'interaction des dislocations avec les atomes en solution dans le réseau cristallin [23]. Il s'agit d'un phénomène contrôlé par deux paramètres majeurs que sont : la température et temps (ou la vitesse de sollicitation mécanique). Dans le cas du phénomène de Lüders c'est l'ancrage initial des dislocations qui est responsable du

crochet de traction. On parle alors de vieillissement statique. Le pic de traction et le plateau de Lüders est un phénomène principalement sensible au temps et à la température de vieillissement qu'aura pu subir l'échantillon avant l'essai.

Dans le cas de l'effet PLC, c'est la compétition durant la déformation plastique entre le mouvement des dislocations et la diffusion des atomes en solution qui génère des instabilités via un effet d'avalanche. On parle alors de vieillissement dynamique. Dans le domaine PLC, les atomes en solution diffusent vers les dislocations temporairement ancrées sur des obstacles fixes (précipités, autres dislocations,...) et freinent le mouvement de ces dernières. La contrainte va donc augmenter en conséquence jusqu'à libérer simultanément un grand nombre de dislocations ce qui va générer une vague de déformation localisée. La déformation ralenti alors afin de suivre la consigne, les dislocations sont arrêtées par des obstacles et le mécanisme se répète. Si la température est trop froide, ou la vitesse de dislocation trop rapide, les atomes en solution n'arrivent jamais à diffuser assez vite pour empêcher le mouvement des dislocations, on se trouve dans le domaine de friction. Si la température est trop chaude, ou la vitesse de déformation trop lente, les atomes en solution saturent en permanence le voisinage des dislocations et ces dernières se déplacent à vitesse réduite, on parle alors de domaine de trainage. Entre ces 2 domaines se trouve le domaine PLC. Il faut aussi noter que dans ce domaine, le vieillissement dynamique induit généralement une sensibilité inverse inhabituelle à la vitesse de déformation.

Mes sujets de recherche liés à l'étude de ces phénomènes sont résumés dans la suite de ce chapitre sous trois axes principaux :

1. La caractérisation expérimentale des instabilités par la réalisation d'essais de traction sur une large plage de vitesse et de température, et par l'observation des phénomènes de localisation de la déformation.

2. La modélisation du vieillissement statique et dynamique et des phénomènes associés à l'aide d'un modèle élasto-visco-plastique régularisé.

3. L'étude de l'influence des instabilités de vieillissement sur la rupture des alliages métalliques.

Un certain nombre de ces résultats expérimentaux et de modélisation sont regroupé sous forme interactive à l'adresse suivante : http://mms2.ensmp.fr/Aging/index.htm

Caractérisation expérimentales des instabilités

Les instabilités visco-plastique de vieillissement (Lüders et PLC) ont été étudiées dans le cadre de plusieurs thèses et stages sur différents alliages métalliques. En fonction des matériaux et des objectifs des études, différentes techniques expérimentales ont été utilisées, le point de départ commun étant la réalisation d'essais de traction sur éprouvettes lisses (plates ou cylindriques).

Dans certaines études c'est une exploration exhaustive des propriétés en traction qui a été réalisée sur une large plage de températures et de vitesses de déformation afin de caractériser le domaine d'existence des instabilités. Ce fut le cas lors de la thèse de H.Wang sur l'étude de l'effet PLC dans un acier C-Mn où le matériau a été testé pour 7 températures (de 20°C à 350 °C) et 4 vitesses de déformation. Le même travail avait été réalisé dans ma thèse sur un super-alliage à base de Nickel pour des température plus élevées, le centre du domaine PLC étant pour cet alliage autour de 500°C. On peut ensuite représenter l'évolution de la contrainte en fonction de la température, de la déformation, ou de la vitesse de déformation ; ou en fonction de 2 de ces 3 variables comme représenté sur la figure 2.

Dans le cas des alliages d'aluminium les instabilités sont maximales à température ambiante. Nos études sur ces alliages se sont concentrées sur l'influence de la vitesse de déformation sur :
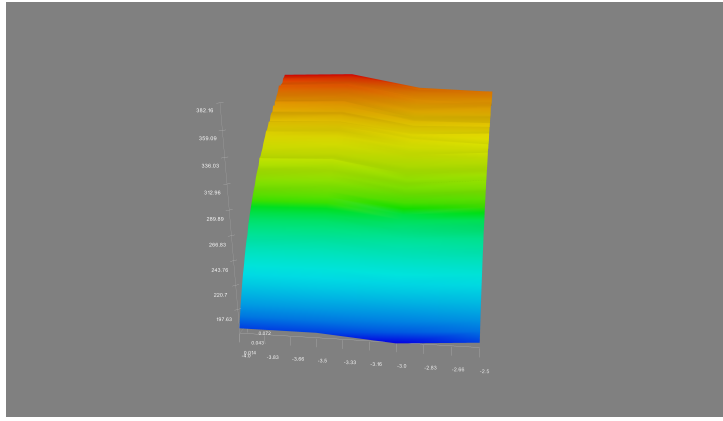
FIGURE 2 – Evolution de la contrainte expérimentale en fonction de la vitesse de déformation et de la déformation pour un alliage d'aluminium (G.Peyre,M.Mazière,2010). On peut observer un domaine de sensibilité inverse à la vitesse de déformation pour les vitesses intermédiaires.

— l'apparition des oscillations sur les courbes de traction et la définition d'une déformation critique (cf. figure 1(b)), travail effectué dans le cadre d'une collaboration avec H.Dierke de TU Braunsweig [199].
— le type et le nombre de bandes observées post-mortem à la surface des éprouvettes comme sur la figure 3, travail réalisé dans le cadre du stage de G.Peyre.
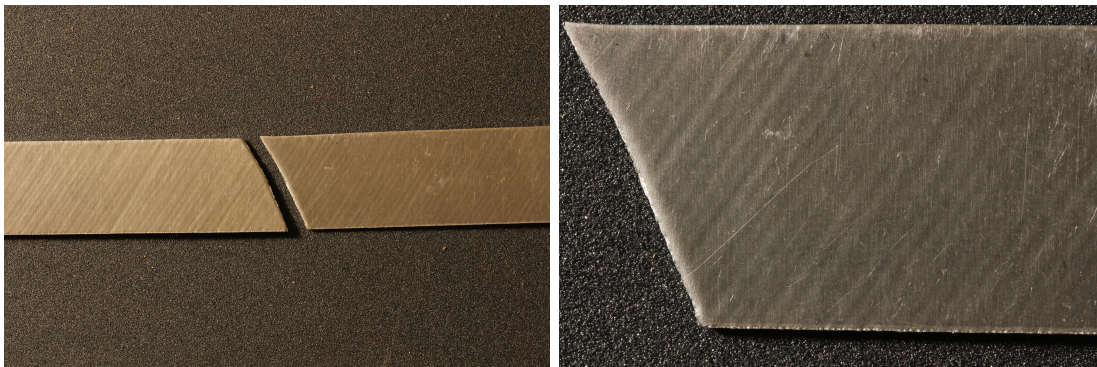
FIGURE 3 – Observation de bandes de localisation de la déformation à la surface d'un éprouvette en aluminium après rupture de cette dernière (G.Peyre,M.Mazière,2010). On remarque que la l'angle de rupture et celui des bandes de localisation est identique ce qui suggère un lien entre les phénomènes de vieillissement observable pour cet alliage et la rupture du matériaux.

Quand cela est possible et utile on peux aussi observer les bandes de localisation de la déformation à l'aide de techniques expérimentales avancées comme la mesure par thermographie optique ou la corrélation d'image. La première méthode à été utilisée dans le cadre de la thèse de D.Colas (cf. figure 4) pour observer les bandes de Lüders dans le tantale à température ambiante [209]. Cette méthode s'est révélée particulièrement efficace pour observer ce phénomène très diffus mais très prononcé (plusieurs % de déformation dans la bande) dans ce matériau. La mesure de champs par corrélation d'image a elle été utilisée dans la thèse d'A.Marais pour observer les bandes de Lüders dans les aciers C-Mn [198]. Il a été possible d'en extraire des profils de déformation et d'en déduire les caractéristiques cinématiques des bandes observées à savoir la largeur, sa vitesse, la déformation transportée,... Le même type de mesure a aussi été réalisé dans la thèse de J.Lorthios pour caractériser les bande de type Portevin - Le Chatelier dans un acier TWIP à très haute résistance.
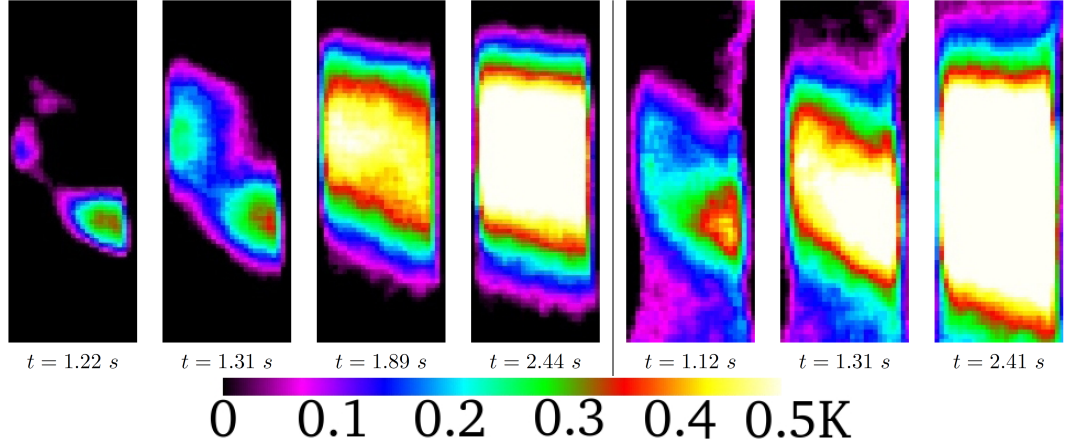
$t = 1.22\ s$ $t = 1.31\ s$ $t = 1.89\ s$ $t = 2.44\ s$ $t = 1.12\ s$ $t = 1.31\ s$ $t = 2.41\ s$

0 0.1 0.2 0.3 0.4 0.5K

FIGURE 4 – Observation d'une bande de Lüders diffuse dans du tantale par thermographie optique. Le passage d'une bande de plasticité engendre un échauffement local observable à l'aide d'une caméra thermique à haute résolution [209].

Enfin plus récemment l'apparition d'instabilités a aussi été relevée dans un super alliage à base de Cobalt lors d'essais cycliques à 600°C [206, 222]. Dans le cadre du stage de Q.Pujol, différentes vitesses et amplitudes de chargement ont été étudiées, cette dernière rajoutant une variable supplémentaire au triptyque température, temps, déformation. Ceci a permis de tester la robustesse des modèles mécaniques présenté dans le section qui suit.

En conclusion de cette partie on peux insister sur le fait que les instabilités visco-plastiques liées au vieillissement sont observables dans de nombreux alliages métalliques, du moins dans une certaine plage de température variant d'un alliage à l'autre. Ces phénomènes sont contrôlés par le trio de variable temps, température, déformation. Les bandes de localisation de la déformation sont observables à l'aide de méthodes modernes de mesures de champs et les grandeurs mesurées permettent une modélisation pertinente et réaliste des effet Lüders et PLC.

Modélisation des instabilités

La modélisation mécanique des instabilités visco-plastique de type Lüders et PLC s'effectue principalement au niveau macroscopique à l'aide du modèle proposé par Kubin, Estrin, et Mc-Cormick (modèle KEMC) en 1988 et 1989 [85, 86]. Ce modèle s'inspire d'une série d'articles consacrés à la compréhension et à la modélisation des effet de vieillissement par la déformation : [23, 50, 57, 66, 76]. Il est construit à partir d'un modèle élasto-visco-plastique classique auquel on ajoute un sur-écrouissage attribué aux effets de vieillissement. Ce sur-écrouissage est une fonction d'une variable interne supplémentaire notée t_a et appelé temps de vieillissement. t_a est contrôlée par une équation d'évolution où intervient la déformation plastique ce qui permet de modéliser d'un point de vue macroscopique les interactions entre les dislocations et les atomes en solution et ses conséquences en terme d'évolution de la contrainte. Ce modèle permet aussi d'obtenir une sensibilité inverse de la contrainte à la vitesse de déformation. Son utilisation lors de simulations par éléments finis d'éprouvettes en traction permet de reproduire les instabilités observées expérimentalement à savoir les oscillations sur la courbe de traction et la localisation de la déformation dans des bandes de plasticité comme sur la figure 5. Une grande partie de mes activités de recherche s'articule autour de ce modèle avec plusieurs objectifs :
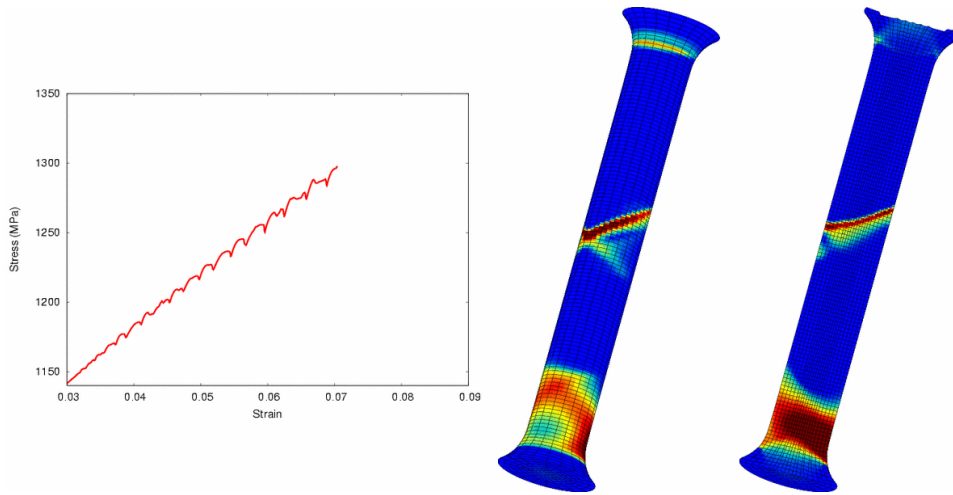
22

FIGURE 5 – Simulation de l'effet PLC dans une éprouvettes lisse cylindrique en super alliage base Nickel à 500°C. La première image montre des bandes de vitesse de déformation plastique à la surface de l'éprouvette lors des oscillation. La seconde est la même image en coupe [189].

1. **Proposer des méthodes robustes d'identification du modèle sur une large plage de vitesse de déformation et de température.**

   Les simulations comme celle de la figure 5 étant très longues, il est indispensable de pouvoir identifier le modèle à l'aide de simulations sur un point matériel – donc en l'absence d'instabilités – tout en garantissant que ces dernières apparaissent ensuite sous une forme cohérente avec les mesures expérimentales lors des calculs sur éprouvettes. Pour cela il est nécessaire d'avoir une bonne compréhension des équations du modèle et de l'effet des différents paramètres. On peut pour cela tracer la surface de réponse du modèle représentant l'évolution de la contrainte en fonction soit du couple déformation/vitesse de déformation (cf. figure 6 ou 8(a)), soit en fonction du couple température/vitesse de déformation (cf. figure 7). Dans le premier cas on peut voir comment l'introduction du sur-écrouissage lié au vieillissement fait apparaître un domaine de sensibilité inverse à la vitesse de déformation dans lequel vont apparaître les instabilités. Dans le second cas qui correspond à l'identification multi-température du modèle sur les résultats expérimentaux obtenus dans le cadre de la thèse de H.Wang sur les aciers C-Mn, on peut observer une fronce et par conséquent là aussi la présence d'une zone d'instabilité hachurée en noir sur la figure 7.

2. **Prédire analytiquement le déclenchement des instabilités lors des calculs par éléments finis.**

   La sensibilité inverse à la vitesse de déformation est une condition nécessaire mais pas suffisante pour l'apparition des instabilités. Un critère basé sur une analyse de perturbation linéaire avait été proposé dans de nombreux articles mais s'était toujours révélé trop prédictif lors des comparaisons avec les simulations par éléments finis [179]. Dans un article issue d'une collaboration avec H.Dierke (pour la mise à disposition de ses résultats expérimentaux), un nouveau critère a été proposé en reprenant l'analyse de perturbation mais en tenant compte du caractère irréversible de la déformation plastique [199]. Le nouveau critère proposé permet une prédiction précise de l'apparition des instabilités et peut ainsi être utilisé pour accélérer fortement les procédures d'identification des paramètres. Ce résultat est illustré sur la figure 8(b) où l'on voit pour différentes vitesses de déformation la valeur de déformation critique de déclenchement des instabilités lors de calculs par élément finis, et les prédictions des 2 critères.
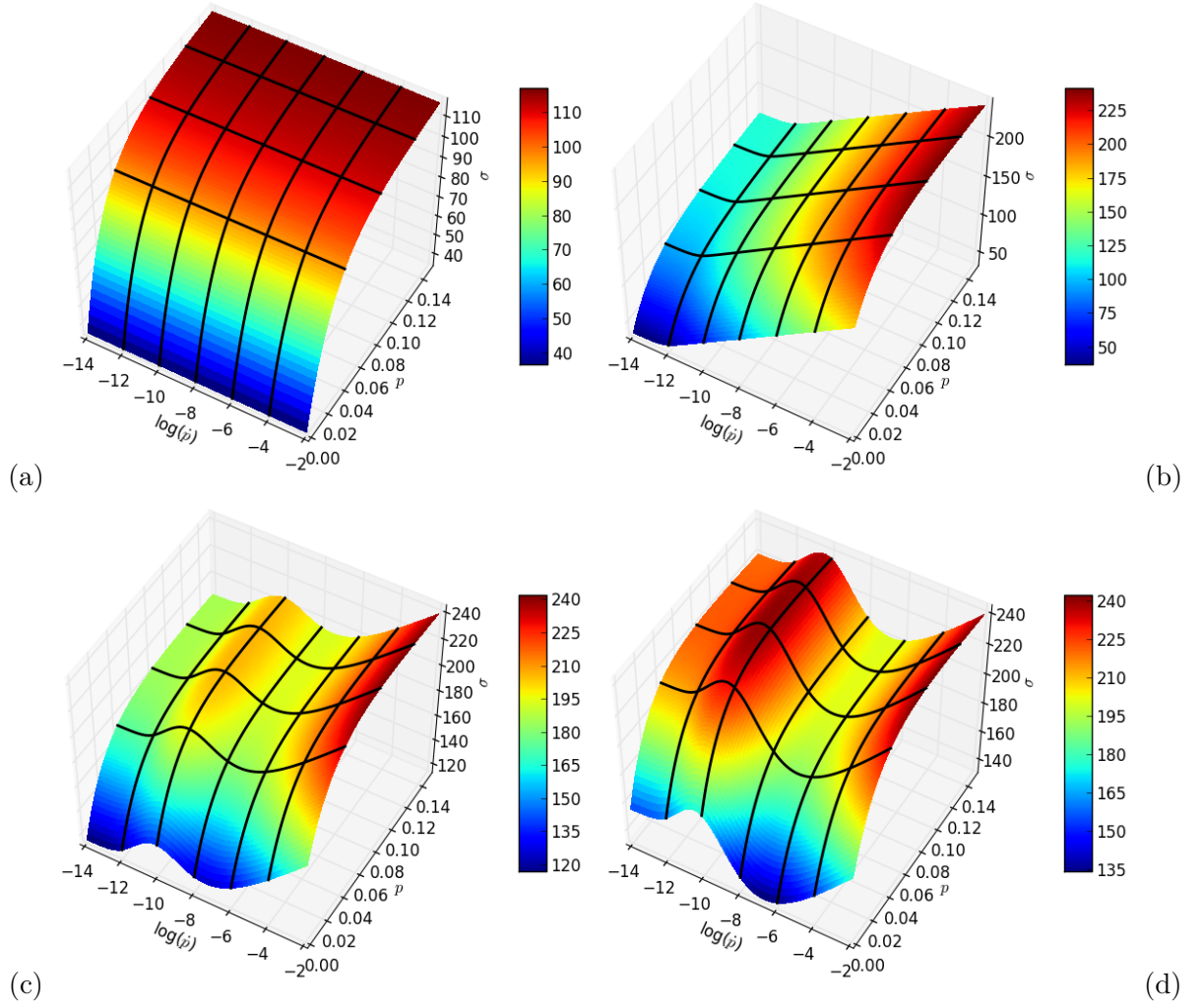
23

FIGURE 6 – Evolution de la contrainte en fonction de la déformation plastique cumulée (p) et de la vitesse de déformation plastique cumulée ($\log(\dot{p})$) pour (a) un modèle élasto plastique, pas de dépendance à la vitesse de déformation, (b) un modèle élasto-visco-plastique classique avec une sensibilité positive à la vitesse de déformation (c) le modèle KEMC avec un terme de sur-écrouissage faible (d) un terme de sur-écrouissage plus élevé. Dans les 2 derniers cas on retrouve une zone de sensibilité inverse à la vitesse de déformation autour de $\dot{p} = 1e - 8s^{-1}$.

3. Régulariser le modèle KEMC.

Les phénomènes de localisation de la déformation donnent naissance dans les simulations élément finis à un problème de dépendance au maillage des résultats. Il est généralement du à une perte d'ellipticité du problème aux limites. Le problème a été résolu dans des cas similaire (striction, endommagement, fissuration) par une régularisation des modèles mécaniques basé sur l'introduction de termes de gradient d'ordre supérieur. Ce phénomène a été mis en évidence pour les instabilité elasto-plastique- de vieillissement dans le cas des localisations de type Lüders [198] et PLC [189]. Une régularisation du modèle KEMC a été proposée en introduisant le second gradient de la déformation. La longueur interne introduite lors de cette régularisation du modèle a été identifiée à partir de mesures de champs expérimentales par corrélation d'image [198]. Dans une étude connexe menée avec S.Forest, une solution analytique a été proposée pour le problème précédant [221]. Il a été démontré dans cet article que le niveau de contrainte du plateau de Lüders peut être
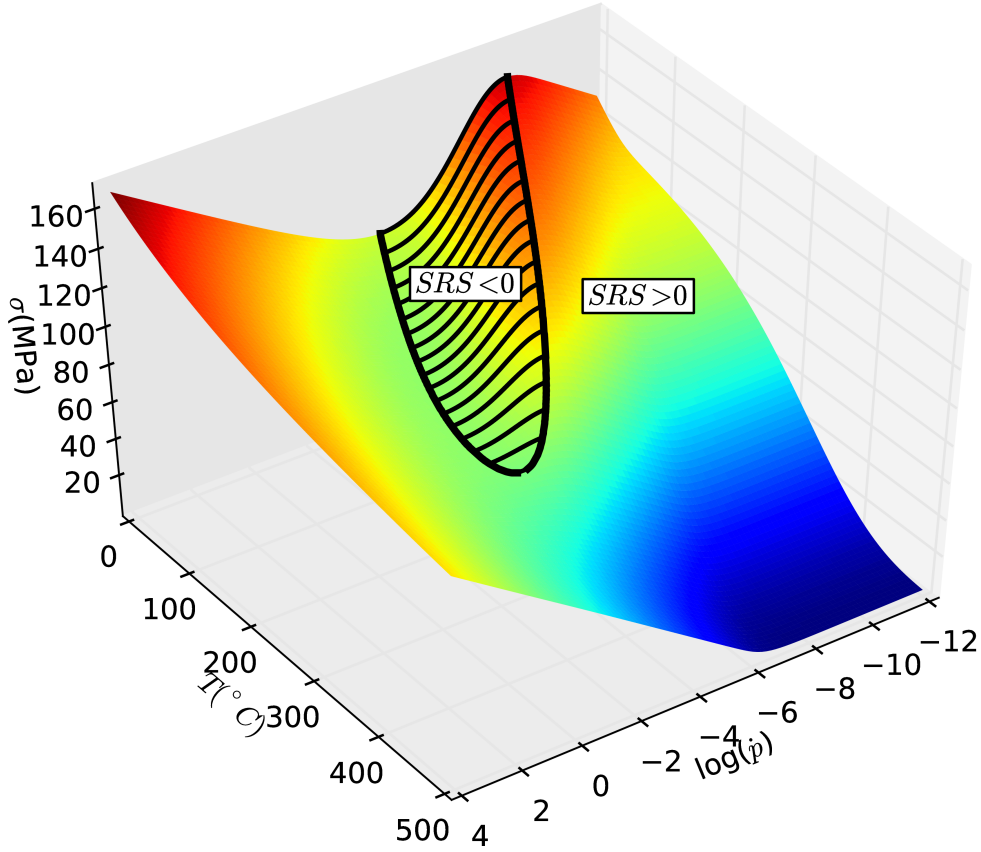
FIGURE 7 – Evolution de la contrainte en fonction de la température et de la vitesse de déformation ($\log(\dot{p})$) pour une déformation de 1%. La contrainte est tracée à partir du modèle KEMC et des paramètres identifiés sur l'acier C-Mn étudié dans la thèse de H.Wang [202]. Une zone d'instabilité ($SRS < 0$) apparaît sur la fronce en dessous de 350°C.

prédit à partir de la loi d'écrouissage locale en suivant une loi des aires de type Maxwell. Ce résultat a permis de proposer une méthode d'identification rapide et robuste du modèle KEMC dans le cas du vieillissement statique.

En conclusion de cette partie sur la modélisation des instabilités visco-plastiques de vieillissement, on peut mettre en avant que nos recherches sur le modèle KEMC ont permis de proposer une méthode d'identification rapide et efficace des paramètres pouvant s'appliquer à de nombreux matériaux sensibles au vieillissement statique ou dynamique. Notre analyse de perturbation linéaire corrigée permet ainsi de faire le lien entre les équations du modèle et l'apparition des phénomènes de localisation. Les travaux sur la régularisation du modèle ont permis de garantir des simulations robustes utilisables pour l'étude de la rupture des matériaux (cf. partie suivante). Enfin la solution analytique de la propagation d'une bande de Lüders dans un milieu du second gradient constitue une solution originale de référence permettant une compréhension fine et exacte du phénomène en explicitant le lien entre le comportement local du matériaux et la réponse de l'éprouvette.
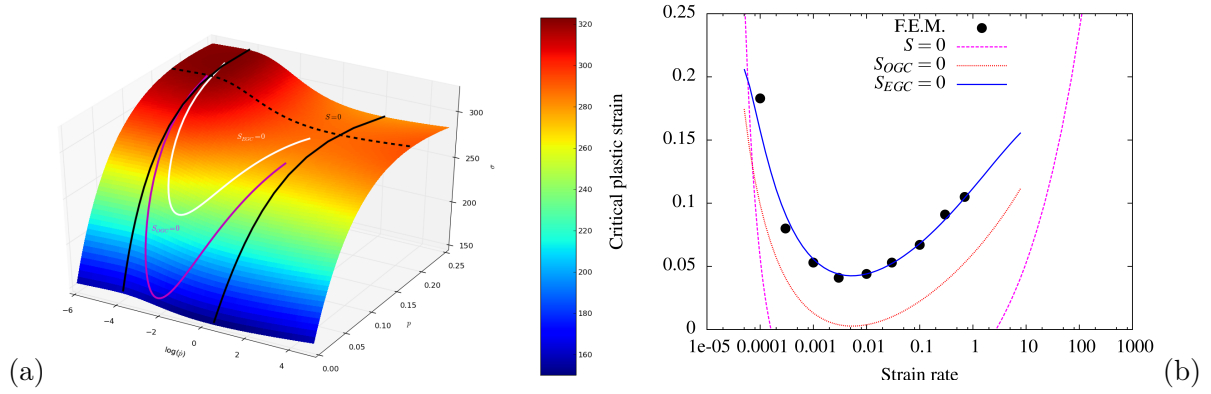
FIGURE 8 – (a) Evolution de la contrainte en fonction de la déformation plastique cumulée (p) et de la vitesse de déformation plastique cumulée ($\log(\dot{p})$) pour un alliage d'aluminium. La zone de sensibilité négative est matérialisée par les trais noir. Les critère de stabilité issus de l'analyse de perturbation linéaire sont matérialisé en violet et blanc. (b) Déformation plastique critique de déclenchement des instabilités pour les simulations éléments finis et comparaison avec les prédiction données par trois critères différents. L'ancien critère est noté $S_{OGC} = 0$, le nouveau proposé dans [199] est noté $S_{EGC} = 0$.

Conséquences des instabilités sur la rupture

Il est admis depuis longtemps que les instabilité visco-plastiques de type vieillissement ont une influence importante sur la rupture des alliages métalliques, pour le vieillissement statique comme pour le vieillissement dynamique, chacun à leur manière.

Dans le cas des bandes de Lüders c'est l'augmentation de limite élastique liée au pic de contrainte qui peut influencer la rupture fragile des éprouvettes de résilience de type Charpy. Ce phénomène a été étudié en détail dans la thèse de A.Marais [198, 220] sur un acier C-Mn. Pour cela le comportement du matériaux a été caractérisé en traction entre -150°C et 20°C, avec une attention particulière portée à l'étude du pic de traction et du plateau de Lüders (cf. figure 1(a)). Le modèle KEMC a été identifié à l'aide des résultats analytiques présentés dans la partie précédente, puis ce modèle a été utilisé pour simuler des essais de résilience de type Charpy (cf. figure 9). En parallèle, des essais de résilience ont été effectués sur la même plage de température pour le matériau de base, le même matériau écroui de 5%, et toujours le même matériau écroui de 5% puis vieilli 30 minutes à 250°C. Des courbes de transition ductile/fragile donnant l'énergie de rupture en fonction de la température ont été tracées pour les 3 conditions. Un modèle d'approche locale de la rupture fragile de type Beremin a ensuite été identifié à -20°C à partir d'un grand nombre d'essais identiques réalisés sur le matériau de base. Le modèle a ensuite été appliqué à toutes les températures et sur les trois conditions afin d'obtenir des courbes numériques de transition ductile/fragile à comparer aux courbes expérimentales. On peux ainsi montrer que l'augmentation de limite élastique liée au pic de traction, combinée à la localisation de la déformation en fond d'entaille liée aux bandes de Lüders augmente la température de transition ductile /fragile et fragilise en conséquence le matériau pour son utilisation industrielle.

Dans le cas de l'effet Portevin - Le Chatelier, la relation entre les oscillations sur la courbe de traction et la rupture précoce d'éprouvettes de résilience est mise en avant dès 1909 par A. Le Chatelier. Il explique ainsi que la chute de résilience du matériau observée autour de 400°C dans les aciers doux est due au même phénomène que les oscillations observées lors d'essais de traction vers 200°, la différence de température s'expliquant par une différence de vitesse de sollicitation
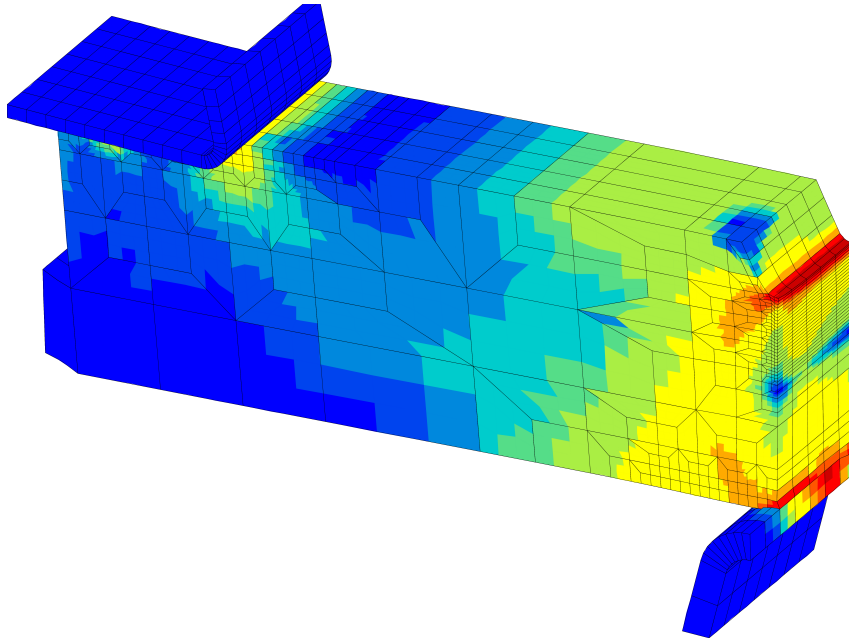
FIGURE 9 – Simulation de la rupture fragile d'une éprouvette de type Charpy en acier C-Mn à l'aide du modèle KEMC identifié entre -150°C et 20°C [220]

entre les deux types d'essais. Ceci est cohérent avec la fronce de la figure 7 ou l'on peut voir que le domaine des instabilité augmente vers les plus hautes températures lorsque la vitesse augmente (et inversement). Ce lien entre vieillissement dynamique et rupture ductile a été ensuite étudié de nombreuses fois depuis cette époque et a fait l'objet de certains de nos travaux sur des alliages modernes.

Dans ma thèse la relation entre l'effet PLC et la rupture des éprouvettes de traction lisses et entaillées a été étudiée sur un super alliage à base de Nickel. Comme on peux le voir sur la figure 10, le mode de rupture d'éprouvette de traction lisse diffère fortement lorsque l'on travaille en présence (à droite) ou non (à gauche) d'instabilités de type PLC. Il semblerait en effet que la localisation de la déformation liée au PLC (visible sur la figure 5) au cours de la déformation plastique entraine la localisation finale (et donc la rupture) sous forme d'une bande de plasticité fixe, ce qui n'est pas le cas à 20°C où la striction est alors plus diffuse.

Le lien entre le mode de rupture observé et la présence des instabilités a été étudié plus en détail dans la thèse de H.Wang sur un acier C-Mn. La série d'essais de traction effectués sur une large plage de température et de vitesse de déformation a permis de confirmer le fait que la rupture s'effectue dans une bande de localisation inclinée uniquement au cœur du domaine d'instabilité, comme on peut le voir sur la figure 11. Le fait que la bande de localisation finale entrainant la rupture soit issue d'une bande de localisation de type PLC a été validé par calculs élément finis en utilisant le modèle KEMC. En complément de cette analyse des essais sur éprouvettes entaillées et de type CT ont également été effectués pour caractériser la perte de ductilité et de ténacité dans le domaine des instabilités. Un critère de rupture ductile de type Rice et Tracey a été utilisé pour tenter de prédire la rupture des éprouvettes entaillées sur une large plage de température. Il a ainsi pu être montré que le vieillissement dynamique entraine une baisse de ductilité principalement en augmentant l'écrouissage du matériaux dans le domaine des instabilités, les phénomènes de localisation de la déformation étant de second ordre pour la rupture de telles éprouvettes [202, 205].

Dans la thèse de J.Lorthios, des oscillations de type PLC et des bandes de localisation ont été observées sur un acier TWIP à température ambiante. L'étude de la rupture de ce matériau
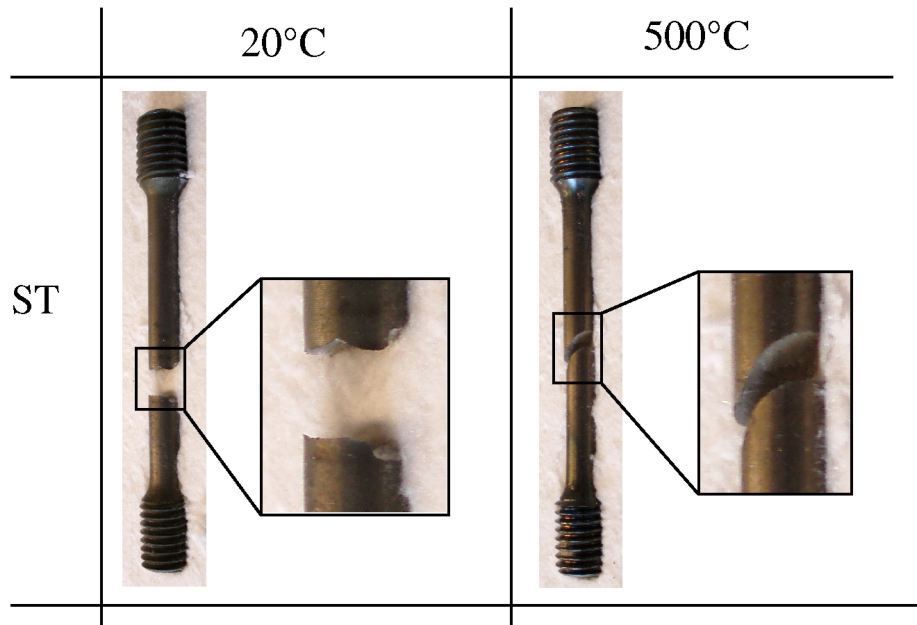
FIGURE 10 – Mode de rupture d'éprouvettes de traction lisses en super-alliage à base Nickel Udimet720. L'éprouvette de gauche est sollicitée en dehors du domaine des instabilités alors que celle de droite montre sur sa courbe de traction de nombreuses oscillations typique de l'effet Portevin - Le Chatelier [159].

a donc été effectuée en tenant compte de sa sensibilité inverse à la vitesse, et des effets de localisation inhabituels pouvant subvenir dans les éprouvettes entaillées et de ruptures testés. L'analyse par éléments finis en utilisant le modèle KEMC a montré que les effets de sensibilité inverse à la vitesse sont de premier ordre pour le calcul des champs mécaniques et par conséquent pour la prédiction numérique de la rupture.

Enfin dans la thèse d'A.Marchenko, des éprouvettes CT en Titane non allié ont été testées dans un domaine ou le matériaux présente des instabilités visco-plastiques de type Lüders et PLC. Le rôle des atomes d'Hydrogène et d'Oxygène (responsables des instabilités) sur la rupture de ce matériau a été étudié en chargeant et en déchargeant ce matériaux en H et en O, et en testant ensuite sa résistance à la rupture.

Dans tous les exemples présentés dans cette partie la démarche est finalement souvent la même :

1. Caractériser le comportement en traction du matériau sur une large plage de température, en portant une attention particulière aux instabilités visco-plastiques et à la localisation de la déformation (par exemple à l'aide de mesures de champs locales).

2. Identifier le modèle KEMC à l'aide des courbes de traction et des mesures locales.

3. Réaliser sur la même plage de température des essais pour caractériser la rupture du matériau : éprouvettes entaillées, de type CT, Charpy,...

4. Identifier un critère de rupture adapté (Beremin, Rice et Tracey,...), ceci à une température de référence en général hors du domaine des instabilités.

5. Simuler les essais de rupture et comparer les prédictions obtenues avec le critère de rupture avec les expériences afin de quantifier et d'expliquer l'influence des instabilités de vieillissement sur la rupture

6. Le cas échéant, extrapoler les résultats obtenus vers des températures et vitesses non sollicitées ou non sollicitables expérimentalement
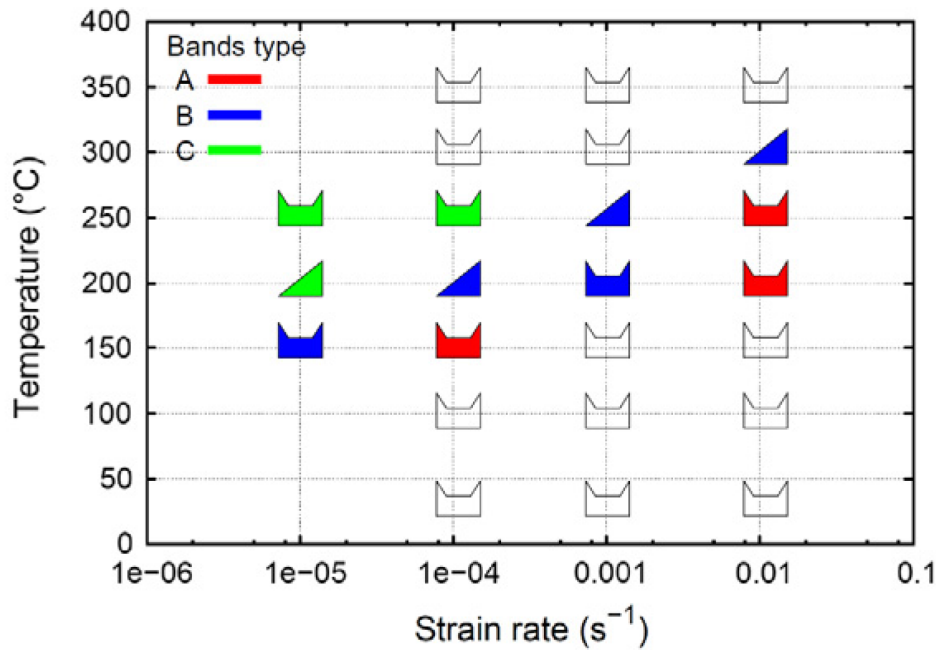
FIGURE 11 – Type de rupture d'éprouvettes de traction lisses cylindrique en acier C-Mn en fonction de la température et de la vitesse de sollicitation. On remarque que la rupture dans une bande de localisation inclinée n'est observée qu'au coeur du domaine PLC.

Il est important d'insister sur le fait que cette démarche s'appuie sur les 3 aspects du vieillissement par la déformations matérialisé par les trois parties de ce document : la caractérisation expérimentale, la modélisation, et les conséquences des instabilités visco-plastiques de type Lüders et PLC.

Pour aller plus loin certains axes de recherche peuvent être évoqués :

— Accéder à une compréhension plus fine des phénomènes de vieillissement en s'intéressant à l'échelle des grains à la localisation de la déformation en présence de bandes de Lüders ou d'effet PLC. Ceci peut être réalisé en associant des mesures de champs lors d'essais de traction in-situ dans un microscope électronique à balayage avec des simulations d'agrégats polycristallin et un modèle adapté tenant compte des effets de vieillissement. Ce type de démarche a été testé avec succès dans les thèses de D.Colas [209] sur le tantale et d'A.Marchenko sur le Titane (cf. figure 12) et constitue à coup sûr un axe de recherche d'avenir.

— Coupler le modèle de vieillissement KEMC et les modèles d'endommagement ductile avancés (type GTN, Rousselier) pour déterminer de manière directe l'influence réciproque d'un phénomène sur l'autre. En utilisant les outils d'imagerie moderne (tomographie, laminographie, corrélation d'image 3D) on peut avoir accès simultanément aux champs de déformation et à la croissance des cavités en présence d'instabilités de vieillissement et les comparer aux prédictions du modèle couplé décrit ci-dessus. Cette étude constitue le cœur de la thèse de S.Ren qui à démarré en 2014.

— S'intéresser aux instabilités de vieillissement pour des cas de chargement plus complexes que la traction simple monotone. Certaines équipes s'intéressent aux instabilités de vieillissement en cisaillement [213]. On peux imaginer faire de même sous chargement biaxial à l'aide d'une machine de traction adaptée. Enfin l'effet des instabilités de vieillissement sous chargement de fatigue, et leur influence sur la durée de vie, abordé lors du stage de Q.Pujol [222] constitue aussi un axe de recherche important à défricher dans le cas de

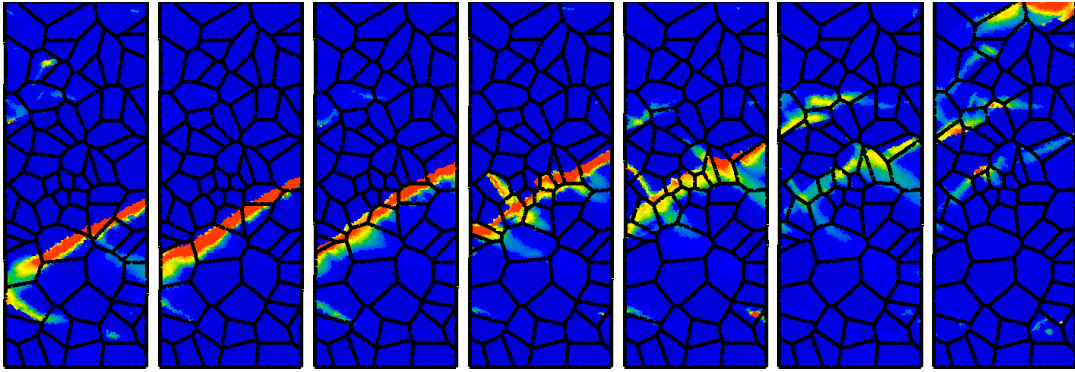nombreux alliages métalliques.

FIGURE 12 – Simulation de la propagation d'une bande de type Lüders dans un agrégat polycristallin en Titane non allié à l'aide du modèle KEMC couplé à un modèle de plasticité cristalline (A.Marchenko).

Résumé des activités d'enseignement

Le cours de mécanique des milieux continus de Mines ParisTech est suivi par l'ensemble des élèves de première année de l'école au premier semestre de première année. Il consiste en 7x2,5h de cours en classe entière donnés par Samuel Forest, et de 5x2,5h de travaux dirigé en petits groupes donnés par Samuel Forest, Gilles Damamme (CEA), Serge Kruch (ONERA), Vincent Maurel, Vladislav Yastrebov et moi même. Dans le cadre de ces petites classes nous apprenons aux élèves à résoudre étape par étape un problème aux limites simple de thermo-élasticité linéarisé. Les différentes étapes permettent aux élèves d'acquérir la maitrise des différents éléments de base de la mécaniques des milieux continus : tenseurs des contraintes et des déformations, compatibilité de la déformation, solutions de St Venant, élasticité linéaire,... Par ailleurs je réalise dans le cadre du cours des supports pédagogiques pour illustrer les cours de Samuel Forest qui sont ensuite disponibles en ligne sur le site du cours : http://mms2.ensmp.fr/mmc_paris/mmc_paris.php. On citera par exemple l'observation par photoélasticimétrie d'une poutre en PMMA en flexion 4 points comme illustré sur la figure 13.
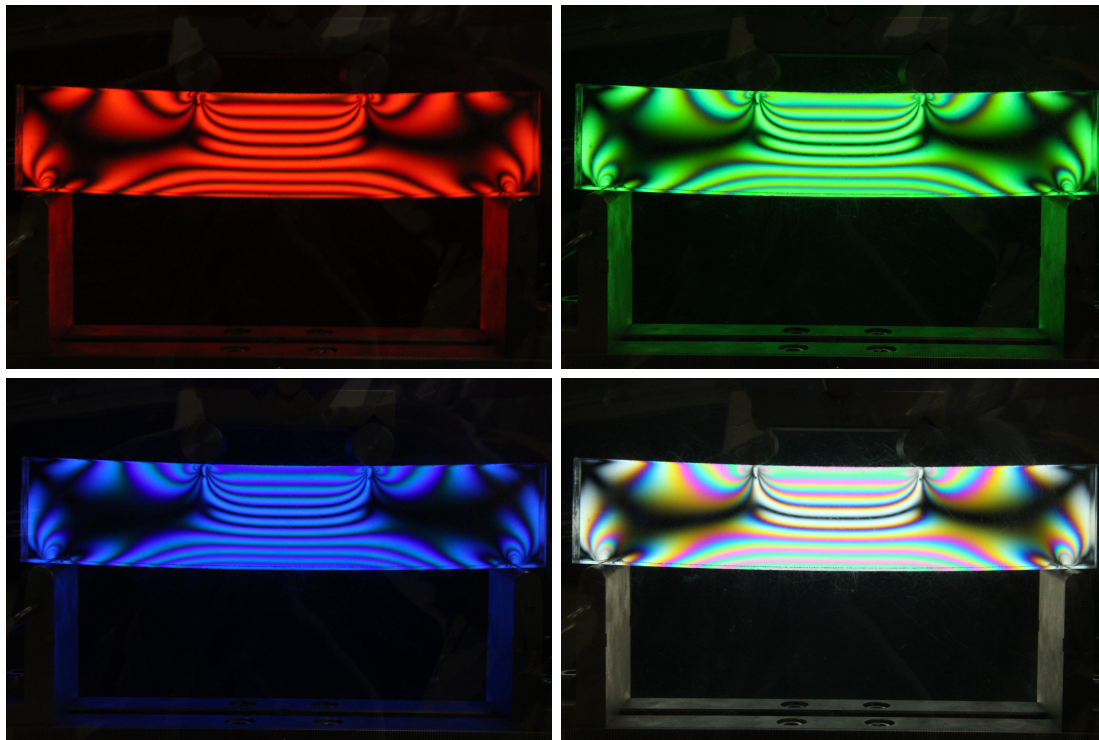

FIGURE 13 – Observation par photoélasticimétrie d'une poutre en PMMA en flexion 4 points (M.Mazière, 2010). La source lumineuse constituée d'un écran d'ordinateur est successivement monochromatique rouge, verte, bleue et poly-chromatique blanche.

Le cours de mécanique des matériaux solides de Mines ParisTech est suivi par l'ensemble des élèves de première année de l'école au second semestre de première année.

Il vient à la suite du cours de mécanique des milieux continus de Samuel Forest en abordant des thèmes complémentaires tels que : la théorie des poutres, la rhéologie des matériaux, l'hyper-élasticité, la mécanique linéaire de la rupture, et la stabilité. Il consiste en 5x1,5h de cours en classe entière donnés par David Ryckelynck et Sabine Cantournet, de 5x1,5h de travaux dirigés en petite classe donnés par les 2 enseignants précédents, Jean-Lin Dequiedt (CEA), et Pierre-Olivier Bouchard, et de 4x2,5h de mini-projets en demi-promotion donnés par une équipe d'environ 13 tuteurs et dont nous sommes responsables avec Henri Proudhon. Dans le cadre des cours en classe entière je réalise comme en MMC des démonstrations lors des séances afin d'illustrer le cours (flambage d'une poutre, rupture fragile et ductile, viscosité des matériaux élastomères, élasticité entropique,...).

Les mini-projets de mécanique des matériaux solides ont été initiés par Georges Cailletaud dans la version précédente du même cours. L'objectif est de proposer une approche inductive de la mécanique des matériaux en confrontant dans un premier temps les élèves à des observations et mesures expérimentales réalisées par eux même, puis en les aidant à modéliser les phénomènes observés à partir des outils théoriques étudiés dans les cours et TD de MMC et MMS. Pour cela on utilise du matériel de laboratoire (machines de traction, microscope optique, caméra HD,...) et quelques dispositifs pédagogiques conçu en général au centre des matériaux avec l'aide de notre atelier. Depuis 2010 j'ai contribué (en collaboration avec G.Cailletaud, H.Proudhon, S.Cantournet, Y.Tillier, P.O.Bouchard notamment) à développer cette approche en mettant en place un certains nombre de nouveaux sujets de mini-projets. On citera par exemple les sujets suivant (qui sont par ailleurs décrit en détail en ligne : http://mms2.ensmp.fr/public/mms_paris/miniprojets/miniprojet_accueil.php#m1t) :

— *Photoélasticimétrie sur une poutre en flexion*
— *Flexion et torsion d'un ski*
— *Traction d'une plaque trouée en PMMA*
— *Comportement vitesse/température d'une balle de squash*
— *Instabilité de type coque dans une balle de ping-pong (cf. figure 14)*
— *Flambage de canettes métalliques*
— *Comportement dans le temps de bouchons de vin en liège et synthétiques*

On trouvera plus d'informations sur le cours de mécanique des matériaux solides sur le site du cours : http://mms2.ensmp.fr/mms_paris/mms_Paris.php
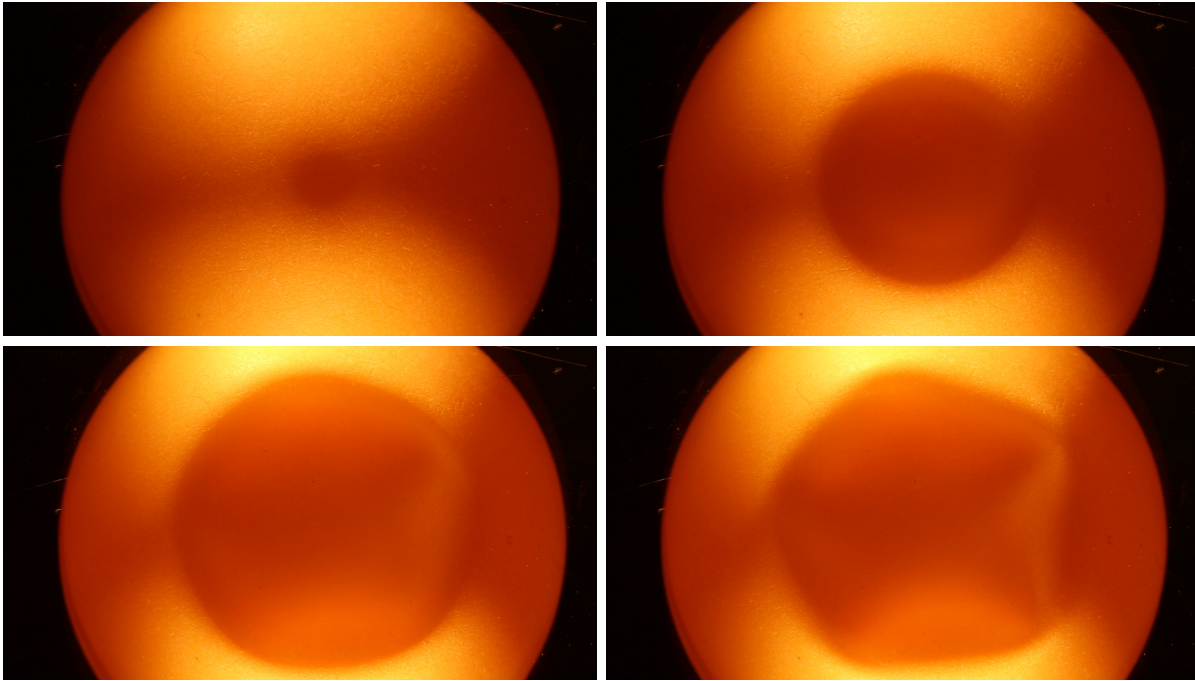
FIGURE 14 – Flambage de type coque d'une balle de ping-pong comprimée entre 2 plans rigides (l'un en acier est le plateau de la machine de compression, l'autre en PMMA). L'observation est rendu possible à travers le plan en PMMA via un renvoi d'angle à 45°par miroir. L'instabilité apparaît entre la deuxième et la troisième image sous forme circulaire, puis se transforme en pentagone lorsque la charge augmente (M.Mazière, 2015).

Semaine ATHENS - ParisTech
Non-Linear Computational Mechanics

Athens est un programme d'échange scientifique et culturel, créé en 1997, qui permet aux étudiants européens de suivre des cours dans les écoles ParisTech ou dans les universités partenaires étrangères et de participer à des activités culturelles. La semaine Non Linear Computational Mechanics a été créée dans ce cadre en 2008 par J.L.Chaboche et G.Cailletaud. Elle offre aux élèves de niveau Master un panorama des modèles et méthodes numériques disponibles en mécanique non-linéaire. La semaine s'articule autour de cours en classe entière et de travaux pratiques sur ordinateurs réalisé en utilisant le logiciel de calcul par éléments finis Zset. Depuis 2009, je participe à cet enseignement en organisant les séances de travaux pratiques et en donnant trois cours de 1,5h :

— *Les grandes déformations : variables et modèles*
— *Stabilité et localisation des évolutions visco-plastiques*
— *Modèles mécaniques pour l'endommagement et la rupture*

Plus d'informations et l'accès aux projets numériques sont disponibles sur le site du cours : http://mms2.ensmp.fr/msi_paris/accueil_msi_paris.php
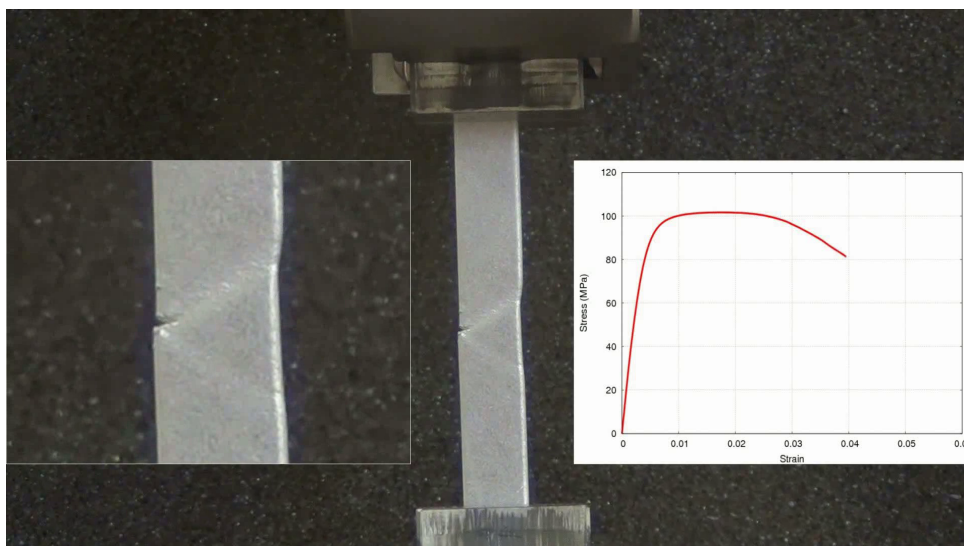
35

FIGURE 15 – Localisation de la déformation dans une bande inclinée lors d'un essai de traction sur une éprouvette en aluminium (M.Mazière, 2011). Cet essai de démonstration est réalisé tous les ans lors du cours sur la *Stabilité et localisation des évolutions visco-plastiques*.

Année pré-doctorale - PSL-ITI
Matériaux avancés : les défis actuels

L'année pré-doctorale du cursus doctoral de PSL - ITI (institut de technologie et d'innovation) est une année de préparation au doctorat destinée principalement aux élèves des écoles à vocation scientifiques de PSL (ENS ULM, Chimie Paris, ESPCI, Mines ParisTech). Crée en 2014 elle propose à une trentaine d'élèves (80 à terme) de suivre des cours de niveau master dans 3 domaines à choisir parmi 8 sans lien direct entre eux afin d'acquérir une culture pluridisciplinaire de haut niveau. Le parcours *"Matériaux avancés : les défis actuels"* a pour but de proposer une formation originale en science et génie des matériaux, en utilisant une approche multidisciplinaire depuis la chimie et la physique, jusqu'à la mécanique et la simulation numérique. Il s'articule autour d'exemples de matériaux modernes et innovants ainsi que de méthodes d'élaboration et de caractérisation avancées. Les grands défis d'aujourd'hui et de demain en science des matériaux sont également mis en avant dans cet enseignement.

En temps que responsable de ce parcours, je coordonne une équipe d'une vingtaine de professeurs des écoles mentionnées plus haut et de quelques intervenants extérieurs présentant sous forme de conférences de 2h leur sujet de prédilection. Je propose également aux élèves un TP de 8h sur la caractérisation des propriétés mécaniques des matériaux. Plus d'informations sur ce cursus sont disponibles à l'adresse suivante : http://www.univ-psl.fr/default/EN/all/research_fr/focus_sur_lannee_predoctorale.htm

Le Mastère Spécialisé de MINES ParisTech "Design des matériaux et des structures" (DMS) est une formation Bac+6 de haut niveau dans le domaine des matériaux et de la modélisation. Il couvre des domaines allant des propriétés physiques - mécaniques ou non - jusqu'au dimensionnement de pièces industrielles.

Dans le cadre de ce mastère, je m'occupe de l'ensemble de l'enseignement de mécanique des milieux continus. Le cours est organisé de manière à permettre aux élèves de résoudre analytiquement un problème aux limites simple, mais aussi de comprendre les éléments (variables, équations, méthodes,...) nécessaires à la résolution de problèmes plus complexes. Ainsi les grandeurs cinématiques et statiques de type tenseurs des déformations et des contraintes sont présentées de manière exhaustive afin de permettre l'écriture de lois de comportement diverses. L'exemple du comportement élastique linéaire et ensuite étudié en détail. Enfin la formulation du problème aux limites est présenté afin de permettre la résolutions des problèmes classiques de la MMC (traction, flexion, torsion, tube sous pression,...), et de servir de base au cours sur les éléments finis.

L'enseignement est dispensé sous forme des 6 blocs de 2x3h (cours+TD) suivants :

— *Cours 1 - Transformations du milieu continu*
— *Cours 2 - Equations de bilan*
— *Cours 3 - Le tenseur des contraintes*
— *Cours 4 - Les lois de comportement*
— *Cours 5 - Thermoélasticité linéarisée*
— *Cours 6 - Formulation du problème aux limites*

Le site du mastère est accessible à l'adresse suivante : http://dms.mat.mines-paristech.fr/

La parcours durabilité des matériaux et des structures pour l'énergie du master Mécanique des Solides et du génie Civil est un bloc d'enseignement de niveau M2 commun à l'université Pierre et Marie Curie et à l'Ecole Nationale des Ponts et Chaussées. Il vise à vise à "former des ingénieurs de très haut niveau scientifique, susceptibles de prendre en charge les problématiques de renforcement des installations anciennes produisant de l'énergie électrique (principalement Réacteur à Eau Pressurisée, thermique à flamme, barrages...) et les questions liées à l'estimation des durées de vie de technologies nouvelles (éolien, off-shore, Station de Transfert de l'Energie par Pompage, biomasse...)."

Dans le cadre de ce parcours nous proposons avec Samuel Forest un enseignement intitulé "Approche multi échelle de la plasticité des métaux" constitué de 5 séances de 4h. Je m'occupe personnellement de 2 séances traitant de :

— *Stabilité et localisation de la déformation liée à la plasticité*
— *Vieillissement par la déformation dans les alliages métalliques, phénomène de Lüders et effet Portevin - Le Chatelier*

Le détail du parcours DMSE est disponible à l'adresse suivante : http://www.master.sdi.upmc.fr/fr/mecanique/m2_specialite_mecanique_des_solides_et_du_genie_civil/parcours_durabilite_des_materiaux_et_des_structures_pour_l_energ.html

MODELING THE PORTEVIN - LE CHATELIER EFFECT IN METALLIC ALLOYS

Table of Contents

1 Introduction

The strain ageing phenomena such as Lüders bands and the Portevin - Le Chatelier effect are among the most fascinating physical and mechanical phenomena that can be observed in metallic alloys. They originate at the atomic scale from the interaction between a single dislocation and some solute atoms, and propagate through the scales up to failure of components. One of the most remarkable feature of strain ageing is from our point of view the ability of a very localized single unstable event lost in a overall stable (but close to instability) media to impose its will to the rest of the matter giving rise to a macroscopically unstable behaviour observable at the specimen level. Indeed, from almost one century mechanics of materials is partially based on the assumption that the global behaviour experienced at the macroscopic specimen scale is an average of all the local collective responses at a lower scale, typically at the dislocation level. The plastic deformation is heterogeneous and intermittent by nature at the dislocation scale, but the collective behaviour appears generally smooth and homogeneous at the macroscopic level. This is not the case for strain ageing manifestations like Lüders band and Portevin - Le Chatelier effect for which the way of thinking and the link between the scale has to be reconsidered.

Another very remarkable feature of strain ageing is to give rise to similar macroscopic manifestations in almost all metallic alloys, at least in a given range of strain rate and temperature. Lüders band and/or Portevin Le Chatelier effect have then been observed in BCC alloys based on α-Iron (Steels), Vanadium and Tantalum; in FCC alloys based on Copper, Aluminium, Nickel, Cobalt, and Gold; and in HCP alloys based on α-Titanium, Magnesium, and Zirconium. The solute atoms responsible for strain ageing differ between all this materials, some are interstitial, some are substitutional, but the basic microscopic mechanisms and the macroscopic manifestations on the stress/strain curves are very similar. This diversity of materials where strain ageing phenomena are observed is in a given sense a chance for the modelling researcher since if the physical mechanism are the same, a unique mechanical model should be able to reproduce strain ageing effects for all these materials. The main difficulty is to get together different communities that have different approaches of a similar problem : the community of aluminium, the community of steels, the community of Nickel and Cobalt based superalloy, and the community of hexagonal materials (Titanium and Zirconium). One objective of the present document is to show how the same mechanical model is suitable to simulate strain ageing phenomena in all these materials and can consequently help to understand the differences between them.

The Portevin - Le Chatelier effect is also one of the most interesting and difficult visco-plastic instability to deal with in the mechanics of material domain. It is neither a pure temporal nor a pure spatial instability but a coupling between both. The time dependant feature of the material is important, its possibility to deform differently in several locations of a given specimen too. The study of PLC bands either experimentally or numerically is somehow magical in the sense that in both cases the researcher is reduced to a simple observer trying to understand at least partially the chaotic behaviour taking place in front of him. It is to our knowledge the most visible macroscopic manifestation of the intermittent and heterogeneous nature of the plastic deformation that is more easy to observe at a lower scale.

Strain ageing has a strong influence on the base mechanical properties used by the engineers for the design of structures : the yield limit is affected by the static strain ageing and Lüders phenomenon, the ultimate tensile stress and the strain to failure are affected by the dynamic

strain ageing and the PLC effect. In the case of static strain ageing, it has been used by engineers as an advantage, giving rise to bake-hardening steels. However a good understanding of the phenomenon together with a reliable modelling are needed for an accurate prediction of strength of structure designed using such metals. In the case of dynamic strain ageing, the blue brittleness has been evidenced in iron and mild steels for more than 135 years, forbidding forming of these metals in a temperature range from 80 °C up to 300 °C. This detrimental behaviour of steels and its link with Portevin - Le Chatelier effect has been extensively studied from this period. This huge experience on steels has however not been fully extended to other metallic alloys. The knowledge on the influence of Portevin - Le Chatelier on mechanical properties – including failure – of Aluminium, Titanium, and Nickel based super-alloys are in a given sense rather late compared with the one on steels.

Contrary to what is affirmed in its subtitle, the present document will probably not assert to draw an exhaustive panorama of all aspect of strain ageing, from the level of dislocation up to design of structures. The topic is too wide and requires some knowledge in many different subjects like chemistry, physics, mathematics, mechanics, and computer science. A less pretentious synopsis of the present document is a detailed presentation of a particular mechanical model able simultaneously to account for some very important physical characteristics of strain ageing at the microscopic scale, but also to be simple enough to compute failure of specimens and industrial component using this model in finite element software. The best candidate for that purpose is a mechanical model inspired by many preliminary studies and proposed at the end of the 80's by Kubin, Estrin and McCormick (this model will consequently be denoted in the present document KEMC model).

The KEMC model is nowadays almost the only one used in finite element simulations of the Portevin - Le Chatelier effect for two main reasons :
— It reproduces the main PLC features i.e. the negative strain rate sensitivity and the propagating strain localisation bands.
— It only requires one additional internal variable and just a few number of additional parameters (between 4 and 8 depending on the version).
However the KEMC model also has some drawbacks that are due to its unstable nature :
— The finite element simulations are very long and hard to carry out. The numerical parameters have to be correctly calibrated to avoid numerical divergences and compute solutions of the mechanical problem.
— The strain localisation phenomena, even propagative, can lead to a strong mesh dependence of the finite element results. This dependence has to be evaluated and if possible eliminated by advanced methods and/or models.
— The identification of the material parameters is a real challenge. It can be done using finite element simulations on full specimens, but because of the first point it can be very long and uncertain. It can be done using material point simulations, but since these latter does not show any serration, the solution of the identification is just an approximate.
This last difficulty can be overcome by a complete knowledge of the KEMC model. For example the prediction of the onset of serration by a theoretical stability analysis as presented in this document enable to fix rapidly and reliably some parameters of the model. The KEMC model is also an excellent solution to model Lüders bands and static strain ageing phenomenon, even if in this case there exists some alternative mechanical models. However since the KEMC model is based on physical mechanisms, it is the only one that success to reproduce complex tensile experiments where ageing heat treatment are inserted during the deformation of the specimen [220].

This document is divided in five main chapters. The chapter 2 is an original and atypical

bibliographic review of experimental, theoretical, and numerical findings concerning strain ageing and principally the Portevin - Le Chatelier effect. Instead of a long list of articles embedded in some long and boring descriptions of each aspects of strain ageing, we decided to draw the history of PLC effect from the middle of the 19th century up to recently selecting 20 articles with an inevitable partial point of view. The aim of this chapter is to illustrate the genesis of the KEMC model in four main steps :

1. Some initial experimental observations of the strain ageing phenomena were made as soon as the first half of the 19th century. The heterogeneous and intermittent nature of the plastic deformation was at this period a subject of debate among scientists between those affirming that it was always the case, and those affirming that the deformation was smooth and homogeneous. At the end of the 19th century two main consequences of strain ageing are reported in details in two remarkable studies : the "blue britleness" of iron and mild steels by D.Adamson in 1878, and the propagating bands of localized plasticity at the surface of specimens by L.Hartmann in 1894-1895.

2. The debate on the nature of plastic deformation has been partially closed at the beginning of the 20th century by André Le Chatelier [2] who explained very clearly that for a given material (here iron or steel), the plastic deformation can be smooth and homogeneous at some temperatures, and serrated and heterogeneous for some others. The serrated yielding has then been reported in copper by E.N.Andrade in 1911, and in aluminium-zinc alloy by W. Rosenhain and L. Archbutt in 1912. Probably because of the very representative picture of serrated yielding in aluminium presented in their article in 1923, this atypical effect will finally be commonly called "Portevin - Le Chatelier" effect (PLC).

3. From 1950 up to 1980, the physics and mathematics of the now called Portevin - Le Chatelier effect are investigated by many authors. The work by A.H.Cottrell and B.A.Bilby in 1949 set the basis or the strain ageing phenomenon detailing the mechanical interactions between dislocations and solute atoms. The work by P.Penning in 1972 explains the link between the two main features of the PLC effect : the serrations on the tensile curves and the negative strain rate sensitivity of the average stress level.

4. At the end of the 80's, the understanding of the PLC effect is mature enough and researcher can propose a complete set of constitutive equations that can be used to simulate the Portevin - Le Chatelier effect at the specimen scale. This mechanical model is presented here via the two funding articles by P.G.McCormick in 1988 and Y.Estrin and L.P.Kubin in 1989.

In addition to these 20 selected articles, three tables are provided at the end of the document with non-exhaustive lists of articles related to :
— Experimental evidences of the PLC effect in aluminium alloys
— Experimental evidences of the PLC effect in other metallic alloys
— Finite element modelling of the Portevin - Le Chatelier effect

The chapters 3 and 4 focuses on the KEMC model based on a selection of our main results on the subject. They are organized as follow :
— In chapter 3 are recalled the constitutive equations of the original model, the extension that have been proposed by different authors during the last 20 years, and an example of identification of the model over a large range of strain rates and temperatures.
— In chapter 4 a detailed stability analysis of the KEMC model is presented. The problem of the numerical parameter (mesh, time step,...) is discussed, and some examples of post-bifurcation analysis are provided.

---

2. A partial Le Chatelier family tree is proposed figure 16. The interested reader can then place the relations between all the famous scientists of this family : Louis, Henry, André, Albert, and François.

Chapter 5 is devoted to failure analysis in presence of strain ageing phenomena like Lüders band or Portevin - Le Chatelier effect. This chapter is composed by two articles that we wrote on the subject in 2015 [220] and 2102 [202] . The first one investigates the influence of static strain ageing and Lüders band on brittle failure, while the second one the influence of dynamic strain ageing on ductile failure.

Instead of a summarizing conclusion, the last chapter number 6 contains 10 innovative projects on the topic for the next 10 years. The limits and the potential improvements of the KEMC model are discussed. It include the very topical question of the relation between strain localisation and ductile failure in metallic alloys. Some axes of research for getting faster and more reliable finite element simulations are proposed, these both objectives being not necessary compatible. Finally the challenges of the modelling of "strain-ageing like" phenomena that appear is some new and advanced materials (advanced high strength steels, metallic glasses, metal matrix composites,...) are presented.
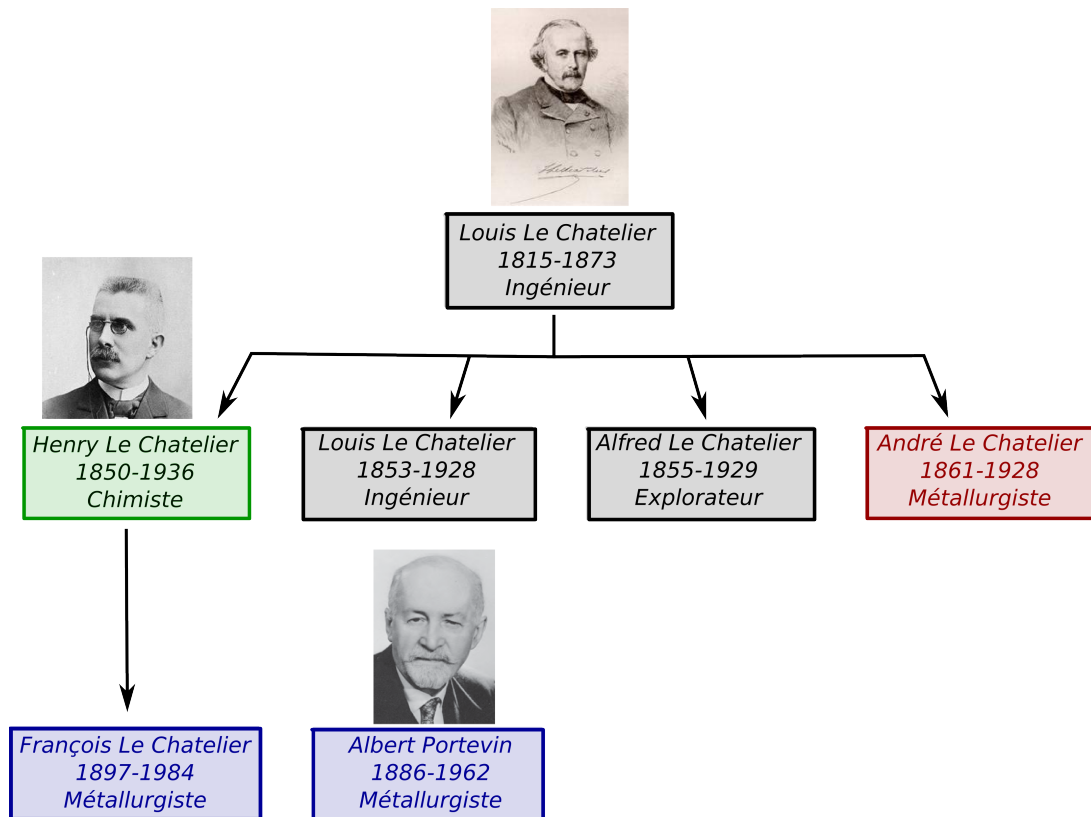
FIGURE 16 – Le Chatelier partial family tree from Louis to François. The Portevin - Le Chatelier effect is named so because of the article from 1923 [21] by the two author in blue : François Le Chatelier and Albert Portevin (included in the picture together with his co-worker). André Le Chatelier (in red on the picture) also wrote an article on serrated yielding and blue brittleness some years earlier in 1909 [18]. The most famous scientist of the family is however Henry Le Chatelier (in green), a French chemist known for the discovery of an equilibrium principle called "Le Chatelier's" principle.

2 Some selected articles relating the story of the Portevin - Le Chatelier effect

A quick research on the bibliographic databases (for example "Web of Knowledge") shows that there are more than 500 article related to Portevin - Le Chatelier effect since 1949. This is probably due to the diversity of the metallic material for which this effect can be observed (steels, aluminium alloys, titanium alloys, nickel or cobalt based super-alloys, zirconium alloys, tantalum,...). There are among them a very large number of articles devoted to the modelling of the PLC effect. Instead of presenting a long list of these articles we have decided in the present document to highlight 20 of them which are from our point of view among the most historically relevant ones. The choice of these 20 articles is highly subjective, the objective of this "best-of" is to describe the origin of KEMC model from the first observations of the PLC effect in the first half of the 19th century, to the development of the constitutive equations in the second half of the 20th century.
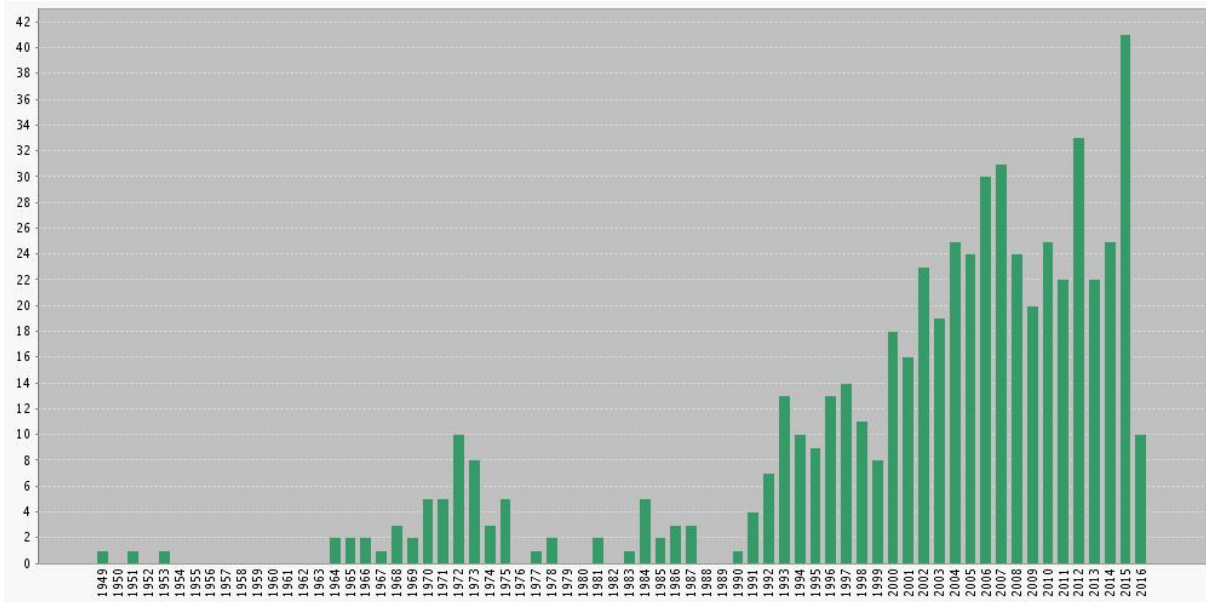
FIGURE 17 – Number of article per year including the words "Portevin - Le Chatelier" either in their title, their abstract, or their keywords.

2.1 The 19th century

Many articles and books of the 19th century dealing with the strength of metallic materials are citing the early work of M.Coulomb in 1784 [1] as one of the first relevant experimental and theoretical work on the topic. In this article some non radial traction/tension experiments are carried out on iron and brass wires using a very ingenious experimental device illustrated on figures 18. In addition to the interesting historical aspect of this work, it is amazing to see in the second part of the article how the author experiences plasticity of wires by applying very large rotation angles. A lot of basic concept of plasticity of metals are by the way intuited by

M.Coulomb and presented in this work like the existence of a yield limit, the hardening curve, and the effect of heat treatments that modify failure strength of the iron but not the elastic properties.
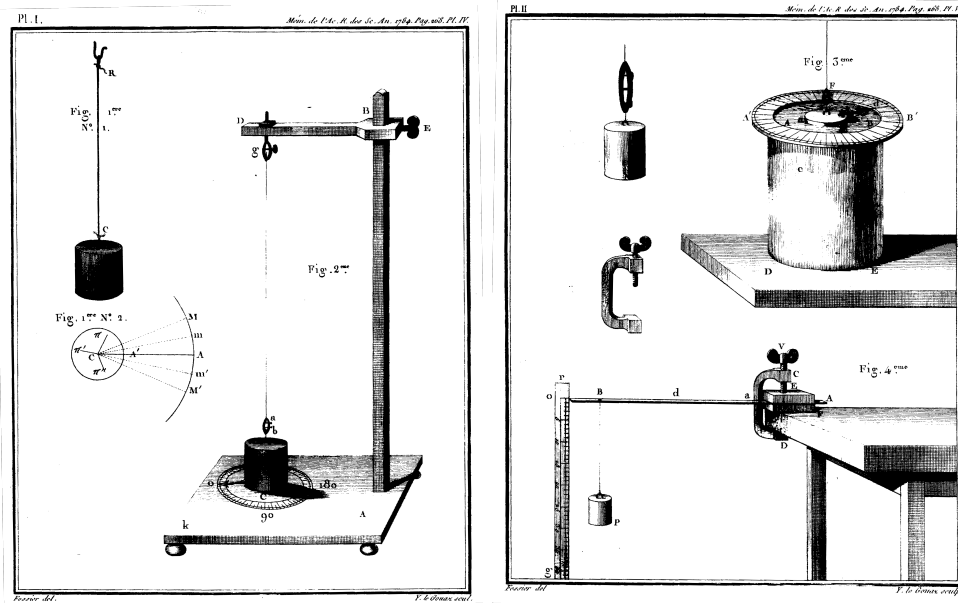

FIGURE 18 – Experimental device used by M.Coulomb for his research on torsion strength and elasticity of metal wires.

Almost 40 years latter, some more advanced experimental devices have been designed in order to load metallic plates, wire, and bars under tension, compression, bending, and torsion as reported for example in the remarkable work by A.Duleau [3]. At this time, the objective of most scientists was to estimate the coefficients of elasticity of metals like iron, copper, zinc, lead, silver, and platinum (see the work by G.Rennie [2] and T.Tredgold [5] for other examples). Indeed, it was yet commonly admitted that metals remain elastic – i.e. the load and elongation are proportional together, and the elongation returns to zero when the load is removed – only up to a given load or elongation level which was for example estimated by A.Duleau to 0.1% for some steels, and 0.45% for some others. Consequently, in the study of A.Duleau and in most of the ones of this period cited pages 70 to 76 in his book [3], the experiments were carried out prescribing relatively small loads in order to remain inside the elastic domain.

It seems that the first extensive study of the deformation of metallic materials in the plastic domain is due to F. von Gerstner almost at the same period [7]. By increasing the weight applied to piano iron wires up to failure, F. von Gerstner has investigated the non-linearity between load and elongation beyond the elastic limit. He even proposed a general equation for the relation between the load F and the elongation Δl formulated as follow :

$$F = \Delta l \left(a_1 - a_2 \times \Delta l \right) \tag{1}$$

A similar non linear (but logarithmic) relation between load and elongation was already proposed by J.Leslie in 1823 [4]. However, the true originality and novelty of the work by F. von Gerstner was the decomposition of the total elongation in a removable and a permanent contributions. This latter can directly be measured by unloading the specimen, giving access to the removable (now called elastic) deformation. F. von Gerstner observed a proportionality between the removable part of the deformation and the applied load, whatever this latter is, i.e. even close to failure. He consequently introduced a new and more convenient method to evaluate elastic constants in metals by making measurements before loading, under loading, and after unloading.

Contrary to what may be written in some recent articles [117], we did not found in the books and articles cited above any observation of non homogeneous and/or serrated plastic deformation that could be consider as an evidence of strain ageing. The first observations and discussions on this kind of phenomena are reported in the articles and books by F. Savart, M.A. Masson, J.V. Poncelet, and M.G. Wertheim that are presented hereafter.

[F. Savart, 1837] : Recherche sur les Vibrations longitudinales (*Annales de Chimie et de Physique*)[8]

In his article untitled *"Recherches sur les vibrations longitudinales"*, published in 1837, F. Savart focuses on the vibration of metallic rods, and on the sound produced by these latter. However some quasi-static tensile experiments are also reported by the author during which rods of copper, brass, steel, iron, and glass are loaded with successively increasing loads. Most of these experiments were carried out for loads small enough to remain in the elastic domain, but two of them reported in table page 387 and 388 of the article are more interesting and have to be commented.

F.Savart reported that during some tensile experiments on rods he observed a non homogeneous deformation of this latter : *"Et, en effet, l'expérience montre que des parties égales d'une bande, par exemple, ou d'un fil de métal, qui ont à supporter une tension égale, ne s'alongent pas, à beaucoup près, de la même quantité.* This heterogeneity of the deformation has been evidenced and quantified by the author using from our knowledge the first local strain measure of the history : he divided some copper rods whose gauge length was 0.8m in 8 divisions of 0.1m, and he carried out some precise measures of the elongation of each division for 5 to 7 different levels. The local and global strain vs. stress curves that can be plotted based on these experiments (tables page 387-388 of [8]) are given on figure 19.
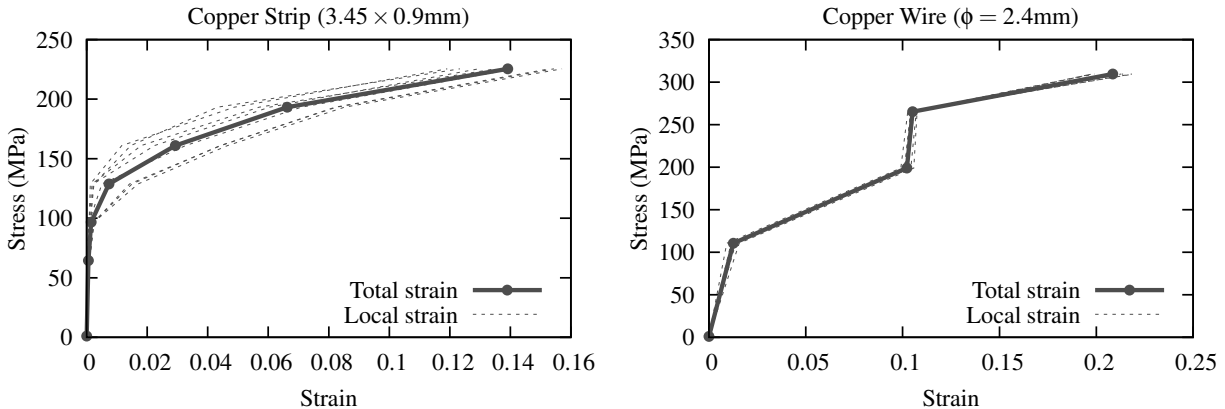
FIGURE 19 – Stress vs. global and local strain measures for tensile tests on copper strip (left) and wire (right) carried out by increasing the load applied to the rod.

The figure 19(left) corresponds to a tensile test on a copper strip. The global curve is rather smooth, but one should notice that the different local curves corresponding to the 8 local strain measures are very different and can even cross each other. This dispersion of the local curves outlines the heterogeneity of the plastic deformation as reported by the author. However this latter can be attributed to material processing of the rod. But it also suggests that the plastic deformation can be intermittent (with the propagation of bands ?) as it will be observed many years latter in the case of Portevin - La Chatelier effect. Another atypical phenomena can be observed on the figure 19(right) corresponding to a tensile test on a copper wire. In this case the

deformation appears much more homogeneous, but the global strain vs. stress curve presents a step in the plastic domain very similar to the ones observed one century and a half latter when Portevin - Le Chatelier effect is observed under constant stress rate.

[M.A. Masson, 1841] : Sur l'élasticité des corps solides (*Annales de Chimie et de Physique*)[9]

This article from M.A.Masson is presented by the author as a additional work to the one by F.Savart presented previously. The most interesting part for the present document is the additional experiment that has been carried out by M.A.Masson on copper rod and whose load vs. elongation curve is plotted on figure 20 [3]. The same steps than the one observed by F.Savart are reported by the author, and this latter comes to a quite definite conclusion concerning the intermittent deformation of solid bodies : *"les corps solides ne s'allongent pas d'une manière continue, mais par saut brusque"*. It will be shown in the following that things are more complex.
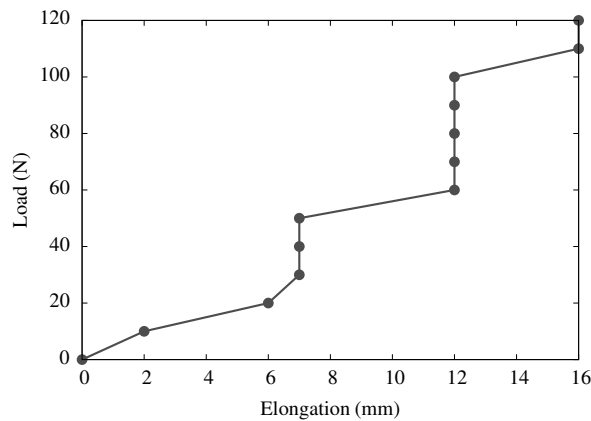

FIGURE 20 – Load vs. elongation diagram based on the measures of M.A.Masson ([9] table page 455). The dimensions of the specimen are not given in this case.

[J.V. Poncelet, 1841] : Introduction à la mécanique industrielle physique ou expérimentale (*Metz*)[10]

This book form J.V.Poncelet is from our point of view the reference one for this period since it contains the main knowledge on strength of materials from a theoretical and experimental point of view. Almost all the articles cited previously in the present document are presented and commented by J.V.Poncelet in his book. It also contain some unpublished results and one very innovative representation of the strength of material that was from our knowledge not used up to this book : the representation of tensile experiments via stress vs. strain diagrams like the one presented on figure 21 and 22.

This diagram is based on experiments on iron, brass, steel, and lead carried out by 3 scientists that are summarized in a table page 345 of the book of J.V.Poncelet. Some of these curves are particularly interesting for the present study because of their irregular aspect. For example the

---

3. The dimension of the specimen tested by M.A.Masson is not given in the article, the stress vs. strain curve has then not been reconstructed.
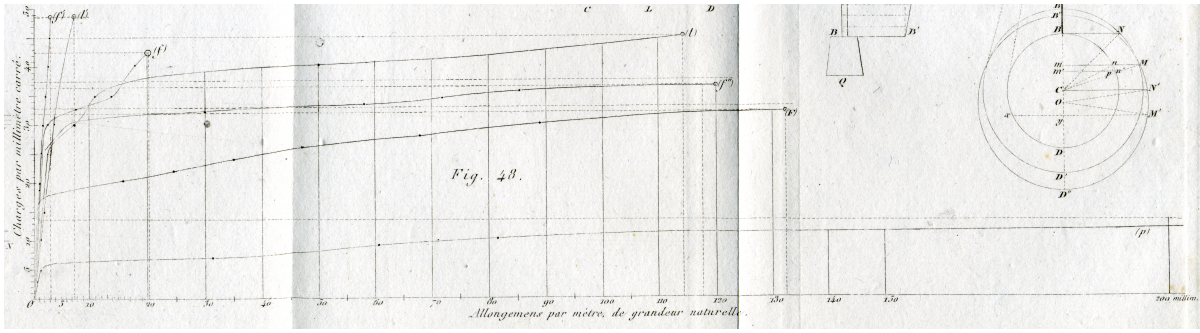
FIGURE 21 – Relative load (in Kg/mm²) vs. relative elongation (in mm/m) curves plotted based on experiments by A.Seguin (f") [6], M.Bornet (F), and M.Ardant (f,f',l,l',p). The corresponding table is given page 345 of the book by J.V.Poncelet [10].

curve referred as (f) which correspond to a tensile experiment carried out by M.Ardant on a soft iron shows a rather usual behaviour up to almost 1.5% (15 on the X-axis) but after that, the slope of the curve increase clearly up to failure around 2%. Even if the elastic plastic transition is rather smooth, this shape of the curve is very similar to the one observed on specimen made of mild steel showing Lüders phenomenon when submitted to tension under constant stress rate. This explication is reinforced by the plot of the same experiment proposed some years latter by A.Morin [4] that can be seen on curve (b) of figure 22(right)).

A other kind of irregular hardening behaviour can be observed on two other curves : the one denoted (l) on figure 21 which corresponds to an experiment on soft brass also carried out by M.Ardant, and the one denoted (f") which corresponds to an experiment on iron wire carried out by M.Seguin (values taken from [6]). Step like evolutions like the ones typical of Portevin - Le Chatelier effect during tensile tests at constant stress rate are observed on both curves. It must be noted that the curve denoted (f") appears rather smooth on the figure by J.V.Poncelet but it was plotted using only a part of the experimental data provided by A.Seguin. When the full original table of A.Seguin (page 89 of [6]) is used, the stress vs. strain curve appears much more irregular with pronounced steps in the plastic domain.

These results have nevertheless to be considered carefully accounting for the precision of the experimental devices used at this period. The load is increased by adding some small additional weight at the extremity of the loaded specimen, the elongation is measured when this latter is stabilized. J.V.Poncelet quoting M.Ardant notices that for some metals, this stabilization phase under constant load can be quite long or even never ends (like for lead wires). However none of these authors do really succeed in explaining the irregularity observed on the specimen presented above. They even report like F.Savart that in some experiments an heterogeneous and intermittent deformation in the gauge length that may probably be seen as a manifestation of strain ageing : *"passé une certaine limite, l'allongement produit par les charges, ne se répartis pas toujours uniformément sur toute la longueur du fil ; qu'il a lieu tantôt aux dépens d'une partie de ce fil, tantôt aux dépens d'une autre"*.

---

4. A.Morin was recruited as a young engineer together with J.Piobert and I.Didion by J.V.Poncelet to work in l'Ecole du génie et de l'artillerie de Metz. In a article written together in 1942 [11], these three scientists are the first ones to report an atypical plastic strain localisation in mild steel, that will latter be described in detail by a German scientist called W.Lüders [13]. The well known Lüders band appearing at the elastic-plastic transition in mild steels should then be denoted Piobert-Lüders band or even Piobert-Morin-Didion-Lüders bands.
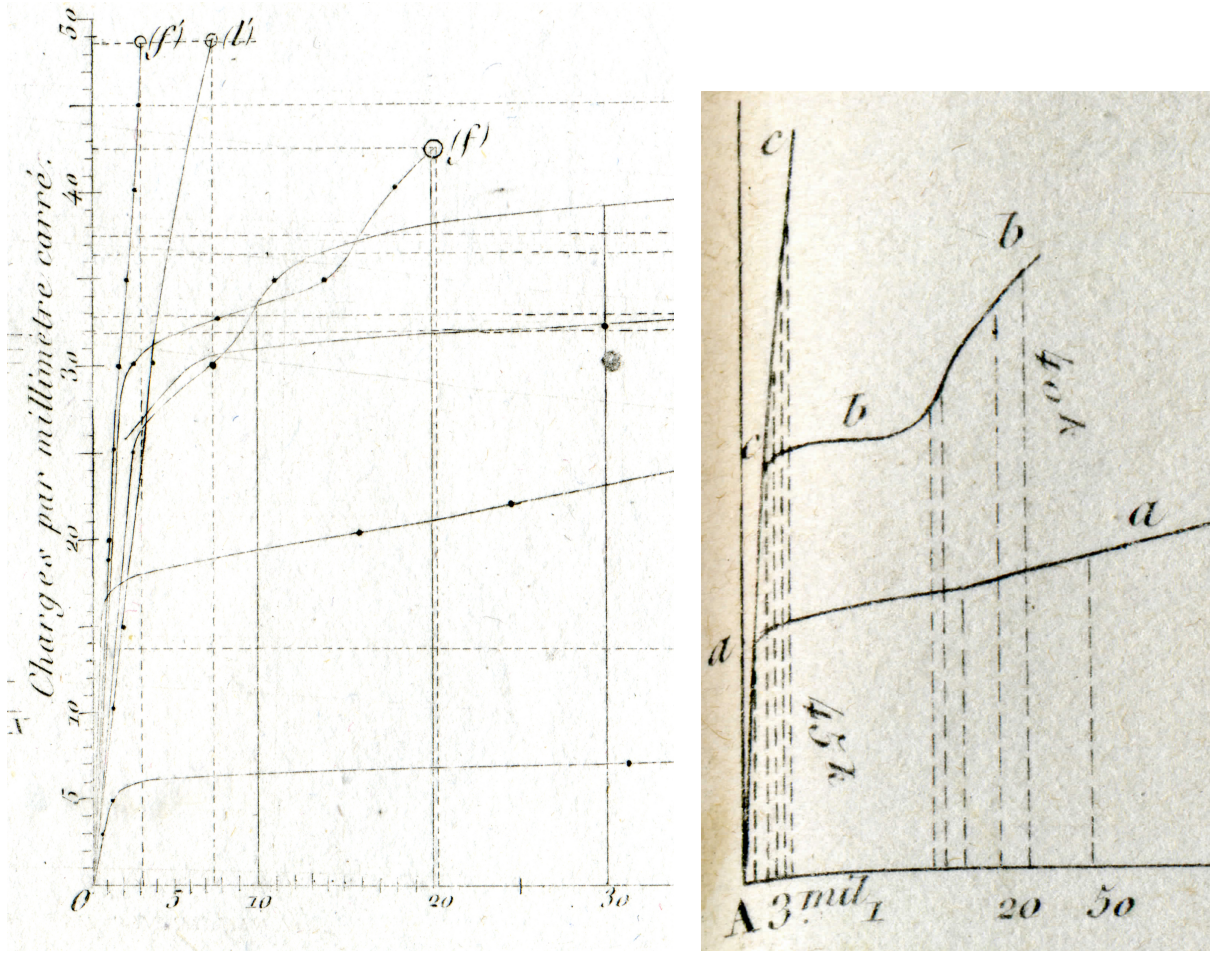
FIGURE 22 – (left) Zoom on the first 3% of the curves plotted on figure 21. (right) Same experiments by M.Borner (a) and M.Ardant (b) plotted some years latter by A.Morin [14].

[M.G. Wertheim, 1844] : Recherches sur l'élasticité (*Annales de Chimie et de Physique*)[12]

This very long article by a rather unknown author is untitled "Research on Elasticity". It should then a priori be out of the scope of our study. On the contrary, it contains one of the most valuable source of data on plasticity of many metallic materials commonly used at this period. Indeed, following the idea of Gerstner [7], M.G.Wertheim conducted tensile experiments on a large range of deformation – in fact a large range of applied loads – and for each applied load, he systematically unloaded the specimen in order to measure the permanent (plastic) and removable (elastic) parts of the deformation. He provided then a large database of tensile results up to failure on lead, tin, cadmium, gold, silver, zinc, palladium, copper, platinum, iron and steel [5] at room temperature but also for some of them at 100 and 200 °C, and even at low temperature i.e. around -15 °C.

These latter tests are very important in our case since their are from our knowledge among the first tensile experiments at intermediate temperatures on metals reported with such a level of precision (i.e. full stress vs. strain curves). We were then able to plot and compare the results of

---

5. in another article of the same author included in the same volume of *Annales de Chimie et de Physique*, some complementary experimental results are provided for many binary and ternary alloys composed with all the metals mentioned here

tensile experiments at room temperature, 100°C, and 200°C (see figure 23) on an annealed iron as reported by the author. The curves at room temperature and 100°C are rather usual while the one at 200°C show some irregularities and a clear loss of convexity. We can imagine that if this latter experiment had been carried out increasing the load more slowly, some typical steps of the Portevin - Le Chatelier effect under constant stress rate would have been observed.
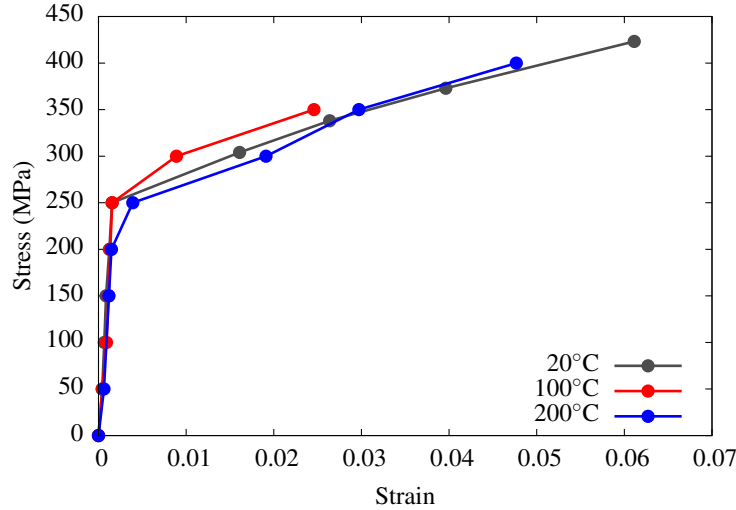

FIGURE 23 – Tensile curves of an annealed iron at room temperature, 100°C, and 200°C plotted using table provided by M.G.Wertheim in [12] pages 424, 431,and 434.

In one of the conclusion of the article, M.G.Wertheim states – contrary to what observed by F.Savart, M.A.Masson, and M.Ardant – that the deformation of metals occurs in a rather smooth manner, without any jumps on the curve : *"Les allongements permanents ne se font pas par sauts, par saccades, mais d'une manière continue ; en modifiant convenablementla charge et sa durée d'action, on pourra produire tel allongement permanent qu'on voudra."* We think that it is probably the case for most of its experiments but the curve at 200°C for annealed iron plotted on figure 23 suggests otherwise.

We have seen that atypical stress/strain curves were obtained by some scientists as soon as the middle of the 19th century. In the case of F.Savart and M.A.Masson this irregular tensile response is observed at room temperature in copper. It seems not irrelevant regarding some studies of the second half on the 20th century (see the table at the end of the document for recent references), even if most of them are carried out on copper based alloys (Cu-Al, Cu-Sn, and Cu-Zn). For J.V.Poncelet, M.Ardant, and A.Seguin, irregularities on tensile curve are observed for soft iron and for brass. For soft iron the non smooth evolution is very probably a manifestation of static strain ageing (Lüders like behaviour). Finally in the case of M.G.Wertheim, the tensile curve at 200°C for the annealed iron shows clearly a loss of convexity which is very similar to the response of some steels at the same temperature obtained one century latter under similar loading conditions. Reading all these articles and books written between 1820 and 1850, it seems that a debate remains between scientists about the nature of plastic deformation of metals : is this latter intermittent or not, homogeneous or heterogeneous, smooth or serrated ? None of the authors of this period have suggested that tensile curves can be smooth for some materials and serrated for some others, or smooth for some temperatures and serrated for some others (for the same metal). This feature of strain ageing – effect of temperature and metal composition – will be understood and reported only 60 years latter by A. Le Chatelier, as it will be explain in the following.

[D. Adamson, 1878] : On the mechanical and other properties of iron and mild steel (*Journal of the Iron and Steel Institute*)[15]

This article is usually recognized as the first evidence of "blue brittleness" in mild steel. Many interesting experimental results on iron and mild steel are provided by D.Adamson. In particular the number and the quality of illustrations is remarkable for the period. The objective of the author is to compare the strength of different irons and mild steels by carrying out usual tensile tests, but also some original explosive tests on plates. Some plates with holes are also submitted to tensile loading in order to outline the loss of ductility produced by punching process compared with drilling one. However the most interesting set of experiments for the present manuscript are the bending tests carried out for several temperatures on different irons and mild steels that are presented on figure 24.

D.Adamson reported some percussive bending test carried out for two different irons and two different mild steels on a large range of temperature i.e. from cold (∼20 °C) up to red heat (∼500 °C). He observed that : *"Few or no malleable metals, such as wrought-iron or mild steels, can be found in the open market that possess a range of endurance at all varying temperatures, say, from cold up to red heat, but nearly all ordinary bar or boiler iron and mild steels will endure considerable percussive force when cold, and up to 450 degrees Fahr., after which, as the heat is increased, probably to near 700 degrees, they are more or less treacherous and liable to break up suddenly by percussive action."* This loss of ductility at intermediate temperature is clearly visible on figure 24-(№47,48,49) corresponding to a bar iron and to two different steels investigated by the author. The fourth investigated metals (№50) does not show such a "brittle" behaviour at intermediate temperature. However D.Adamson outline the fact that this latter is very pure (see composition figure 24), and that its tensile strength properties (yield and ultimate stresses) are almost twice lower than the three other metals.

The inability of iron and steels to endure percussive force in a given range of temperature will be commonly referred to as "blue brittleness" in the 20th century because of the colour of these metals at the temperature where the ductility is the most reduced. The link with strain ageing and the not yet called Portevin - Le Chatelier effect that appear in these metals almost at the same temperature will be made some years latter by A.Le Chatelier.

[L. Hartmann, 1896] : Distribution des déformations dans les métaux soumis à des efforts (*Paris*)[16]

It was mentioned in the paragraph devoted to J.V.Poncelet's book the discovery in 1842 by G.Piobert, I.Didion, and A.Morin of a phenomenon of strain localisation that will be called latter Lüders band. These bands are then sometime called Piobert-Lüders but also Piobert-Lüders-Hartmann because of the extensive study that has been proposed on the topic by this last scientist at the end of the 19th century. In a series of article published in 1894, 1895, and 1896 in a journal called "Revue d'Artillerie" (and latter brought together into a book), these localisation bands are described and drawn by L.Hartmann in many different materials under many different loading conditions. He was then one of the first researcher to report in detail the spatial heterogeneous and intermittent nature of the plastic deformation.

The materials characteristics are not very well documented in this book and one should wonder on the nature of some bands observed by L.Hartmann. However among the numerous examples of localisation bands reported by the author, it is very probable that a large part of them are due to strain ageing (either Lüders or Portevin - Le Chatelier ones). L.Hartmann gives a precise description of plastic localisation bands that he succeeded to observe under tension,

	20 °C		230 – 370 °C		> 500 °C

FIGURE 24 – Bending tests on iron and mild steel bars carried out at room temperature (20°C), light straw to dark blue heat temperature (230-370 °C), and red hot temperature (>500 °C). The bending ability of all investigated metals is reduced in the intermediate temperature range, excepted for the very pure one (№50).

Figs.	Material	Fe	C	Mn	Si	S	P
47	Bar Iron	98.389	0.063	0.204	0.206	0.018	0.334
48	Steel	99.38	0.170	0.296	0.042	0.009	0.104
49	Steel	99.224	0.200	0.500	0.009	0.035	0.032
50	Bar Iron	99.8	0.023	Trace	0.037	0.013	0.033

compression, bending, and stamping as it can be seen on figure 25. For tensile experiments carried out on many plates made of several materials, he reported for each of them the constant angle measured between the band direction and the tensile axis : *"Dans un corps solide soumis à la traction, les déformations ont pout traces sur un plan quelquonque, parallèle à l'axe, des lignes, droites ou courbes, qui jouissent de la propriété de faire un angle constant avec cet axe."* He then reported an angle of 64° for platinum and tin, 62° for red copper, 61° for silver, 58° for annealed steel, and 53° for lead. These differences probably due to the anisotropy of the tested plates are out of the scope of the present study.

The work by L.Hartmann is to our knowledge the first exhaustive study on propagating plastic strain localisation bands in metallic alloys. Some very particular type of specimens and loading have maybe not tested afterwards and it could be very interesting to test the ability of modern
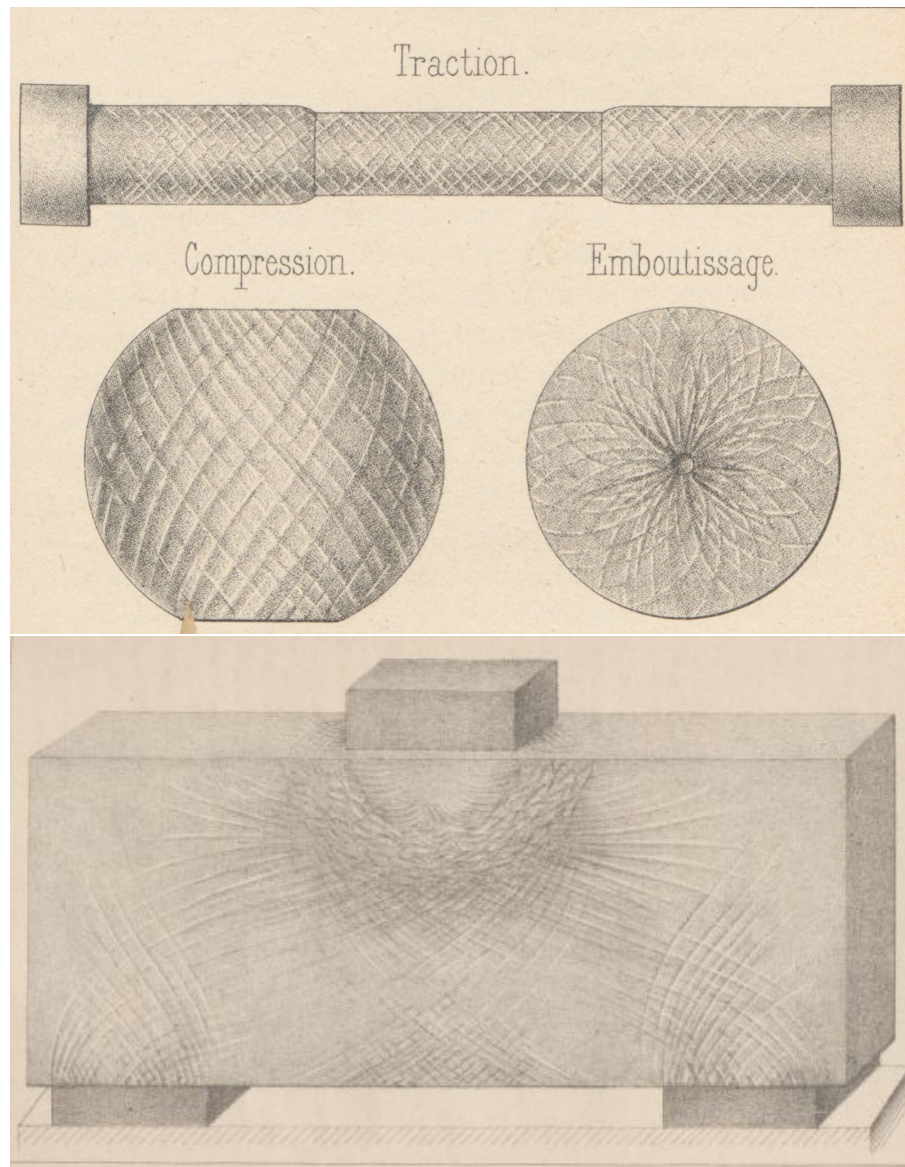
FIGURE 25 – Plastic strain localisation bands observed by L.Hartmann under tension, compression, stamping and 3 points bending. The description of bands observed in 1842 by G.Piobert, I.Didion, and A.Morin due to shooting experiments on a metal plate is very similar to the stamping picture of L.Hartmann.

modelling methods – KEMC model and finite element simulations – to correctly reproduce this huge database of observations.

2.2   1900-1950 : The initial experimental observations

[A. Le Chatelier, 1909] : Influence du temps et de la température sur les essais au choc (*Revue de métallurgie*)[18]

This article is from our knowledge one of the first one where the unusual tensile behaviour –which is obviously not yet called the Portevin - Le Chatelier effect– is reported in iron and steel between 100 °C and 300 °C. It was written by A. Le Chatelier in order to provide a brief comment to the work presented some month earlier by M. Guillet and Revillon concerning the toughness of steel at high temperature. Indeed at this period the atypical response of iron and steel called blue brittleness reported by D.Adamson in 1878 [15] is the subject of many studies. This latter presented before consists in a loss of toughness properties of the metal that can occur in a temperature range between 200 °C and 500 °C. This effect is denoted blue brittleness ("fragilité au bleu" in french), by opposition with the cold brittleness (corresponding to the low temperature transition from ductile failure mode to brittle one) which is also investigated at this period.

Most of the main characteristics of the PLC effect are already reported by A. Le Chatelier in this article. The author describes in particular the non-continuous deformation pattern that he was able to observe during tensile tests on iron. It seems that these experiments were carried out on a quite soft machine since the stress/strain evolution which is reported is the following one :

"on a une série d'allongements brusques, pouvant atteindre des amplitudes de 2 à 3 0/0, et séparés par des périodes pendant lesquelles la charge peut monter de 5 à 8 kg. par millimètre carré , sans qu'il se produise aucun allongement".

A. Le Chatelier also reports that the unusual behaviour appears around 100°C and disappears for temperatures higher than 300°C. As a consequence of this phenomenon, the material properties such as ultimate tensile stress (R_m), strain at necking (A_m) and strain at failure (A_r) follow some non-monotonic evolutions with temperature. R_m increases in the temperature domain where serrations are observed while A_m and A_r decrease. Schematic view of such evolutions based on A. Le Chatelier description are given on figure 26.
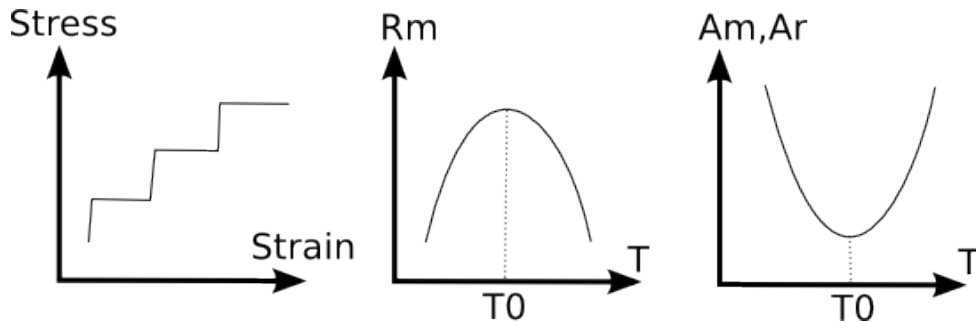
FIGURE 26 – Some schematic representation of the observation made by A. Le Chatelier described in [18].

The negative strain rate sensitivity at 170°C is also reported in this article comparing two tensile experiments carried out one in 20 minutes, the other in 2 seconds. Another very important phenomenon reported in this very early article is the equivalence between temperature and strain rate : a tensile experiment at a high strain rate and 250°C shows the same result than a tensile experiment at a low strain rate and 150°C. Consequently, the temperature T_0 corresponding to the maximum of R_m (and respectively the minimum of A_m and A_r) will be shifted toward higher temperature when the strain rate is increased. A. Le Chatelier deduces that the same physical mechanism is responsible for the serrated yielding observed around 150°C during quasi-

static test, and the blue brittleness observed in the same alloys around 475°C. Indeed blue brittleness is generally evidenced by toughness test carried out at with high strain rate level (Charpy experiments). A. Le Chatelier finally insists on the difference between the cold brittleness and the blue brittleness :

— The cold brittleness is inter-granular, and seems not to be related to the tensile behavior in that the ductile to brittle transition is not directly observable on tensile curves.
— The blue brittleness is intra-granular, and is a direct consequence of the modification of mechanical tensile properties in the temperature domain where the unusual serrated yielding is observed.

It is interesting to notice that the relation between the Portevin - Le Chatelier effect and the ductility and toughness of metallic alloy is still a topical issue investigated in very recent studies as it will presented all along this manuscript.

[E. Andrade, 1910] : On the viscous flow in metals, and allied phenomena (*Proceedings of The Royal Society of London*)[19]

This article from E.N. da C. Andrade investigates viscous flow in metals and alloys by mean of creep tests. It was inspired by some similar earlier work carried out by Trouton and Rankine in 1904 [17]. One very interesting experimental device is proposed to carry out creep tests at a constant stress level and not only at a constant load level. Creep test are carried out on pure lead, on an alloy of lead and tin, and on approximately pure copper. This latter material is historically very interesting for the present work, since the author has noticed the following atypical feature of copper : *"A peculiarity of copper wire was that it showed sudden slips at irregular intervals, which, perhaps, may be called "copper quakes" as being analogous to the geological slipping supposed to result in earthquakes"*.

This intermittent and heterogeneous deformation mode is illustrated on figure 27. This is from our knowledge the first report of a behaviour similar to Portevin - Le Chatelier effect in copper.
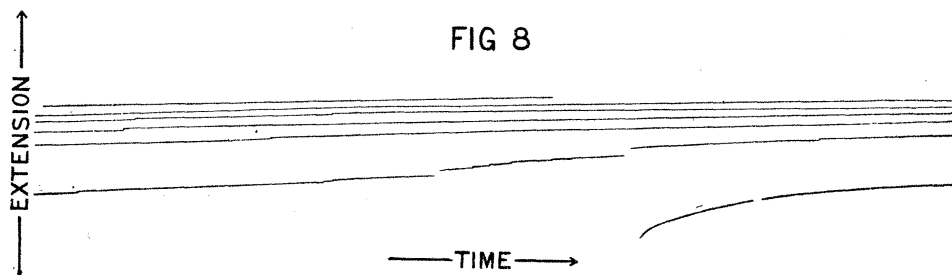

FIGURE 27 – Extension of a copper wire as a function of time during creep test. Sudden slip can be observed at the centre of the picture.

[W. Rosenhain and L. Archbutt, 1912] : Tenth report to the alloys research committee : on the alloys of aluminium and zinc (*Proceedings institution mechanical engineers*)[20]

W. Rosenhain and L. Archbutt have investigated in this long report the mechanical properties of binary alloys of aluminium and zinc. They studied the rôle of the concentration of Zinc in the alloy (between 5% and 90%), and compared cast and wrought alloys. During some of their tensile experiments on hot-rolled and cold-drawn cylindrical specimens with a low content of Zinc (from 5% to 20%) at room temperature they reported serrated yielding as it can be seen on some curves of figure 28. The description of this unusual phenomena given by the authors is the following :

"In some of the alloys the diagram, above the yield-point, shows a jagged or stepped appearance ; this arises from the peculiar manner in which many of these alloys undergo plastic deformation, that is, by a succession of more or less sudden yields."

This description is the same than the one made by A. Le Chatelier in 1909 on iron and steels. However from our knowledge this article is the first one in which the whole tensile curve is reproduced and where serrations can consequently be observed. No other comments are provided by the authors concerning this atypical phenomenon.
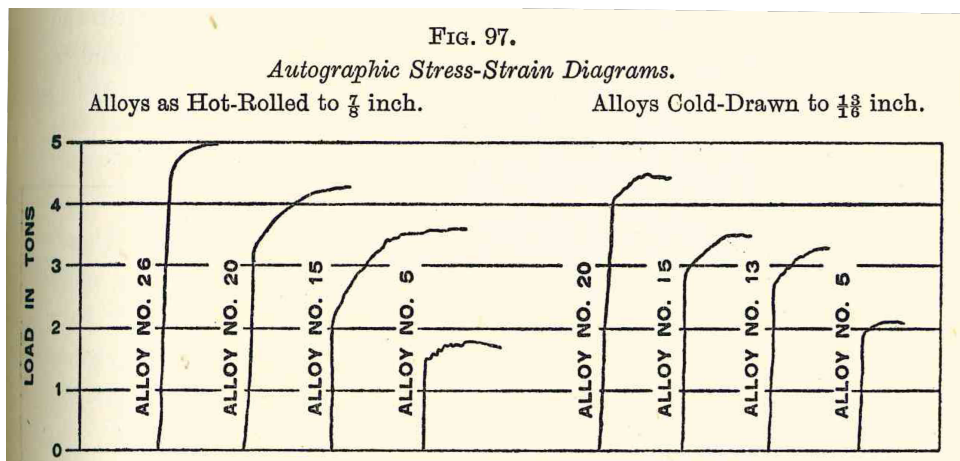
FIGURE 28 – Serrated yielding as observed in [20] in some aluminium-zinc alloys.

[A. Portevin and F. Le Chatelier, 1923] : Sur un phénomène observé lors de l'essai de traction d'alliages en cours de transformation (*Comptes Rendus de l'Académie des Sciences*)[21]

The serrated yielding observed during tensile tests on many metallic alloys is called Portevin - Le Chatelier effect most probably because of this article. These latter report an anomalous yielding phenomenon in flat and cylindrical specimens designed with different aluminium alloys. The pictures showing this phenomenon are reproduced on figure 29.

The authors also report that some strain localisation bands have been observed during experiments at the surface of the specimen. These bands already denoted at this period "Piobert, Hartmann, or Lüders" bands are inclined with an angle of 60° to 70° with the tensile axis. Many

Fig. 1. — Courbe de traction d'une éprouvette cylindrique (diamètre = 13ᵐᵐ,8) en alliage Al-Cu-Mn. Abscisses : allongements (échelle : 27ᵐᵐ = 10 %); ordonnées : efforts (échelle : 3oᵐᵐ = 10 kg : mm²).

Fig. 2. — Courbe de traction d'une éprouvette plate (section = 20 × 2ᵐᵐ) en alliage Al-Cu-Mg-Mn. Abscisses : allongements (échelle : 10ᵐᵐ = 10 %); ordonnées : efforts (échelle : 10ᵐᵐ = 5 kg : mm²).

(a)   (b)

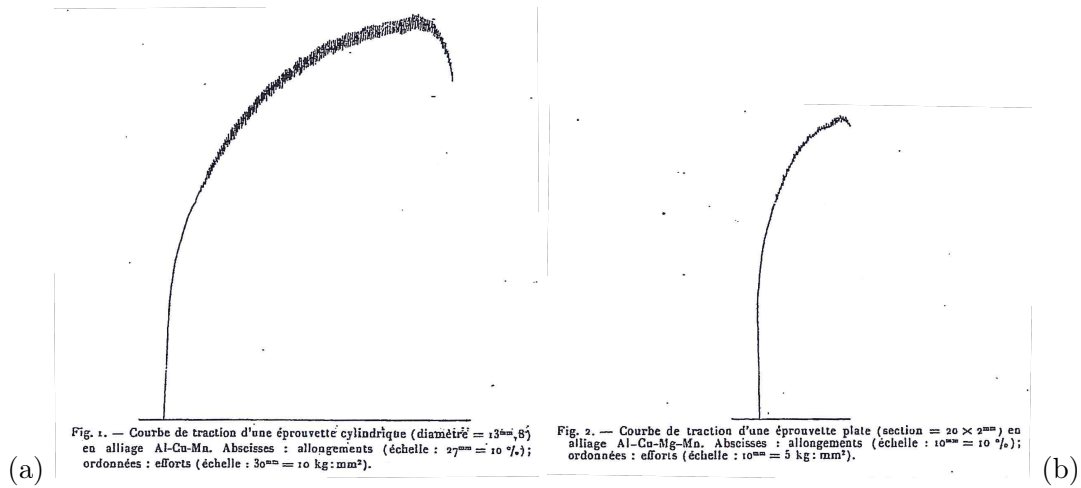FIGURE 29 – (a) Serrated yielding at room temperature in a cylindrical specimen made of Al-Cu-Mn alloy (b) Serrated yielding at room temperature in a plate specimen made of Al-Cu-Mg-Mn alloy. Both pictures are taken from [21].

of them are observed simultaneously, they propagate all along the specimen and a popping noise can be heard when a group of bands nucleate at one end of the specimens. A. Portevin and F. Le Chatelier then explain that the anomalous yielding is maximal if the material is tested just after quenching, but may disappear if a tempering heat treatment is applied. Finally the composition of alloys of figure 29 is given : Cu=4.5% and Mn=0.8% for the first one ; Cu=4.8%, Mn=0.6%, Mg=0.5% and Si=0.3 % for the second one.

[M.J. Manjoine, 1944] : Influence of rate of strain and temperature on yield stresses of mild steel (*Journal of Applied Mechanics*)[22]

In this article is presented a very detailed analysis of yielding behaviour of a mild steel for various temperatures and strain rates. Based on some experiments carried out by the author and A.Nadai, the effect of strain ageing on yield stress and hardening is investigated. The range of strain rate varies from 10^{-6} to 10^3 per second, for room temperature, 200, 400, and 600°C. The most interesting temperature from our point of view is 200°C for which serrated yielding is observed at $8.5 \times 10^{-4}/sec.$ and $2 \times 10^{-2}/sec.$ (see figure 30(a)).

A very interesting representation of yielding behaviour is proposed by the author and reproduced on figure 30(b) : the true stress is plotted as a function of the prescribed strain rate for different level of strain. It is very interesting to notice the strong difference between the hardening behaviours for low and high strain rate. Between these to domains, a significant negative strain rate sensitivity can be observed. The comment on the authors on that point outline the link between negative strain rate sensitivity and occurrence of serrations : *"discontinuous yielding can be expected when the stress versus strain-rate curve has a negative slope. This means that the material can yield more rapidly at a lower stress, as it does ; to keep the average constant, the material will be stretched much more slowly during another part of the cycle ; this causes the load to build up again and the cycle is repeated."*

This link between negative strain rate sensitivity, serrated yielding, and localized deformation will inspire many studies some years latter that will be described in the following. Another very useful representation is proposed by M.J. Manjoine in his article : the true stress is plotted as a function of temperature for different level of strain (see figure 31). This evolution is in agreement with the description made by A. Le Chatelier in 1909, with a local maximum of stress located in
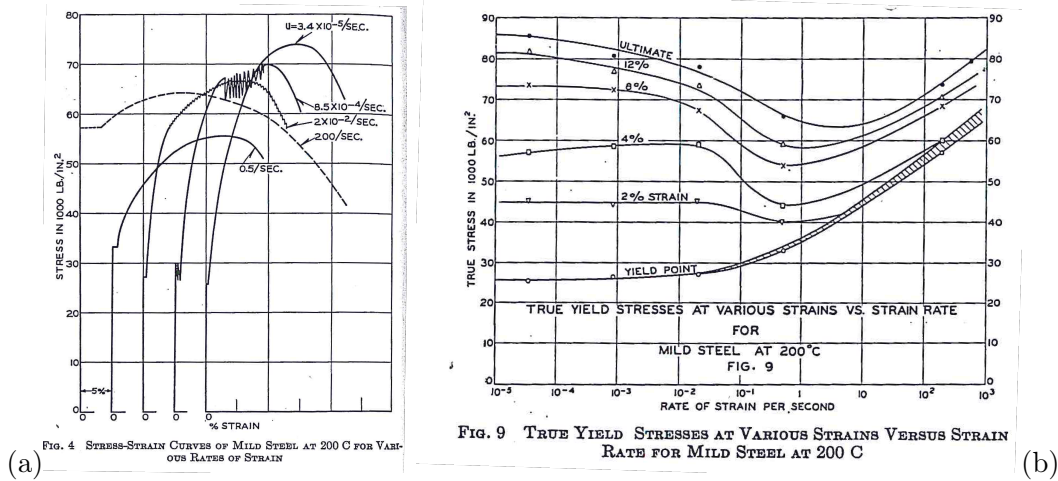
FIGURE 30 – (a) Stress versus strain and (b) Stress versus strain rate at 200°C in a mild steel reported by [22].

the domain where serrations are observed. It can be seen that the evolution of true stress with respect to temperature looks like the one with strain rate if the temperature axe is reversed. This means that the inverse of the temperature and the strain rate play similar rôles regarding strain ageing phenomenon.
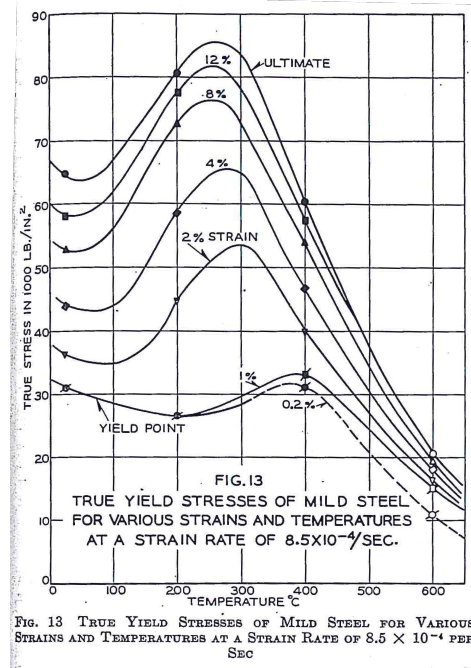
FIGURE 31 – Stress vs. temperature in a mild steel at $8.5 \times 10^{-4} s^{-1}$ for different levels of strain [22].

61

2.3   1950-1985 : The physics and mathematics of the PLC effect

[A.H. Cottrell and B.A. Bilby, 1949] : Dislocation theory of yielding and strain ageing of iron (*Revue de métallurgie*)[23]

This article is probably one of the most important contribution concerning strain ageing understanding and modelling. Even if some of the explanations and equations presented in this work by A.H. Cottrell and B.A. Bilby have been reconsidered and modified latter, most of the basis of the actual models for strain ageing have been designed based on this work.

In the introduction of the article some generalities on strain ageing phenomenon are recalled. The stresses generated around dislocations can be equilibrated by some solute atoms either in substitutional of interstitial solution when these latter diffuse towards some favourable positions. The authors explain the two modes of plastic flow that can be experienced by a dislocation surrounded by such an atmosphere of solute atoms :

— If the force applied on the dislocation is too small the dislocation moves together with its atmosphere, this mode will be called latter the dragging mode.
— If the force is large enough the dislocation can escape from its atmosphere, and will then move rapidly even for an applied force very lower than the one required to turn off from the atmosphere.

These two modes explain on a simple way the yield peak that is observed during tensile tests on some mild steel gives rise to the Lüders band nucleation and propagation. If a specimen in which dislocations have turn off from their atmosphere is rested for a sufficiently long time at a sufficiently high temperature the phenomenon can occur again, since solute atoms will migrate again towards immobile dislocations, and rebuild solute atmospheres around them. According to the authors, strain ageing is due in steel to carbon or nitrogen atmosphere, but the study only focuses on carbon atoms.

Two types of interaction between solute atoms and dislocations have to be accounted for. The first one is the interaction due to the hydrostatic stress generated by an edge dislocation. The expended area below the dislocation will attract solutes while the compressed part above it will reject them. The hydrostatic stress can be relieved by either substitutional or interstitial atoms since both of them generate a spherical volume change of the cell. Another interaction may exist between the shear stress field around a screw dislocation and solute atoms in interstitial positions that engender a non-symmetrical distortion of the cell. This is the case for carbon atoms in α-iron that dissolves interstitially and create a tetragonal distortion of the cubic cell. This second interaction is not accounted for in the paper of A.H.Cottrell and B.A.Bilby and only the interaction wit an edge dislocation is studied.

The general expression of the interaction energy between a positive edge dislocation and a solute atom in either substitutional or interstitial position is :

$$V = A\frac{\sin\alpha}{r} = \Delta v.\frac{G\lambda}{3\pi}\frac{1+\nu}{1-\nu}\frac{\sin\alpha}{r} \qquad\qquad \text{if } r \geqslant r_0 \qquad\qquad (2)$$

$$V = 0 \qquad\qquad\qquad\qquad\qquad \text{if } r < r_0 \qquad\qquad (3)$$

Where Δv is the volume change caused by the introduction of the solute atom, G is the shear modulus, ν is the Poisson's ratio, and λ is the slip distance in the dislocation. r and α are the polar coordinates of the solute atom with respect to the dislocation, $\alpha = 0$ corresponding to the slip direction. Since the first formula fails when r is two small $r_0 \sim \lambda$ is the minimum distance for

this formula to be valid, otherwise $V = 0$. 2D and 3D representations of this interaction energy are plotted on figure 32.
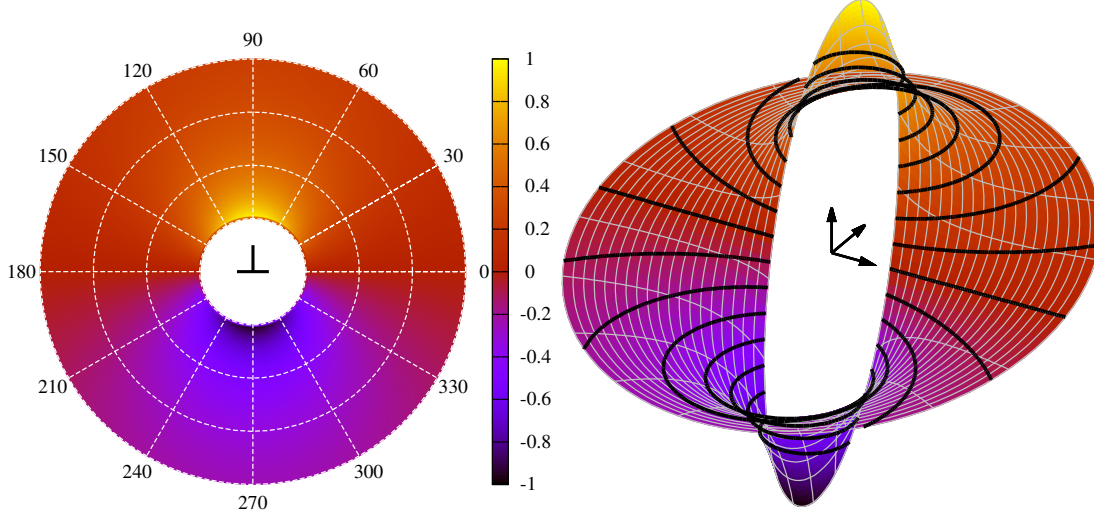

FIGURE 32 – Polar and 3D plots of the interaction energy V given by equation 2. V is normalized with respect to A and plotted from $r = r_0$ to $r = 4r_0$.

In addition to this interaction energy, the authors explain that a saturation in carbon atoms occurs in the lower part of the dislocation. The hydrostatic stress is not relieved by a diffuse atmosphere of solute but by *"a central row of carbon atoms, situated just below the dislocation centre, which is surrounded in the lower half-crystal by a dilute distribution of the Maxwell-Boltzmann type"*. This central row is located at the most favourable position, i.e. the minimum value for V, at $r = r_0$ and $\alpha = 3\pi/2$.

Using this description of the atmosphere and based on the fact that most of the interaction is due to this central row located just below the dislocation, the authors give an estimate of the force required to pull a dislocation from its atmosphere. If the dislocation is moved at a distance x along the slip direction, its interaction energy (per atom plane) with the atom located at a distance $\rho = r_0$ just below it becomes :

$$V(x) = -A\frac{r\sin\phi}{r^2} = -A\frac{\rho}{x^2 + \rho^2} \tag{4}$$

The corresponding force per atom plane required for this displacement is :

$$F(x) = \frac{\partial V}{\partial x} = 2A\rho\frac{\rho}{(x^2 + \rho^2)^2} \tag{5}$$

The evolutions of $V(x)$ and $F(x)$ proposed by A.H.Cottrell and B.A.Bilby are plotted on figure 33. The force $F(x)$ has a maximum value at $x = \rho/\sqrt{3}$ equal to $F_{max} = 3\sqrt{3}A/8\rho^2$. The critical stress under tensile condition required to pull a dislocation from its atmosphere is then :

$$\sigma_0 = \frac{3\sqrt{3}A}{4\lambda^2\rho^2} \tag{6}$$

The authors then give some explanation on the local and collective unpinning behavior. Helped with thermal fluctuations a single dislocation will first be torn from one atom of its atmosphere, and then by a unbuttoning process, the entire dislocation line will be released. This free dislocation will then accelerates and help the unpinning of other dislocations by modifying
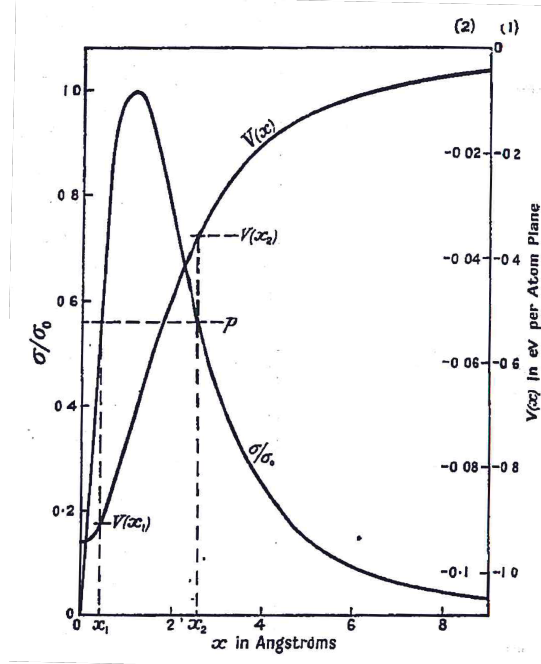
FIGURE 33 – Evolution of the interaction energy $V(x)$ between a gliding dislocation and a solute atom located at the most favourable position, and the corresponding force $F(x)$.

the elastic field around them. A collective unpinning behaviour will take place and lead to the well know stress drop observed just beyond the yield peak during tensile tests.

The last part of the article is devoted to the rate of formation of the atmosphere. Due to thermal activation the solute atoms diffuse around dislocation towards minimal value of the potential V. Their path follow some curves perpendicular to isovalues of V (see figure 32) with a velocity defined by :

$$\underline{v} = -\frac{D}{kT}\boldsymbol{\nabla}\, V \tag{7}$$

where D is the diffusion coefficient, and k is the Boltzmann constant.

Based on this velocity, and using some complex mathematical developments the author provide a useful expression of the rate of formation of the atmosphere, i.e. the number of carbon atoms $N(t)$ per unit length of dislocation arriving at time t around the dislocation divided by the number of atom N_s required to complete the atmosphere :

$$N(t)/N_s = 3n_0\lambda \left(\frac{\pi}{2}\right)^{1/3} \left(\frac{ADt}{kT}\right)^{2/3} \tag{8}$$

where n_0 is the average bulk concentration. The author warn that this expression is adequate for $N(t)/N_s$ up to 0.3 but not above since some concentration and saturation effects are neglected in this study. These latter effects will be accounted for in a modified formula proposed some years latter by Louat [66]. However the exponent 2/3 in the formula is still present for some alloys in the constitutive model used nowadays to simulate strain ageing phenomena.

[J. Friedel, 1964] : Dislocation, Chapter XVI (*Oxford*)[27]

This chapter of the very famous book from J.Friedel is very similar to the fundamental article of A.H. Cottrell described in the previous section. However since this latter is written 15 years latter, some equation are slightly different. The author begins the chapter by giving the concentration of solute atoms arriving on a dislocation at time t :

$$c - c_0 = \frac{\pi c_0}{b^2} \left[\frac{n(n+2)D|W_M|b^n t}{kT} \right]^{\frac{2}{n+2}} \tag{9}$$

This equation is very similar to the one proposed by A.H.Cottrell (see eq. 8) for $n = 1$ which corresponds to size effects according to J.Friedel ($n = 2$ means differences in elastic constants). The time t_s necessary to saturate the dislocation is then provided :

$$t_s \simeq \left(\frac{c_1}{\pi c_0} \right)^{\frac{n+2}{2}} \frac{kT b^2}{n(n+2)D|W_M|} \tag{10}$$

where $c_1 \gg c_0$ is the saturation concentration. These equations are commented by the author and it seems that the first one is valid only at the beginning of the ageing process. Indeed, a saturation effect is expected in a second time that should lead to a decrease in the dislocation saturation rate.

J.Friedel attempts in the second part of the chapter to validate the two equations by comparison with experimental results. The diffusion coefficient of Nitrogen in soft steel is evaluated for that purpose. This latter is said to be more mobile than carbon ; that is probably the case at room temperature but less obvious at higher temperatures [59]. Another proposition done by the author is that ageing process is much more slower in non-ferrous alloy in which substitutional solute atoms are involved compared with steel in which interstitial solute atoms diffuse. However the Portevin - Le Chatelier effect occurs in aluminium alloys at room temperature while it occurs around 200°C in steels. On the contrary there is in general no yield point in aluminium alloys. This point is discussed latter in the article. An estimate of the yield point increase $\Delta\sigma$ due to static strain ageing is then given as a function of time and temperature assuming that this latter is proportional to the concentration of solute atoms arriving on the dislocation :

$$\Delta\sigma = const.(Dt/T)^{2/3} \tag{11}$$

The third part of the chapter is devoted to the repeated yield point phenomenon that occurs in steels during plastic yielding in a given range of temperature and strain rate. The author points out the relation between this phenomenon and the blue brittleness of steels that occurs almost in the same temperature range. Based on some simplified assumptions and choosing some parameters values in the literature, J.Friedel provide the range of strain rate in which repeated yield point should appear :

$$10^8 D(T) \leqslant \dot\varepsilon \leqslant 10^9 D(T) \tag{12}$$

At this step a difference is made with non-ferrous light alloy in which substitutional atoms diffuse. Since repeated (serrated) yielding is observed in this alloys after a given deformation level, the author suggests to introduce the influence of vacancies in the strain ageing equations. This point is discussed with more details in many articles presented in the following.

The article ends with two rather simple fundamental propositions summarizing the mechanics of the PLC effect. Serrated yielding occurs :
 — *"when the hardening rate $d\sigma/d\varepsilon$ decreases for increasing strain rates $d\varepsilon^d t$"*
 — *"in the exact range of temperature where the stress σ necessary to produce a given strain at a given strain rate increases with temperature"*

This article is from our knowledge the only one from P.Penning devoted to Portevin - Le Chatelier effect. However this latter investigates almost every fundamental aspects of the mechanics of PLC effect :
— a propagative localized plastic deformation band within tensile specimens
— some associated serrations on the stress strain curves
— the negative strain rate sensitivity of the stress during yielding
— the influence of machine stiffness, of prescribed strain rate, of band width, ...

The article is based on a 1D analysis of a tensile test carried out on a tensile specimen (lenght L), at a prescribed velocity v_0, on a tensile machine whose compliance is M (this latter includes the elastic part of specimen deformation). If the tensile direction is denoted x and the plastic strain ε the evolution of stress is given by :

$$
\underbrace{M\dot{\sigma}}_{\substack{\text{Machine and elastic} \\ \text{strain rate}}} + \underbrace{\int_0^L \dot{\varepsilon}\, dx/L}_{\text{Plastic strain rate}} = \underbrace{v_0/L}_{\text{Total strain rate}} \tag{13}
$$

At time t, if the deformation rate is assumed to be localized in a band of width L_b into which the strain rate is assumed to be homogeneous and equal to $\dot{\varepsilon}$, this equation becomes :

$$
\dot{\sigma} = \frac{v_0}{ML}\left(1 - \frac{\dot{\varepsilon}}{\dot{\varepsilon}_0}\right), \quad \dot{\varepsilon}_0 = \frac{v_0}{L_b} \tag{14}
$$

Using this equation it can be seen that the sign of the stress rate depends on the ratio between $\dot{\varepsilon}$ and $\dot{\varepsilon}_0$. Consequently, the fact that the stress increase (hardening), decrease (softening), or oscillates during plastic flow only depends from the band width L_b, the prescribed displacement rate v_0 and the strain rate in the band $\dot{\varepsilon}$.
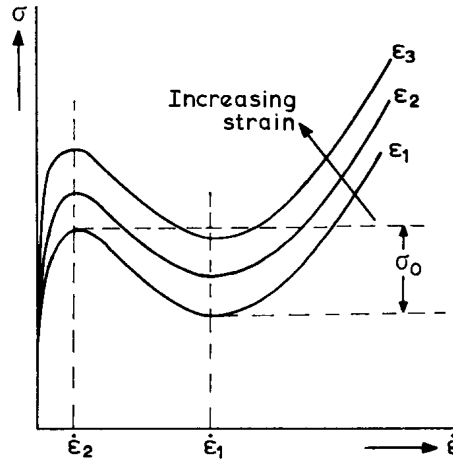

FIGURE 34 – Material characteristic $\sigma(\varepsilon, \dot{\varepsilon})$ as proposed by P.Penning.

The evolution of this strain rate in the band $\dot{\varepsilon}$ can be investigated more in details using the "material characteristic" which is defined by P.Penning as the expression of the stress as a

function of strain and strain rate $\sigma(\varepsilon, \dot{\varepsilon})$ (see figure 34) :

$$\dot{\sigma} = \frac{\partial \sigma}{\partial \dot{\varepsilon}} \ddot{\varepsilon} + H \dot{\varepsilon}, \quad H = \frac{\partial \sigma}{\partial \varepsilon} \tag{15}$$

$$\Rightarrow \frac{\partial \sigma}{\partial \dot{\varepsilon}} \ddot{\varepsilon} + \left(H + \frac{L_b}{ML} \right) \dot{\varepsilon} = \frac{v_0}{ML} \tag{16}$$

$$\Rightarrow \frac{\partial \sigma}{\partial \dot{\varepsilon}} \ddot{\varepsilon} = \frac{v_0}{ML} \left(1 - \frac{\dot{\varepsilon}}{\dot{\varepsilon}_s} \right), \quad \dot{\varepsilon}_s = \frac{v_0}{MLH + L_b} \tag{17}$$

Consequently, the strain rate remains constant in the band only if :

$$\dot{\varepsilon} = \dot{\varepsilon}_s = \frac{v_0}{MLH + L_b} \tag{18}$$

In this case the stress increase monotonically (without serrations) with a rate $\dot{\sigma} = H\dot{\varepsilon}_s$. In all other cases, "$\dot{\sigma}$ and $\dot{\varepsilon}$ will vary with time".

At this step of the article, the brilliant idea of P.Penning is to introduce the "dynamic $\sigma - \dot{\varepsilon}$ curve". Indeed when the band pass at a given position x of the specimen, the material at this point yields and the local strain increase. The stress does not consequently evolves following a continuous curve at constant strain as plotted of figure 34, but follows a more complex evolution which can not be directly estimated without some more details on the material characteristic $\sigma(\varepsilon, \dot{\varepsilon})$. However, the slope of this dynamic curve[6] can be estimated as follow, based on equations 14 and 17 :

$$\left. \frac{\partial \sigma}{\partial \dot{\varepsilon}} \right|_{DYN} = \frac{\dot{\sigma}}{\ddot{\varepsilon}} = \left. \frac{\partial \sigma}{\partial \dot{\varepsilon}} \right|_{STA} \left[\frac{1 - \dfrac{\dot{\varepsilon}}{\dot{\varepsilon}_0}}{1 - \dfrac{\dot{\varepsilon}}{\dot{\varepsilon}_s}} \right] \tag{19}$$

This equation implies that :
 — the slope of the dynamic curve is infinite for the stationary solution $\dot{\varepsilon} = \dot{\varepsilon}_s$
 — this slope is null for $\dot{\varepsilon} = \dot{\varepsilon}_0 = v_0/L_b$ and when $\frac{\partial \sigma}{\partial \dot{\varepsilon}} = 0$ i.e. at $\dot{\varepsilon} = \dot{\varepsilon}_1$ and $\dot{\varepsilon} = \dot{\varepsilon}_2$ as it can be seen on the material characteristic evolution of figure 34.
 — the stress increases for $\dot{\varepsilon} < \dot{\varepsilon}_0$ and decreases for $\dot{\varepsilon} > \dot{\varepsilon}_0$ as defined by equation 14.
Based on these three observations and on the fact that $\dot{\varepsilon}_0 > \dot{\varepsilon}_s$ $(MLH > 0)$, the dynamic curve can be plotted at least schematically but including some mandatory evolutions arrows like on the example proposed on figure 35(a) (in this particular case $\dot{\varepsilon}_0$ is such that $\dot{\varepsilon}_2 < \dot{\varepsilon}_s < \dot{\varepsilon}_0 < \dot{\varepsilon}_1$).

The dynamic curve shows that the strain rate domain between $\dot{\varepsilon}_2$ and $\dot{\varepsilon}_1$ can not be experienced by the band. Indeed when the band arrives at a given material point, the strain rate $\dot{\varepsilon}$ rises from 0 to $\dot{\varepsilon}_2$, but at this point it cannot follow the dynamic curve continuously any more. The strain rate $\dot{\varepsilon}_b$ needs consequently to jump to a quite high value denoted $\dot{\varepsilon}_H$ which gives the same stress level on the dynamic curve but on the right part of this latter. The strain rate then decreases towards $\dot{\varepsilon}_1$ following the arrows where it is blocked again and has to jump to a very low value denoted $\dot{\varepsilon}_L$ at the same stress level. The band then jump to an adjacent region where the same cycle is retrieve, this hopping behaviour of the band is commonly referenced as B-type.

The cyclic behaviour in the stress vs. strain rate plane is represented on the material characteristic on figure 35(b) and explains the serrations observed in the tensile curves. However the amplitude of serrations on this latter curve is not equal to the depth of the valley of the material characteristic (denoted σ_0 on figure 34). When the material within the band experiences relatively high strain rates (i.e. between $\dot{\varepsilon}_H$ and $\dot{\varepsilon}_1$), this latter will deform and harden such that the material characteristic will increase towards higher stress levels as it can be seen on figure 34. The correct cyclic evolution is consequently the one proposed on figure 36(a).

---

6. Because of the hardening in the band, this "dynamic" slope is different from the "static" one that can be directly observed on figure 34.
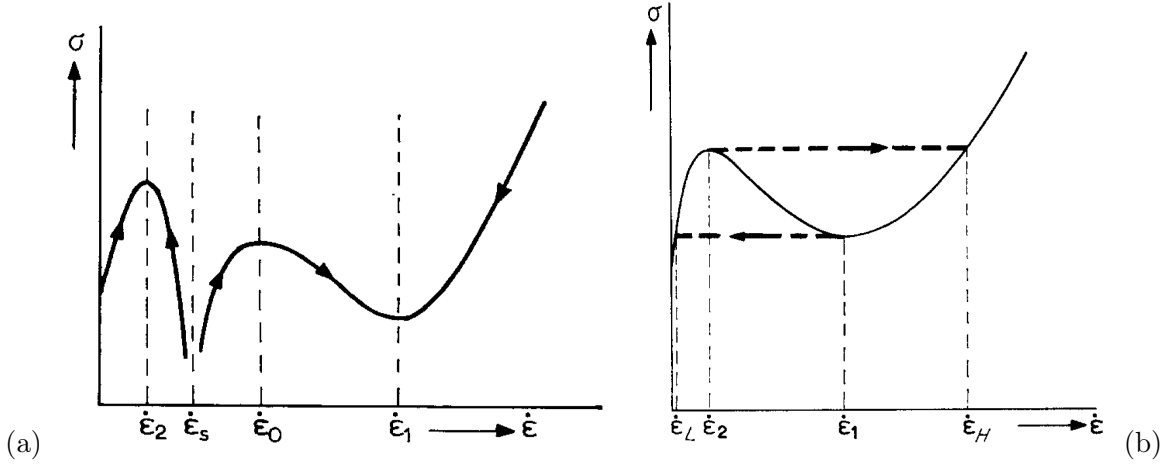
FIGURE 35 – (a) Qualitative dynamic curve based on equation 19 (b) Hysteresis like evolution in the stress vs. strain rate plane.
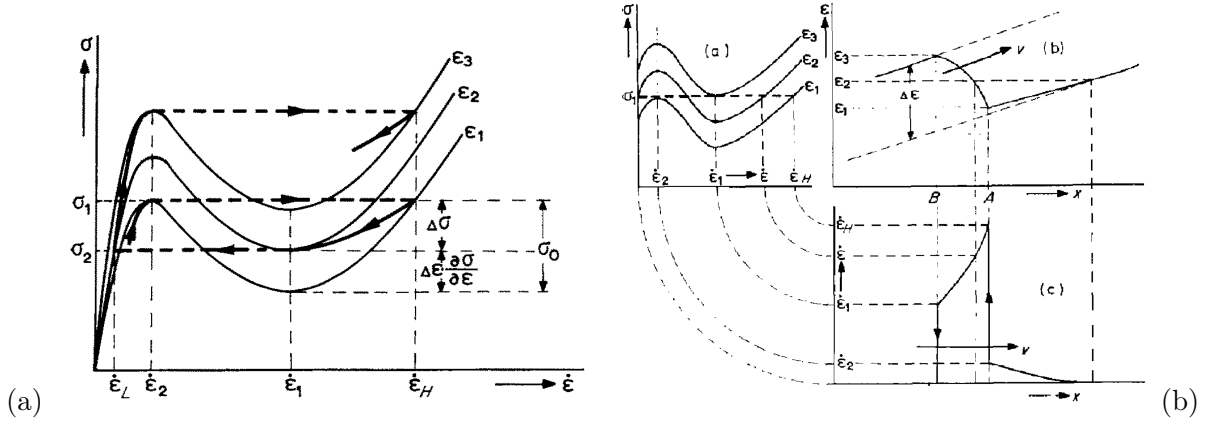

FIGURE 36 – (a) Actual stress evolution during passing of a B-type band accounting for (i) the material characteristic, (ii) the strain hardening between $\dot{\varepsilon}_H$ and $\dot{\varepsilon}_1$. (b) Characteristics of a continuous propagating A-type band in three different planes $(\sigma, \dot{\varepsilon})$, (ε, x), $(\dot{\varepsilon}, x)$

It appears at this step of the analysis that the hardening rate H and the value of the reference strain rate $\dot{\varepsilon}_0 = \frac{v_0}{L_b}$ will influence the sharpness of serrations on the following way :

— If $\dot{\varepsilon}_0$ is smaller than $\dot{\varepsilon}_1$ like on figure 35(a), the stress decreases from $\dot{\varepsilon}_H$ to $\dot{\varepsilon}_1$ where the band is blocked and a hopping B-type behaviour will be observed associated with sharp serrations on the tensile curve.

— On the contrary when $\dot{\varepsilon}_0$ is larger than $\dot{\varepsilon}_1$, the stress decreases from $\dot{\varepsilon}_H$ to $\dot{\varepsilon}_0$ but also increases before the band is blocked at $\dot{\varepsilon}_1$ [7]. If the stress level reached at $\dot{\varepsilon}_1$ is large enough, this latter can propagate quite continuously to the adjacent region. The A-type band is then observed with relatively smooth serrations with the characteristics presented on figure 36(b).

— The hardening rate seems to play almost the same role than $\dot{\varepsilon}_0$ since it will control the actual evolution of stress between $\dot{\varepsilon}_H$ to $\dot{\varepsilon}_1$.

Based on these observations it can be concluded that B-type bands must be observed for lower strain rates or smaller hardening rates, while A-type must appear at higher strain rates or for

---

7. To see that, one can exchange on figure 35 $\dot{\varepsilon}_0$ and $\dot{\varepsilon}_1$ and change the direction of the arrow on the part of the curve between $\dot{\varepsilon}_0$ and $\dot{\varepsilon}_1$.

larger hardening rates.

Many of the propositions formulated in this article by P.Penning from a mathematical point of view will be verified some years latter using experimental or numerical devices as it will be presented in the following.

[A. van den Beukel, 1975] : Theory of the effect of dynamic strain agging on mechanical properties (*Physica Status Solidi*)[57]

This article by A. van den Beukel is the perfect companion of the previous one by P.Penning. A physical based modelling of strain ageing is proposed that provides the material characteristics $\sigma(\varepsilon, \dot{\varepsilon}, T)$ assumed as an input in the article by P.Penning. The influence of strain rate, temperature and strain on the effective stress are investigated. All the equations presented in this article constitute the bases of the model proposed some years latter by P.McCormick for strain ageing and the Portevin - Le Chatelier effect.

A very important point in this article is the difference of mechanism that is proposed compared to the original Cottrell's concept of dislocation moving continuously dragging solute atoms with them. In the present paper the main idea is the following one :

— Mobile dislocations motion is an intermittent process. They are either arrested by obstacles during a given waiting time t_w or moving with a very high velocity between two obstacles.

— During the waiting time, solutes atoms diffuse towards arrested dislocations and an over stress is required to enhance dislocation motion.

— The concentration of solute atoms c around an arrested dislocation is a function of the waiting time t_w and the diffusion coefficient D : $c = c(Dt_w)$.

— The solute diffusion process and consequently the stress is controlled by the quantity Dt_w and consequently depends on the temperature, the strain rate, and the strain.

Based on these ideas, and on some commonly admitted equations, A. van den Beukel suggest the following dependence for the quantity Dt_w

$$Dt_w(T, \varepsilon, \dot{\varepsilon}) \propto \frac{\varepsilon^{m+\beta}}{\dot{\varepsilon}} \exp\left[\frac{Q_m}{kT}\right] \tag{20}$$

where m, β are parameters, and Q_m is the activation energy of the diffusion process. Then, following the proposition of J.Friedel [27], the over-concentration around an arrested dislocation is estimated, at least for small values of Dt_w :

$$c - c_0 \propto \left[\frac{W_m}{T} \frac{\varepsilon^{m+\beta}}{\dot{\varepsilon}} \exp\left(\frac{Q_m}{kT}\right)\right]^{2/3} \tag{21}$$

For large value of Dt_w, the over concentration will saturate as represented on figure 37(left).

The solute atoms concentration c is introduced together with the effective stress σ in the activation enthalpy $H(\sigma, c)$ that appears in the thermally activated strain rate equation :

$$\dot{\varepsilon} = \dot{\varepsilon}_0 \exp\left(-\frac{H(\sigma, c)}{kT}\right); \quad H(\sigma, c) = -kT \log\left(\dot{\varepsilon}/\dot{\varepsilon}_0\right) \tag{22}$$

The differentiation of equation 22 with respect to strain rate $\dot{\varepsilon}$ provide the evolution of the strain rate sensitivity of the stress :

$$\frac{\partial \sigma}{\partial \dot{\varepsilon}} = \frac{kT}{\dot{\varepsilon} V_a} - \frac{1}{\dot{\varepsilon} V_a} \frac{\partial H}{\partial c} Dt_w \frac{dc}{d(Dtw)} \tag{23}$$

where $V_a = -\partial H/\partial \sigma$. The first part of the right term represents the usual positive strain rate sensitivity of the stress. The second part is due to strain ageing and may induce a non monotonic evolution of the effective stress with respect to the strain rate, as plotted on figure 37(centre). This picture also illustrate how the negative strain rate sensitivity domain (i.e. the decreasing part of the curve) is shifted towards higher strain rates when the strain increase because of the influence of ε on Dt_w.

The differentiation of equation 22 with respect to temperature T provide the evolution of the temperature sensitivity of the stress :

$$V_a \frac{\partial \sigma}{\partial T} = -\frac{H}{T} + \frac{Q_m}{kT} \frac{\partial H}{\partial c} Dt_w \frac{dc}{d(Dtw)} \tag{24}$$

The first term on the right represents the usual negative temperature sensitivity of flow stress. The second term is due to strain ageing and, analogously to the strain rate sensitivity may induce a non monotonic evolution of flow stress with respect to the temperature. This kind of unusual evolution is plotted on figure 37(right).
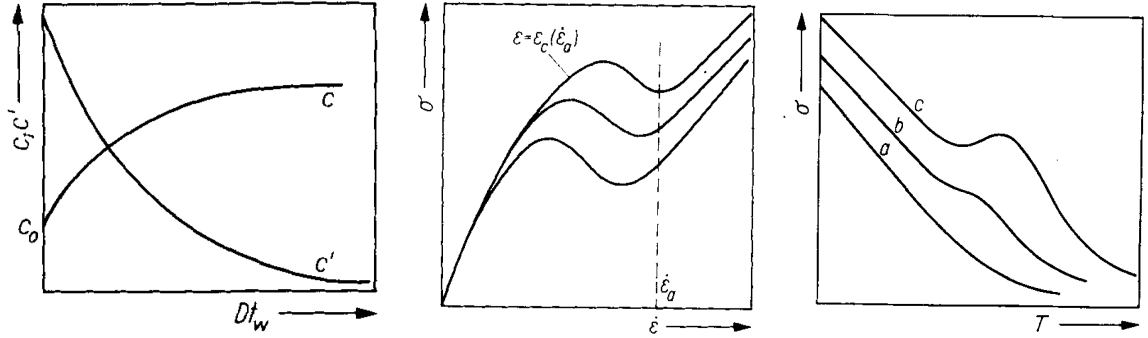
FIGURE 37 – (left) Evolution of the solute concentration c (and $dc/d(Dt_w)$) with respect to Dt_w, (centre) Dependence of stress on strain rate for different strain level (right) Dependence of stress on temperature for different values of Dt_w.

The article ends with a discussion on strain rate sensitivity in which the author suggest that strain rate jumps during tensile tests may help to identify many parameters of the model. In particular A. van den Beukel makes the difference between the instantaneous flow stress response to a sudden change in strain rate that is related to the usual positive strain rate sensitivity, and the relaxed flow stress value which is affected by the strain ageing contribution.

[N. Louat, 1981] : On the theory of the Portevin - Le Chatelier effect (*Scripta Metallurgica*)[66]

In this short article from N.Louat is proposed a rather simple but very important modification of the Cottrell's equation – or the very similar one from J.Friedel – relative to the diffusion of solute atoms towards arrested dislocations. The original formula (see eq. 8 9) proposes a non-saturating evolution of the solute concentration $c(t_w)$ around a dislocation arrested during a

waiting time t_w. :

$$c(t_w) - c_0 \propto f c_0 \left(\frac{D t_w}{T} \right)^{2/3} \tag{25}$$

$$\Rightarrow \frac{dc}{dt_w} \propto f c_0 \left(\frac{D}{T} \right)^{2/3} t_w^{-1/3} \tag{26}$$

In this latter (and in the following), f is the fraction of occupied sites required to complete the atmosphere, c_0 is the initial concentration, D is the diffusion coefficient, T is the temperature. However, as mentioned by A.H.Cottrell and B.A.Bilby : *"Equation 25 represents the observed behaviour fairly well up to about $c(t_w)/f \approx 0.3$ but beyond this range it gives a rate of ageing which is too high; this is to be expect since the neglect of the effect of saturation..."*

Based on this observation, N. Louat propose a semi-empirical modification of the rate of saturation $dc(t_w)/dt_w$, replacing the factor f in equation 26 by $(f - c)/f$. This modification is based on the assumption that : *"the rate of filling of core positions should be proportional to the ratio of the numbers of unoccupied to ultimately fillable sites."* The evolution equations for $dc(t_w)/dt_w$, and $c(t_w)$ then become :

$$\frac{dc}{dt_w} \propto \left(\frac{f - c}{f} \right) c_0 \left(\frac{D}{T} \right)^{2/3} t_w^{-1/3} \tag{27}$$

$$\Rightarrow c(t_w) - c_0 \simeq f \left[1 - \exp \left(-\frac{k c_0}{f} \left(\frac{D t_w}{T} \right)^{2/3} \right) \right] \tag{28}$$

To obtain equation 28 from equation 27, it is assumed that c_0 is small compared with f. The corresponding schematic evolutions of $c(t_w)$ as proposed respectively by A.H.Cottrell and N.Louat are plotted on figure 38. Both evolutions coincide at the beginning of the curve (i.e. up to $(c - c_0) \approx f/3$), and then differ.
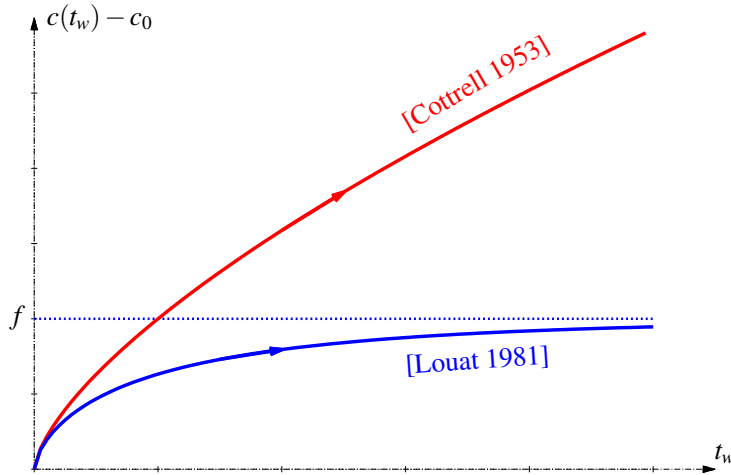

FIGURE 38 – Evolution of the over-concentration $c(t_w) - c_0$ around a dislocation arrested during waiting time t_w following A.H.Cottrell [23], and N.Louat [66] equations.

The rest of the article is devoted to the define some bounds for the serrated yielding domain in the temperature vs. strain rate space. This point is described in details in some following article.

71

This article investigates the Portevin - Le Chatelier effect appearing in a stainless steel in the temperature range between 350°C and 700°C. The tensile experiments are carried out under constant stress rate which is quite unusual and correspond to an infinitely soft machine. The stress strain curve is no longer serrated but looks like stairways alternating straining and loading parts like on the left of figure 39(right). This article is very useful for the understanding of dynamic strain ageing thanks to some very clear 3D schematic figures representing the stress as a function of strain rate and temperature – see figure 39(left) –, or as a function of strain rate and strain – see figure 39(right).
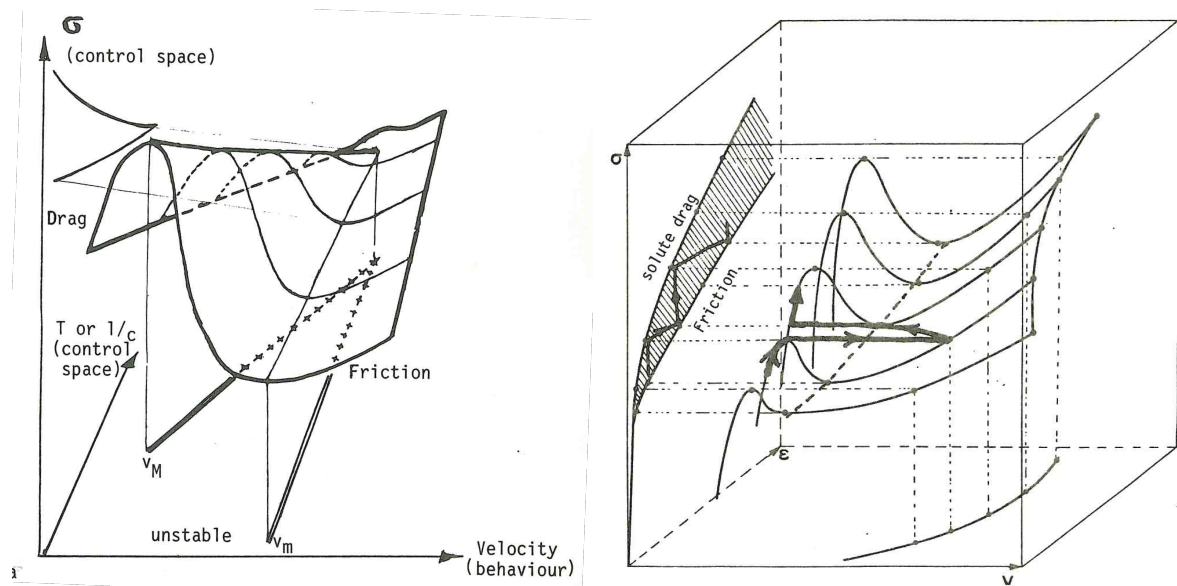
FIGURE 39 – Schematic stress evolution accounting for strain ageing with respect to strain rate and temperature (left), strain rate and strain (right)

Three distinct domains are defined in the strain rate vs. temperature plane :
— The dragging domain exists at low stress or strain rates, or high temperatures. In this domain the velocity of dislocations is limited and solute atoms *"are able to diffuse along with them"*.
— The friction domain is located at large stress or strain rates, or low temperatures. The motion of dislocations is fast enough to avoid pinning by solute atoms. However these latter increase the frictional stress of the lattice.
— The PLC domain is defined as the domain between the friction and dragging domains. Both physical mechanism may coexist in space and time inducing an intermittent and heterogeneous plastic deformation in the specimens.

Another very interesting discussion is proposed in this article concerning the relation of strain ageing phenomena with the catastrophe theory. The surface plotted on figure 39(left) can then be considered as a cuspoïd associated with a 2-dimensional control space also called "cusp" catastrophe. The control parameters are the stress σ and the temperature T, while the output variable is the strain rate $\dot{\varepsilon}$ (or dislocation velocity like on figure 39(left)). The potential function V associated with this cusp catastrophe may then probably be written under the following form :

$$V(\dot{\varepsilon}, \sigma, T) = \frac{1}{4}f(\dot{\varepsilon})^4 - h(\sigma)f(\dot{\varepsilon}) - \frac{1}{2}g(T)f(\dot{\varepsilon})^2 \qquad (29)$$

where f, g, h are some functions not defined here. It is well known that for such a catastrophe, a part of the surface that correspond here to the negative strain rate sensitivity domain can never be reached. Such a potential function also gives rise – if the temperature parameter is small enough – to some hysteresis loops as it is proposed in the previously presented article by P.Penning [50] or latter by Y.Estrin and L.Kubin [76].

2.4   1985-2000 : Modeling the PLC effect

[P.G. McCormick, 1988] : Theory of flow localisation due to dynamic strain ageing (*Acta Metallurgica*)[85]

This article is probably the most important one among those presented in this document, since it summarizes all the concepts and equations that have been presented up to now, and provide a complete mechanical model that will be used latter in numerous numerical studies to simulate the Portevin - Le Chatelier effect. The author analysis is based on two fundamental statements :
   — The occurrence of Portevin - Le Chatelier effect is associated with a negative strain rate dependence of the flow stress [50].
   — This latter can results from *"the diffusion of solute atoms to dislocations temporarily arrested at obstacles in the slip path"* [57].
P.G.McCormick add in this article a third fundamental feature of the PLC effect : the transient nature of strain ageing i.e. the fact that the local composition of solute atoms cannot response instantaneously to a sudden change in the mechanical solicitation controlled by the prescribed strain rate. This statement is based on experimental observations of the stress response to discontinuous increase in strain rate during tensile test (also called sometimes jump tests). The different situations that are observed in this case are represented on figure 40 using the model proposed by the author.
Two different strain rate sensitivities can be defined :
   — The instantaneous strain rate sensitivity M_i can be observed directly after the strain rate jump (see $\Delta\sigma_i$ on figure 40). This latter is always positive and is not affected by strain ageing phenomenon. It is only related to the usual thermal activation of the flow stress.
   — The steady-state strain rate sensitivity M_f is observed after a transient period (see $\Delta\sigma_{ss}$ on figure 40) during which the solute concentration around arrested dislocations has relaxed towards its new steady-state value. This latter can be positive, or negative since it contains the usual thermal activation of the flow stress (always positive), and a contribution due to the strain ageing (always negative or null).
A very important consequence of this transient behaviour proposed by the author is that $M_f \leq 0$ is a necessary but not sufficient criterion for the occurrence of the Portevin - Le Chatelier effect as it is detailed further in the article or in the present document.
The brilliant and original idea of P.G.McCormick was to account for this transient behaviour by making a difference between the waiting time of dislocations at obstacles t_w, and *"the effective time that the arrested mobile dislocation have aged"* denoted t_a (as "ageing time"). The ageing time t_a obeys a Boltzmann type relaxation equation :
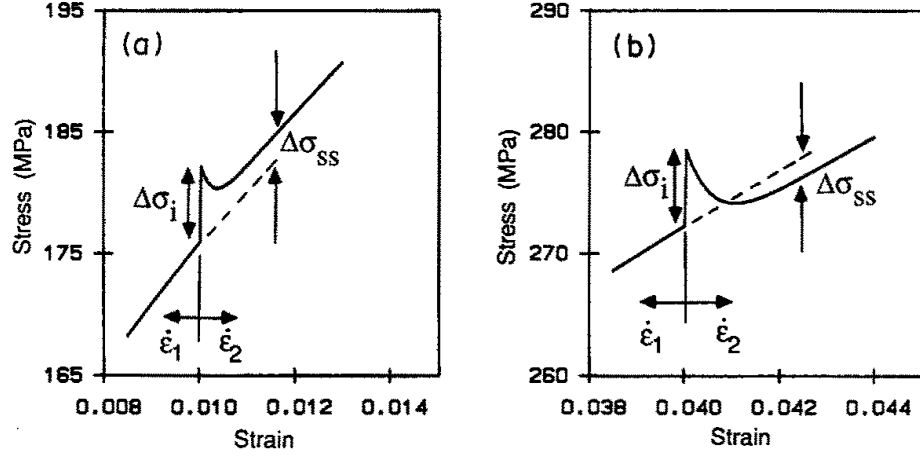
$$\frac{dt_a}{dt} = \frac{t_w - t_a}{\tau} \qquad (30)$$

73

FIGURE 40 – Calculated transient flow stress associated with a sudden strain rate increase from $\dot\varepsilon_1$ to $\dot\varepsilon_2$ ($\dot\varepsilon_2/\dot\varepsilon_1 = 10$) for two different strain levels. The instantaneous strain rate sensitivity is always positive, while the steady-state (relaxed) one is positive (left) or negative (right).

where t_w is the equilibrium value and τ the relaxation time which will be taken equal to t_w in almost all the following studies using this model.

Based on that, the author suggests to introduce t_a instead of t_w in the solute composition equation initially proposed by Cottrell-Bilby [23] and Friedel [27], and modified by Louat [66] :

$$C_s(t_a) = C_m \left[1 - \exp\left(\frac{-C_0(KDt_a)^{2/3}}{C_m} \right) \right] \tag{31}$$

where C_0 is the average bulk concentration, C_m is the saturation concentration, and $C_s(t_a)$ is the current concentration. Finally, based on the equations proposed by van den Beukel [57], the total flow stress equation is given as :

$$\sigma = \sigma_f(\varepsilon) + M_i \ln\left(\frac{\dot\varepsilon}{\dot\varepsilon_0} \right) + M_i H_c' C_s(t_a) \tag{32}$$

The first term σ_f is the strain rate independent internal stress, usually taken to be a function of the forest dislocation density (or of the strain ε). The second term is due to the usual thermal activation of the flow stress, controlling the instantaneous strain rate sensitivity M_i, which is always positive. The third term is related to strain ageing. Because of (i) the relaxation equation 30 that controls the evolution of the ageing time t_a, (ii) the dependence of t_w with respect to strain rate (not given here, see the next article [86] for more details), the steady state strain rate sensitivity M_f can differ from the instantaneous one M_i, and becomes negative or positive[8].

The second part of the article focuses on the stability analysis of the proposed model using the linear perturbation method. This analysis is presented in a more general framework in section 4.1 of the present document and will then not be detailed here. The main results of this analysis are the following ones :

— Three criteria can be defined, the first one corresponding to the negativeness of steady state strain rate sensitivity $M_f \leq 0$, the second one to the oscillating growth of the perturbation, the third one to the exponential growth of the perturbation.

---

8. Practically, the steady state value of t_a is a decreasing function of $\dot\varepsilon$, consequently the steady state value of C_s is a decreasing function of $\dot\varepsilon$.

74

— A comparison with experimental results – based on measures of M_i and M_f using jump tests to calibrate the model – shows that serrations and localized plastic flow occur between the two last criterion, quite close from the third one (exponential growth of perturbations).

The conclusion of this work is admirably summarized by the author in the last part of the article : *"The time dependent character of C_s is fundamental to dynamic strain ageing phenomena. If C_s was an instantaneous function of strain and strain rate, transient effects would be described by a single parameter, M. In this case $M < 0$ would be a valid criterion for localised yielding [50, 76]. However, this is clearly not the case, and flow localisation is determined by both the local strain hardening rate and the rate of change of C_s."*

[Y. Estrin and L.P. Kubin, 1989] : Collective dislocation behaviour in dilute alloys and the Portevin - Le Chatelier effect (*Journal of the Mechanical Behavior of Metals*)[86]

This pair of author has written more than 10 articles [76, 78, 79, 82, 83, 84, 86, 87, 90, 93, 96] on dynamic strain ageing and the Portevin - Le Chatelier effect between 1985 and 1992. The article that we decided to highlight in the present manuscript is a good summary of most of the works presented by the Y.Estrin and L.P.Kubin in this series of articles. The content of the article is way too large for a complete description in this manuscript and we will only focus on the first part of this latter in which some very important concepts concerning strain ageing modelling at the micro-scale are presented.

The authors first recall that the stress σ required to move a dislocation can be decomposed in three main contributions as follow :

$$\sigma = \sigma_d^a + \underbrace{\sigma_d^{th} + f}_{F} \tag{33}$$

where σ_d^a and σ_d^{th} are respectively the athermal and temperature dependant components of stress in the absence of solute atoms. The stress component f called "friction stress" is due to the interaction of dislocations with solute atoms. The total thermal stress $F = \sigma_d^{th} + f$ depends on both temperature and dislocation velocity. The evolution of f with respect to dislocation density v is non monotonic and was already described in the summary of J.L.Strudel article [74]. This evolution is plotted on figure 41(left). The evolution of the total thermal stress F as a function of the plastic strain rate $\dot{\varepsilon}$ plotted on figure 41(right) can be deduced from $f(v)$ and from the Orowan relation between this plastic strain rate and the dislocation velocity :

$$\dot{\varepsilon} = \phi \rho_m b v \tag{34}$$

where ϕ is a geometric factor, ρ_m is the mobile dislocation density, and b the magnitude of the Burgers vector.

The waiting time t_w of dislocation at localized obstacle is then introduced. Assuming that between two obstacles the dislocation velocity is infinite, and that the mean distance between obstacles l is proportional to the average spacing between forest dislocations $\rho_f^{-1/2}$, the mean dislocation velocity becomes :

$$v = l/t_w \propto (\rho_f^{1/2} t_w)^{-1} \tag{35}$$

Coupling equations 34 and 35, we obtain an expression for the waiting time t_w as a function
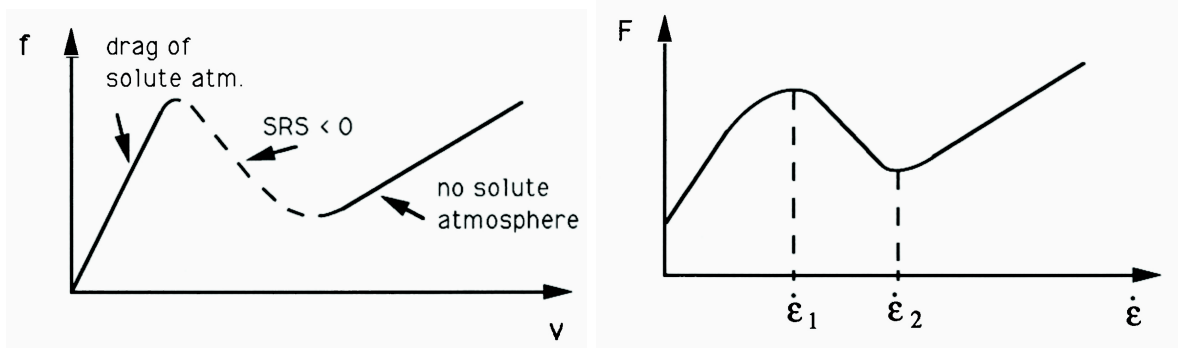
FIGURE 41 – Influence on dynamic strain ageing in the thermal components of stress : (left) friction stress f as a function of dislocation velocity, (right) total thermal stress F as a function of plastic strain rate

of the plastic strain rate $\dot{\varepsilon}$:

$$t_w = w/\dot{\varepsilon} \tag{36}$$

$$w = \phi b \rho_m \rho_f^{-1/2} \tag{37}$$

This parameter w is then a strain quantity which depends on both dislocation densities (mobile and forest). It is defined by the authors as *"the deformation obtained when an elementary activation step is accomplished by all mobile dislocations"*. A complementary model for the evolutions of mobile and forest dislocation densities is given as an appendix in another article by the same authors [90]. Based on these evolutions, the authors show that the parameter w generally increases with global deformation, then decreases , and finally stabilize towards and intermediate value. However in the same article it can be observed that the transient behaviour for w is limited to the first 3% of the deformation, after which this latter is almost constant. That may explain why in many following study, w will be kept constant, and consequently the waiting time t_w will be directly inversely proportional to the plastic strain rate $\dot{\varepsilon}$: $t_w = w/\dot{\varepsilon}$.

This last equation defining the waiting time, associated with the ageing time relaxation equation 30 proposed by McCormick [44], and the solute composition equation 31 proposed by Louat [66] compose the bases of the Kubin-Estrin-McCormick (KEMC) model that will be used afterwards in almost all the finite element simulations of the Portevin - Le Chatelier effect.

[F. Springer and Ch. Schwink, 1991] : Quantitative investigations on dynamic strain ageing in polycrystalline CuMn alloys (*Scripta Metallurgica et Materialia*)[94]

A legacy of the initial studies on strain ageing by A.H.Cottrell [23] and J.Friedel [27] is the exponent $n = 2/3$ on the waiting time present in the solute composition equation 31. The origin of this exponent is recalled and discussed in this article by F.Springer and C.Schwink some years latter. The value of $n = 2/3$ is explain as follow : *"For sufficiently short times the diffusion distance R increases as $R \propto (Dt)^{1/3}$ ($D(T) =$ diffusion constant). In the case of free diffusion in volume only, solutes inside a tube of radius R enclosing the dislocation can arrive at it within t. The volume of the tube being proportional to R^2, the line concentration of solutes pinned at an arrested dislocation increases proportional to $t^{2/3}$. It follows $n = 2/3$ and $-M_0 \propto \dot{\varepsilon}^{-2/3}$ "* (this latter results is detailed below).

In this article, the authors propose to check this value of 2/3 by carrying out some selected tensile experiments on Cu-Mn alloys with different concentrations of Mn from 0 to 14%. The tensile tests are carried out at different temperatures avoiding the serrated yielding domain,

starting with a rather slow prescribed strain rate $\dot{\varepsilon}_1$ (from $3 \times 10^{-6} s^{-1}$ to $3 \times 10^{-4} s^{-1}$) and applying a sudden strain rate change of a factor 2 at different strain (or stress) level (see figure 42(left)).
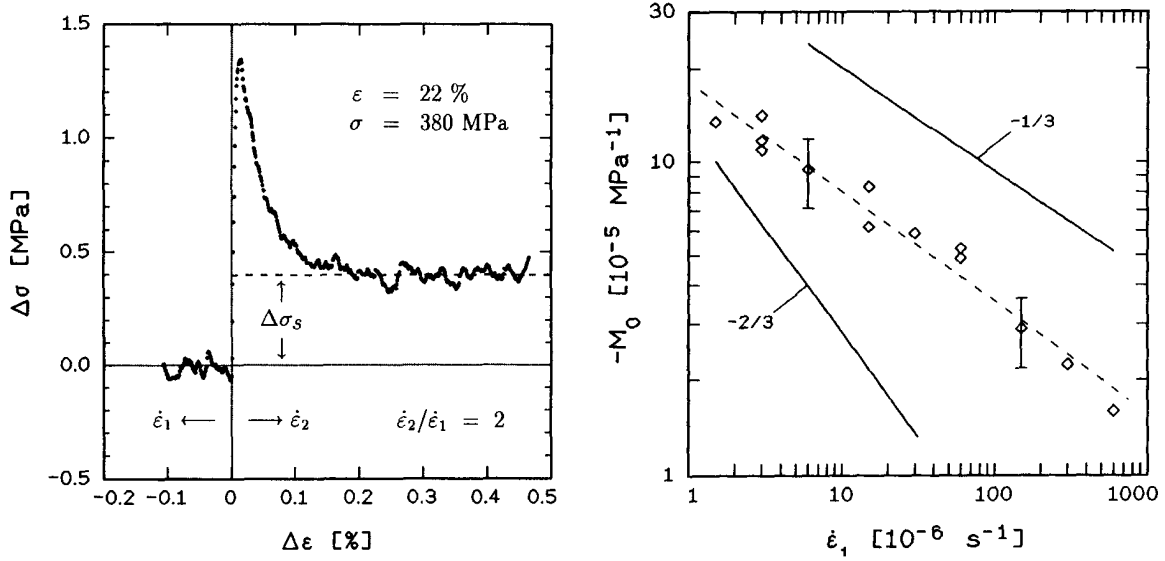

FIGURE 42 – (left) Strain rate change test where the hardening contribution as been retrieve. The steady state stress variation is $\Delta\sigma_s$. (right) Logarithmic plot of the steady state strain rate sensitivity M_0 as a function of initial strain rate $\dot{\varepsilon}_1$.

The steady-state strain rate sensitivity M_0 (denoted M_f in the article by McCormick [44]) can then be estimated for different temperatures, solute concentration, and strain rates. This method of identification of ageing parameters follow the idea proposed in 1975 by S.H. van den Brink, A. van den Beukel, and P.G. McCormick on Au-Cu alloys [58] and can be retrieve from equation (6) of the article from McCormick [85] presented below [9] :

$$M_f = \frac{\Delta\sigma_s}{\Delta \log \dot{\varepsilon}} = M_i \left[1 - K_1 \left(\varepsilon^{m+\beta}/\dot{\varepsilon} \right)^{2/3} \right] \tag{38}$$

where M_i is the instantaneous strain rate sensitivity and K_1 a temperature and solute concentration dependant parameter. It appears obviously that using strain rate jump tests carried out for a given temperature, solute concentration, and level of deformation, but for different initial strain rate should validate (or not) the exponent 2/3 in the equation. That is exactly the work carried out very carefully by F.Springer and C.Schwink in this article that is presented on figure 42(right).

They found in this logarithmic plot that the slop of 2/3 is not in agreement with the experimental data while an exponent of 1/3 should be more appropriate. There physical explanation is that the diffusion of solute atoms is not a bulk diffusion but a pipe-diffusion, meaning that these latter move along dislocations. Consequently *"the diffusion path is restricted to a line. Therefore, not the whole volume of the enclosing tube proportional to $R^2 \propto (Dt)^{2/3}$ is the possible source for the solute diffusion within t ; instead only the whole number of forest lines up to a length $R \propto t^{1/3}$ ending at the arrested glide dislocation provide the diffusion. Such a mechanism results in $n = 1/3$ and $-M_0 \propto \dot{\varepsilon}^{-1/3}$."*

---

9. It is important to note that this equation is valid since (i) the change in strain rate during the jump is small, (ii) the local solute concentration is small enough such that the modification proposed by N.Louat accounting for saturation is not mandatory, (iii) the usual thermal stress (also called viscous stress) is a logarithmic function of the plastic strain rate $\sigma_v = \sigma_0 \log(\dot{\varepsilon}/\dot{\varepsilon}_0)$

The experimental results presented in this article seems to clearly indicate that an exponent of 1/3 should be used in the strain ageing models, and that the pipe diffusion is the main diffusion mechanism of solute atoms towards arrested dislocations [10]. However this analysis was made assuming for a given material using an exponential flow rule. If this latter is change, the whole analysis in no longer valid and another exponent could probably be obtain. The physical explanation is also based on many assumption and carried out at a very small scale compared with macroscopic one. It will be shown in the main part of the document that the parameter n may also finally be fitted directly on tensile experiments at different strain rate.

---

10. This mechanism of pipe diffusion of solute atoms from stationnary dislocation towards temporary arrested ones was already suggested in 1958 by A.W.Sleeswyk [24]

3   Mechanical and material modelling of strain aging phenomena

The main feature of the Kubin-Extrin-McCormick model are presented in this chapter. The origin of this model and its physical motivations have been detailed in section 2, only the final equations will be detailed in the the following under a 3 dimensional mechanical framework [11]. A special attention will be paid on the rôle of the different parameters of the model in order to provide some keys on how to identify them accurately. In a second part, some recent extensions of the model will be presented : introduction of kinematic hardening, dislocation density, or crystal plasticity. Finally an example of how this model can be identified on a large range of temperature and strain rate will be presented based on the work of H.Wang [202].

3.1   The original KEMC model

The Kubin-Estrin-MacCormick model

The mechanical model used in this work has been mainly introduced by MacCormick [85] and modified in some following work [122, 179]. The constitutive equations are written using general expressions such that the models used in the aforementioned studies are encompassed by the following theoretical developments. The strain rate tensor $\dot{\underset{\sim}{\varepsilon}}$ is split into elastic and plastic contributions :

$$\dot{\underset{\sim}{\varepsilon}} = \dot{\underset{\sim}{\varepsilon}}_e + \dot{\underset{\sim}{\varepsilon}}_p \tag{39}$$

$$\underset{\sim}{\sigma} = \underset{\approx}{E} : \underset{\sim}{\varepsilon}_e \tag{40}$$

$$\tag{41}$$

where $\underset{\approx}{E}$ is the tensor of elastic moduli. The evolution of the plastic part is provided by the yield function and the plastic flow rule :

$$f(\underset{\sim}{\sigma}, p, t_a) = \sigma_{eq}(\underset{\sim}{\sigma}) - R(p) - R_a(t_a) \tag{42}$$

$$\dot{\underset{\sim}{\varepsilon}}_p = \dot{p}\underset{\sim}{n} \tag{43}$$

$$\underset{\sim}{n} = \frac{\partial f}{\partial \underset{\sim}{\sigma}} \tag{44}$$

where p is the cumulated plastic strain, and t_a the ageing time. σ_{eq} can be any of the well-known equivalent stress measures associated with classical yield criteria (von Mises, Tresca, Hill, ...). $R(p)$ is one of the conventional hardening function. The cumulated plastic strain rate $\dot{p}$ is computed using the following viscoplastic flow rule.

$$\dot{p} = R_v^{-1}(< f >), \qquad < \mathrm{f} > = \max(0, \mathrm{f}) \tag{45}$$

$$f = R_v(\dot{p}) \tag{46}$$

where R_v is the reverse form of one of the classical flow rule (such as Norton's law $\dot{p} = < f/K >^n$ for example).

---

11.   The KEMC model is presented here in a small strain formulation. However, since the strain hardening contribution is isotropic by nature the extension to a finite strain formulation is very convenient and similar to what is done for usually for elasto-visco-plastic models (see [179] or [199] for examples).

The ageing hardening R_a related to dynamic strain ageing, is calculated from the over-concentration C_s of solute atoms around dislocations. C_s is a function of both internal variables of the model, the cumulated plastic strain p and the ageing time t_a. The ageing time increment is computed from an evolution law in which the cumulated plastic strain rate $\dot{p}$ intervenes :

$$R_a(t_a) = P_1 C_s(t_a) = P_1 C_m \left[1 - e^{-\left(\frac{t_a}{t_0}\right)^n} \right] \tag{47}$$

$$\dot{t}_a = 1 - \frac{t_a}{t_w}; \qquad t_w = \frac{w}{\dot{p}} \tag{48}$$

where $P_1 C_m$, t_0, n, and w are 4 material parameters controlling the strain ageing contribution to the flow stress.

Steady-State analysis

A steady-state analysis of the KEMC model can be carried out assuming that t_a has reached its steady-state value, also called the waiting time :

$$\dot{t}_a = 0 \Rightarrow t_a = t_w = \frac{w}{\dot{p}} \tag{49}$$

A one-dimensionnal tensile stress state is assumed, without accounting for the testing machine stiffness. Based on equation (42), the only non zero component in the stress tensor is the tensile stress σ :

$$\sigma = R(p) + R_v(\dot{p}) + R_a(\dot{p}) \tag{50}$$

where R, R_v are defined previously in the text and :

$$R_a(\dot{p}) = P_1 C_m \left[1 - e^{-\left(\frac{w}{t_0 \dot{p}}\right)^n} \right] \tag{51}$$

Based on this latter equation, the evolution of R_a with respect to strain rate $\dot{p}$ and the roles of the four parameters $P_1 C_m$ (these two parameters can in fact be replaced by a single one), t_0, w, and n are plotted on figure 43. The left part of the curve i.e. for low strain rates is associated with the dragging mode : the dislocations are continuously pinned by solute atoms and they move together with their atmospheres. The right part of the curve i.e. for high strain rates is associated with the friction domain : the solute atoms cannot diffuse fast enough to pin dislocations that can consequently move freely around them. The part of the curve between these two area defines the strain ageing domain in which the velocity af dislocations and the diffusion of solute atoms is equilibrated.

The evolution of R_a with respect to $\dot{p}$ depends on the ageing parameters $P_1 C_m$, t_0, w, and n as it can be observed on figures 43 and 44. Many observations can be done concerning the rôle of the model parameters on the steady state behaviour using this picture.

1. Parameters w and t_0 have the same influence with opposite directions on the evolution of R_a under steady state conditions. This evolution is unique for a given value of the ratio w/t_0 has it can be seen from equation 51. The difference between the rôle of these two parameters will be highlighted by the transient behaviour analysis.

2. The parameter n controls the slope of the transition between the pinned state (i.e. at low strain rate) and the unpinned one (i.e. at high strain rate). Combined with the parameters of the flow rule (see equation 46), this parameter will determine if a negative strain rate sensitivity domain exists or not and its slope.
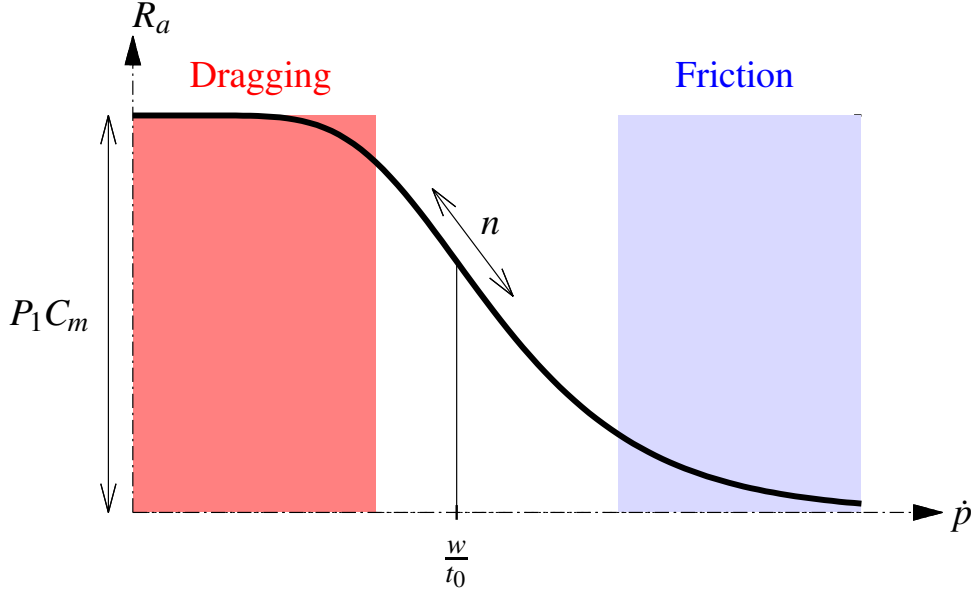
FIGURE 43 – Steady state evolution of R_a as a function of the plastic strain rate $\dot{p}$. Roles of the four ageing parameter $P_1 C_m$, t_0, w, and n.

3. It can also be seen on that same curve and from equation 51 that the center of the transition domain does not depend from n but is related to w/t_0.

4. Finally $P_1 C_m$ control the maximal value of the overstress R_a which appears in the fully pinned state (dragging domain). It also have an indirect influence on the slope in the negative strain rate sensitivity domain.

σ and its contributions R, R_v, and R_a are plotted on figure 45 as functions of plastic strain rate for 1% of plastic strain for a given set of parameters (see [199]). R induces no strain rate dependency. R_v implies a positive strain rate dependency. R_a induces a negative strain rate dependency in a given range of strain rate. Finally when all the three contributions are added, the tensile stress σ follows a non monotonic evolution with respect to the prescribed strain rate.

It is also possible to plot the evolution of σ as a function of p and $\dot{p}$, using the steady state value for t_a. Such 3D surfaces have been plotted on figure 46. The equivalent surfaces for a purely plastic (figure 46(a)) or visco-plastic without ageing (figure 46(b)) have also been plotted in order to highlight the influence of the strain ageing contribution R_a.

Transient behavior - the static strain ageing case

The KEMC model is also suitable to model the well known yield peak phenomenon followed by the Lüders plateau that can be observed on the tensile curve of many metallic alloy at the transition between elastic and plastic domains. For that purpose an initial value t_{aini} is prescribed to the ageing time t_a, representing the fact that the material is initially in the fully pinned state. When plasticity occurs (i.e. when the stress has reached the yield peak value), the variable t_a slowly decrease towards its steady state value $t_w = w/\dot{p}$. If t_{aini} is larger than t_w, the overstress R_a will then decrease and can induce a softening on the global stress strain curve. Once t_a has reached its steady state value, the overstress remain constant and the hardening is then only control by the usual isotropic term $R(p)$.
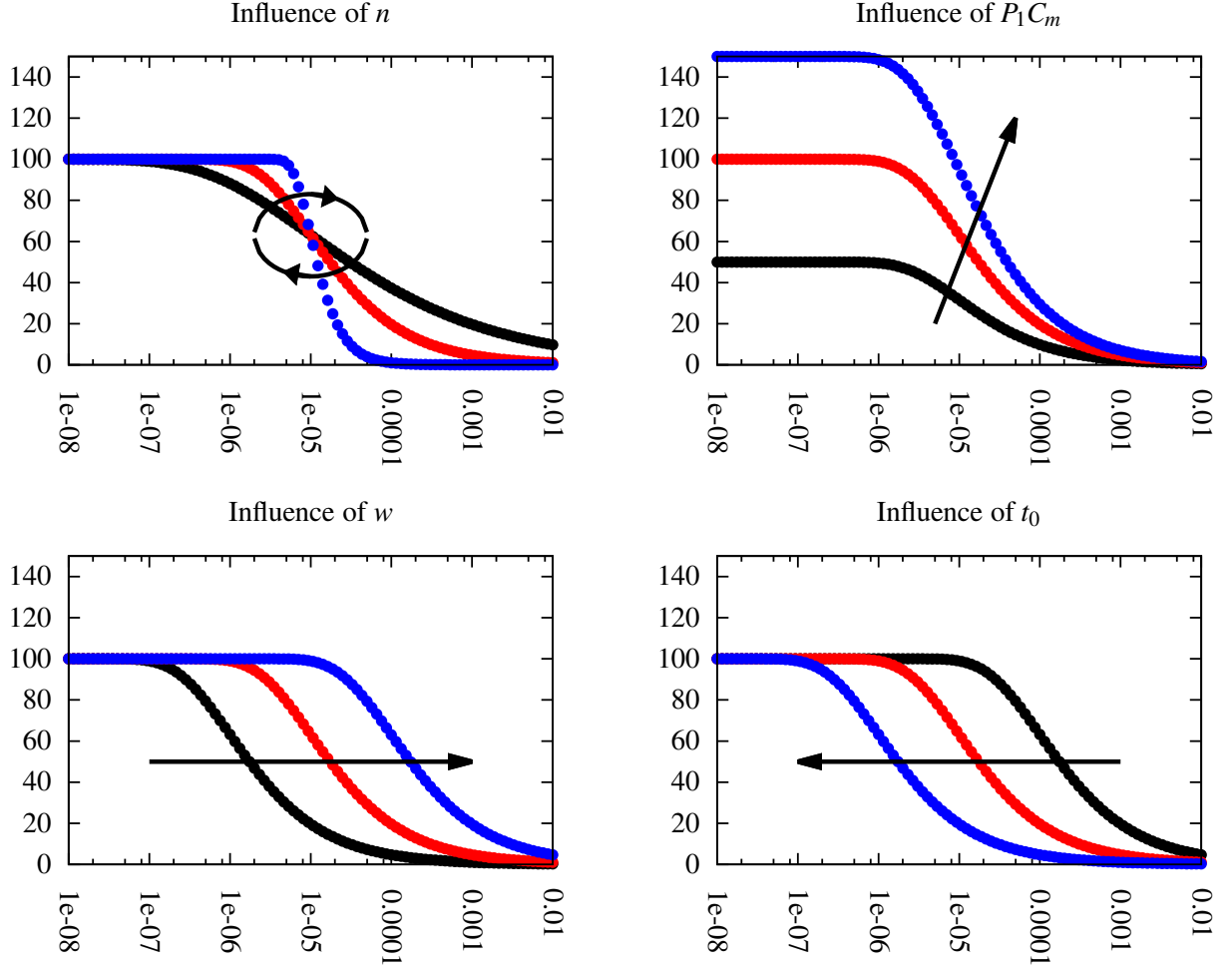
FIGURE 44 – Influence of the ageing parameters P_1C_m, t_0, w, and n on the steady state evolution of the over-hardening R_a with respect to the plastic strain rate $\dot{p}$.

Assuming a constant plastic strain rate $\dot{p}$ that can be taken equal to the global prescribe strain rate $\dot{\varepsilon}$ neglecting the elastic strain rate $\dot{\varepsilon}_e$, the evolution equation 48 on the ageing time can be solved to provide the evolution of $t_a(p)$ with respect to p :

$$ta(p) = \frac{w}{\dot{p}}\left[1 - e^{\left(-\frac{p}{w}\right)}\right] + t_{aini}e^{\left(-\frac{p}{w}\right)} \tag{52}$$

This expression introduced in $R_a(t_a)$ provides the evolution of the ageing overstress with respect to p, $\dot{p}$, and to all material parameters : w, t_{aini}, t_0, n, P_1C_m. The influence of all these parameters on the evolution of R_a with p are plotted on figure 47. The main informations that can be observed on these evolutions are :

1. The plastic strain rate $\dot{p}$ (or the total strain rate $\dot{\varepsilon}$) only affects the final value of R_a via the steady state value t_w. For small values of $\dot{p}$, the totally unpinned state is never reached.

2. The parameter w has the same role (with a reverse influence) as $\dot{p}$, but also affects the slope of the decrease of R_a (unpinning process).

3. t_{aini} and t_0 have the same influence with opposite directions and play a very important role for the existence of a yield peak. It must be notice that prescribing the same value
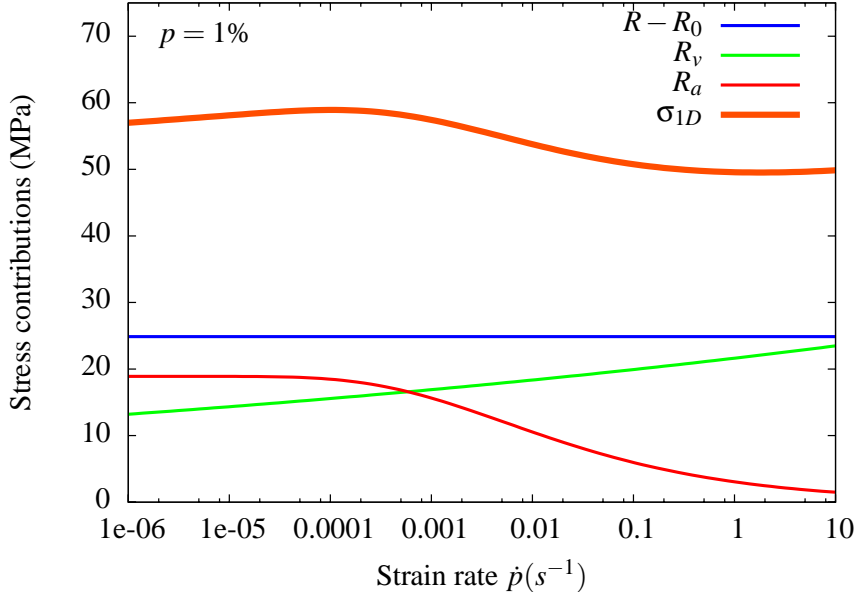
FIGURE 45 – Evolution of the 1D stationary stress as a function of the plastic strain rate $\dot{p}$ The negative behaviour is introduced by the ageing hardening part R_a.

for t_{aini} and t_0 will guarantee a constant initial value for R_a equal to $0.63 P_1 C_m$ whatever the other parameters are. This particular case can be useful for step by step identification like in [198].

4. n and $P_1 C_m$ have almost the same influence as in the previous steady state analysis controlling respectively the slope of the unpinning process and the maximal overstress value.

Another important point to remark is that a yield peak may appear even if t_{aini} is initially set to 0. Indeed during the elastic loading, $\dot{t}_a = 1$, and then at yielding $t_a = t_y$ which is generally small but not null. This time to yielding is approximately to $t_y = \frac{\sigma_{yield}}{E\dot{\varepsilon}}$. If t_y is larger than the steady state value of t_a equal to t_w, then a small yield peak will occur followed by a softening [12].

Transient behavior - the dynamic strain ageing case

In order to understand the transient behaviour of the KEMC model (i.e. the evolution of stress and strain during pinning and unpinning), it can be convenient to derive an evolution equation for the over-concentration C_s (or in the same way for the ageing hardening R_a). For that purpose equations 47 giving the relation between C_s and t_a, and equation 48 providing the evolution of t_a are combined to obtain the equation 53.

In the following, the parameter C_m is set to 1, the over-concentration consequently evolve between 0 and 1, and the ageing hardening R_a evolve between 0 and P_1.

$$\dot{C}_s = n \underbrace{(1 - C_s)}_{>0} \left[\underbrace{\frac{[-\log(1 - C_s)]^{1 - \frac{1}{n}}}{t_0}}_{>0,\ \text{pinning}} + \underbrace{\frac{\log(1 - C_s)}{t_w}}_{<0,\ \text{unpinning}} \right] \tag{53}$$

---

12. Example of order of magnitude for a mild steel : $\sigma_y \sim 200\text{MPa}$, $E \sim 200\text{GPa}$, $\dot{\varepsilon} \sim 10^{-4}\text{s}^{-1}$ give $t_y = 10\text{s}$ to compare with $t_0(T)$ in section 3.3.
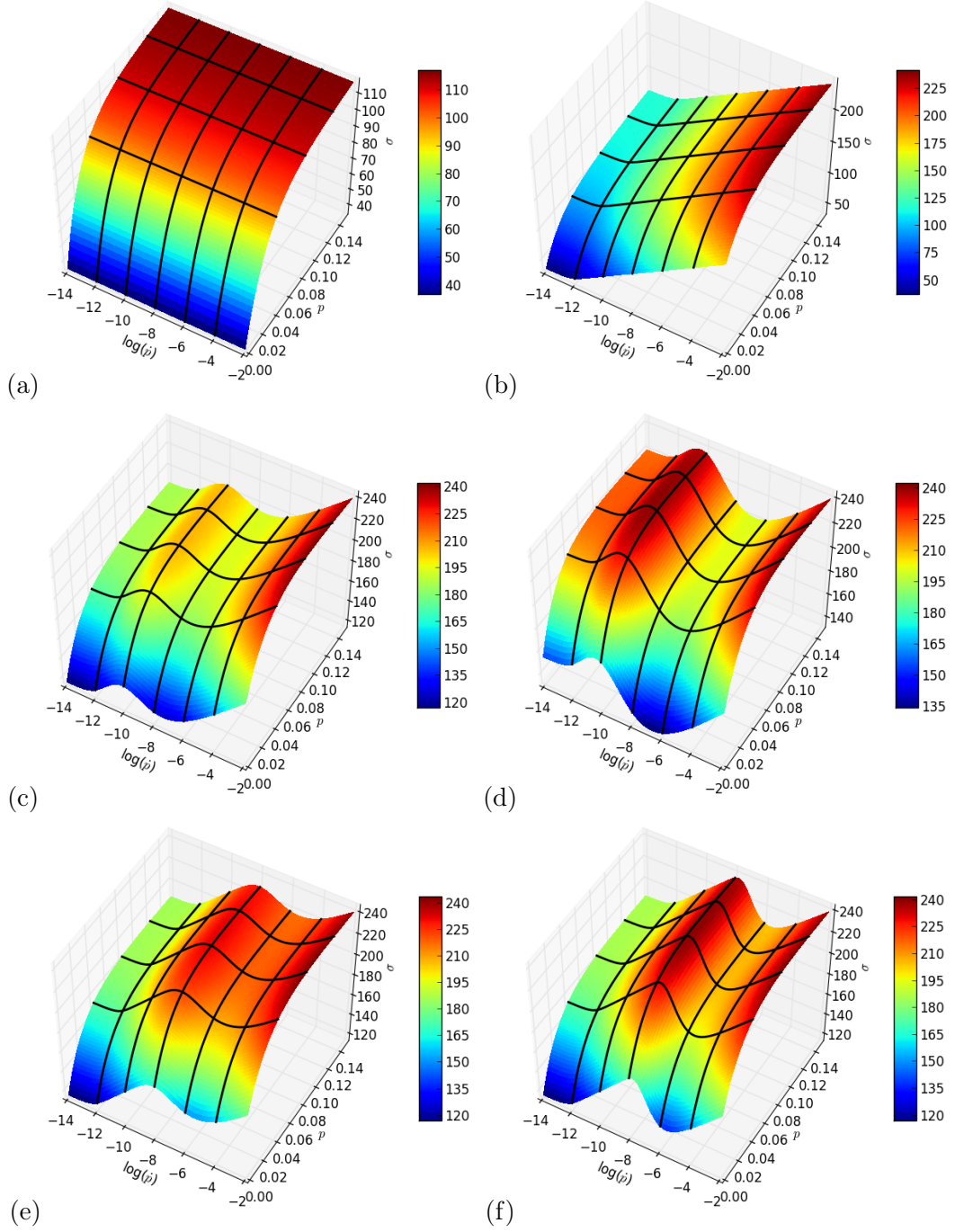
FIGURE 46 – Evolution of the 1D stationary stress as a function of the plastic strain p and plastic strain rate $\dot{p}$. (a) Purely plastic behaviour with a non-linear saturating hardening. (b) Visco-plastic behaviour generated by introducing an hyperbolic sinus flow rule in the model (a). (c) Same model than (b) with the introduction of the over-hardening R_a. The surface becomes non-smooth and a negative strain rate sensitivity domain appears. The same behaviour is then used with (d) a larger value for P_1, (e) a larger value for w (or a smaller value for t_0), (f) a larger value for n.

where $t_w = w/\dot{p}$ is the waiting time.

The competition between the pinning and the unpinning processes is clearly evidenced in equation 53. The value of the over-concentration C_s and consequently the ageing hardening R_a
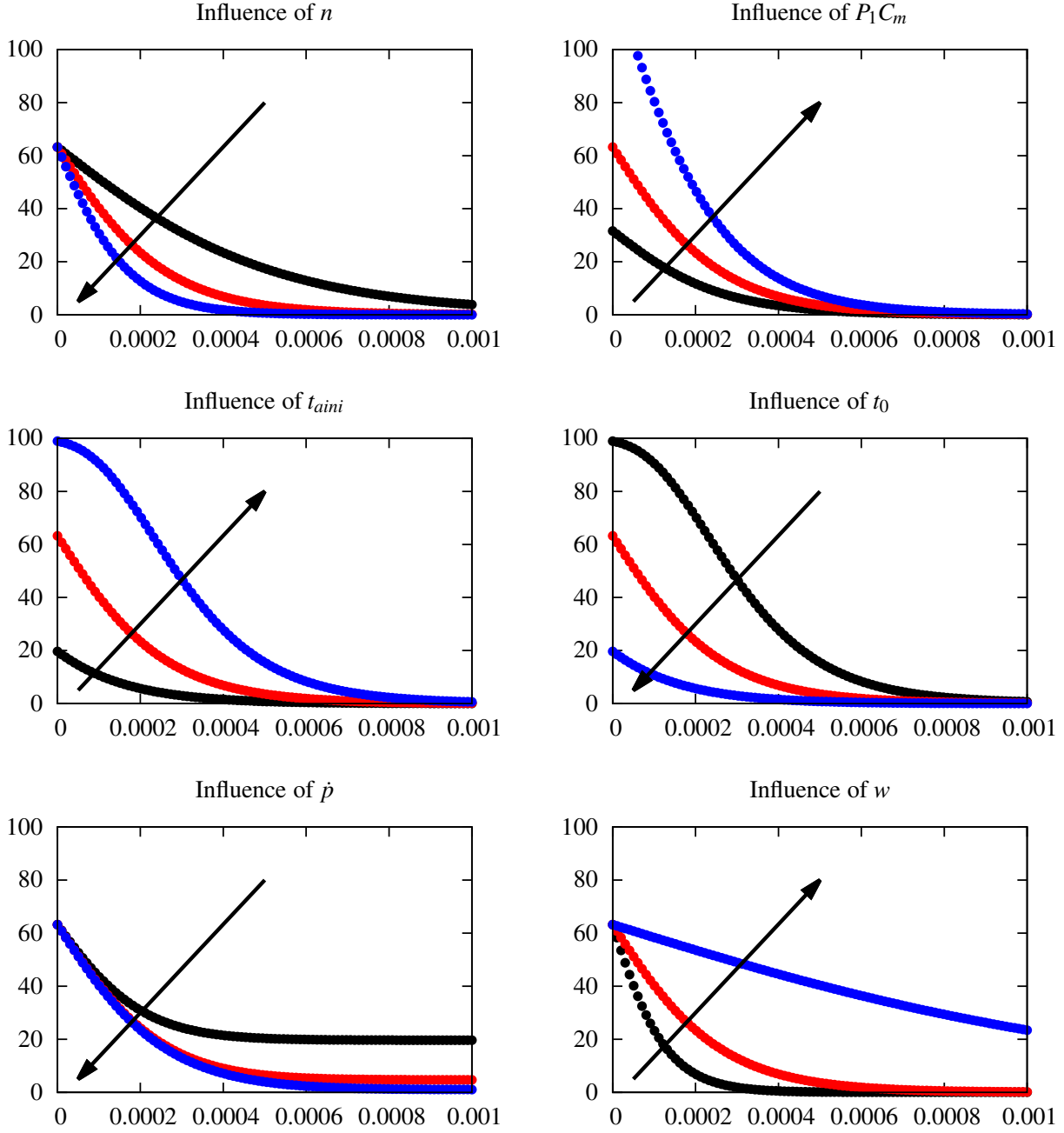
FIGURE 47 – Influence of the strain rate $\dot{p}$ and the ageing parameters $P_1 C_m$, t_0, w, n and t_{aini} on the transient evolution of the over-hardening R_a with respect to the plastic strain p for the static strain ageing case (Lüders phenomenon).

increase with the pinning term (i.e. the left one in the brackets). On the contrary the unpinning term (i.e. the right one in the brackets) will decrease the value of C_s and R_a and bring them back to 0.

If $t_w = w/\dot{p}$ is very large compared to t_0 (this case will occur for very low or null value of the plastic strain rate $\dot{p}$), the pinning term will be large compared to the unpinning one which becomes consequently negligible :

$$\dot{C}_s^p = n\left(1 - C_s^p\right)\left[\frac{\left[-\log\left(1 - C_s^p\right)\right]^{1-\frac{1}{n}}}{t_0}\right] \tag{54}$$

Equation 54 is not obvious to solve. However, accounting for equation 48 on the evolution of t_a, the investigated situation corresponds to $\dot{t}_a \simeq 1$ and consequently $t_a \simeq t$. The evolutions of the over-concentration $C_s(t)$ and the ageing hardening $R_a(t)$ are then easy to obtain obtained assuming for example that $C_s(t=0) = 0$:

$$C_s^p(t) = 1 - e^{-\left(\frac{t}{t_0}\right)^n} \tag{55}$$

$$R_a^p(t) = P_1 \left[1 - e^{-\left(\frac{t}{t_0}\right)^n} \right] \tag{56}$$

The pinning part C_s^p of the evolution of C_s acts in the model as a time-driven hardening. During pinning process, the ageing hardening follows a saturating evolution towards its maximal value. The rate of this process is mainly controlled by the characteristic time t_0 (and to a lesser extent n). t_0 will consequently necessary depend on the temperature since it is obvious that the saturation rate will have to increase with this latter. The evolution of $\dot{C}_s^p$ and $C_s^p(t)$ are given on figure 48(left).
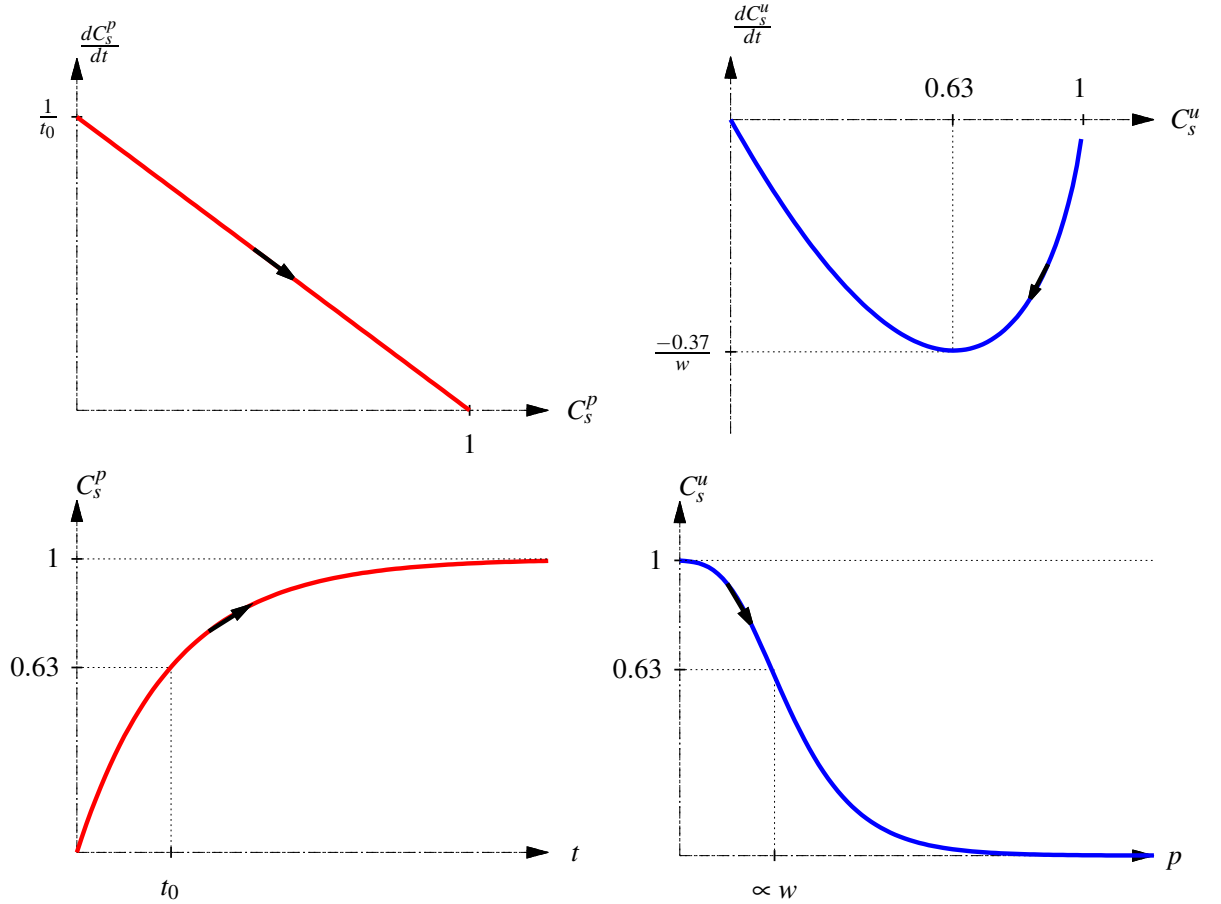

FIGURE 48 – Transient evolutions of the ageing over-concentration C_s for the two extremal cases : pinning process (C_s^p) on the left and unpinning process on the right (C_s^u).

If t_w is small compared to t_0 (this case will occur for large values of the plastic strain rate $\dot{p}$), the unpinning term will be large compared to the pinning one which becomes consequently

negligible :

$$\dot{C}_s^u = n\left(1 - C_s^u\right)\left[\frac{\log\left(1 - C_s^u\right)}{t_w}\right] \tag{57}$$

Since t_w is directly related with the plastic strain rate $\dot{p}$, this equation can be rewritten under the following form :

$$\frac{dC_s^u}{dp} = \frac{n}{w}\left(1 - C_s^u\right)\log\left(1 - C_s^u\right) \tag{58}$$

The unpinning part C_s^u of the evolution of C_s acts in the model as a strain-driven softening. Equation 58 can be solved for an unpinning event between two over-concentration levels $C_s^u(ini)$ and $C_s^u(end)$ (and consequently two ageing stress levels) corresponding to two different plastic strain levels p_{ini} and p_{end} :

$$\Delta p = p_{end} - p_{ini} = \int_{p_{ini}}^{p_{end}} dp = \frac{w}{n}\int_{C_s^u(ini)}^{C_s^u(end)} \frac{dC_s^u}{(1 - C_s^u)\log(1 - C_s^u)} \tag{59}$$

$$= \frac{w}{n}\left[\log\left(\frac{\log(1 - C_s^u(ini))}{\log(1 - C_s^u(end))}\right)\right] \tag{60}$$

This situation corresponds to the passing of a plastic band at a given point of the structure. The amount of plasticity carried out by the band $\Delta p = p_{end} - p_{ini}$ is then mainly controlled by the material parameter w (and to a lesser extent by n). The evolution of $\dot{C}_s^u$ and $C_s^u(t)$ are given on figure 48.

One of the most interesting conclusion of this analysis is that w and $1/t_0$ have a similar influence on the steady state response of the model but not on the transient one. t_0 controls the pinning process while w plays a rôle on the unpinning process.

3.2 Some extensions of the KEMC model

Introduction of the plastic strain in the ageing stress function

In the original model proposed by MacCormick, the plastic strain p is not directly introduced in the constitutive equations but is implicitly present in the expression of t_w. If one forget this dependence accounting that R_a and t_w are independent from the plastic strain p, the position of the negative strain rate sensitivity domain remains when the strain increase located between two constant values of strain rate as it can be seen on figure 49. The introduction of a dependency on p in the constitutive equations has been suggested later to improve the model by Zhang [122] and Böhlke [179], introducing $w(p)$, $t_0(p)$, and $C_m(p)$.

The first modification ($w = w(p)$) was implicitly suggested in 1990 by Kubin and Estrin [86] since this latter was defined as :

$$w = \phi b \rho_m \sqrt{\rho^f} \tag{61}$$

where ϕ is a constant, b is the magnitude of the burger vector, ρ_m and ρ_f the mobile and forest dislocation densities that are related to the cumulated plastic strain p. This modification is detailed in the paragraph devoted to the aforementioned article in section 2.4.

The second modification ($t_0 = t_0(p)$) was already implicitly present in the initial model by McCormick in 1988 [85]. Indeed t_0 is the characteristic time of the solute diffusion process and is consequently proportional to the inverse of the solute diffusion coefficient D, this latter being

FIGURE 49 – Definition of the negative strain rate sensitivity domain with respect to strain rate $\dot{p}$ and strain p for the KEMC model where w, t_0, and P_1 are constant functions of p.

a function of the temperature, but also of the plastic strain via the increase in the vacancy concentration C_v [57] :

$$t_0 \propto 1/D, \quad D = C_v D_0 \exp\left[\frac{-Q}{k_B T}\right], \quad C_v = K_1 \varepsilon^\alpha \tag{62}$$

These two modifications influence the position of the negative strain rate sensitivity domain and its evolution with strain. As it can be seen on figure 49, in the version of the KEMC model without any dependence on p for w, t_0, or P_1, the NSRS domain remain the same whatever the level of strain is. The introduction of increasing functions for $w(p)$ and $t_0(p)$ will shift this domain towards higher strain rates when the strain increases like on figure 50. However, this kind of evolution is not fully consistent with the experimental ones, in particular the evolution of the critical plastic strain at low strain rates (see chapter 4) cannot be reproduced with such an evolution.
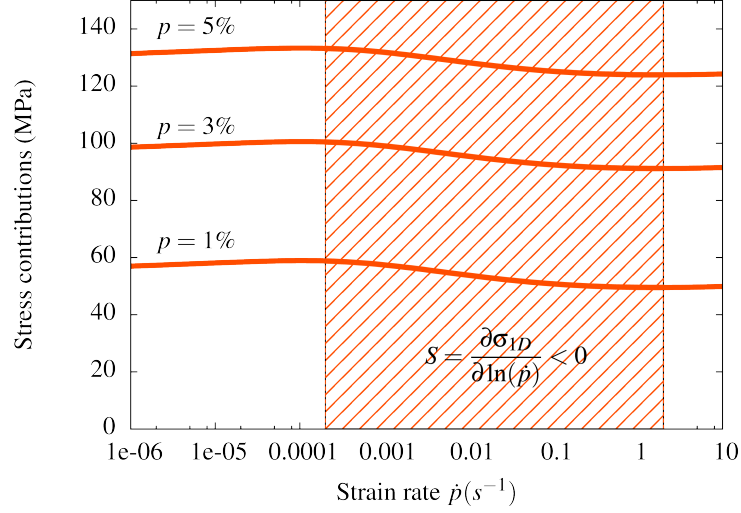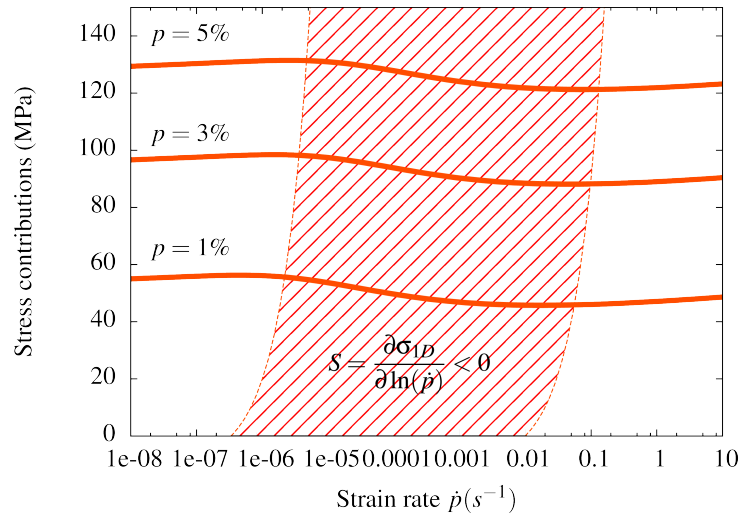

FIGURE 50 – Definition of the negative strain rate sensitivity domain with respect to strain rate $\dot{p}$ and strain p for the modification proposed by Zhang [122] ($w = w(p)$ and $t_0 = t_0(p)$).

The third modification ($P_1 = P_1(p)$) has then been proposed recently by T.Böhlke [179] in order to provide an evolution of the NSRS domain in agreement with experimental observations. For that purpose a linear increasing function $P_1(p)$ is introduced in the model, leading to an evolution for the left part of the NSRS domain plotted on figure 51. The physical meaning of this modification is that the solute atoms diffusion restrict the initial movement of the dislocations (increase in the yield stress level), but also the annihilation of these latter during the plastic deformation. Consequently the level of the stress but also the hardening rate have to be larger in the pinned domain (i.e. for low strain rates) than in the unpinned one. An alternative elegant solution to account for such phenomenon is detailed in a following paragraph.
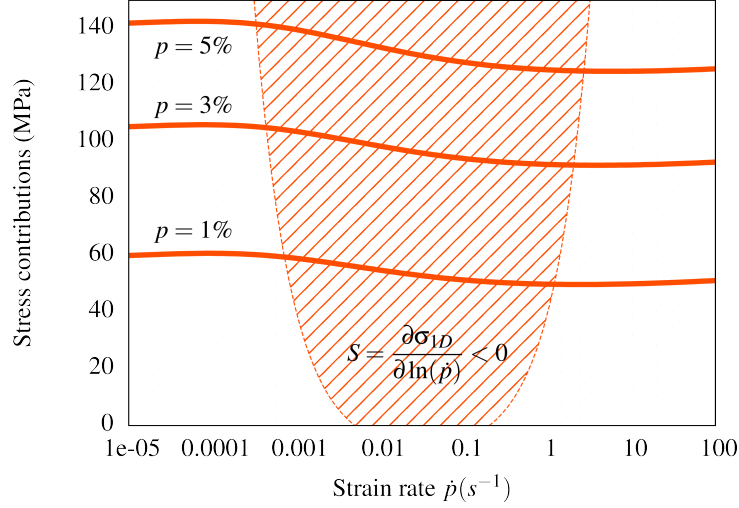
FIGURE 51 – Definition of the negative strain rate sensitivity domain with respect to strain rate $\dot{p}$ and strain p for the modification proposed by Böhlke [179] ($w = w(p)$ and $P_1 = P_1(p)$).

Extension for cycling loading

An extension of the KEMC model for cyclic loadings has recently been proposed in [221]. The equations of the model are almost all the same excepted the definition of the yield function in which a back stress contribution is included in the equivalent stress σ_{eq}. This back stress is constituted by the sum of many contributions depending on the complexity of the stress/strain loops.

$$f(\underset{\sim}{\boldsymbol{\sigma}}, \underset{\sim}{\boldsymbol{X}}, p, t_a) = \sigma_{eq}(\underset{\sim}{\boldsymbol{\sigma}} - \underset{\sim}{\boldsymbol{X}}) - R(p) - R_a(p, t_a) \tag{63}$$

$$\underset{\sim}{\boldsymbol{X}} = \underset{\sim}{\boldsymbol{X}}_1 + \underset{\sim}{\boldsymbol{X}}_2 + ... \tag{64}$$

$$\dot{\underset{\sim}{\boldsymbol{X}}}_i = \left(\frac{2}{3} C_i \underset{\sim}{\boldsymbol{n}} - D_i \underset{\sim}{\boldsymbol{X}}_i \right) \dot{p} \ , \ i = 1, 2 \tag{65}$$

The main difference with this extension of the model is that the serrations can occur during finite element simulations after a given number of cycles even if the total deformation remains within a given finite range like in strain controlled fatigue tests. The stability analysis as described in chapter 4 is then devoted to define a critical cycle number and not a critical strain level. An example of such simulation and the corresponding analytical prediction given by the modified stability criterion are plotted on figure 52. The details of this stability analysis will be given in chapter 4.

FIGURE 52 – Occurrence of serrations during the critical cycle of a fatigue finite element simulation. The occurrence of serration is in agreement with the prediction provided by the stability analysis.
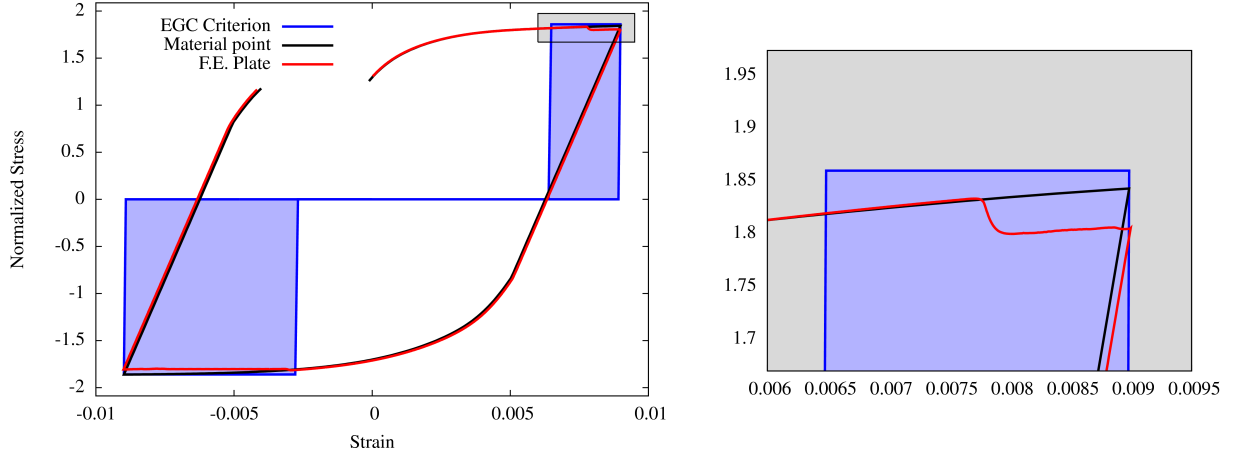
Dislocation density based model

A modified KEMC model based on a physically inspired description of the strain hardening has been recently used in finite element simulations by Marais [198] and Colas [209] for the case of stating strain ageing. Based on the equations proposed by Fressengeas [139], a dislocation density ρ is introduced in the model to control the evolution of the strain hardening $R(\rho)$:

$$f(\underset{\sim}{\boldsymbol{\sigma}}, p, t_a) = \sigma_{eq}(\underset{\sim}{\boldsymbol{\sigma}}) - R(\rho) - R_a(t_a) \tag{66}$$
$$R(\rho) = \sigma_0 + \gamma \mu b \sqrt{\rho} \tag{67}$$
$$\tag{68}$$

The evolution of ρ is based on the usual Kocks-Mecking formulation with a small but very important modification highlighted in red in the following equation :

$$\dot{\rho} = \left[a_0 \sqrt{\rho} - (1 - \delta_0 C_s(t_a)) b_0 \rho \right] \dot{p} \tag{69}$$

The left term in the brackets describes the creation of dislocation from sources and is assumed to be independent from strain ageing. On the contrary the right term represents dislocation annihilation (dynamic recovery) from dipoles and is modified by strain ageing phenomenon. Indeed, the movement of dislocations is blocked by solutes atoms (at least at low strain rates or high temperatures). Consequently the dynamic recovery process has to be at least partially suppressed by strain ageing. The term $(1 - \delta_0 C_s(t_a))$ has been introduced in the dislocation density evolution equation in order to model such a coupling between strain hardening and strain ageing. A value of δ_0 equal to 0 means no influence of strain ageing (usual Kocks-Mecking equation), on the contrary a value of δ_0 equal to 1 means that the whole dynamic recovery process may be suppressed by strain ageing.

The actual value for parameter δ_0 is probably between 0 and 1 and has to be identified together with other material parameters. In the original model by McCormick the ageing over-hardening influences the yield level in a way such as a pair of stress/strain curves for two different prescribed strain rates appear shifted by a given constant stress range all along strain evolution.

90
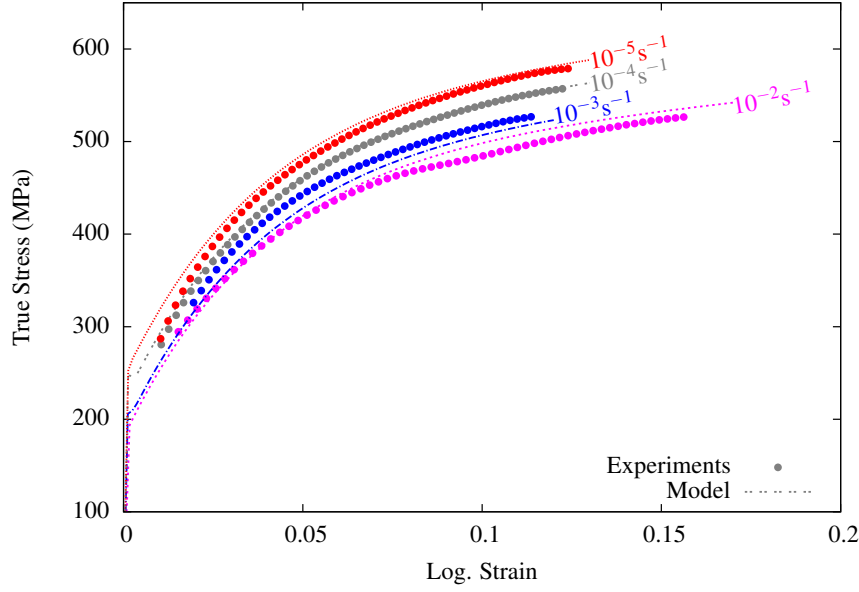
FIGURE 53 – Example of identification of the original KEMC model on tensile experiments on a C-Mn steel at 200°C for 4 different strain rates. Only the mean experimental stress level is used for identification [202].

As it can be seen on figure 53 such a behaviour is not in agreement with experimental results for which the distance between curves increases with strain.

It appears clearly that the apparent hardening rate should also be influenced by strain ageing . A solution for that is to prescribe a linear increasing evolution for P_1 with respect to p as proposed by Böhlke [179]. The dislocation density model proposed in this paragraph that includes a strain ageing influence on the dislocation annihilation term is another elegant and physically inspired solution to reach the same goal. The results that can be obtained with this new model can be compared on figure 54 with the best results that can be obtained with the original model on figure 53.

Crystal plasticity

The over-hardening as proposed by McCormick has been recently included in a crystal plasticity model in order to account for the ageing effect at the grain scale in polycrystalline simulations. The plastic part of the deformation depends on the plastic slip activity on all slip systems :

$$\dot{\underset{\sim}{\varepsilon}}^p = \sum_s \underset{\sim}{M}^s \dot{\gamma}^s \tag{70}$$

For each slip system, the orientation tensor $\underset{\sim}{M}^s$ is defined using the slip plane normal $\underline{n}^s$ and the slip direction $\underline{m}^s$:

$$\underset{\sim}{M}^s = \frac{1}{2}(\underline{n}^s \otimes \underline{m}^s + \underline{m}^s \otimes \underline{n}^s) \tag{71}$$

The viscoplastic flow rule follows the Sellars-Tegart equation :

$$\dot{v}^s = \dot{v}_0 \sinh\left(\frac{|\tau^s - X^s| - r^s - R_a^s}{\sigma_0}\right) \tag{72}$$

91
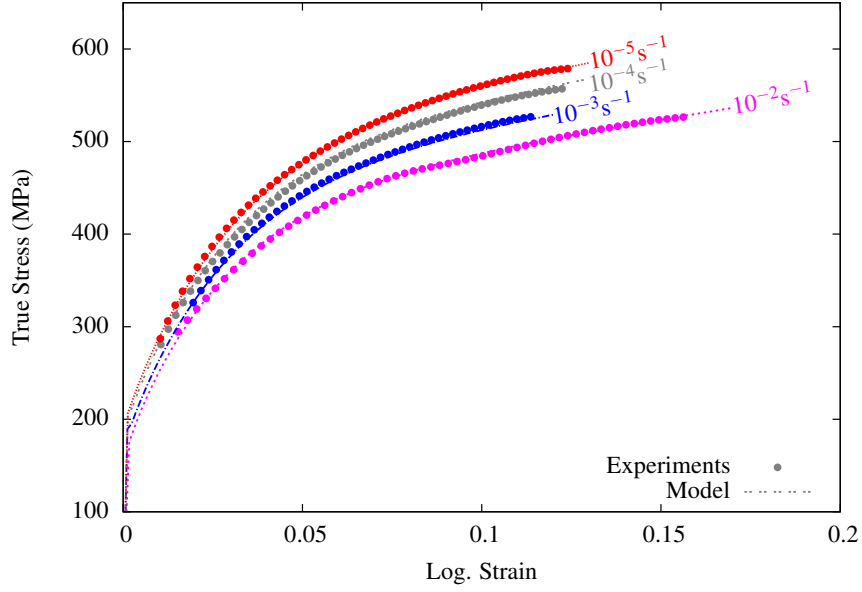
FIGURE 54 – Example of identification of the new dislocation density based model presented in the present paragraph on tensile experiments on a C-Mn steel at 200°C for 4 different strain rates.

The isotropic hardening is non-linear :

$$r^s = bQ \sum_r h^{sr} \rho^r \tag{73}$$

with b and Q are two parameters and h^{sr} is the interaction matrix. In equation 73 the isotropic hardening term is written using a dislocation density ρ. This latter follows his own evolution equation :

$$\dot{\rho}^s = (1 - b\rho)\dot{v}^s \tag{74}$$

A kinematic hardening term is included is the model to describe Bauschinger effect :

$$X^s = c\alpha^s \tag{75}$$

with :

$$\dot{\alpha}^s = \dot{\gamma}^s - d\alpha^s \dot{v}^s \tag{76}$$

The yield surface is based on the resolved shear stress τ^s computed for each slip system s using the stress tensor $\underset{\sim}{\sigma}^g$ and the orientation tensor $\underset{\sim}{M}^s$ provided by the Schmid's law.

$$\tau^s = \underset{\sim}{\sigma}^g : \underset{\sim}{M}^s = \frac{1}{2}\underset{\sim}{\sigma}^g : (\underline{n}^s \otimes \underline{m}^s + \underline{m}^s \otimes \underline{n}^s) \tag{77}$$

$$\dot{\gamma}^s = \dot{v}^s sgn(\tau^s - X^s) \tag{78}$$

This quite usual model has been enriched by the introduction for each system of another isotropic hardening R_a^s associated with strain ageing. This latter is very similar to the one introduced on the macroscopic McCormick strain ageing model. A single ageing time t_a has been introduced for all slip system instead of 12, this choice is highly discussable but was made for sake of simplicity.

$$R_a^s = P_1[1 - \exp(-P_2 t_a^n)] \tag{79}$$

The ageing time is controlled by the same evolution equation than for the macroscopic model :

$$\dot{t}_a = 1 - \frac{t_a}{t_w} \tag{80}$$

with $t_w = \frac{\omega}{\dot{\varepsilon}_{cum}^p}$ An initial value $t_a(t = 0) = t_{a0}$ can be prescribed for static strain ageing modelling.

This modified crystal plasticity model allow to simulate the propagation of Lüders and Portevin - Le Chatelier bands in polycrystalline aggregates, as it can be seen on figure 55. The strain localisation occurs in some favourably oriented grains but propagate in a second time in the neighbour grains to from a mesoscopic band. This latter propagates then over a short distance (1 or 2 grains) and another appears somewhere else in the specimen. This kind of simulation is very recent but very promising to investigate with a fine level of details the nucleation and propagation bands at the grain level.

3.3 An exemple of identification of the KEMC model over the temperatures and the strain rates

An example of identification of the KEMC model on large range of temperature and strain rate is proposed in this section. The results are based on the works of Belotteau [178] and Wang [202] on a C-Mn steel. The equations of the model that are used here are the ones presented on section 3.1 with a hyperbolic sine function introduced for the flow rule, and a non-linear evolution for the isotropic hardening function :

$$\dot{p} = R_v^{-1}(<f>) = \dot{\varepsilon}_0 \exp\left[-\frac{E_a}{k_B T}\right] \sinh\left[\frac{V_a <f>}{k_B T}\right] \tag{81}$$

$$R(p) = R_0 + Hp + Q\left[1 - \exp(-bp)\right] \tag{82}$$

The parameters of the model can be sorted in 4 different families :
— Elasticity : E, ν
— Yield and Hardening : R_0, H, Q, b
— Flow : $\dot{\varepsilon}_0$, E_a, V_a
— Ageing : $P_1 C_m$ (or P_1 if $C_m = 1$), t_0, w, n

The isotropic hardening evolution (excepted the yield stress R_0) is not accounted for in this section in order to focus on the role of strain rate and temperature. Furthermore the explicit formulation for $R(p)$ is not very adequate to describe experimental results as it can be seen on figure 53. The elastic properties are also not discussed and the present section and the investigated parameters are then the ones relative to flow and ageing.

In the work of Belotteau and Wang [178, 202], some of the parameters are assumed to be temperature independent :

$$\dot{\varepsilon}_0 = 6.2 \times 10^{-3} s^{-1} \tag{83}$$

$$E_a = 0.6 eV = 9.6 \times 10^{-20} J \tag{84}$$

$$w = 1.5 \times 10^{-3} \tag{85}$$

$$n = 0.33 \quad or \quad 0.66 \tag{86}$$

The other ones have been identified temperature by temperature with a special attention given to the monotony of their evolution with respect to temperature. In the present section, we have decided to propose for these 4 parameters some continuous functions of the temperature in

93
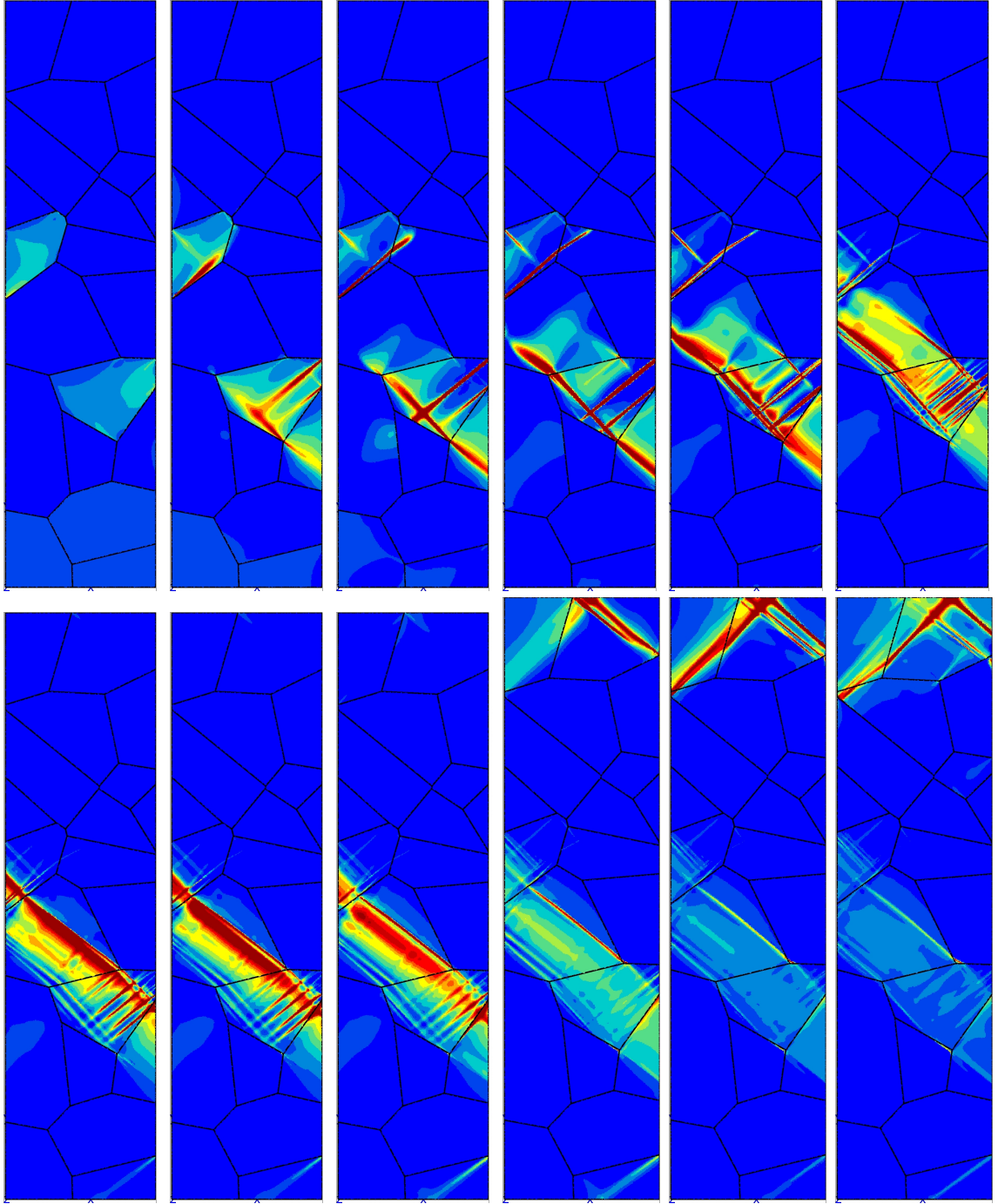
FIGURE 55 – Propagation of a Lüders band in a flat polycrystalline aggregates made of steel using the modified crystal plasticity model presented in the present paragraph.

order to get an explicit description of the initial apparent yield stress as a function of strain rate and temperature :

$$\sigma_{YS}(\dot{p}, T) = R_0(T) + R_v(\dot{p}, T) + R_a(\dot{p}, T) \tag{87}$$

The functions for R_0, V_a, P_1, and t_0 have been identified on the values proposed by Belotteau for 7 different temperatures ($20°C$, $100°C$, $150°C$, $200°C$, $250°C$, $300°C$, $350°C$). $R_0(T)$ and $V_a(T)$

are assumed to be linear functions of the temperature as it can be seen on figure 56.

$$R_0(T) = R_0^{0K} \left[1 - \frac{T}{T_{R_0}} \right] \tag{88}$$

$$V_a(T) = V_a^{0K} \left[1 + \frac{T}{T_{V_a}} \right] \tag{89}$$

$P_1(T)$ follows a non-linear function which tends to 0 for high temperatures and to a finite value P_1^{0K} for low temperatures (see figure 56).

$$P_1(T) = P_1^{0K} \exp \left[-\exp \left(\frac{T - T_{ref}}{T_{P_1}} \right) \right] \tag{90}$$

$t_0(T)$ has been chosen based on the physical origin of this latter as proposed in [57] :

$$\frac{t_a}{t_0} \propto KDt_a, \quad K \propto T, \quad D \propto \exp \left(-\frac{Q_m}{k_B T} \right) \tag{91}$$

$$\rightarrow t_0 \propto T \exp \left(\frac{Q_m}{k_B T} \right) \tag{92}$$

$$t_0(T) = T \exp \left[\frac{T_{t_0}}{T} - \gamma_0 \right] \tag{93}$$

These evolutions functions [13] can coincide rather well with the identified results proposed by Belotteau as it can be seen on figure 56.

Based on the evolution equations proposed for R_0, V_a, P_1, and t_0 it is possible to plot the surface describing the initial yield stress σ_{YS} as a function of strain rate and temperature (see equation 87). The initial negative strain rate sensitivity domain ($SRS < 0$) can be highlighted on this surface as it can be seen on figure 57.

It must be observed that :

— The $SRS < 0$ domain is half-closed. For temperatures or strain rates large enough, the strain rate sensitivity is always positive.

— A singular point exists for which the $SRS < 0$ domain appears, this latter is located in the present case at $T = 381°C$ and $\dot{p} = 0.15 s^{-1}$.

— When the temperature decreases below this critical value, the $SRS < 0$ domain move towards smaller strain rates. At room temperature this latter is located between $\dot{p} = 10^{-10} s^{-1}$ and $\dot{p} = 10^{-7} s^{-1}$.

— The average slope in the $SRS < 0$ domain is mainly controlled by the parameter n. When this latter is changed from 2/3 to 1/3 (as proposed in [94]), the yield stress surface has a slightly different form as it can be seen by comparing figures 57 and 58.

The $NSRS < 0$ domain and the influence of parameter n can be also observed by plotting the surface from a point of view perpendicular to this latter (see figure 59). This type of plot was used in many former articles on the topic [74, 107, 119] using $1/T$ (or $1000/T$) on the X axis and $log(\dot{p})$ on the Y axis. In the article by J.L.Strudel [74], this type of plot is useful to separate the dragging, the PLC, and the friction domains. In the second one by S.Mesarovic [107], the influence of parameter n is evidenced on the diagram, especially the size of the $SRS < 0$ as it can be seen comparing both plot of figure 59. In the last one by M.Lebyodkin [119], the PLC domain

---

13. The parameters identified in the functions $R_0(T)$, $V_a(T)$, $P_1(T)$, and $t_0(T)$ are not physically meaningful, excepted the parameter T_{t_0} since this latter must be equal to Q_m/k_B where Q_m is the activation energy of the solute diffusion process. In this study, T_{t_0} has been found equal to 9575K that lead to $Q_m = 19$ kcal/mol. which is very close to the value of $Q = 18.65$ kcal/mole estimated by J.da Silva in 1976 [59] for the diffusion of Carbon in B.C.C. iron. The value estimated by the same author for the diffusion of Nitrogen in B.C.C. iron is smaller and equal to 17.54 kcal/mole.
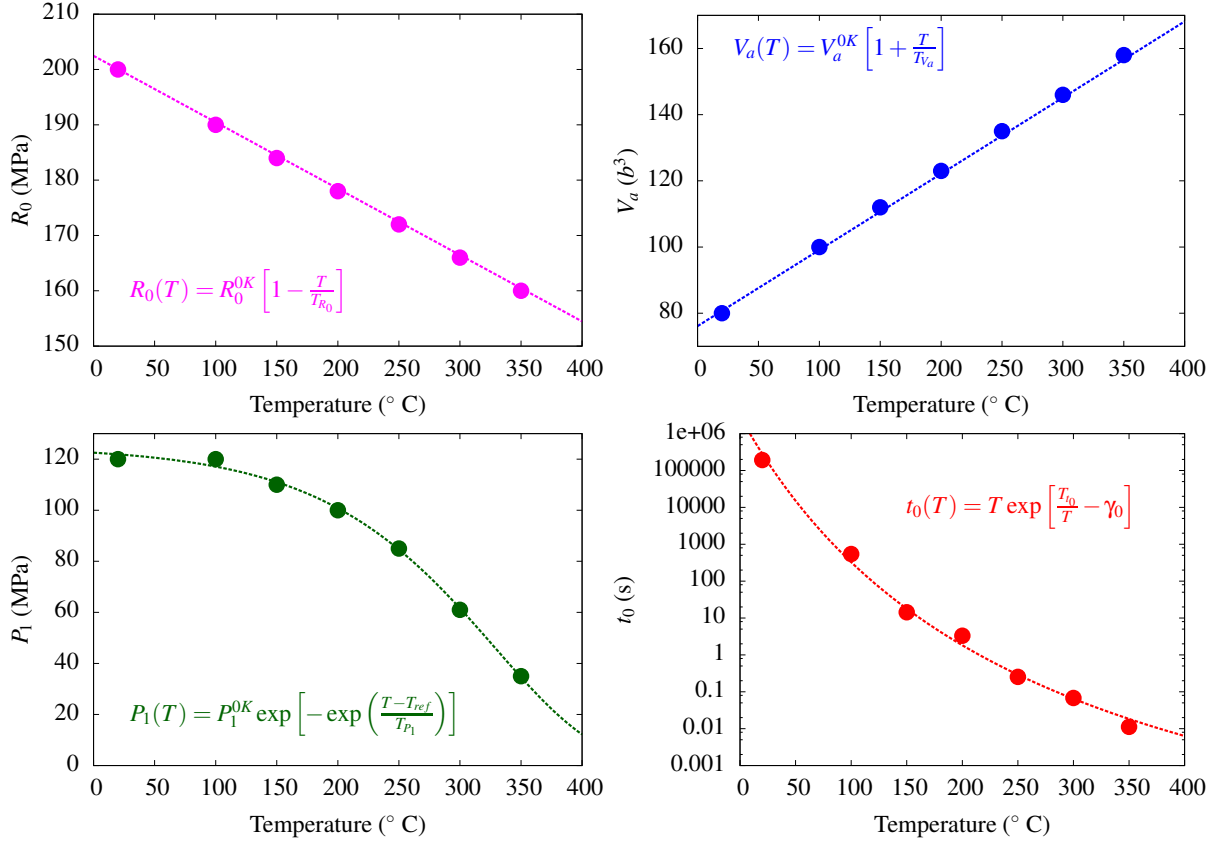
FIGURE 56 – Evolution of the material parameters R_0, V_a, P_1 and t_0 identified by Belotteau [178] on 7 different temperatures and the corresponding proposed functions $R_0(T)$, $V_a(T)$, $P_1(T)$ and $t_0(T)$.

is plotted, and inside this latter some sub-domains are defined corresponding to different types of spatio-temporal features of the band propagation. This aspect of the Portevin - Le Chatelier effect is not investigated in the present chapter.

Finally it must be notice that the $SRS < 0$ domain and the PLC domain –i.e. the one where serration are observed– are not coincident. Indeed it will be derived in the following chapter devoted to the stability of the KEMC model that the negativity of the strain rate sensitivity is a necessary but not sufficient condition for the serrations to occur. The level of plastic strain will also play a role on the occurrence of serrations due to the evolution of the hardening rate.
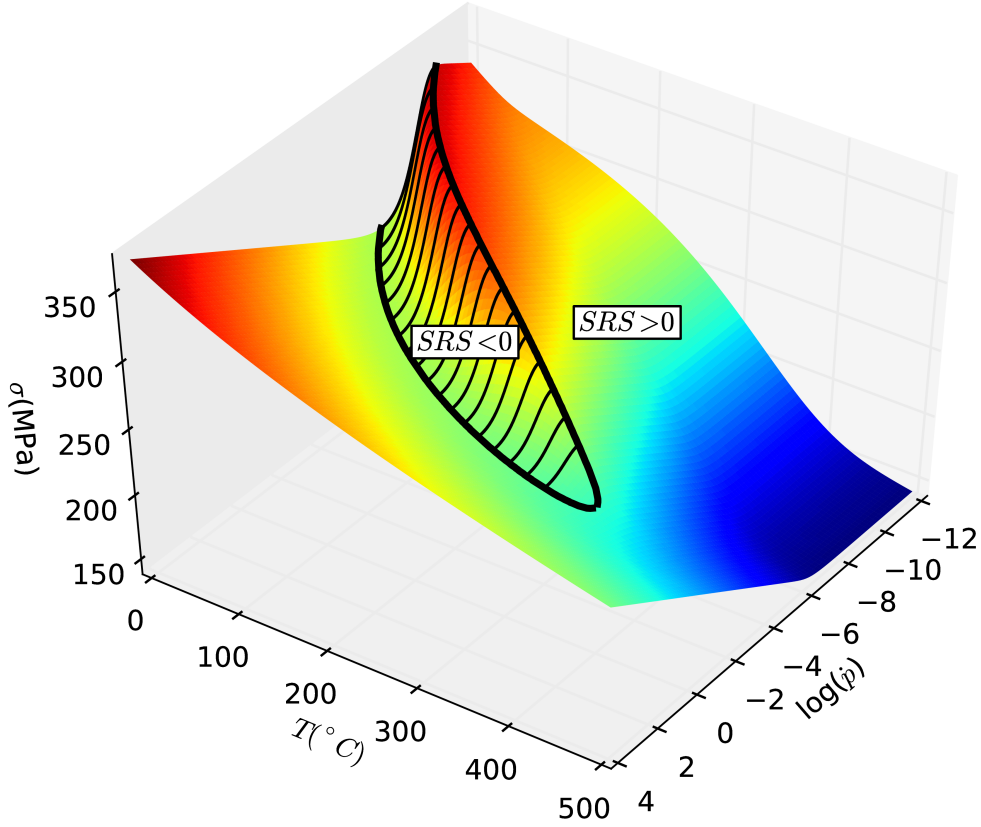
FIGURE 57 – Surface representing the initial yield stress $\sigma_{YS}(\dot{p}, T) = R_0(T) + R_v(\dot{p}, T) + R_a(\dot{p}, T)$ as a function of the temperature T and the plastic strain rate $\dot{p}$. The negative strain rate sensitivity ($SRS < 0$) domain is highlighted on the surface with shading. In this picture, the ageing parameter n is equal to $2/3$.
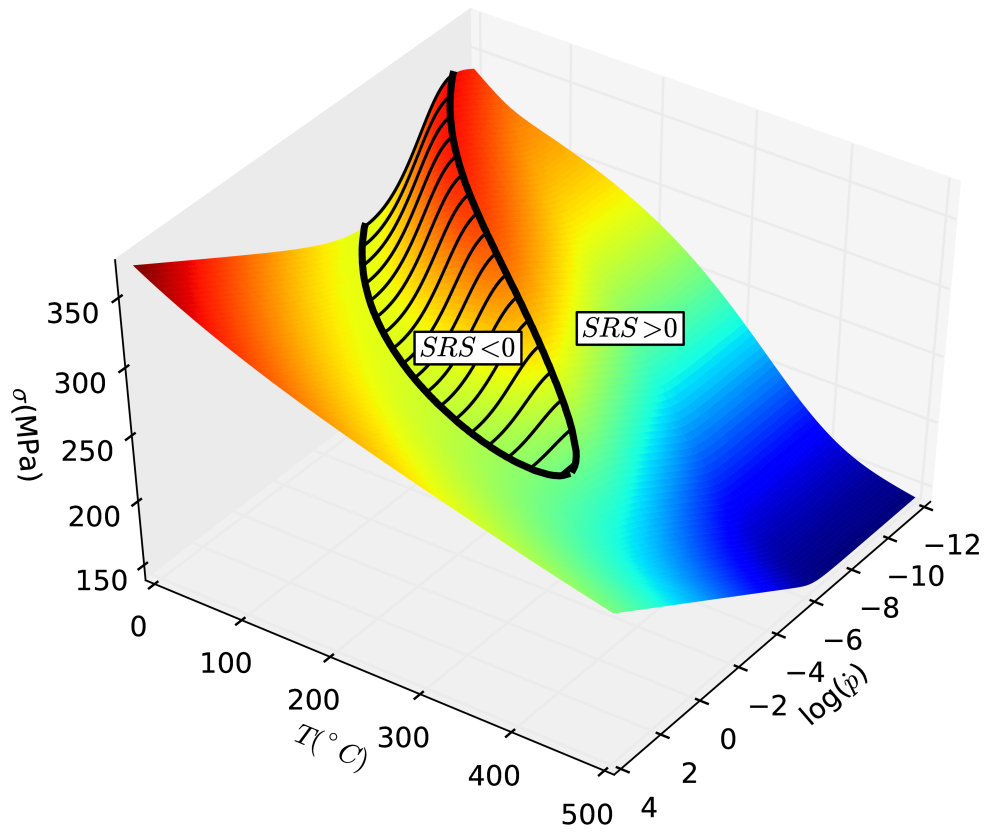
FIGURE 58 – Same picture than figure 57 but with the ageing parameter n equal to $1/3$
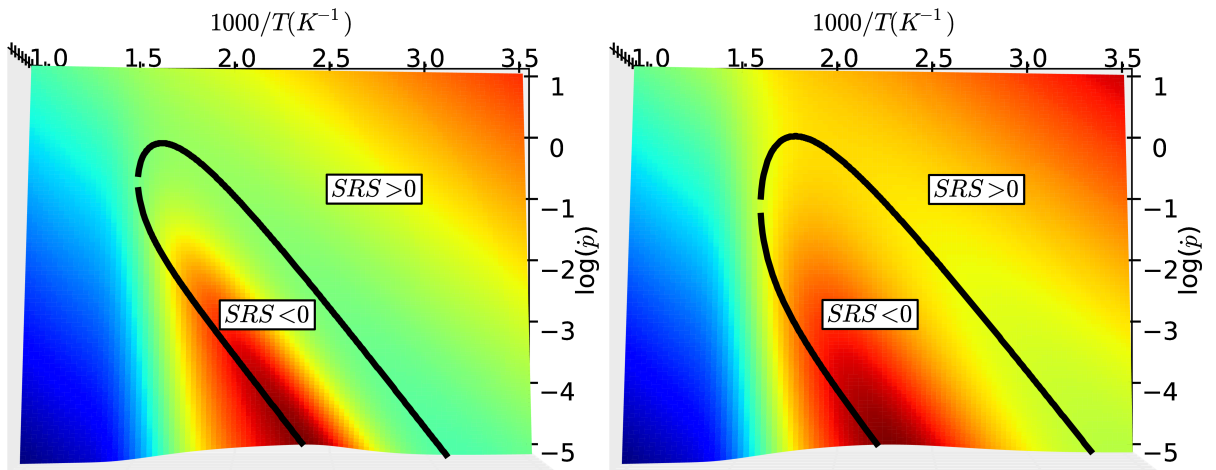
FIGURE 59 – Localisation of the negative strain rate sensitivity domain ($SRS < 0$) on a temperature vs. strain rate map for $n = 2/3$ (left) and $n = 1/3$ right. The size of the $SRS < 0$ domain increases when n decreases.

4 Analytical and finite element stability analysis of the KEMC model

One of the most notable property of the KEMC model is its ability to reproduce the spatio temporal instabilities observed experimentally during tensile tests i.e. the serrations on the stress/strain curve associated with the propagation of localized plastic bands in the specimens. The localisation phenomena and the associated serrations on the stress vs. strain curves that can be obtain with the KEMC model and a finite element model can be seen on figure 60. The
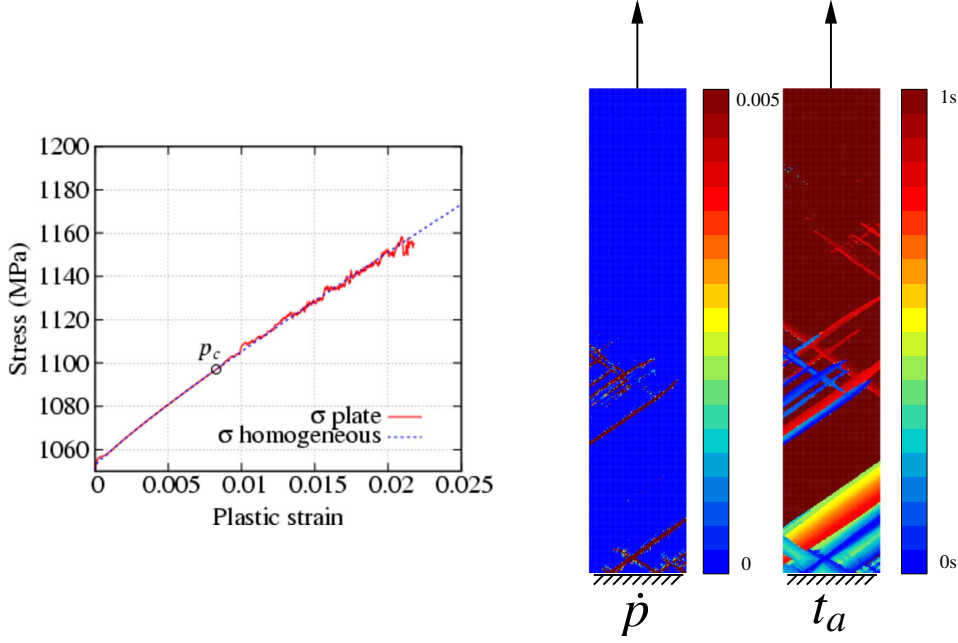
FIGURE 60 – Propagation of a Portevin - Le Chatelier band in a flat tensile specimen and corresponding stress vs. strain curve. The quantity plotted on the maps are the plastic strain rate $\dot{p}$ and the ageing time t_a. The elastic part of the curve is not visible because of the scale of the axis. The critical plastic strain corresponding to the occurrence of serrations can be detected comparing the response of the finite element plate (denoted σ plate) and the response of a single material point (denoted σ homogeneous).

KEMC model is able to account for the fact that a given level of deformation – called the critical strain in the following – is required to trigger instabilities, and in particular the non monotonic evolution of this latter with respect of strain rate. However the relation between the material parameters and this critical deformation is not explicitly provided by the equations of the model. A stability analysis can be carried out based on the linear perturbation method to estimate the critical strain. This analysis was already proposed in the original article of McCormick [85]. It has been completed and compared with numerous finite element results in some of our recent articles [189, 199, 222] The main results on that topic are summarized in this chapter.

4.1 Stability criterion

A stability criterion to forecast the occurrence of serrations during finite element simulations like the one presented on figure 60 is derived in this section using the linear perturbation method, and compared with finite element results. The complete investigation including mathematical developments can be found in two recent articles [199, 222].

Linear perturbation analysis for KEMC model with two state variables

The stability analysis presented in this paragraph is not carried out on the original KEMC model but on a more general formulation like the one proposed by Böhlke [179]. It can be applied to any modified formulation of the KEMC model with two state variables (p, t_a). An extension of the analysis for models with three state variables is presented in the following paragraph.

The perturbation analysis leading to the prediction of the numerical critical plastic strain under simple tension loading conditions requires two main hypotheses. These hypotheses are possible since up to the critical strain, the mechanical state remains uniform in the gauge length of specimens. The mechanical behaviour of the specimen is in this case equivalent to the behaviour of a volume element on which a uniaxial tension is applied. Up to the critical strain, the two assumptions lead to a mechanical solution close from the one provided by the corresponding 3D finite element analysis.

Firstly, a one-dimensionnal stress state is assumed. The investigated load is uniaxial tension. The testing machine stiffness is not accounted for. The only non zero component in the stress tensor is then the tensile stress σ :

$$\sigma = R(p) + R_v(\dot{p}) + R_a(p, t_a) \tag{94}$$

where R, R_v, and R_a, are defined in section 3.1.

Secondly, it is assumed that $\dot{p}$ remains almost constant (no strain rate jump), and that t_a is close to its steady-state value, also called the waiting time t_w.

$$t_a = t_w = \frac{w}{\dot{p}} \tag{95}$$

The latter assumption is generally valid, at least if p is large compared to w. Using both assumptions, σ becomes a function of p and $\dot{p}$. σ and its contributions R, R_v, and R_a can be plotted like on figure 45 in section 3.1 as functions of plastic strain and plastic strain rate.

In order to simplify the mathematical developments presented in this part, the following notations are introduced :

$$S = \left.\frac{\partial \sigma}{\partial \ln(\dot{p})}\right|_p \qquad \text{(steady state SRS)} \tag{96}$$

$$S_i = \left.\frac{\partial \sigma}{\partial \ln(\dot{p})}\right|_{p, R_a} = \dot{p}\frac{dR_v}{d\dot{p}} \qquad \text{(instantaneous SRS)} \tag{97}$$

$$S_a = -\left.\frac{\partial \sigma}{\partial \ln(t_a)}\right|_p = -t_a\frac{\partial R_a}{\partial t_a} \qquad \text{(ageing SRS)} \tag{98}$$

$$\Theta = \left.\frac{\partial \sigma}{\partial p}\right|_{\dot{p}} = \frac{dR}{dp} + \frac{\partial R_a}{\partial p} \qquad \text{(strain hardening modulus)} \tag{99}$$

$$S = S_i + S_a \qquad \text{(if } t_a = \frac{w}{\dot{p}}\text{)} \tag{100}$$

These new variables are the same as those introduced in most theoretical works on the prediction of the PLC critical plastic strain [88, 90, 111]. In the linear perturbation method, a small exponential perturbation is introduced in the set of internal variables, assuming the usual separable form between space x and time t contributions [107].

$$\delta[\mathbf{X}(x,t)] = [\mathbf{X}_0(x)]\exp(\lambda t) = \begin{bmatrix} \delta p \\ \delta t_a \\ \delta \sigma \end{bmatrix} \tag{101}$$

The parameter λ is directly related to the growth (or decrease) of the perturbation and to the shape of its evolution (oscillating or hyperbolic). This perturbation is then introduced in the constitutive one-dimensional equations.

$$\delta \sigma = \frac{dR}{dp}\delta p + \frac{dR_v}{d\dot{p}}\delta \dot{p} + \frac{\partial R_a}{\partial p}\delta p + \frac{\partial R_a}{\partial t_a}\delta t_a \tag{102}$$

$$w\delta \dot{t}_a = -t_a\delta \dot{p} - \dot{p}\delta t_a \tag{103}$$

$$\delta \sigma = \sigma \delta p \tag{104}$$

In displacement-controlled tests, the total strain ε_{tot} is prescribed by the machine, increasing at a constant strain rate $\dot{\varepsilon}_{tot}$. This total strain must consequently not be perturbed in the analysis. Furthermore, Zaiser has shown in [113] that for a strongly localized perturbation, such as PLC bands, the external axial force F_{ext} that acts on the specimen is not perturbed either, but only the Cauchy stress is. Equation (104) [14] is related to the condition of plastic incompressibility, and to the uniformity of this axial load along the tensile specimen axis, and can be introduced into equation (102).

$$\delta \dot{p} = \frac{1}{dR_v/d\dot{p}}\left[\left(\sigma - \frac{dR}{dp} - \frac{\partial R_a}{\partial p}\right)\delta p - \frac{\partial R_a}{\partial t_a}\delta t_a\right] \tag{105}$$

$$\delta \dot{t}_a = -\frac{1}{w}[t_a\delta \dot{p} + \dot{p}\delta t_a] \tag{106}$$

The ability of the perturbation to grow is investigated by carrying out a spectral analysis of the transfer matrix $\mathbf{M}$. This latter links the perturbation of internal variables with the perturbation of their rates.

$$\begin{bmatrix} \delta \dot{p} \\ \delta \dot{t}_a \end{bmatrix} = \frac{\dot{p}}{S_i}\underbrace{\begin{bmatrix} (\sigma - \Theta) & \dfrac{S_a}{t_a} \\ \dfrac{t_a}{w}(\Theta - \sigma) & -\dfrac{1}{w}(S_i + S_a) \end{bmatrix}}_{\mathbf{M}} \cdot \begin{bmatrix} \delta p \\ \delta t_a \end{bmatrix} \tag{107}$$

Since $\mathbf{M}$ is a 2x2 matrix, the spectral analysis can be carried out analytically. One successively computes the trace of $\mathbf{M}$, its determinant, and its two eigenvalues using its characteristic equation.

---

14. This last equation is required only if a difference is accounted for in the mechanical problem between the Cauchy and nominal stresses, i.e. for finite strain formulations, otherwise $\delta \sigma = 0$

$$\mathrm{Tr}\,(\mathbf{M}) = -\frac{\dot{p}}{wS_i}[S + w\,(\Theta - \sigma)] \tag{108}$$

$$\det(\mathbf{M}) = \left(\frac{\dot{p}}{S_i}\right)^2 \frac{(\Theta - \sigma)}{w} S_i = \left(\frac{\dot{p}}{wS_i}\right)^2 w\,(\Theta - \sigma)\,S_i \tag{109}$$

$$\mathrm{eq}(\mathbf{M}): \lambda^2 - \mathrm{Tr}\,(\mathbf{M})\lambda + \det(\mathbf{M}) = 0 \tag{110}$$

$$\Delta(\mathbf{M}) = \mathrm{Tr}\,(\mathbf{M})^2 - 4\det(\mathbf{M}) \tag{111}$$

$$= \left(\frac{\dot{p}}{wS_i}\right)^2 \left[\left(S + w\,(\Theta - \sigma)\right)^2 - 4w\,(\Theta - \sigma)\,S_i\right] \tag{112}$$

Depending on the sign of $\Delta(\mathbf{M})$, the eigenvalues of $\mathbf{M}$ are either purely real (if $\Delta(\mathbf{M}) > 0$), or complex (if $\Delta(\mathbf{M}) < 0$) :

$$\text{If } \Delta(\mathbf{M}) \geq 0 : \tag{113}$$

$$\mathrm{Re}(\lambda_{1,2}) = \frac{\mathrm{Tr}\,(\mathbf{M}) \pm \sqrt{\Delta(\mathbf{M})}}{2} \tag{114}$$

$$\mathrm{Im}(\lambda_{1,2}) = 0 \tag{115}$$

$$\text{If } \Delta(\mathbf{M}) < 0 : \tag{116}$$

$$\mathrm{Re}(\lambda_{1,2}) = \frac{\mathrm{Tr}\,(\mathbf{M})}{2} \tag{117}$$

$$\mathrm{Im}(\lambda_{1,2}) = \pm\sqrt{-\frac{\Delta(\mathbf{M})}{4}} \tag{118}$$

Based on this analysis 4 different situations can occur for the perturbation evolution :

1. $\Delta(\mathbf{M}) \geq 0$ and $\mathrm{Re}(\lambda_{1,2}) \leq 0$: the eigenvalues $\mathbf{M}$ are real with a negative real part, the perturbation decreases exponentially

2. $\Delta(\mathbf{M}) < 0$ and $\mathrm{Re}(\lambda_{1,2}) \leq 0$: the eigenvalues $\mathbf{M}$ are complex with a negative real part, the perturbation decreases and oscillates

3. $\Delta(\mathbf{M}) < 0$ and $\mathrm{Re}(\lambda_{1,2}) > 0$: the eigenvalues $\mathbf{M}$ are complex with a positive real part, the perturbation grows and oscillates

4. $\Delta(\mathbf{M}) \geq 0$ and $\mathrm{Re}(\lambda_{1,2}) > 0$: the eigenvalues $\mathbf{M}$ are real with a positive real part, the perturbation grows exponentially

It must be noted that a situation with two real eigenvalues with different signs (one positive and one negative) may not occur in our case since $\det(\mathbf{M})$ remains always positive at least up to the Considere necking point ($(\Theta - \sigma) \geqslant 0$).

During finite element simulations of a plate in tension during which PLC serrations occur, these 4 situations occur successively as it can be seen on figure 61 for a representative simulation.

It can also be seen on figure 61 that serrations occur close to the beginning of stage 4, i.e. when the perturbation can grow exponentially.

Three main criteria are generally introduced to analyse the stability of a strain ageing model, such as MacCormick's one. The first one is not based on the perturbation analysis and define the positiveness of the steady state strain rate sensitivity as it appears on figure 45.

$$S = S_i + S_a < 0 \tag{119}$$

This criterion is generally inadequate to detect occurrence of serrations on the strain-stress curve.
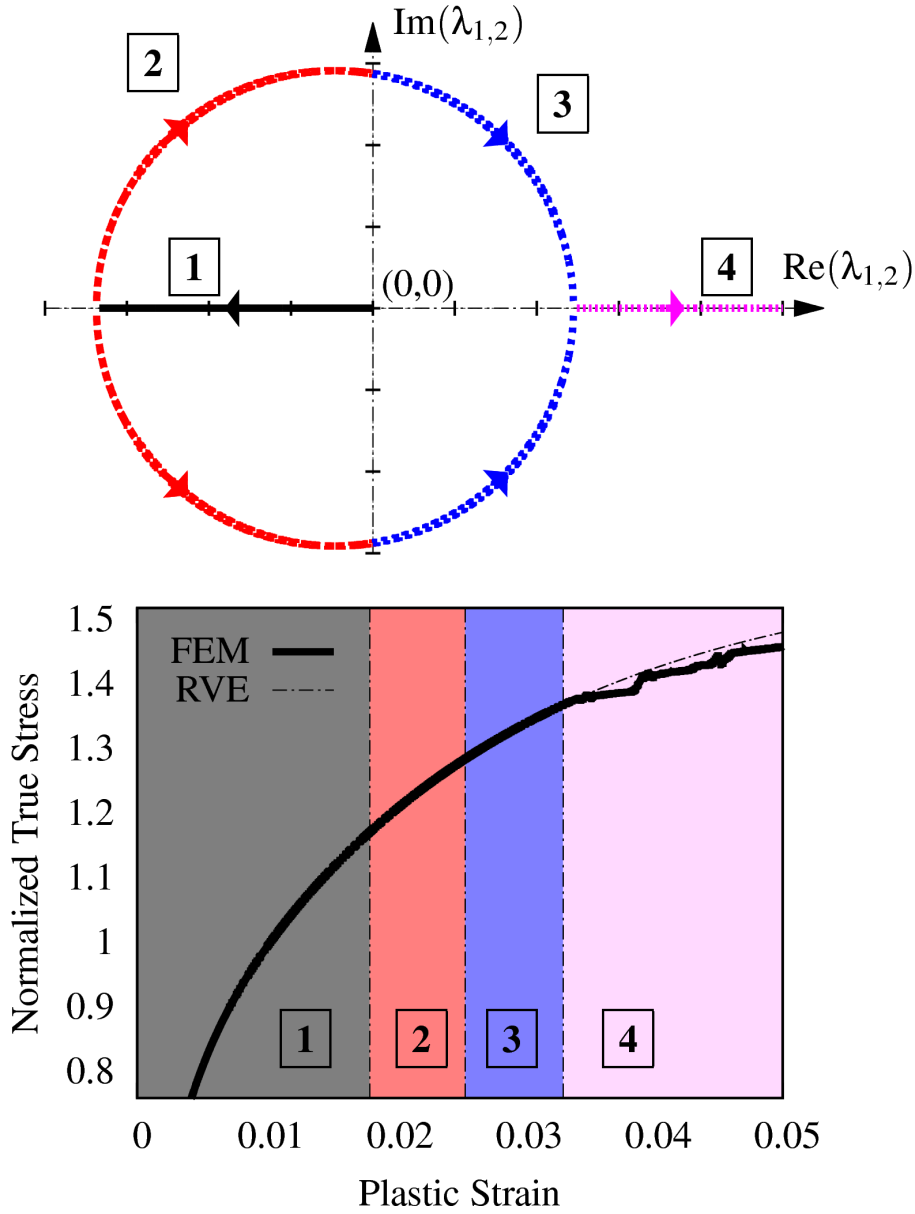
FIGURE 61 – Stress vs. strain curves given by a material point (RVE) and a finite element plate (FEM) under a monotonic tensile loading [222]. The evolution of the eigenvalues resulting from the spectral analysis of matrix $\mathbf{M}$ is also provided in the complex space. The 4 different situations encountered for the possible evolutions of the perturbation are denoted 1,2,3,4.

Experimental negative strain rate sensitivity has then been observed without serrations [88, 179]. From a numerical point of view, serrations occur beyond the critical point defined using this criterion as show on figure 62.

The second criterion is presented in most studies as the relevant one for the occurrence of serration [90, 111]. It is activated when the real part of the eigenvalues λ presented previously becomes positive. Indeed it means that the perturbation may follow a growing oscillating evolution. This criterion corresponds to the transition between stages 2 and 3. It is generally presented as follow, and will be denoted the oscillating growth criterion (OGC) :

$$S_{OCG} = S + w(\Theta - \sigma) < 0 \tag{120}$$

This criterion cannot be activated prior to the well known Considere point (i.e. $\Theta = \sigma$) if S has not yet reached a negative value.

The third criterion, called exponential growth criterion (EGC), detects when the perturbation may follow a growing but exponential evolution. The eigenvalues previously calculated must be real and positive to ensure such an evolution. This criterion corresponds to the transition between stages 3 and 4. Based on equations (108) ($\text{Tr}(\mathbf{M}) < 0$) and (112) ($\Delta(\mathbf{M}) > 0$), this criterion can be written as follow :

$$\left(S_{OGC}\right)^2 - 4w(\Theta - \sigma)S_i > 0 \text{ and } S_{OGC} < 0 \tag{121}$$

Up to the Considere point (i.e. as long as $\Theta > \sigma$), since S_i is always positive, $\left(w(\Theta - \sigma)S_i\right)$ remains positive. Then the exponential criterion will be fulfilled for a higher value of plastic strain than for the oscillating criterion, and can be reduced to the following form :

$$S_{EGC} = S + w(\Theta - \sigma) + 2\sqrt{w(\Theta - \sigma)S_i} < 0 \tag{122}$$

The three criteria have been tested using the material model and parameters given by Böhlke for an Al-Cu alloy [179]. Nine finite element simulations of plates in tension have been carried out for the nine investigated strain rates. The specimen geometry is detailed in [179]. The numerical critical plastic strains extracted from finite element strain/stress curves, and the evolution of the three criteria are plotted on figure 62. The relevant criterion in this case seems to be the exponential one, while the usually proposed oscillating one provides predictive but imprecise results.
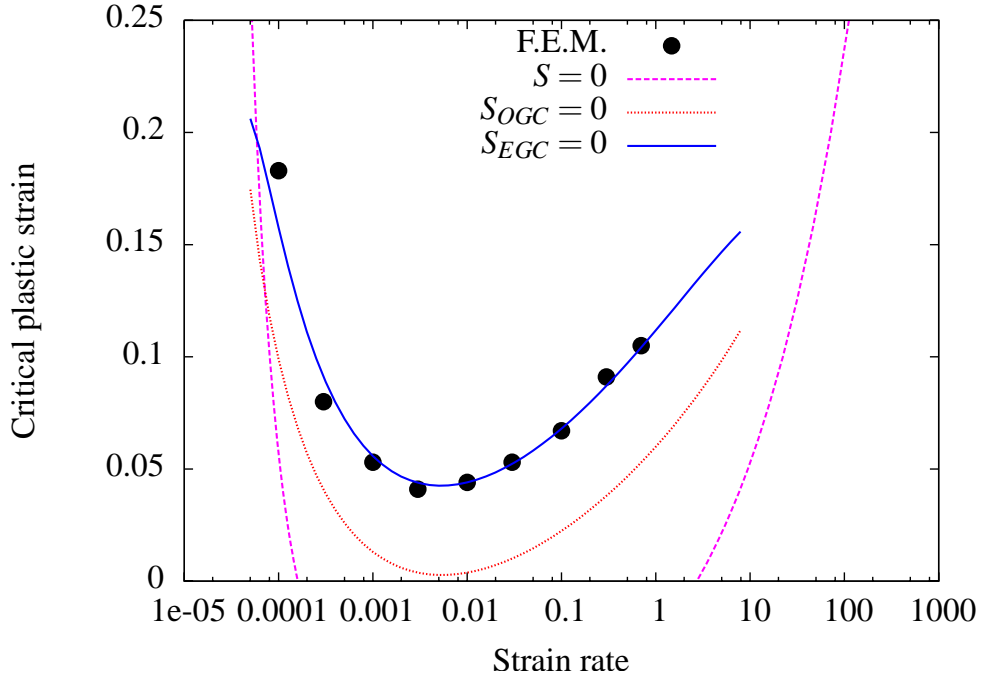
FIGURE 62 – Critical strain provided by finite element simulations using data from Böhlke [179], and by the three analytical criteria presented in this section. $S = 0$ is the negative strain rate sensitivity criterion. $S_{OGC} = 0$ is the oscillating growth criterion. $S_{EGC} = 0$ is the exponential growth criterion.

This unusual result is probably related to positivity of the plastic strain rate $\dot{p}$. This feature is due to the particular form of expression 46 ($\dot{p} = R_v^{-1}(<f>)$). The plastic strain p is consequently

an increasing function of time t. A complex value for the growth parameter λ is then prohibited in equation 101.

The U-shape evolution of the critical plastic strain is plotted on the stress surface on figure 63. In agreement with equation 122, the critical domain is included in the negative strain rate sensitivity domain, at least up to the Considere point defined by $\sigma = \Theta$.
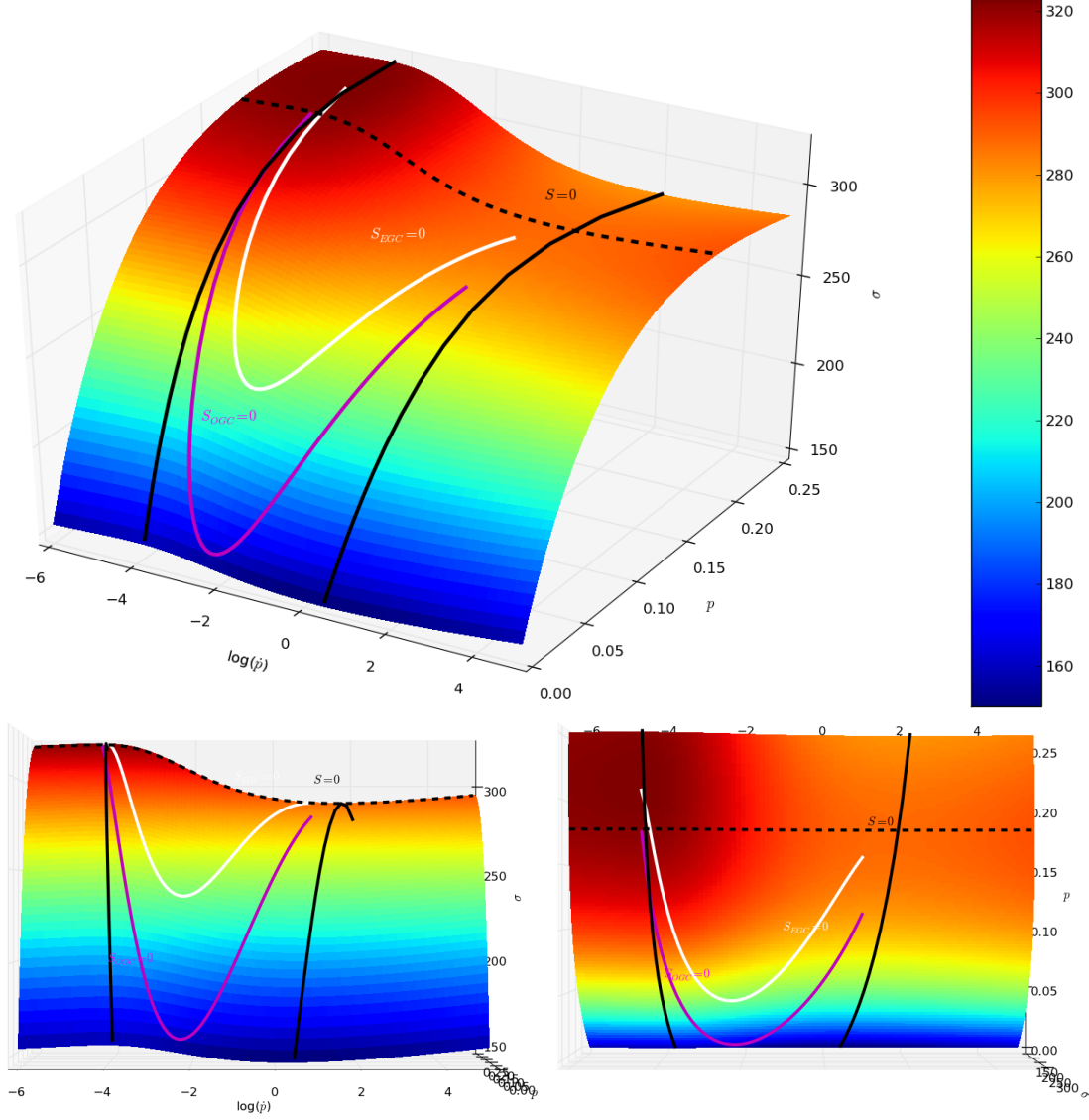
FIGURE 63 – Stress surface and critical strains provided by the three analytical criteria presented in this section using data from Böhlke [179]. The dash line follows the Considere criterion.

The influence of the ageing parameters $P_1 C_m$, t_0, w, and n on the evolution of critical strain with respect to the plastic strain rate is plotted on figure 64. The direction of the black arrow indicates an increase in the corresponding parameter value. It can be seen that each parameter plays a different rôle on this evolution :

— When n increases, the U-shape of the critical plastic strain evolution narrows and decreases towards smaller values.

— When $P_1 C_m$ increases, the U-shape decreases.

— When w increases, the U-shape increases towards higher critical strain and strain rates.

— When t_0 increases, the U-shape is translated towards higher strain rates.
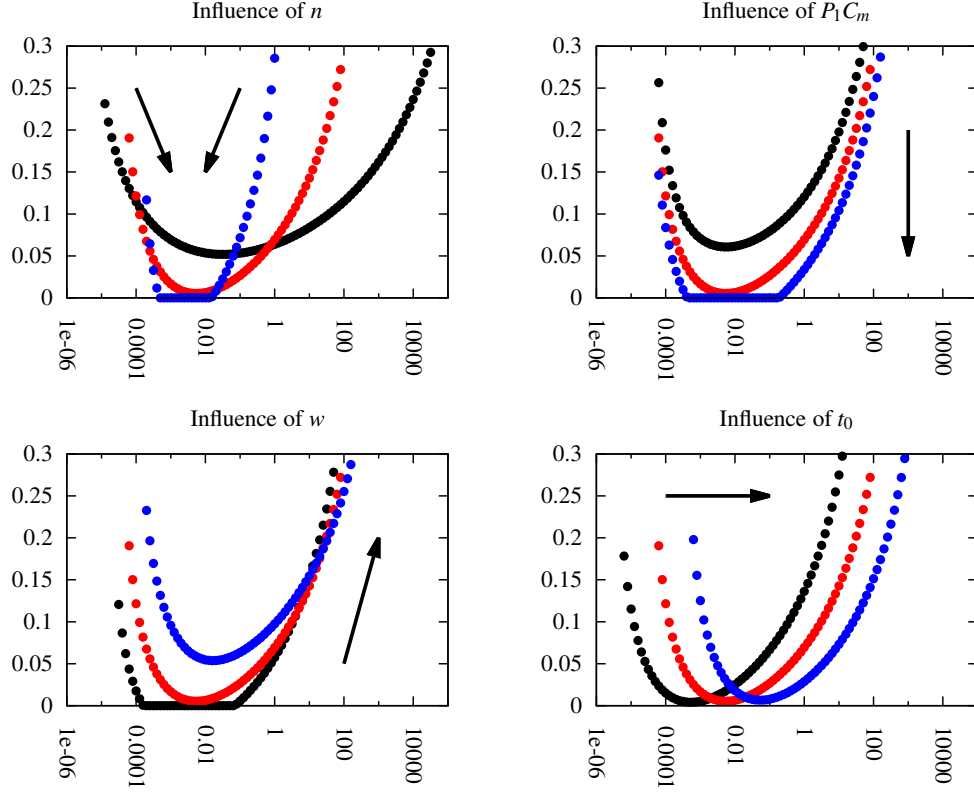
FIGURE 64 – Influence of the ageing parameters $P_1 C_m$, t_0, w, and n on the critical strain evolution with respect to the plastic strain rate $\dot{p}$.

Extension to models with three states variables

The extension of the linear perturbation analysis in the case of a KEMC like model with three state variables is presented in this section. The model accounting for kinematic hardening presented in section 3.2 is investigated. The set of internal variable becomes :

$$\delta[\mathbf{X}(x,t)] = [\mathbf{X}_0(x)] \exp(\lambda t) = \begin{bmatrix} \delta p \\ \delta t_a \\ \delta \underset{\sim}{\boldsymbol{\sigma}} \\ \delta \underset{\sim}{\boldsymbol{X}} \end{bmatrix} \tag{123}$$

One must notice that the stress tensile component σ has been replaced here by the whole tensor $\underset{\sim}{\boldsymbol{\sigma}}$. It will be described in the following how to recover a unidimensional formulation of the perturbation analysis. The yield function in the model is recalled :

$$f(\underset{\sim}{\boldsymbol{\sigma}}, \underset{\sim}{\boldsymbol{X}}, p, t_a) = \sigma_{eq}(\underset{\sim}{\boldsymbol{\sigma}} - \underset{\sim}{\boldsymbol{X}}) - R(p) - R_a(p, t_a) \tag{124}$$

$$= R_v(\dot{p}) \tag{125}$$

This latter is perturbed :

$$\underbrace{\frac{\partial \sigma_{eq}}{\partial \underset{\sim}{\boldsymbol{\sigma}}}}_{\underset{\sim}{\boldsymbol{n}}} : \delta \underset{\sim}{\boldsymbol{\sigma}} - \underbrace{\frac{\partial \sigma_{eq}}{\partial \underset{\sim}{\boldsymbol{X}}}}_{\underset{\sim}{\boldsymbol{n}}} : \delta \underset{\sim}{\boldsymbol{X}} - \frac{dR}{dp} \delta p - \frac{\partial R_a}{\partial p} \delta p - \frac{\partial R_a}{\partial t_a} \delta t_a = \frac{dR_v}{d\dot{p}} \delta \dot{p} \tag{126}$$

106

For a pure tensile state (see previous paragraph for details) :

$$\underset{\sim}{n} : \delta\underset{\sim}{\sigma} = \delta\sigma = \sigma\delta p \qquad (127)$$

The perturbation of the back stress tensor $\delta\underset{\sim}{X}$ can be related to the perturbation of the plastic strain δp :

$$\underset{\sim}{n} : \delta\underset{\sim}{X} = \underset{\sim}{n} : \frac{d\underset{\sim}{X}}{dp}\delta p = \underset{\sim}{n} : \left(\frac{2}{3}C\underset{\sim}{n} - D\underset{\sim}{X}\right)\delta p = \left(\frac{2}{3}C\underset{\sim}{n} : \underset{\sim}{n} - D\underset{\sim}{n} : \underset{\sim}{X}\right)\delta p \qquad (128)$$

This term in the brackets is then added in the calculation of the strain hardening coefficient Θ :

$$\Theta = \underset{\sim}{n} : \frac{d\underset{\sim}{X}}{dp} + \frac{dR}{dp} + \frac{\partial R_a}{\partial p} \qquad (129)$$

The rest of the stability analysis is then similar to the one presented in the previous paragraph with two state variables. This method has been tested on the extended KEMC model accounting for kinematic hardening as presented in section 3.2, and identified for a Cobalt based superalloy at 600 °C. The ability of the stability criterion to predict the critical plastic strain is presented on figure 65. More details can be found in the corresponding article [222].
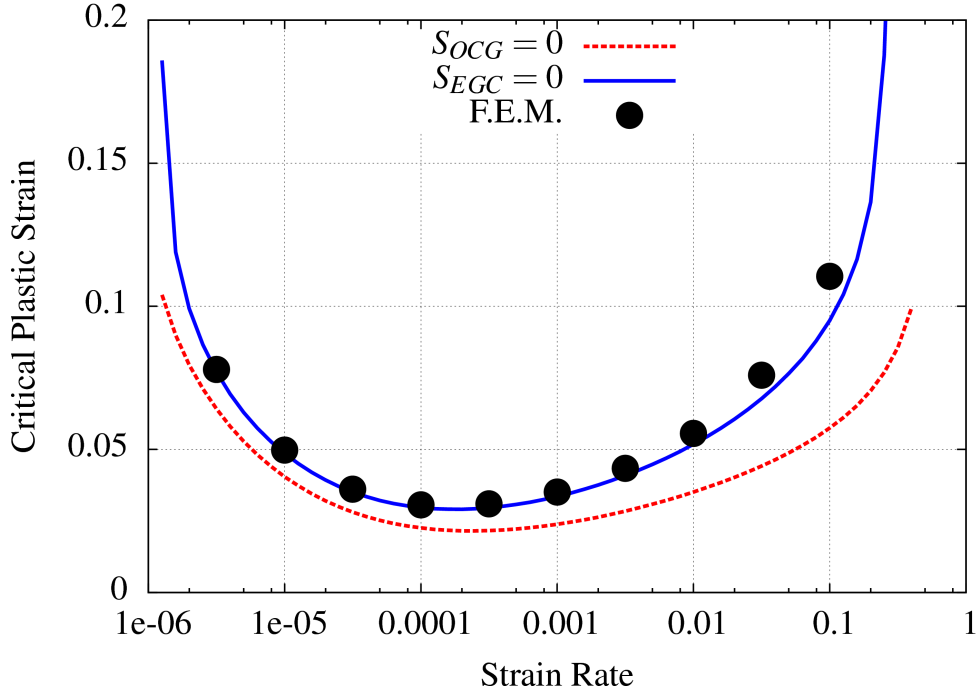
FIGURE 65 – Critical strain provided by finite element simulations using data from Maziere [221] for a Cobalt based superalloy at 600 °C, and by the two analytical criteria. $S_{OGC} = 0$ is the oscillating growth criterion. $S_{EGC} = 0$ is the exponential growth criterion.

In this paragraph the back stress tensor was constituted by one single contribution but the analysis is exactly the same with numerous contribution $\underset{\sim}{X}_i$. The simplification of the linear perturbation analysis was possible because the back stress tensor $\underset{\sim}{X}$ can be eliminated in the perturbation analysis since this latter only appear in the equivalent stress expression and its rate $\dot{\underset{\sim}{X}}$ is linearly related to the plastic strain rate. For a more strongly coupled system of equations for which no state variable can be eliminated, the spectral analysis has to be carried out on a 3×3 transfer matrix $\mathbf{M}$. This latter has consequently 3 eigenvalue, one of them (let's call it λ_1) being purely real. The two others ($\lambda_{2,3}$) are either purely real, or complex with the same real

part. The 4 possible cases presented in the first paragraph of this section can then be applied to $\lambda_{2,3}$ and for each case two situations can be encountered for λ_1. One finally get 8 different cases to investigate. This work is not carried out in the present document.

4.2   Numerical analysis of the critical strain

The influence of the numerical parameters (time step, mesh size, integration method) on the critical plastic strain measured during finite element simulations of the PLC effect is analysed in this section. The influence of mesh size on the post-critical behaviour is also briefly presented, even if this aspect of the problem remains an open question (see the corresponding paragraph for more details).

Time sensitivity

The evolution equations of the KEMC model are highly non-linear, leading to some difficulty to compute the local stress increment from the strain increment. The complete numerical scheme used to solve the global equilibrium problem and the integration of the local behaviour are described in details in [189]. Only the most relevant results are presented in this paragraph.

Concerning the global equilibrium resolution of the non-linear finite element problem, an implicit scheme is used, associated with an automatic time step process. Consequently, the analysis of the time step influence on the finite element simulations of the PLC effect carried out using the KEMC model is relevant only before the critical plastic strain (i.e. the occurrence of serrations), when the prescribed time step is actually experienced by the simulation. Beyond this point two situations can be observed :

— If the maximal allowed time step is small enough, the bifurcation occur and the serrations are followed respecting this maximal and constant time step. For some very sharp serration, this latter can be temporary reduced by the automatic time process but remain in general more or less constant all along the simulation.

— If the maximal time step is two large to reach convergence of the scheme at the occurrence of serrations or during serrations, this latter is reduced by the automatic time step process and a more or less constant value is reached during the rest of the simulation

However it has been observed than in both cases the apparent shape, amplitude, or frequency of the serrations seem not to be influenced by the effective time step.

The maximal prescribed time step plays on the contrary a very important role on the occurrence of serrations. As it can be seen on figures 66 and 67, if the time step is two large, the numerical critical plastic strain –i.e. when the serrations occur during finite element simulations– is larger than the theoretical one predicted by the linear perturbation analysis. On the contrary, when this latter becomes small enough, the numerical critical plastic strain converges towards the theoretical value for both models presented on figures 66 and 67.

In the case of the original KEMC model (see figure 66), the convergence is reached for a maximal global strain step (this quantity is more relevant than the maximal time step which depend on the strain rate) equal to :

— 10^{-4}, if the local behaviour is integrated using an implicit mid-point θ-method

— 5×10^{-5} if an explicit Runge-Kutta method is used

The same value of 10^{-4} for the maximum strain step at convergence has been retrieved for an other set of parameter corresponding to another material when the original KEMC model (denoted ISO on figure 67) is used together with the θ-method. On the contrary, for a modified KEMC model accounting for kinematic hardening (denoted KINE on figure 67) with the same

FIGURE 66 – Evolution of the numerical critical plastic strain with the maximum allowed strain step and comparison with the theoretical value provided by the linear perturbation analysis for a Nickel based super alloy at 500 °C [189]. Two numerical schemes are used for the local law integration : an explicit Runge-Kutta method and an implicit mid-point θ-method.

theoretical critical plastic strain, the convergence is reached for a maximal global strain step equal to 10^{-5}. This result exhibits the fact that the form of the constitutive equations can play a role on the maximal global strain step required to reach convergence and that this analysis has to be carried out for each modified version of the KEMC model

Mesh sensitivity

A topical challenge associated with finite element simulation of elasto-visco-plastic instabilities like Portevin - Le Chatelier effect is to ensure reproductive results. Indeed, like for many other cases of strain localisation, the type, size, and orientation of the mesh can play a huge role on the localisation process itself [198, 221].

The issue of the mesh sensitivity of Portevin - Le Chatelier finite element simulations has been addressed as soon as 2001 in the work by S.Zhang. It has almost not been studied latter till recently by B.Klusemann [218]. A theoretical framework that should help to answer this question has been proposed by A.Benallal [190], however this latter has not yet been compared extensively with finite element results.

The results presented in this section are extracted from one of our former work published in 2010 [189]. The KEMC model and an associated set of material parameter are used to simulated the Portevin - Le Chatelier effect observed at 500°C in a Nickel based super alloy. Six different meshes with element size varying from 1/2 to 1/48 of specimen width (the specimen length is equal to five time the specimen width) where used to investigate the mesh sensitivity of :
  — the critical plastic strain, all other numerical parameters like time step and precision ratio remaining unchanged.
  — the post-critical behaviour, in particular the strain localisation bands characteristics

The figure 68 shows the relative mesh insensitivity of the critical plastic strain, which is almost the same for all investigated meshes. This result has been observed for many different prescribed strain rate, and even for simulations carried out prescribing a constant stress rate (see figure 68(right)). It seems that the occurrence of serrated yielding is only controlled by the
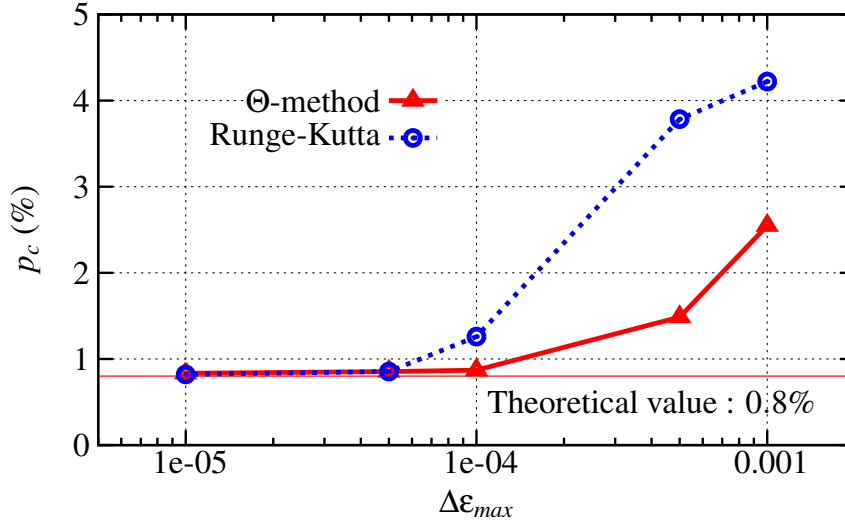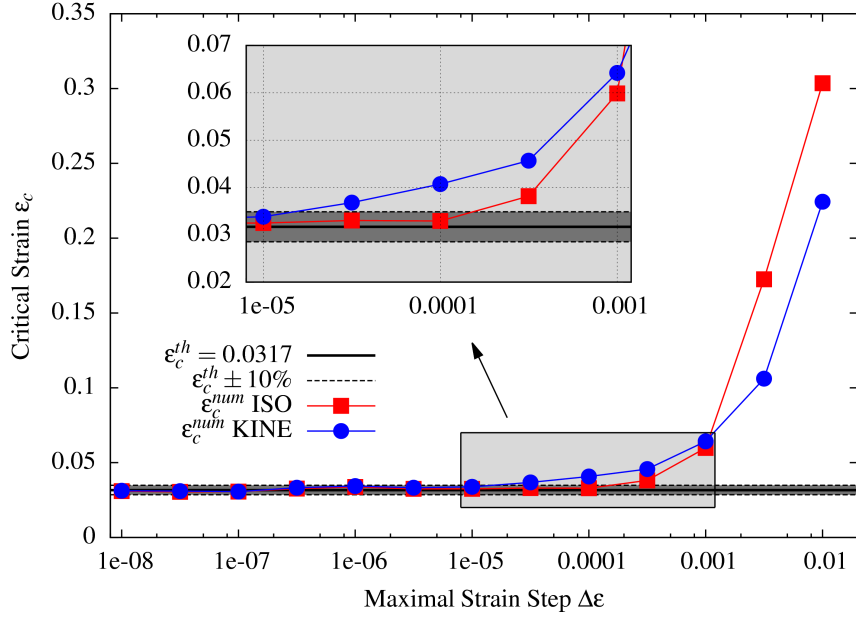
FIGURE 67 – Evolution of the numerical critical plastic strain with the maximum allowed strain step and comparison with the theoretical value provided by the linear perturbation analysis for a Cobalt based super alloy at 600 °C [222]. The identified model including kinematic hardening terms (KINE) is compared with an equivalent one with only isotropic hardening terms (ISO).

stability of the model as described above since for all meshes it occurs close to the theoretical value predicted by the criterion 122.
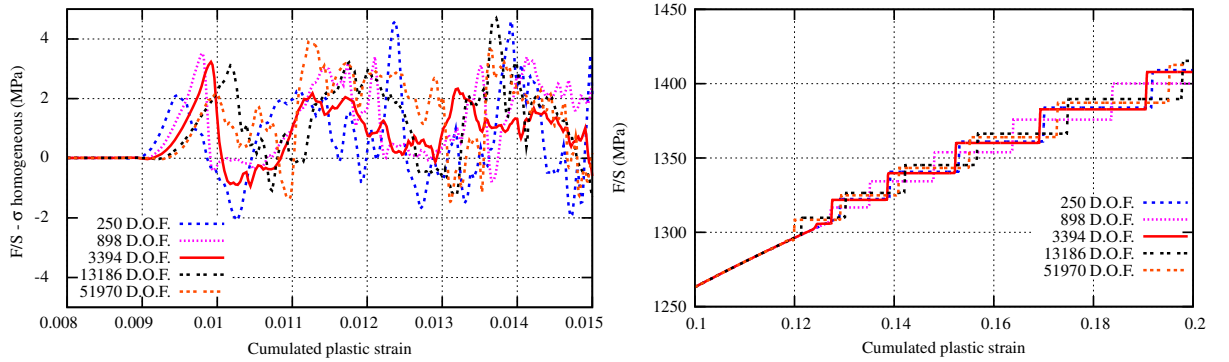
FIGURE 68 – Influence of the mesh size on the occurrence of serrations for strain controlled (left) and stress controlled (right) simulations.

The post-critical behaviour can be regarded based on two different aspects : the serrations on the stress/strain curve, and the spatio-temporal kinetics of band. Some detailed analysis of this post-critical behaviour will be presented on the following section. Here is just discussed the mesh sensitivity of the unstable behaviour from a qualitative point of view. The observation of serrations on figure 68 tends to point out a relative mesh insensitivity of this aspect of the post-critical behaviour. Neither the amplitude nor the frequency of serrations shows an apparent trend with respect to mesh size. This should be confirmed by some more quantitative analysis.

The problem of strain localisation bands is more complex as it can be seen on figure 69. The maps of plastic strain rate $\dot{p}$ and ageing time t_a are plotted for 4 different mesh sizes for the same level of deformation and with the same colour scale (which is just given here for $\dot{p}$).

110
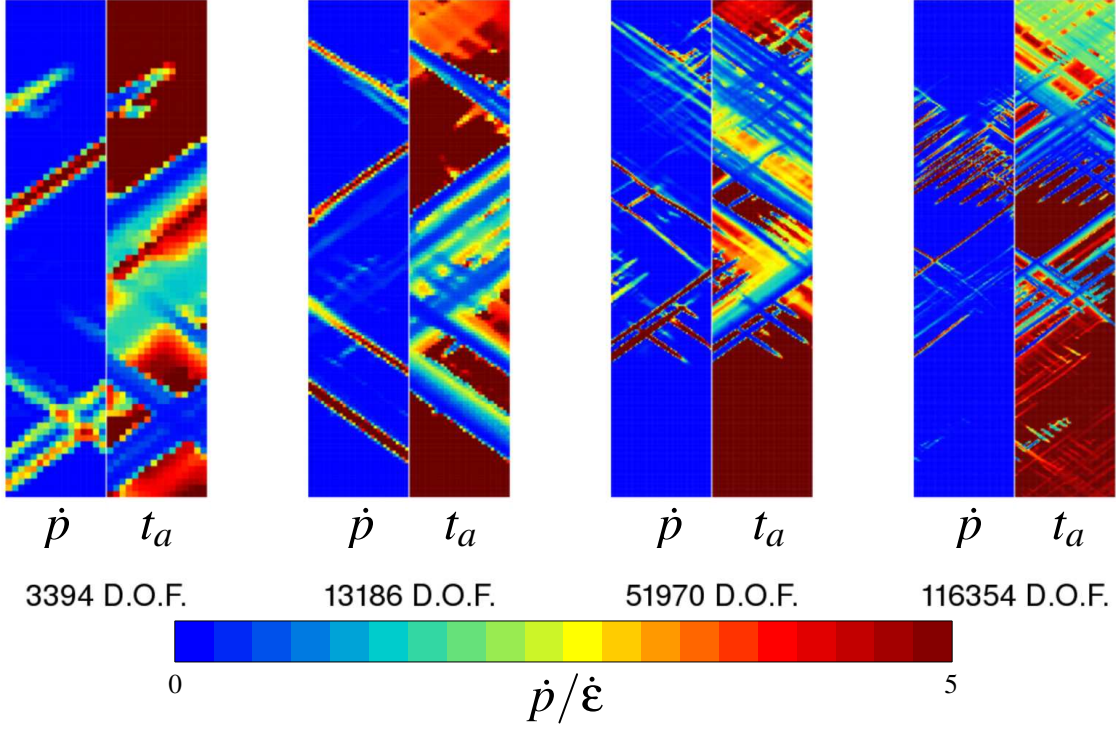
FIGURE 69 – Maps of the plastic strain rate and ageing time for four different simulations carried out using the same material behaviour and four different mesh sizes (see [189] for details).

It appears that the size of bands seems to decrease proportionally with the element size. Some qualitative measures carried out to validate this observation are presented on figure 70. Four different characteristics of the bands are plotted as a function of the element size [15] :

— The band velocity V_b

— The band width L_b

— The strain carried by the band Δp

— The maximum strain rate within the band $\dot{p}_{max}$ (or the inverse of this quantity $(\dot{p}_{max})^{-1}$)

It is obvious on figure 70 that the band velocity V_b and the strain carried by the band Δp are almost mesh insensitive, while the band width L_b and the inverse of the maximum strain rate in the band $(\dot{p}_{max})^{-1}$ are directly proportional to the element size.

The analysis presented here has been conducted under 2D plane stress conditions with regular meshes which constitute a very favourable framework for strain localisation. It may explain why such a mesh sensitivity of some bands propagation parameters has been found. The same study should be carried out extensively on 3D meshes with different specimen thickness and meshes conditions (free or oriented meshes for example). Such an analysis has been begun in the case of Lüders band in two recent articles [198, 221].

---

15. for more details about how this quantities are estimated from finite element simulation please refer to [159]
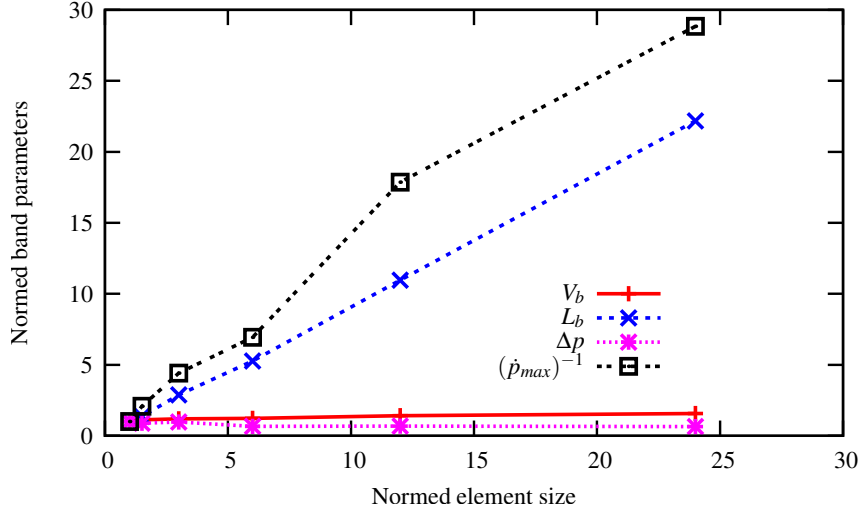
FIGURE 70 – Evolution of the band velocity (V_b) and band width (L_b), of the plastic increment carried by the band (Δp), of the maximum plastic strain rate ($\dot{p}_{max}$) for different element sizes. Values are normalized with respect to values at the minimum element size. DOF number goes from 250 to 116354.

4.3   Post-critical behavior

In this section are presented some post-critical analysis – i.e. when Portevin - Le Chatelier effect runs – that are usually carried out on experiments based on (i) the serrations on the tensile curves, (ii) the spatio-temporal diagrams built from digital image correlation, digital infrared thermography, or other local extensometry measures. The statistical analysis based on the serrations on the stress strain curves can be found in many articles like the ones from M.Lebyodkin and co-workers [119, 171, 179]. The spatio-temporal diagrams can be found in the articles by F.Chmelik [123, 152], Ait-Amokhtar [145, 146, 164, 187], and A.Benallal and co-workers [166, 192, 193]. Some more mathematically advanced post-critical analysis may also be carried out [141, 141, 153, 154, 161, 167, 176]. They are not presented in detail in the present manuscript.

In the present section, the KEMC model has been used for finite element simulations of a tensile plate associated with material parameters identified for an aluminium alloy AA5754 as described in a previous article [199]. Five different strain rates have been prescribed from 10^{-5}s^{-1} to 10^{-1}s^{-1}. As proposed above, two different post-treatments have been applied, one based on the serrations on stress/strain curves, the second one based on the spatial organisation of bands. The results are presented on figure 71 to 75.

The post-treatment based on serrations consist in a statistical analysis of stress drop. For that purpose the steady-state part of the stress is subtracted using the analytical steady state formula 50 of section 3.1. Then each stress drop is characterized by two parameters namely $\Delta\sigma$ the decrease in stress and $\Delta\varepsilon$ the corresponding increase in strain. The histograms of stress drops can then be plotted for the different investigated strain rates. It can be seen on figures 71 to 75 that :

— at high strain rates a lot of small events are found, and the number of events counted increases when the drop size decreases.
— at lower strain rates a second population appears (which seems to be Gaussian) centred on a stress drop value of several MPa.
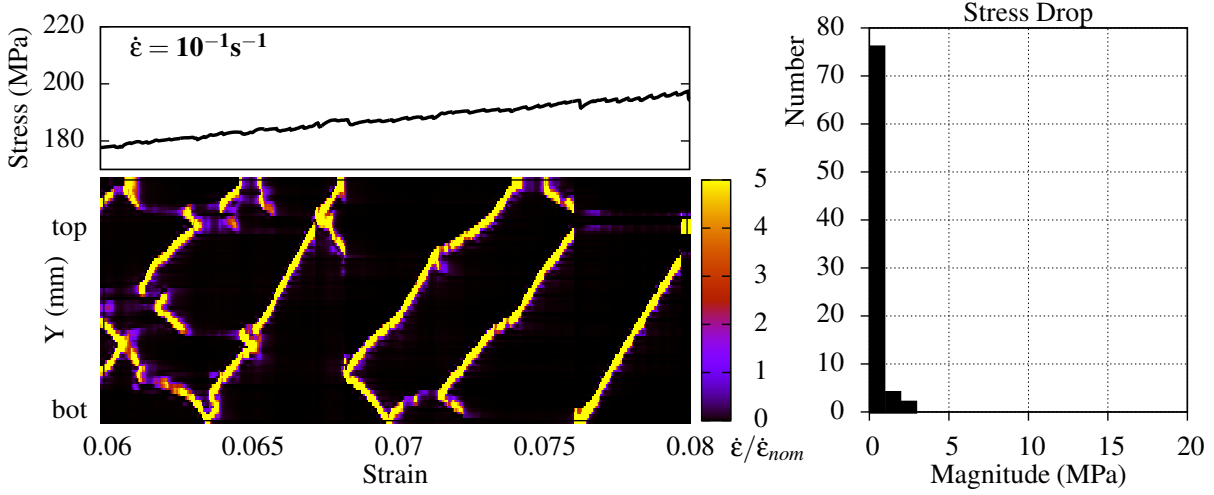
FIGURE 71 – Finite element simulation response of a plate under tensile loading at a prescribed strain rate of 10^{-1}s^{-1}. (top left) serration shape. (bottom left) corresponding spatio-temporal organization of strain localisation bands. (right) statistics of stress drops.
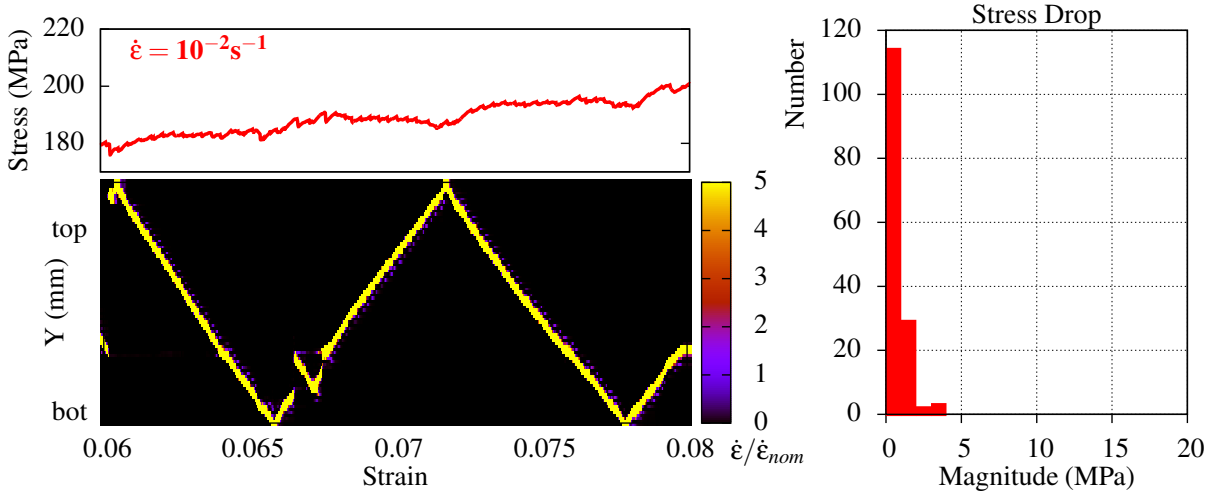
FIGURE 72 – Same results than figure 71 for a strain rate of 10^{-2}s^{-1}.

This influence of strain rate on stress drop distribution is consistent with experimental results obtain with the same method, and with the serration classification in three type A,B, and C type (see [119] for more details).

The serration classification was already mentioned in rather old articles of the 70th [45, 50]. They have been latter associated with some specific spatio-temporal organisations of the strain localisation band during serrated yielding. This organisation can be observed by plotting spatio-temporal diagrams like on the bottom left part of figures 71 to 75. It requires local strain field measures provided experimentally by digital image correlation, digital infrared thermography, or other local extensometry measures, and/or by finite element simulations. The evolution of the cumulated (or axial) strain along a line located in the middle of the specimen is estimated as a function of time and its intensity is plotted using a colour scale. The band type characteristics are the following :

— Type A bands (associated with type A serrations) are propagating continuously in a smooth manner all along the specimen gauge length. They can then either reflect on the specimen boundary like on figure 72, or restart from the other size 73. In both case a more

113
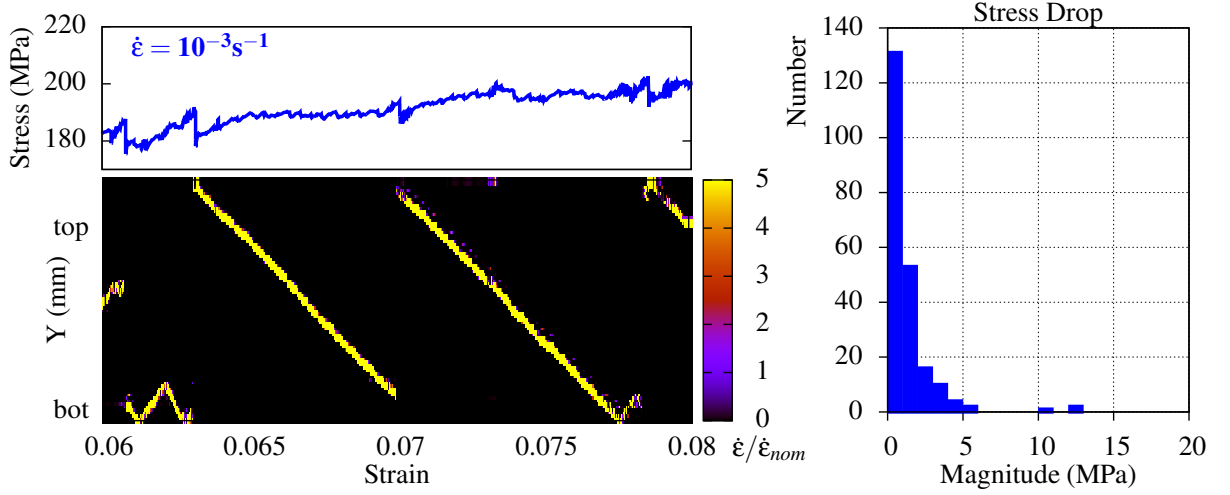
FIGURE 73 – Same results than figure 71 for a strain rate of $10^{-3}\mathrm{s}^{-1}$
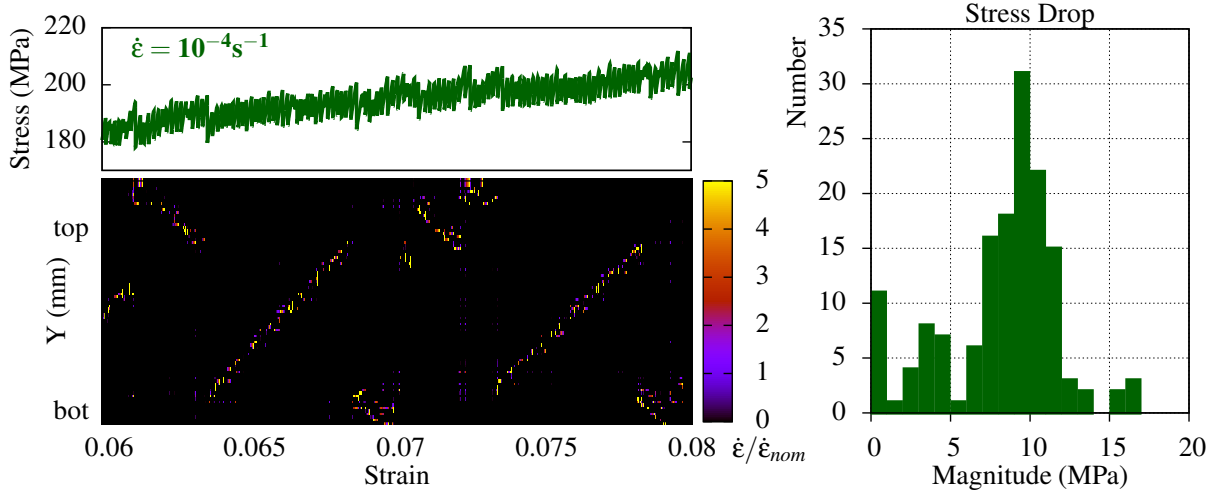
FIGURE 74 – Same results than figure 71 for a strain rate of $10^{-4}\mathrm{s}^{-1}$

important stress drop is observed on the stress vs. strain curve when the band reach one specimen end.

— Type B bands (associated with type B serrations) are propagating all along the specimen gauge length but with a hopping behaviour. They propagate on a very short distance before jumping to another very close position with a very clear discontinuity that can be observed on the spatio-temporal diagrams like on figure 74. The serrations on the stress/strain curve corresponds to each band jump inducing a very regular population of stress drops that can be observed around 10 Mpa on figure 74.

— Type C bands (associated with type C serrations) are randomly nucleating in the whole specimen gauge length. They can propagate over very short distances, but the spatio-temporal diagram finally appears very chaotic like on figure 75. The serrations are rather similar to B-type but with an even more important population of large stress drop centred in this case around 15 Mpa.

This repartition of band type with respect of prescribed strain rate is in agreement with usual experimental observations [119]. The same work should be done investigating the temperature influence in order to evaluate the ability of the KEMC model reproduce accurately the experimental trends.
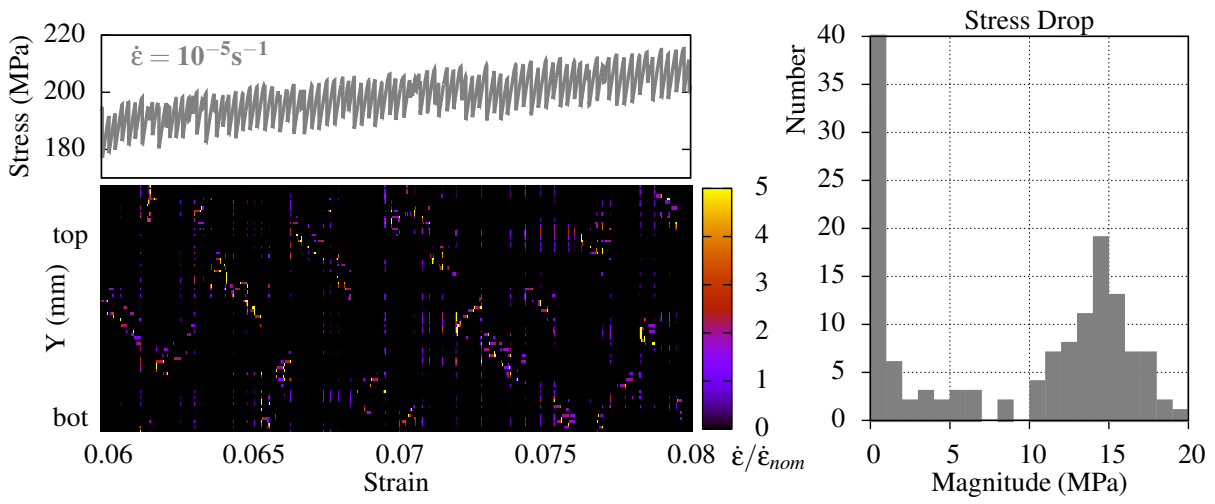
FIGURE 75 – Same results than figure 71 for a strain rate of $10^{-5}\mathrm{s}^{-1}$

5   Application to failure prediction accounting for strain aging

This chapter consists of two articles recently published that investigate the link between strain ageing phenomena and failure of different type of specimens. The same material is used in both article namely a C-Mn steel used in secondary circuit of nuclear power plants.

The first article by A. Marais, M. Mazière, S. Forest, A. Parrot, and P. Le Delliou [220] focuses on the brittle failure of the C-Mn steel in the low temperature domain. The influence of static strain ageing (yield peak and Lüders band) on the ductile-to-brittle transition is studied from an experimental and numerical point of view. One of the main conclusion of the article is that static strain ageing has a detrimental effect on material properties by shifting the ductile-to-brittle transition towards higher temperature i.e. even close to room temperature.

The second article by H.D. Wang, C. Berdin, M. Mazière, S. Forest, C. Prioul, A. Parrot, and P. Le-Delliou [202] investigates the influence of dynamic strain ageing on ductile failure. Experiments on cylindrical notched and compact tensile specimens show a loss of ductility of the material in a domain of intermediate temperatures (150-300°C). This phenomenon also called "blue brittleness" is documented in chapter 2 of the present manuscript. It appears generally in the same temperature range as Portevin - Le Chatelier effect. This article aims to make the link between the features of the PLC effect – principally the negative strain rate sensitivity and the propagative strain localisation – and the loss of ductility of notched or cracked specimen.

5.1   SSA and brittle failure of C-Mn steels

Influence of static strain aging on the cleavage fracture of a C–Mn steel

CrossMark
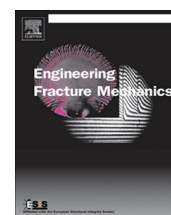
A. Marais [a,b], M. Mazière [a,*], S. Forest [a], A. Parrot [b], P. Le Delliou [b]

[a] Mines ParisTech, Centre des Matériaux, CNRS UMR7633, BP 87, 91003 Evry Cedex, France
[b] EDF R&D/MMC, Site des Renardières, 77818 Moret s/Loing Cedex, France

ARTICLE INFO

ABSTRACT

Recent advances in the constitutive modeling of strain aging effects in elastoviscoplasticity are used to predict the ductile-to-brittle transition curve for a C–Mn steel depending on pre-straining and heat treatment. The parameters of the Beremin model are identified from a large experimental basis of Charpy tests. 3D finite element simulations of Charpy V-notched specimens based on a constitutive model accounting for static strain aging, are performed for the first time to predict the fracture behavior of the pre-strained and aged material. The constitutive model includes the strain localization phenomena occurring in the notch due to Lüders effects. Good agreement between experiment and modeling is demonstrated. The introduction of kinematic hardening improves the prediction of the lower part of the ductile-to-brittle transition region. The proposed approach aims at optimizing pre-strain values and heat treatments for nuclear steels.

© 2015 Elsevier Ltd. All rights reserved.

1. Introduction

The local approach to fracture is based, first, on a detailed metallurgical description of deformation and fracture mechanisms in metals and alloys, second, on a precise constitutive modeling of the elastoviscoplastic material behavior and, third, on coupled or uncoupled fracture criteria [13,39]. One major recent success of this approach has been to reconcile the interpretation in terms of fracture toughness of Charpy test results and fracture of Compact Tension specimens. In particular, some of the difficulties in the experimental and computational analysis of the Charpy test have been overcome in a series of works [45,43,44,27,26,52,53,47,49]. These works address in particular the Charpy tests at low temperature and the ductile-to-brittle transition in nuclear steels.

At low temperature and in the transition, cleavage is the main mechanism for brittle fracture in the ferritic nuclear steels, even though cleavage is always accompanied locally by intragranular plastic slip which becomes dominant with increasing temperature [41]. The fracture properties in the low temperature and transition regimes are statistical by nature due to the distribution of defects including inclusions or second phase in the material. They are very often satisfactorily described by means of the Beremin model which relates the Weibull distribution of fracture probability to a power-law distribution of defects and plasticity phenomena [10,11]. Such statistical fracture models can be applied to fracture mechanics samples like CT specimens [60], Charpy tests and structural components. They benefit from a detailed knowledge of the distribution of defects [51] and can incorporate the influence of loading rate [42]. More elaborate statistical models of fracture can be found in Bordet et al. [15].

---

* Corresponding author.
  E-mail address: matthieu.maziere@mines-paristech.fr (M. Mazière).

Nomenclature

CVN	Charpy V-notch impact energy (J)
$\underset{\sim}{\boldsymbol{D}}$	strain rate tensor
E_a	activation energy (eV)
$J_2(\underset{\sim}{\boldsymbol{\sigma}})$	von Mises equivalent stress
k_B	Boltzmann constant (1.38e−23 J/K)
$\underset{\sim}{\boldsymbol{L}}$	gradient of velocity field
m	Weibull exponent
p	cumulated plastic strain
$\dot{p}$	cumulated plastic strain rate (s^{-1})
P_r	failure probability
$\underset{\sim}{\boldsymbol{Q}}$	material rotation
t_a	current aging time (s)
t_{a0}	initial aging time (s)
T	temperature (K)
$\underset{\sim}{\boldsymbol{T}}$	Cauchy stress tensor (MPa)
V_a	activation volume
$\underset{\sim}{\boldsymbol{X}}$	kinematic hardening stress tensor (MPa)
$\underset{\sim}{\boldsymbol{\alpha}}$	hardening internal variable
$\underset{\approx}{\boldsymbol{\Lambda}}$	tensor of elastic moduli (MPa)
ρ	current dislocation density (m^{-2})
ρ_0	initial dislocation density (m^{-2})
$\rho_{5\%}$	dislocation density for the 5% pre-strained state (m^{-2})
$\underset{\sim}{\dot{\varepsilon}}$	observer invariant strain rate tensor
$\underset{\sim}{\dot{\varepsilon}_e}$	elastic strain rate tensor
$\underset{\sim}{\dot{\varepsilon}_p}$	plastic strain rate tensor
$\underset{\sim}{\boldsymbol{\sigma}}$	observer invariant stress tensor (MPa)
σ_w	Weibull stress (MPa)
σ_I	maximum principal stress (MPa)

Strain aging characterizes the mechanical behavior of most nuclear steels due to the interaction of solute atoms present in the alloys and dislocations [16,54]. Static strain aging (SSA) is observed at lower temperature for instance in the form of Lüders peak stress and plateau accompanied by the propagation of plastic strain localization bands along the sample or at geometrical singularities in structural components. In service conditions at higher temperatures very often correspond to the domain of dynamic strain aging (DSA) which can be associated with the Portevin–Le Chatelier effect, i.e. the formation and propagation of plastic strain rate localization bands. In the context of fracture mechanics, the Lüders and Portevin–Le Chatelier effects are usually not taken into account in the computational modeling of fracture processes. Heuristic rules are chosen to fix the initial yield stress and the strain localization phenomena are not incorporated. DSA effects are smoothed out and the possible negative strain rate sensitivity is usually not accounted for. However, reliable constitutive equations have been available for more than ten years that include the strain aging effects in the elastoviscoplastic material laws. The associated instabilities have been investigated by Mesarovic [35], Benallal [6], and Benallal et al. [8,7]. Finite element (FE) simulations of plastic strain and strain rate phenomena in tensile or fracture mechanics samples were first performed by Zhang et al. [63] and Graff et al. [20,21] for aluminum alloys and mild steel. The constitutive models are mature for full 3D implicit FE computations and detailed comparison with experimental data like strain field measurements, as done for the Lüders effect by Ballarin et al. [4,3], Hallai and Kyriakides [23,24], Marais et al. [30], and Hallai and Kyriakides [25]. The simulations include the local stress and strain rate concentration induced by the development of spatio-temporal instabilities.

The importance of strain aging on the fracture properties of engineering steels is well recognized in the mechanical metallurgy community. DSA effects in C–Mn steels were investigated by Wagner et al. [55–57], for CT specimens but also in welded zones, taking heat treatments into account. More recent works are based on constitutive modeling of dynamic strain aging and explicit modeling of PLC bands in notched and CT specimens [5,58,59,9]. In the latter work, it was shown that a reduction of ductility is observed in the DSA domain of material behavior. The impact of static strain aging on fracture toughness was first addressed in Houssin et al. [28] and Amar and Pineau [1] in the case of CT specimens. Recent contributions make use of Zhang and McCormick's model for the computation of the elastoviscoplastic response of a CT specimen, including a detailed 3D analysis of strain localization phenomena at the crack tip by Wenman and Chard-Tuckey [61].

What is missing in the literature is the direct use of strain aging constitutive models for the prediction of brittle-to ductile transition curves. This is the objective of the present work in the case of a C–Mn nuclear steel. For that purpose, the proposed methodology combines the tools of local approach to fracture as presented in Pineau [40] and the detailed elastoviscoplastic

constitutive modeling of static strain aging in this alloy, as established by Marais et al. [30]. Novel aspects of the work include the direct simulation of Charpy tests at different temperatures and the identification of a statistical fracture model delivering the ductile-to-brittle transition curve as a function of SSA induced by pre-straining, heat treatment and loading path history.

The outline of the paper is as follows. The experimental methods and mechanical test results are presented in Section 2. They include the Charpy V-notch (CVN) test results for three different material strain aging states over a range of temperatures from −100 °C to 100 °C. The equations and material parameters of the constitutive model accounting for strain aging dependent elastoviscoplasticity are given in Section 3. In the same section, the finite element results of the CVN simulations are used to identify the Beremin model for the base material state. Predictions of the constitutive and fracture models are then provided for other aging states and compared to experimental results. The influence of the Bauschinger effect on CVN predictions at the lower part of the ductile-to-brittle transition region is also investigated. The results are finally discussed in Section 4.

2. Experimental procedure

2.1. Material

All experiments were conducted on a C–Mn steel used for pipes of the secondary circuit in power plants, called here A42, whose chemical composition is given in Table 1. This alloy is very sensitive to strain aging due to the small *Al* content. The material is extracted from a seamless secondary coolant pipe obtained by a circular rolling process. The microstructure is composed of ferrite and pearlite in alternate bands along planes parallel to the axial and circumferential directions. The crystallographic texture was not analyzed. However, the cross-section of cylindrical tensile specimens remains circular up to fracture strain. This indicates a quasi-isotropic mechanical behavior at least in the long and short transverse plane. By extension, we considered the mechanical behavior as fully isotropic, weakly affected by the morphological texture, nor by the crystallographic texture, thus following Belotteau et al. [5].

The mechanical behavior of this material under simple tension has been investigated in a previous article [30]. This contribution was devoted to the experimental analysis and modeling of the stress peak and Lüders plateau experimentally observed at several temperatures from −150 °C to 20 °C. The tensile curves are recalled in Fig. 1 and show the temperature dependence of peak stress and Lüders plateau. The constitutive model identified in the latter work is used in the numerical simulations of the present paper.

2.2. Testing conditions

Standard Charpy V-notch specimens with a (10×10) mm^2 section, a central 45° V-notch of 2 mm depth and a 0.25 mm notch root radius were tested in accordance with the French standard for impact testing of Charpy specimens (NF EN 10045-1) on an instrumented 450 J capacity impact tester. The notch plane is perpendicular to the transverse direction T and crack growth direction parallel to the longitudinal direction L of the plate. The acquisition frequency is 250 kHz. These impact tests were carried out with an impact velocity equal to 5 m s^{-1}. The testing temperature varies over the range −100 °C to 80 °C.

Table 1
Chemical composition (weight percent) of the Carbon Manganese steel A42.

Steel	C	N	Al	Si	P	S	V	Cr	Mn	Ni	Cu	Nb	Mo	Sn
A42	0.15	0.004	0.019	0.19	0.034	0.021	<0.002	0.034	0.73	0.05	0.041	<0.002	0.006	0.003
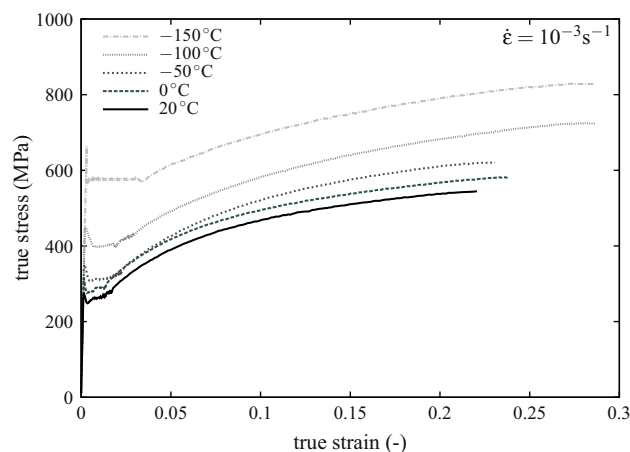
Fig. 1. Experimental tensile curves for different temperature from Marais et al. [30]. A stress peak and Lüders plateau is evidenced at all temperatures.

Table 2
Number of specimens tested for each state and each temperature. Dispersion of results is determined using the numerous experiments at −20 °C.

Charpy impact tests	Temperature (°C)							
	−100	−50	−20	0	20	40	60	80
BS	2	2	20	3	3	×	2	2
5% pre-strained	2	2	18	3	5	2	2	2
5% pre-strained + aged	2	2	18	3	5	2	2	2

Three different states for the C–Mn steel were tested using the same procedure. The first state is denoted "BS" and corresponds to the as-received material without any additional heat treatment or pre-straining. The second material state denoted "5% pre-strained" was designed in order to study the influence of pre-straining on fracture. Numerous Charpy specimens were then cut in a 5% pre-strained 710 mm × 40 mm × 40 mm bar. This pre-straining was carried out along the transverse orientation (T) of the plate. The third material state is denoted "5% pre-strained + aged". Half of the specimens cut from the pre-strained bar were subjected to an aging heat treatment (30 min at 250 °C) in order to generate this last material state. The influence of the aging heat treatment on fracture is investigated by comparison of these specimens with the "5% pre-strained" ones. The number of Charpy tests performed for each material state and each temperature is given in Table 2.

2.3. Fracture tests

Representative Charpy experimental load displacement curves for the three aforementioned material states are shown in Fig. 2 for temperature $T = 0$ °C and $T = 20$ °C. The load level is higher for the 5% pre-strained and 5% pre-strained + aged states than for the base state because of hardening. The height of the second peak is also higher for the 5% pre-strained + aged than for the 5% pre-strained as expected due to the aging effect. At both temperatures, the energy required to break the specimens seems to be smaller in the 5% pre-strained + aged state than for the 5% pre-strained, than for the state BS.
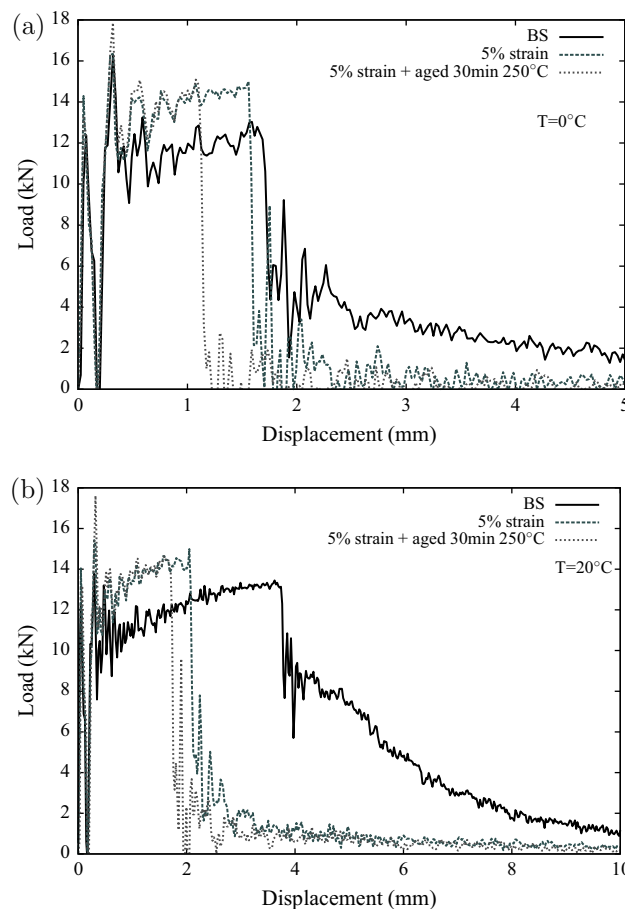
Fig. 2. Load–displacement curves for Charpy test on the 3 material states: (a) at 0 °C and (b) at 20 °C.
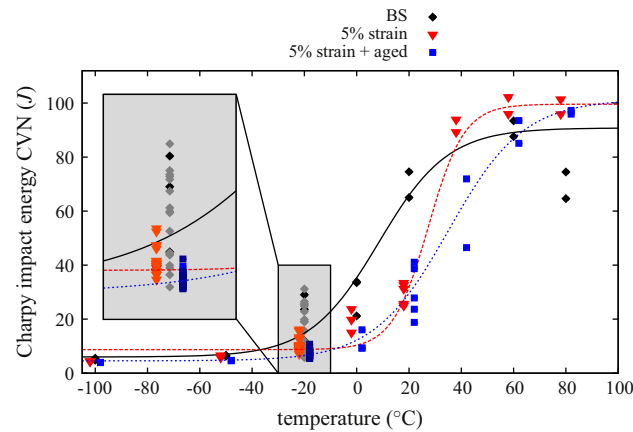
Fig. 3. Charpy fracture energy transition curves of C–Mn steel for Charpy specimens tested at different states, BS, 5% pre-strained and 5% pre-strained + aged.

Table 3
Parameters of the CVN energy fitting function and index TK$_7$ for different material states.

Material state	A (J)	B (J)	T_0 (°C)	C	TK$_7$ (°C)
BS	48.4	42.4	8.67	30.29	13.2
5% pre-strained	54.2	45.4	27.39	13.67	28
5% pre-strained + aged	52.96	48.4	35.17	28.65	37

The material state significantly affects the dependence of experimental Charpy impact energies on temperature, as shown in Fig. 3. The energies of the Charpy V-notch (CVN) tests obtained from Table 2 were fitted for each state with an hyperbolic tangent function of temperature as proposed by Oldfield [38]:

$$\text{CVN}(J) = A + B \tanh\left((T - T_0)/C\right) \tag{1}$$

Parameters A, B, C, T_0 of Eq. (1) are given in Table 3. For each condition, only the three first experiments were taken into account at $-20\,°C$ in the parameter identification in order to give to this temperature the same weight as the other ones. The temperature denoted TK$_7$ is also reported in Table 3 since this temperature is currently used in Charpy impact tests analysis. It is defined as the temperature for which the CVN energy is 56 J (CVN$/S_r = 7$ da J/cm^2 with S_r the fracture surface, $S_r = 0.8$ cm^2).

The ductile-to-brittle transition is shifted towards higher temperatures for the 5% pre-strained state. This shift is increased for the 5% pre-strained + aged state, as shown by the corresponding value of the TK$_7$ parameter from Table 3.

The scatter of CVN energies at $-20\,°C$ for the three material states is plotted in Fig. 4 for the three material states. The mean value of this energy decreases from 18.1 J to 10.5 J for the base and 5% pre-strained states respectively, and to 7.29 J for the 5% pre-strained + aged state. This result is consistent with the transition curves plotted in Fig. 3. A large number of experiments were carried out at this temperature (almost 20 for each state) so as to obtain a reliable estimation of the scatter which is high at this temperature. The standard deviation follows the same trend as the mean value and decreases from 7.8 J for the based state to 2.57 J for the 5% pre-strained state and to 1.43 J for the 5% pre-strained + aged state. The scatter of experimental results is therefore significantly affected by the pre-strain and by the aging treatment.

Based on all these results (Figs. 3 and 4), it can be concluded that at $-20\,°C$, the material in its as-received state still is in the ductile-to-brittle transition. In contrast at the same temperature for the two other conditions, the material is below the transition in the brittle fracture domain and the ductile-to-brittle transition is then shifted towards higher temperatures. The shift in the transition domain is emphasized by the aging treatment applied to the prestrained material, and can lead to unexpected failure of the material.

3. Numerical modeling

3.1. Constitutive equations

The simulation of strain aging requires a suitable choice of an elastoviscoplasticity model including the physical mechanisms of pinning and unpinning of dislocations. The model retained in this work and initially proposed by Kubin, Estrin, McCormick [29,34] is based on the introduction of an internal variable t_a called aging time with a suited evolution law coupled with plastic flow. It has been implemented in the finite element code Zset and used in several previous studies
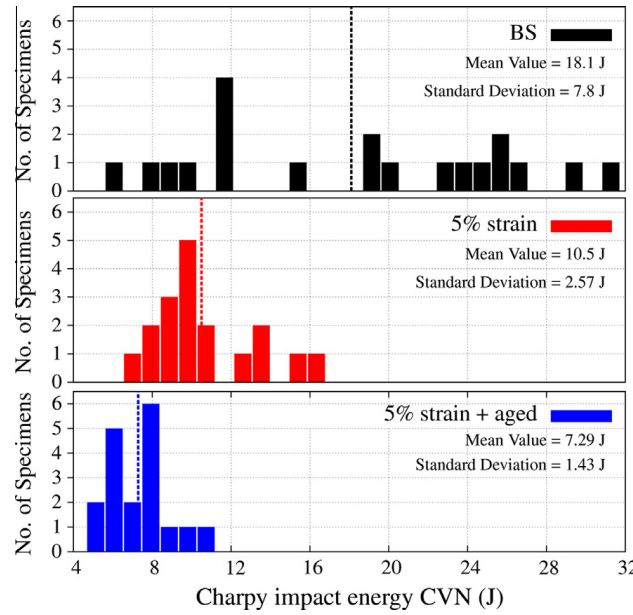
Fig. 4. CVN energies at $-20\,^\circ$C (scatter temperature) for the 3 material states, including the corresponding average values and standard deviations.

[5,31,58,32]. For more details about the model, its implementation and the identification process, the reader is referred to a previous article by the same authors [30].

A finite strain formulation for isotropic nonlinear material behavior is adopted in this work based on the concept of local objective frame as proposed in Sidoroff and Dogui [48], Bertram [12], and Besson et al. [14]. Observer invariant stress and strain rate measures $\underset{\sim}{\sigma}$ and $\underset{\sim}{\dot{\varepsilon}}$ are defined by transport of the Cauchy stress tensor $\boldsymbol{T}$ and the strain rate tensor $\boldsymbol{D}$ into the corotational frame characterized by the rotation $\underset{\sim}{\boldsymbol{Q}}(\underline{\boldsymbol{x}}, t)$. This change of frame takes place at each material point:

$$\begin{cases} \underset{\sim}{\sigma} = \underset{\sim}{\boldsymbol{Q}} \cdot \underset{\sim}{\boldsymbol{T}} \cdot \underset{\sim}{\boldsymbol{Q}}^T \\ \underset{\sim}{\dot{\varepsilon}} = \underset{\sim}{\boldsymbol{Q}} \cdot \underset{\sim}{\boldsymbol{D}} \cdot \underset{\sim}{\boldsymbol{Q}}^T \\ \underset{\sim}{\boldsymbol{Q}} \text{ such as } \underset{\sim}{\dot{\boldsymbol{Q}}}^T \cdot \underset{\sim}{\boldsymbol{Q}} = \underset{\sim}{\boldsymbol{\Omega}} \text{ (corotational)} \end{cases} \tag{2}$$

where $\underset{\sim}{\boldsymbol{\Omega}}$ is the skew-symmetric part of the gradient $\boldsymbol{L}$ of the velocity field, and $\boldsymbol{D}$ its symmetric part [48,14].

The strain rate tensor $\underset{\sim}{\dot{\varepsilon}}$ is split into elastic and plastic contributions, the evolution of the latter being given by the plastic flow rule. The stress is computed from the elastic strain $\underset{\sim}{\varepsilon_e}$ through Hooke's law:

$$\underset{\sim}{\dot{\varepsilon}} = \underset{\sim}{\dot{\varepsilon}_e} + \underset{\sim}{\dot{\varepsilon}_p}, \quad \underset{\sim}{\sigma} = \underset{\approx}{\boldsymbol{\Lambda}} : \underset{\sim}{\varepsilon_e} \tag{3}$$

The plastic strain is computed from the normality rule

$$\underset{\sim}{\dot{\varepsilon}_p} = \dot{p}\, \underset{\sim}{\boldsymbol{n}}, \quad \underset{\sim}{\boldsymbol{n}} = \frac{\partial f}{\partial \underset{\sim}{\sigma}} \tag{4}$$

and the equivalent plastic strain rate $\dot{p}$ follows a thermal activation law defined as:

$$\dot{p} = \dot{p}_0 \sinh\left(\frac{\langle f \rangle}{K}\right) = \dot{\varepsilon}_0 \exp\left(-\frac{E_a}{k_B T}\right) \sinh\left(\frac{V_a \left\langle f\left(\underset{\sim}{\sigma}, \rho, t_a\right) \right\rangle}{k_B T}\right) \tag{5}$$

where T is the temperature in Kelvin, k_B is the Boltzmann constant and $\dot{\varepsilon}_0, E_a$ and V_a respectively are a strain rate parameter, the activation energy and the activation volume of the physical mechanisms of plasticity.

The function f in Eq. (4) is the yield function which is based on a von Mises criterion with isotropic hardening:

$$f\left(\underset{\sim}{\sigma}, \rho, t_a\right) = J_2(\underset{\sim}{\sigma}) - R(\rho) - R_a(t_a) \tag{6}$$

$$R(\rho) = \sigma_0 + \gamma \mu b \sqrt{\rho}, \quad \dot{\rho} = A\left(1 - \frac{\rho}{B}\right)\dot{p}, \quad R_0 = \sigma_0 + \gamma \mu b \sqrt{\rho_0} \tag{7}$$

where $J_2(\boldsymbol{\sigma})$ is the von Mises equivalent stress. The dislocation density ρ is introduced in the model (initial value ρ_0). The classical strain hardening is given by the term $R(\rho)$ which follows the evolution law defined in Eq. (7), the multiplication and dynamic recovery parameters characterizing the evolution law of this variable being A and B, respectively. The dislocation density evolution rule is driven by the cumulative plastic strain rate $\dot{p}$, as done for instance in Fressengeas et al. [19]. The yield stress R_0 is the "virtual" initial microscopic yield stress that would be measured in the same steel in the absence of static strain aging.

The second contribution to the yield stress, $R_a(t_a)$, is due to strain aging, following [63,20,31]. It depends on an additional internal variable t_a called the aging time, and takes the form

$$R_a(t_a) = P_1 C_s(t_a), \quad \text{with} \quad C_s = 1 - \exp\left[-\left(\frac{t_a}{t_0}\right)^n\right] \tag{8}$$

$$\dot{t}_a = 1 - \frac{t_a \dot{p}}{\omega} \tag{9}$$

The strain aging term R_a is proportional to the variable C_s that is related to the over-concentration of solute atoms around pinned dislocations. This variable increases with the aging time t_a, the condition corresponding to fully pinned dislocations being given by $C_s = 1$. The unpinned state corresponds to $C_s = 0$. The parameter P_1 corresponds to the maximal additional stress needed to switch from unpinned to pinned conditions. The parameter t_0 and the power n control the kinetics of the pinning and unpinning processes. Another parameter labeled ω appears in the evolution law of the aging time. It is related to the incremental strain resulting from the freeing of unpinned dislocations.

The identification of this model over a large range of temperatures (from $-150\,°C$ up to $20\,°C$) and strain rate (from $1e{-}5\,s^{-1}$ up to $1e{-}1\,s^{-1}$) was carried out using numerous simple tensile experiments as described in Marais et al. [30]. The identification procedure which takes into account the characteristics of the Lüders phenomenon is not recalled. The parameters for the five temperatures of interest in the present work are given in Table 4.

3.2. Cleavage fracture prediction

The constitutive material model is associated with a non-coupled brittle (cleavage) fracture model according to Mudry [36,37], Beremin [11], and François et al. [18], which is one of the most popular local approach models in this area, denoted Beremin model. It is based on the hypothesis of a (temperature-independent) critical cleavage stress, and on weakest link theory. The failure probability P_r is given as:

$$P_r = 1 - \exp\left[-\left(\frac{\sigma_w}{\sigma_u}\right)^m\right] \tag{10}$$

with σ_w, the "Weibull stress"

$$\sigma_w = \sqrt[m]{\int_{V_p} \max_{0 \leqslant \tau \leqslant t} (\sigma_I^\tau)^m \frac{dV}{V_0}} \tag{11}$$

where σ_I^τ denotes the maximum principal stress (here defined as its maximum value with time), m the Weibull exponent which is related to the scatter in the distribution of defects responsible for fracture, and σ_u is closely linked to the intrinsic cleavage stress. The integral denotes the summation of σ_I^τ over the entire plastified volume V_p of the structure (i.e., all

Table 4
Constitutive parameters describing elasticity, viscoplasticity, hardening and aging.

T (°C)	**-150**	**-100**	**-50**	**0**	**20**
E (GPa)	214	220	219	221	218
v	0.3	0.3	0.3	0.3	0.3
R_0 (MPa)	360	225	145	147	150
σ_0 (MPa)	340	205	124	126	130
ρ_0 (m^{-2})	1e13	1e13	1e13	1e13	1e13
A (m^{-2})	2.26e16	3.5e16	4.15e16	3.87e16	3.09e16
B (m^{-2})	1.47e16	9.2e15	8.08e15	5.12e15	5.11e15
$\dot{\varepsilon}_0$ (s^{-1})	1e−7	1e−7	1e−7	1e−7	1e−7
E_a (eV)	0.0022	0.0022	0.0022	0.0022	0.0022
V_a (b^3)	27	59	90	121	133
P_1 (MPa)	396.6	316	285	220	183.2
t_0 (s)	3.49e13	1.24e12	2.81e8	1.01e5	1.59e4
t_{a0} (s)	3.49e13	1.24e12	2.81e8	1.01e5	1.59e4
ω	5e−4	5e−4	5e−4	5e−4	5e−4
n	0.137	0.144	0.199	0.306	0.334

Bold was a way to highlight the temperatures.

elements that have undergone plastic deformation), since plastic deformation is a necessary precursor to slip-induced cleavage (e.g., by a dislocation pile-up mechanism). Two independent parameters are required: m and $V_0\sigma_u^m$.

The fracture criterion is thus based on one mechanical variable, i.e., namely the maximum positive principal stress. Fracture is assumed to occur as soon as this quantity reaches a critical value for unstable propagation of a cleavage micro-crack. There are some guidelines for the choice of V_0. On the one hand, V_0 should be large enough in order to allow for the presence of a critical defect. On the other hand, V_0 should be small enough in order to resolve strong stress gradients, as they occur ahead of a crack tip. In "local" FEM computations (i.e. if no averaging over several finite elements is carried out) the size of V_0 is related to the mesh size, see [13]. Thus the choice of the mesh size is important for ductile crack growth modeling, as well as for cleavage fracture modeling. V_0 was chosen equal to $(50\,\mu m)^3$ [18].

The model parameters σ_u and m are first identified using Charpy impact tested at temperature $-20\,°C$ for the base state. Twenty tests were performed. The parameters are identified using an automatic identification procedure which minimizes the quadratic difference between the theoretical and experimental failure probabilities [53] described briefly below:

1. For each Charpy experiment, the CVN energy is computed from the load vs. displacement curves, and experiments are sorted in ascending order.
2. The failure probability associated to the stress reached by specimen at rank i is evaluated using the following formula: $P_{f,i}^{exp} = \frac{i}{N+1}$ where N is the total number of specimens and $i = 1, \ldots, N$ the rank of the specimen.
3. The displacement (of the striker) at failure is evaluated for each experiment.
4. A finite element simulation of the Charpy test at $-20\,°C$ is carried out beyond the maximal experimental displacement reached by the 20 experiments. The corresponding finite element model is detailed in Section 3.3.
5. For each calculation step corresponding to an experimental failure displacement, the experimental Weibull stress σ_w^{exp} is estimated from the finite element results.
6. The experimental evolution of $P_{f,i}^{exp}$ as a function of σ_w^{exp} is compared to the Beremin model $P_f^{mod}(\sigma_w)$ given by Eq. (10).
7. If both evolutions are in agreement, the iterative process is stopped. Otherwise, m and σ_u are modified and the algorithm goes to step 5.

Experimental and theoretical failure probabilities are compared in Fig. 5 as functions of the computed Weibull stress. In this figure, a good agreement between experimental and theoretical values is observed when adopting the following values for the Weibull parameters: $m = 23$ and $\sigma_u = 1654$ MPa. The value found for the Weibull shape factor m is close to those reported in the original Beremin work on another pressure vessel steel [11], or in a more recent article on ferritic steels [2].

3.3. Modeling of the Charpy transition curve for the base state

In order to understand the effect of strain and aging on the transition curve, finite element simulations of the Charpy impact test were carried out using the finite element software Zset [62]. All the simulations were performed on the 2D mesh presented in Fig. 6 using plane strain formulation. Some simulations using plane stress formulation or full 3D mesh have also been carried out. The global force vs. displacement curve for plane strain and plane stress formulation were found to be located respectively above and below that of the 3D curve. However when the evolution of the maximum principal stress is plotted beyond notch tip, results for plane strain and 3D simulation are very close and different from the corresponding plane stress result. Since this variable is the most important one for the application of the Beremin model presented in Section 3.2, the plane strain formulation is selected for this study, in agreement with recommendations from Rossoll et al. [44].
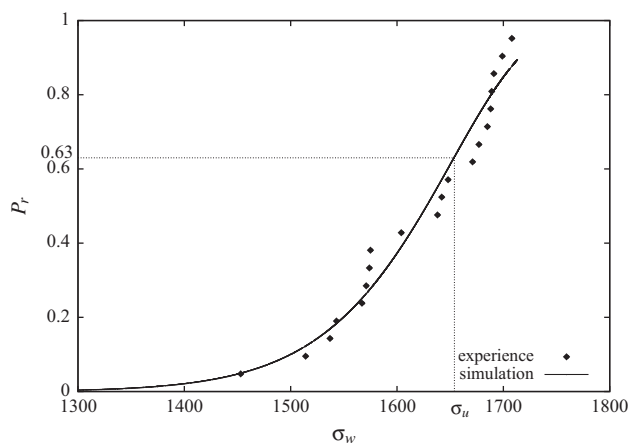

Fig. 5. Identification of the Beremin model parameters for brittle fracture of the C–Mn steel.
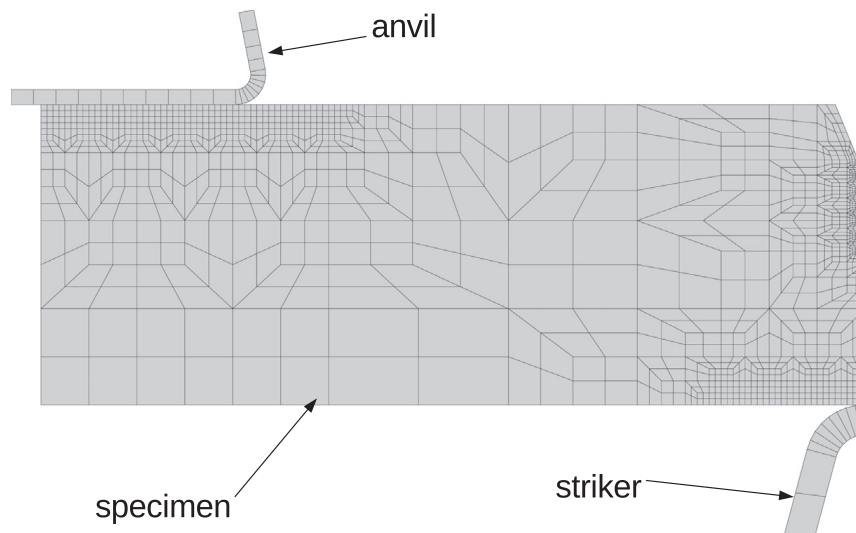
Fig. 6. Two-dimensional finite element mesh of the Charpy specimen, including the anvil and the striker parts. The mesh size beyond notch tip is 60 µm.

The finite elements chosen were four node linear square elements with selective integration [14] in the contact zones and eight node quadratic squares in the rest of the specimen, using a continuous interface condition between both zones. The influence of mesh size was investigated in order to reach convergence of the maximal principal stress beyond notch tip. As a result of this analysis, the element size was fixed equal to 60 µm.

The boundary conditions of the finite element simulations are the following. A velocity of $V = 5$ m s^{-1} is prescribed to the striker, while the anvil remains fixed. The friction coefficient between these two parts and the specimen is equal to 0.1. This coefficient is particularly significant in case of ductile failure propagation (i.e. for high level of CVN energy), but less important in our case where the lower part of the ductile-to-brittle transition is investigated. The striker and the anvil are modeled as rigid bodies in order to improve the convergence of the contact algorithm. It has been shown in Rossoll et al. [44] that accounting for the elasticity of these parts does not modify significantly the results.

The simulations were carried out using a quasi-static isothermal formulation as suggested in Rossoll et al. [44]. This point may be reconsidered in future work especially at low temperature for which inertial effects may play a more significant role.

The material model described in Section 3.1 was used at 6 different temperatures ($-150\,°C$, $-100\,°C$, $-50\,°C$, $-20\,°C$, $0\,°C$, $20\,°C$) to simulate the Charpy impact tests using the numerical model presented above. At each temperature, the CVN energies for a fracture probability of 10%, 50%, and 90% are evaluated using the area under the force vs. displacement curve at the corresponding calculation steps. These steps are defined after applying the Beremin model with the parameters identified in Section 3.2.

The results are plotted in Fig. 7 giving the energy at 10%, 50%, and 90% as a function of temperature. At $-20\,°C$, the numerical prediction is in exact agreement with experimental results due to the fact that the Beremin model parameters were identified at this temperature for this material state. At all other temperatures the experimental points remain inside the 10–90% bounds, even at higher temperature ($20\,°C$), thus showing the predictive capabilities of the model. Note that at this temperature the fracture of the material is probably not fully brittle and that the Beremin model should be associated with a
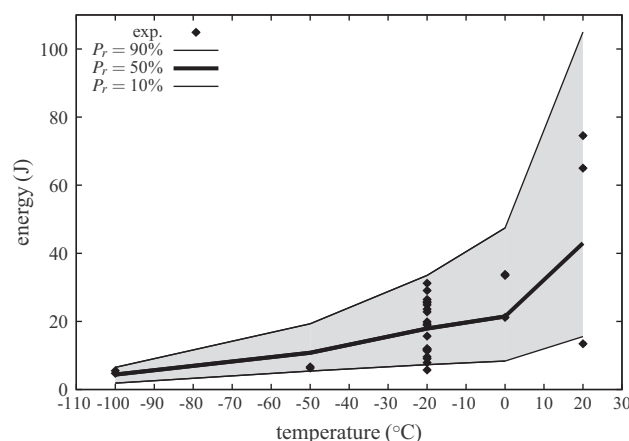

Fig. 7. Prediction of the Charpy transition curve at cleavage initiation assuming a constant value for σ_u for the base state (BS).

coupled ductile damage model as done in some previous work [53]. However, in this study we are focusing on the influence of pre-straining and aging on the lower part of the ductile-to-brittle transition curve.

The parameter σ_u remains constant for all temperatures. The predictions of the model can be improved if a temperature dependence of σ_u is introduced. In this study, the Beremin parameter values are kept constant for all temperatures and all material states in order to highlight the ability of the model to describe the observed phenomena.

3.4. Simulation of the Charpy transition curve for the 5% pre-strained and 5% pre-strained + aged states

The Charpy experiments for the 5% pre-strained state were simulated by changing, in the material model, the initial values of the internal variables, namely the dislocation density ρ and the aging time t_a. The initial values to be prescribed were calculated after simulating a tensile test up to 5% (see [30] for details). They are given as $\rho_{5\%}$ and t_{a0} in Fig. 9 and can be compared to the base state values.

The same approach was applied to the 5% pre-strained + aged state simulation of Charpy impact tests. The initial value of ρ is the same as for the 5% pre-strained state based on the assumption that the aging treatment (30 min at 250 °C) does not modify the dislocation density. This assumption could be reconsidered accounting for the influence of static recovery due to time driven and thermally activated dislocation annihilation. In order to evaluate the impact of the aging treatment at 5% pre-strained on the mechanical behavior and particularly of the aging part of this model related to the internal variable t_a, an original specific experiment was performed. It is presented in Fig. 8.

The strain stress curve denoted "ST" on this figure is a simple tensile experiment from Marais et al. [30] at 20 °C and a prescribed strain rate $1 \cdot e{-}3\,\text{s}^{-1}$. The second curve denoted "ST 0–5%/30 min at 250 °C/ ST 5–10%" is the mechanical response of a specimen made of the same material with slightly different dimensions submitted to the following thermo-mechanical path:

- Simple tension up to 5% of global strain at 20 °C and a prescribed strain rate $1 \cdot e{-}3\,\text{s}^{-1}$.
- Unloading to zero force.
- Aging treatment 30 min at 250 °C.
- Reloading up to 10% of global strain at 20 °C and a prescribed strain rate $1 \cdot e{-}3\,\text{s}^{-1}$.

Both curves slightly differ in the first stage before 5% because of the difference of specimen dimension and experimental scatter. After 5% the aging treatment gives rise to a stress peak and a Lüders plateau. After the Lüders stage, the curve is parallel but not superimposed to the ST curve. This means that the unpinning did not free all dislocations so that the stress level is higher. Note that this feature, although frequent in steels, is not reproduced by the constitutive model of this work. The precise modeling of the amount of unpinning remains an open question from the constitutive modeling point of view. Since the size of the stress peak is close to the initial one, the initial value of t_a for the 5% pre-strained + aged state is then prescribed at each temperature at the same value as for the base state (see Fig. 9).

The numerical procedure of Section 3.3 has been applied to the modified material behaviors presented in Fig. 9. For both states the Charpy experiments were simulated at 6 different temperatures (−150 °C, −100 °C, −50 °C, −20 °C, 0 °C, 20 °C). The Beremin model was applied to evaluate the CVN energy vs. temperature curves for three fracture probability values (10%, 50%, and 90%). The Beremin parameters m and σ_u identified at −20 °C for the base state were kept constant in order to highlight the influence of strain and aging on fracture through the material behavior. The results of this analysis are plotted in Fig. 10. The predictions for both states are in good agreement with the corresponding experimental results since
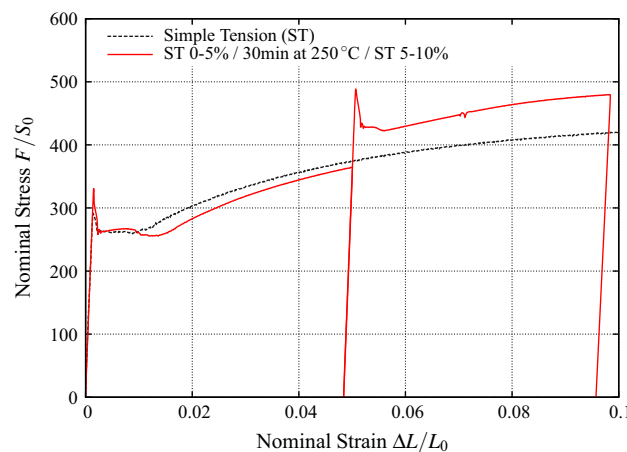
Fig. 8. Comparison between a monotonic simple tensile experiment at 20 °C and a prescribed strain rate $1 \cdot e{-}3\,\text{s}^{-1}$, and the same experiment interrupted at 5% of global strain to carry out an aging treatment of 30 min at 250 °C at zero force. The aging treatment gives rise to a Lüders peak and plateau when the specimen is reloaded.

Initial values	BS	5% pre–strained	5% pre–strained + aged
$\rho_0, \rho_{5\%}$ (m^{-2})	1.e13	1.3e15	1.3e15
t_{a0} (s)	1.6e4	$\simeq 0$	1.6e4
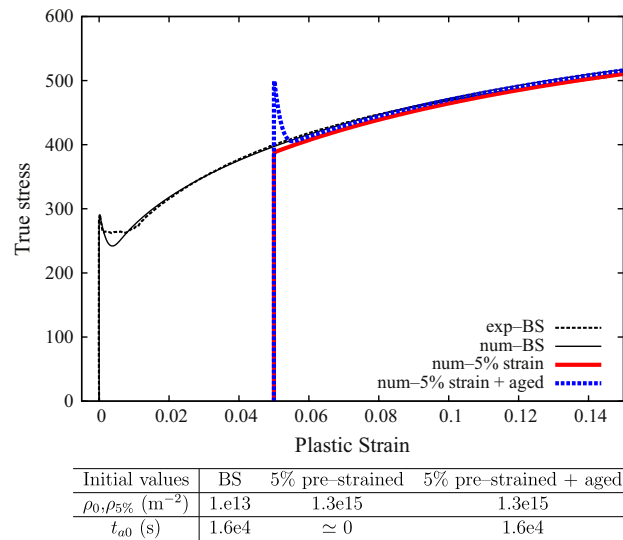
Fig. 9. Initial values of the internal variables for the three material states at 20 °C. ρ_0 controls the level of prestraining while t_{a0} sets the level of dislocation pinning and allows to switch between aged and non-aged states. The stress vs. plastic strain responses of the model on a material point associated with each initial condition are plotted above the table.
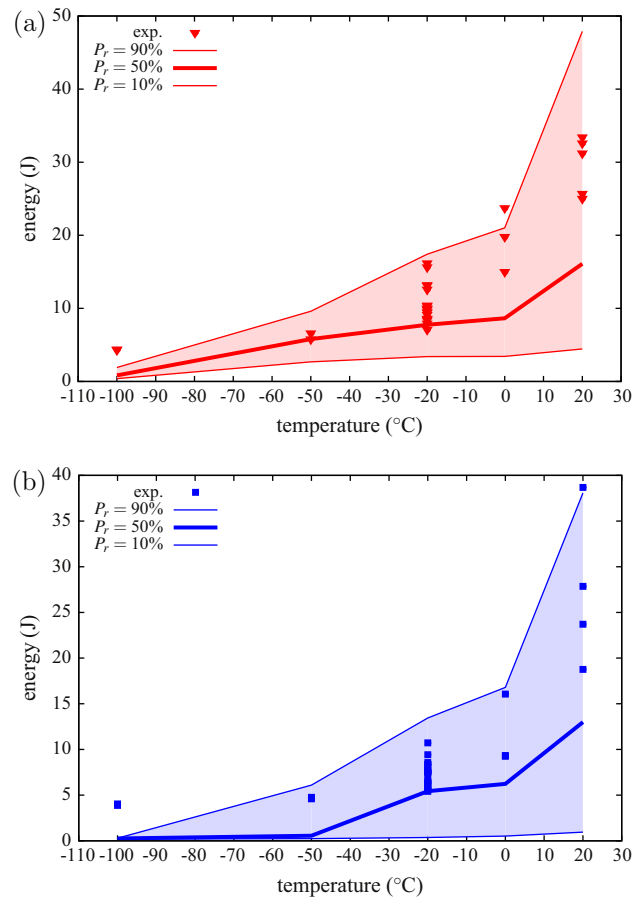
Fig. 10. Prediction of the Charpy transition curve at cleavage initiation assuming a constant value for σ_u: (a) 5% pre-strained material state and (b) 5% pre-strained + aged material state.

almost all experimental points are included inside the 10–90% fracture probability interval, even if most of them are above the 50% fracture probability curve. However, at −100 °C the model turns out to be too conservative since the numerical prediction is half that of the experimental results. Some tensile experiments at −100 °C on specimens pre-strained at 5% and prestrained at 5% + aged should be carried out in order to validate if the hypothesis made for the initial values of ρ_0 and t_{a0} remain valid at this temperature.
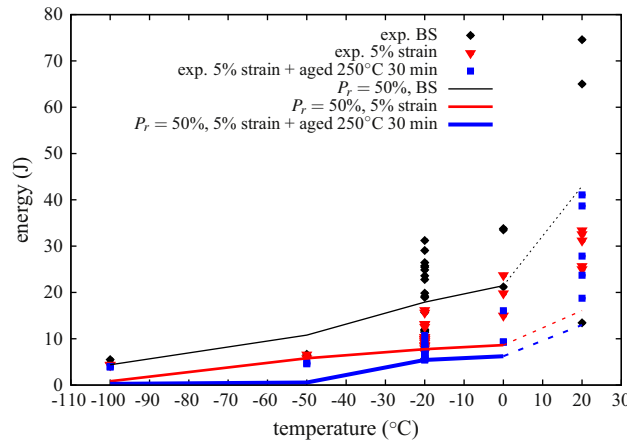
Fig. 11. Prediction of the Charpy transition curve at cleavage initiation assuming a constant value for σ_u for the three different material states, BS, 5% pre-strained and 5% pre-strained + aged material states.

A comparison of the numerically obtained fracture probability for the three states is reported in Fig. 11 that combines all the experimental and simulation results. Only the 50% probability is plotted on the figure for the sake of clarity. A shift of the lower part of the ductile-to-brittle transition is clearly observed between base state and 5% pre-strained state, and to a lesser extent between the 5% pre-strained and 5% pre-strained + aged states. These shifts are in good agreement with the ones experimentally observed in Houssin et al. [28] or in Section 2.3 (see Fig. 3).

Maps of the cumulated plastic strain in finite element simulations of Charpy impact tests at a displacement equal to 0.215 mm for the 5% pre-strained and 5% pre-strained + aged states are plotted in Fig. 12. This value of displacement is located on the force/displacement just beyond the apparent yielding, where the difference between the two curves is most pronounced. It can be seen that the localization phenomenon is much more pronounced for the 5% pre-strained + aged states than for the 5% pre-strained one.

### 3.5. Improved description of the pre-strained material response using kinematic hardening

According to the previous simulations, the mechanical model tends to overestimate the CVN energy compared to experimental results for the 5% pre-strained and 5% pre-strained + aged states. In this section a modification of the mechanical model is proposed in order to improve the prediction of fracture. The main idea is to investigate the effect of local non-proportional loading paths on fracture of the specimen. Indeed, the 5% pre-strained and 5% pre-strained + aged specimens are cut along the transverse direction of the sheet in a bar also pre-strained in this direction. Then just beyond the notch, the loading path remains more or less monotonic (pure tension). However beyond the striker, the loading path switches from pure tension to compression between the prestraining and the Charpy test, and is no longer proportional. In the remainder of the sample, the loading follows most likely some complex paths in the stress space.

If the assumption of a pure isotropic hardening is not verified, it can then lead to inexact results, especially if the plastic zone is large i.e. at the lower end of the ductile-to-brittle transition region. The material model was therefore modified to include kinematic hardening in addition to isotropic hardening. To estimate the balance between kinematic and isotropic hardening parts, two complex uniaxial experiments have been performed on the same type of specimens as the 5% pre-strained-aged–5% pre-strained experiments presented in Fig. 8. The first specimen was loaded at 20 °C at a prescribed strain rate of 10^{-3} s^{-1} in tension up to 5%. Then the sample was deformed in compression at the same strain rate to bring the global strain back to zero. The second specimen underwent the same cycle at 20 °C except that it was subjected to an ageing time of 30 min at 250 °C at zero force between the tensile and compression sequences. The stress vs. strain curve of these two experiments are plotted respectively in Fig. 13(a) and (b) together with the associated initial (purely isotropic hardening) and modified (combined isotropic/kinematic hardening) model responses. The experimental result of Fig. 13(a) clearly shows the strong Bauschinger effect exhibited by the material.

A kinematic hardening stress $\underset{\sim}{\boldsymbol{X}}$ is introduced in the yield function of the initial model, associated with the hardening internal variable $\underset{\sim}{\boldsymbol{\alpha}}$ (for more details see [14]):

$$f(\underset{\sim}{\boldsymbol{\sigma}}, \underset{\sim}{\boldsymbol{X}}) = J_2(\underset{\sim}{\boldsymbol{\sigma}} - \underset{\sim}{\boldsymbol{X}}) - R(\rho) - R_a(t_a) \tag{12}$$

$$\underset{\sim}{\boldsymbol{X}} = \frac{2}{3} C \underset{\sim}{\boldsymbol{\alpha}} \tag{13}$$

$$\dot{\underset{\sim}{\boldsymbol{\alpha}}} = \dot{\underset{\sim}{\boldsymbol{\varepsilon}}}_p - D\dot{p}\underset{\sim}{\boldsymbol{\alpha}} = \left(\underset{\sim}{\boldsymbol{n}} - D\underset{\sim}{\boldsymbol{\alpha}}\right)\dot{p} \tag{14}$$
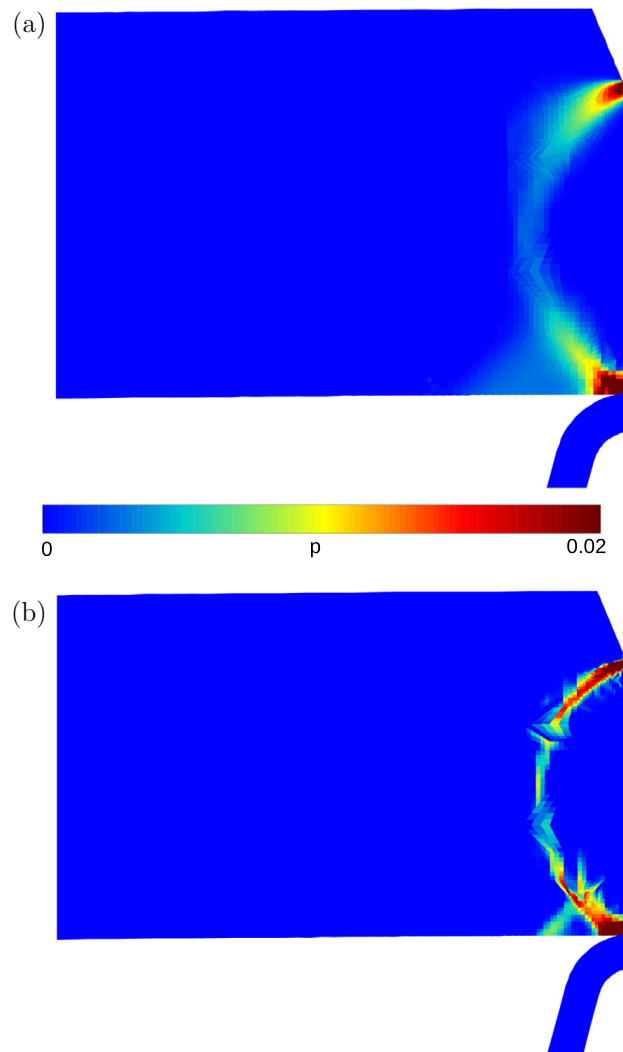
Fig. 12. Cumulated plastic strain for a displacement of 0.215 mm. (a) 5% pre-strained state and (b) 5% pre-strained + aged state.

The parameters C and D were identified from the experimental curve of Fig. 13(a) together with a modification of the parameters A and B to balance the isotropic hardening contribution with the kinematic one. The parameter σ_0 has also been modified in order to reproduce at least partially the Bauschinger effect experimentally observed. Finally the parameter P_1 is modified to correctly describe the level of the initial stress peak (for more details on the role of σ_0 and P_1 on the stress peak modeling, the interested reader should refer to Marais et al. [30]). The initial and modified values for all these parameters are given in Table 5.

It can be seen from Fig. 13(a) that the purely isotropic model fails at describing the reverse path, while using the modified one improves the description of the compressive part. The second experiment presented in Fig. 13(b) reveals another striking phenomenon already investigated in some Refs. [17,46] with dissimilar results: the existence of the Lüders stress peak and plateau after aging at zero force and reversal of the applied stress. This experiment has been repeated twice under the same conditions with very similar results. The results of Fig. 13(b) show that tension followed by aging at zero force and compression leads to a stress peak in the compression regime with a stress drop amplitude comparable to the one observed in the first tension. The strong Bauschinger effect and the higher final stress level are also observed for this loading sequence. Neither the initial model nor the modified one are able to accurately describe the reverse path for this experiment because of the overstress due to partial unpinning already observed in Fig. 8. However in order to remain consistent with the rest of the study, the modified model is used to investigate the effect of kinematic hardening introduction on prediction of the fracture of Charpy specimens.

The influence of the introduction of kinematic hardening on fracture of Charpy specimens was investigated at 20 °C, since the reverse tensile experiments were only carried out at this temperature. Five Charpy specimens were tested at 20 °C for the 5% pre-strained and the 5% pre-strained + aged states. Following the approach proposed in part Section 3.2 at the temperature of −20 °C at which fracture stress scatter was studied, the smallest CVN energy experimental values are associated with a fracture probability equal to 16.7% $(1/(1+5))$. These experimental values are compared in Table 6 with the corresponding numerical predictions provided by the initial and modified models for both states.
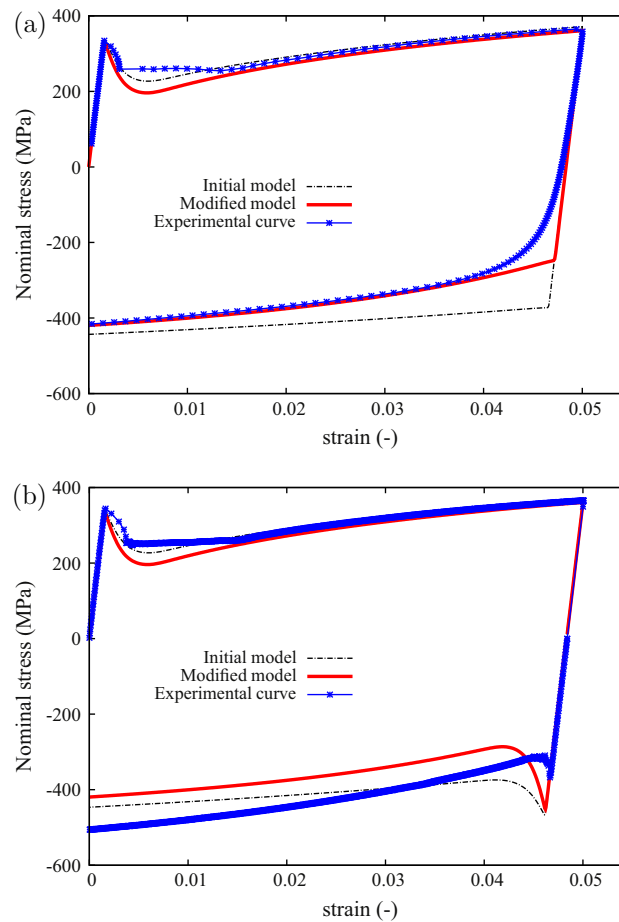
Fig. 13. (a) 5% tension–5% compression and (b) 5% tension–30 min at 250 °C–5% compression experiments at 20 °C and a prescribed strain rate of $1 \cdot e-3 \, s^{-1}$. Comparison between the stress–strain curves generated using the initial and modified models.

Table 5
Modified and initial sets of parameters at 20 °C for non-linear isotropic and kinematic hardening.

	Modified model	Initial model
A (m^{-2})	2.15e16	3.086e16
B (m^{-2})	4.80e15	5.115e15
σ_0 (MPa)	55	130
C (MPa)	3140	×
D	49.5	×
P_1 (MPa)	350	183.2

Table 6
Experimental (5% pre-strained state, 20 °C) and numerical CVN energies for a fracture probability equal to 16.6%.

	Initial model (J)	Modified model (J)	Experimental value (J)
5% pre-strained	6.7	19.4	25
5% pre-strained + aged	4.9	5.7	18.7

As it was already observed in the previous part, the initial model tends to underestimate the CVN energies for both states. The modified model prediction for the 5% pre-strained state is more accurate by increasing the CVN energy close to the experimental value, even though at this temperature the ductile failure propagation should also be accounted for in addition to the brittle failure model. Nevertheless, at this temperature and for this state the average ductile fracture surface fraction measured on the five specimens does not exceed 35%. The brittle fracture is then still the prevailing mode. The estimation of CVN energy is significantly modified by the introduction of the kinematic hardening term. Kinematic hardening tends to "weaken" the area located close to the striker. By a structural effect, this "softening" will modify (i) the stress field beyond

the notch, (ii) the global force vs. displacement evolution; which will both be lower than using the initial model. Both effects lead to a significant increase of the predicted CVN energies given by the Beremin model.

The modified model prediction for the 5% pre-strained + aged state is less affected by the introduction of the kinematic term. Indeed the plastic zone is smaller than for the 5% pre-strained and consequently the "softening" in the area located close to the striker is less pronounced. The inclusion of kinematic hardening is then important in the prediction of accurate CVN at the lower end of the ductile-to-brittle transition region (5% pre-strained state) but less important in the very beginning of this transition (5% pre-strained + aged state).

4. Discussion and conclusion

A good agreement was found between the predicted ductile-to-brittle transition curve for the pre-strained and aged material state showing the interest of using a constitutive model including strain aging effects. The advantage of the approach is that the optimal magnitude of pre-straining and duration of heat treatments can be determined computationally in a systematic way. Zhang and McCormick's model turns out to be a simple and efficient approach to the constitutive modeling of strain aging, even though several limitations have been evidenced. In particular, the current knowledge on diffusion of solute atoms in steels in relation to dislocation densities, as discussed in Ballarin et al. [4], should be incorporated in the model to allow for a reliable simulation of heat treatments. The experimental results provided in this work confirm that the freeing of dislocations at obstacles at the yield point is generally not complete so that the stress drop remains a quantity that is difficult to predict. The model used in this work invariably leads to complete release of dislocation and maximum stress drop. Improvements require a detailed account of dislocation populations evolution in the model, like a separation into forest and mobile dislocation densities as done by Fressengeas et al. [19].

This work must be followed by efforts to address the ductile part of the ductile-to-brittle transition curve. Such an attempt can be found in Berdin and Wang [9] for uncoupled ductile damage models. Existing fully coupled ductile fracture models like Gurson and Rousselier potentials should be combined with the strain aging model by introducing the relevant internal variable t_a [50]. FE simulations of ductile tearing are usually associated with mesh dependence that can be overcome by the introduction of intrinsic length scales in the continuum model. The use of strain gradient plasticity in the context of Lüders band formation and propagation was recently examined by Mazière and Forest [33], following initial ideas by Hähner [22].

The main contributions of the present work are the following:

1. The first FE simulations of a Charpy test involving a strain aging elastoviscoplastic model were reported in this work.
2. The Beremin fracture model was identified for a nuclear C–Mn steel from a large set of experimental data including the scatter distribution at $-20\,°C$ for the base material state.
3. The prediction of the ductile-to-brittle transition curve was then possible for the pre-strained material and pre-strained and aged material states. Aging was shown to be associated with a translation of the ductile-to-brittle transition temperature towards higher temperatures.
4. The importance of kinematic hardening for an improved description of the pre-strained material's behavior was pointed out, leading to a better prediction of CVN energy at the lower end of the ductile-to-brittle transition region.
5. The existence of a Lüders peak and plateau after tension followed by unloading, aging and reverse loading was evidenced experimentally for the considered C–Mn steel.

Acknowledgements

References

[1] Amar E, Pineau A. Interpretation of ductile fracture-toughness temperature-dependence of a low strength steel in terms of a local approach. Engng Fract Mech 1985;22(6):1061–71.
[2] Andrieu A, Pineau A, Besson J, Ryckelynck D, Bouaziz O. Beremin model: methodology and application to the prediction of the euro toughness data set. Engng Fract Mech 2012;95:102–17.
[3] Ballarin V, Perlade A, Lemoine X, Bouaziz O, Forest S. Mechanisms and modeling of bake-hardening steels: Part II. Complex loading paths. Metall Mater Trans A 2009;40:1375–84.
[4] Ballarin V, Soler M, Perlade A, Lemoine X, Forest S. Mechanisms and modeling of bake-hardening steels: Part I. Uniaxial tension. Metall Mater Trans A 2009;40:1367–74.
[5] Belotteau J, Berdin C, Forest S, Parrot A, Prioul C. Mechanical behavior and crack tip plasticity of strain aging sensitive steel. Mater Sci Engng A 2009;526:156–65.
[6] Benallal A. Perturbation and stability of rate-dependent solids. Eur J Mech A/Solids 2000;19:S45–60.
[7] Benallal A, Berstad T, Borvik T, Clausen A, Hopperstad S. Dynamic strain aging and related instabilities: experimental, theoretical and numerical aspects. Eur J Mech A/Solids 2006;25:397–424.
[8] Benallal A, Borvik T, Clausen A, Hopperstad O. Dynamic strain aging, negative strain-rate sensitivity and related instabilities. Tech Mech 2003;23:160–6.
[9] Berdin C, Wang H. Local approach to ductile fracture and dynamic strain aging. Int J Fract 2013;182:39–51.

[10] Beremin F. Cavity formation from inclusions in ductile fracture of A508 steel. Metall Mater Trans 1981;12(5):723–31.
[11] Beremin FM. A local criterion for cleavage fracture of a nuclear pressure vessel steel. Metall Trans A 1983;14:2277–87.
[12] Bertram A. Elasticity and plasticity of large deformations. Springer; 2005.
[13] Besson J. Local approach to fracture. Ecole des Mines de Paris–Les Presses; 2004.
[14] Besson J, Cailletaud G, Chaboche J-L, Forest S. Non linear mechanics of materials. Springer; 2009.
[15] Bordet S, Tanguy B, Besson J, Bugat S, Moinereau D, Pineau A. Cleavage fracture of RPV steel following warm pre-stressing: micromechanical analysis and interpretation through a new model. Fatigue Fract Engng Mater Struct 2006;29:799–816.
[16] Cottrell AH, Bilby BA. Dislocation theory of yielding and strain ageing of iron. Proc Phys Soc 1949;A62(1):49–62.
[17] Elliot RA, Orowan E, Udoguchi T, Argon AS. Absence of yield points in iron on strain reversal after aging, and the Bauschinger overshoot. Mech Mater 2004;36:1143–53.
[18] François F, Pineau A, Zaoui A. Mechanical behaviour of materials. Fracture mechanics and damage. Solid mechanics and its applications, vol. 191. Springer; 2013.
[19] Fressengeas C, Beaudoin A, Lebyodkin M, Kubin L, Estrin Y. Dynamic strain aging: a coupled dislocation-solute dynamic model. Mater Sci Engng 2005;A400:226–30.
[20] Graff S, Forest S, Strudel JL, Prioul C, Pilvin P, Béchade JL. Strain localization phenomena associated with static and dynamic strain ageing in notched specimens: experiments and finite element simulations. Mater Sci Engng A 2004:181–5.
[21] Graff S, Forest S, Strudel J-L, Prioul C, Pilvin P, Béchade J-L. Finite element simulations of dynamic strain ageing effects at V-notches and crack tips. Scr Mater 2005;52:1181–6.
[22] Hähner P. Modelling the spatio-temporal aspects of the Portevin–Le Chatelier effet. Mater Sci Engng A 1993;164:23–34.
[23] Hallai J, Kyriakides S. On the effect of Lüders bands on the bending of steel tubes. Part I: Experiments. Int J Solids Struct 2011;48:3275–84.
[24] Hallai J, Kyriakides S. On the effect of Lüders bands on the bending of steel tubes. Part II: Analysis. Int J Solids Struct 2011;48:3285–98.
[25] Hallai J, Kyriakides S. Underlying material response for Lüders-like instabilities. Int J Plast 2013;47:1–12.
[26] Haušild P, Berdin C, Bompard P. Prediction of cleavage fracture for a low-alloy steel in the ductile-to-brittle transition temperature range. Mater Sci Engng A 2005;391:188–97.
[27] Haušild P, Nedbal I, Berdin C, Prioul C. The influence of ductile tearing on fracture energy in the ductile-to-brittle transition temperature range. Mater Sci Engng 2002;A335:164–74.
[28] Houssin B, Slama G, Moulin P. In: Steele LE, Stahlkopf KE, editors. Assuring structural integrity of steel reactor pressure vessels. London: Applied Science Publishers; 1980. p. 57.
[29] Kubin LP, Estrin Y. The Portevin–Le Chatelier effect in deformation with constant stress rate. Acta Metall 1985;33:397–407.
[30] Marais A, Mazière M, Forest S, Parrot A, Le Delliou P. Identification of a strain-aging model accounting for Lüders behavior in a C-Mn steel. Philos Mag 2012;92(28–30):3589–617.
[31] Mazière M, Besson J, Forest S, Tanguy B, Chalons H, Vogel F. Numerical aspects in the finite element simulation of the Portevin–Le Chatelier effect. Comput Methods Appl Mech Engng 2010;199:734–54.
[32] Mazière M, Dierke H. Investigations on the Portevin Le Chatelier critical strain in an aluminum alloy. Comput Mater Sci 2012;52(1):68–72.
[33] Mazière M, Forest S. Strain gradient plasticity modeling and finite element simulation of Lüders band formation and propagation. Continuum Mech Thermodyn 2015;27(1–2):83–104.
[34] McCormick P. Theory of flow localization due to dynamic strain ageing. Acta Metall 1988;36:3061–7.
[35] Mesarovic S. Dynamic strain aging and plastic instabilities. J Mech Phys Solids 1995;43:671–700.
[36] Mudry F. Etude de la rupture ductile et de la rupture par clivage d'aciers faiblement alliés. PhD thesis, Université de Technologie de Compiègne; 1982.
[37] Mudry F. A local approach to cleavage fracture. Nucl Engng Des 1987;105:65–76.
[38] Oldfield W. Curve fitting impact test data: a statistical procedure. ASTM Stand News 1975:24–9.
[39] Pardoen T, Pineau A. Comprehensive structural integrity. In: Milne I, Ritchie RO, Karihaloo B, editors. Failure mechanisms of metals, vol. 2. Elsevier; 2007. p. 684–797 [chapter 6].
[40] Pineau A. Modeling ductile to brittle fracture transition in steels—micromechanical and physical challenges. Int J Fract 2008;150:129–56.
[41] Pineau A, Tanguy B. Advances in cleavage fracture modelling in steels: micromechanical, numerical and multiscale aspects. CR Phys 2010;11:316–25.
[42] Rittel D, Tanguy B, Pineau A, Thomas T. Impact fracture of a ferritic steel in the lower shelf regime. Int J Fract 2002;117:101–12.
[43] Rossoll A, Berdin C, Forget P, Prioul C, Marini B. Mechanical aspects of the Charpy impact test. Nucl Engng Des 1999;188:217–29.
[44] Rossoll A, Berdin C, Prioul C. Determination of the fracture toughness of a low alloy steel by instrumented Charpy impact test. Int J Fract 2002;115:205–26.
[45] Rossoll A, Tahar M, Berdin C, Piques R, Forget P, Prioul C, et al. Local approach of the Charpy test at low temperature. J Phys IV 1996;6:279–86 [EUROMECH – MECAMAT 96/1st European mechanics of materials conference on local approach to fracture 86–96, Fontainebleau, France, September 09–11, 1996].
[46] Saada G, Kruml T. Removal of plastic instabilities by reversal of the applied stress. Philos Mag 2012;93(1-3, SI):256–71.
[47] Shterenlikht A, Howard IC. The CAFE model of fracture – application to a TMCR steel. Fatigue Fract Engng Mater Struct 2006;29(9–10):770–87.
[48] Sidoroff F, Dogui A. Some issues about anisotropic elastic–plastic models at finite strain. Int J Solids Struct 2001;38:9569–78.
[49] Strnadel B, Hausild P. Statistical scatter in the fracture toughness and Charpy impact energy of pearlitic steel. Mater Sci Engng A-Struct Mater Prop Microstruct Process 2008;486(1–2):208–14.
[50] Tanguy B, Besson J. An extension of the Rousselier model to viscoplastic temperature dependent materials. Int J Fract 2002;116:81–101.
[51] Tanguy B, Besson J, Pineau A. Comment on "Effect of carbide distribution on the fracture toughness in the transition temperature region of an SA 508 steel". Scr Mater 2003;49:191–7.
[52] Tanguy B, Besson J, Piques R, Pineau A. Ductile–brittle transition of a A508 steel characterized by the Charpy impact test. Part-I: Experimental results. Engng Fract Mech 2005;72:49–72.
[53] Tanguy B, Besson J, Piques R, Pineau A. Ductile–brittle transition of a A508 steel characterized by the Charpy impact test. Part-II: Modelling of the Charpy transition curve. Engng Fract Mech 2005;72:413–34.
[54] Van den Beukel A. Theory of the effect of dynamic strain aging on mechanical properties. Phys Status Solidi a 1975;30:197.
[55] Wagner D, Moreno J, Prioul C. Influence of post weld heat treatment on the dynamic strain aging of C–Mn steels. J Phys IV 1996;6:159–62.
[56] Wagner D, Moreno J, Prioul C. Dynamic strain aging sensitivity of heat affected zones in C–Mn steels. J Nucl Mater 1998;252:257–65.
[57] Wagner D, Moreno J, Prioul C, Frund J, Houssin B. Influence of dynamic strain aging on the ductile tearing of C–Mn steels: modelling by a local approach method. J Nucl Mater 2002;300:178–91.
[58] Wang H, Berdin C, Mazière M, Forest S, Prioul C, Parrot A, et al. Portevin–Le Chatelier (PLC) instabilities and slant fracture in C–Mn steel round tensile specimens. Scr Mater 2011;64:430–3.
[59] Wang H, Berdin C, Mazière M, Forest S, Prioul C, Parrot A, et al. Experimental and numerical study of dynamic strain ageing and its relation to ductile fracture of a C–Mn steel. Mater Sci Engng A 2012;547:19–31.
[60] Wenman M. Fitting small data sets in the lower ductile-to-brittle transition region and lower shelf of ferritic steels. Engng Fract Mech 2013;98:350–64.
[61] Wenman MR, Chard-Tuckey PR. Modelling and experimental characterisation of the Lüders strain in complex loaded ferritic steel compact tension specimens. Int J Plast 2010;26:1013–28.
[62] Z-set package. Non-linear material & structure analysis suite; 2013. <www.zset-software.com>.
[63] Zhang S, McCormick P, Estrin Y. The morphology of Portevin–Le Chatelier bands: finite element simulation for Al–Mg–Si. Acta Mater 2001;49:1087–94.

5.2 DSA and ductile failure of C-Mn steels
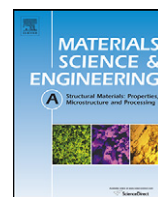
Experimental and numerical study of dynamic strain ageing and its relation to ductile fracture of a C–Mn steel

H.D. Wang [a,b], C. Berdin [a,c,*], M. Mazière [d], S. Forest [d], C. Prioul [a], A. Parrot [b], P. Le-Delliou [b]

[a] Laboratoire de Mécanique Sols, Structures et Matériaux, CNRS UMR 8579, Grande Voie des Vignes, 92290 Châtenay-Malabry, France
[b] Electricité de France, R&D Division, Département MMC, Les Renardières, 77818 Moret-sur-Loing, France
[c] University Paris-Sud 11, ICMMO/LEMHE CNRS UMR 8182, 91400 Orsay, France
[d] Centre des Matériaux, Mines ParisTech, CNRS UMR 7633, BP 87, F-91003 Evry cedex, France

ARTICLE INFO

ABSTRACT

Ductile fracture of a C–Mn steel was characterized by tensile tests performed in a large temperature range (from 20 to 350 °C) on round notched and CT specimens. The experimental results revealed a sharp decrease in fracture strain and fracture toughness around 200 °C. These temperatures correspond to the domain of dynamic strain ageing (DSA). The Portevin-Le Chatelier (PLC) effect, which is the most classical manifestation of DSA, was simulated for round notched and CT specimens with a mechanical constitutive model which includes the strain ageing effect and the stiffness of the testing machine. It is shown that changes in stiffness can amplify the DSA effect. 3D-Modeling was used to correctly capture the complex space-time correlation of strain localization, particularly in side-grooved CT specimens. The results were compared to classical elastic–plastic simulations. The local approach to fracture was then applied to predict the ductile fracture of round notched specimens using the Rice and Tracey criterion. In the DSA domain, the approach used in this study predicts a decrease of the fracture strain which is less than observed experimentally.

1. Introduction

The dynamic strain ageing (DSA) effect can occur in many metal alloys. This phenomenon is due to the interaction between solute atoms and mobile dislocations [1,2] during straining. DSA reduces the strain rate sensitivity of the flow stress and induces a jerky flow when the strain rate sensitivity becomes negative [3]. In such a case, strain localizes into narrow bands inducing stress drops on the overall stress–strain curve [4,5] usually referred to as "serrations". This phenomenon is called the "Portevin-Le Chatelier (PLC)" effect. Dynamic strain ageing occurs for temperatures and strain rates within a certain range, and in some cases a critical strain level has to be reached for serrated yielding to take place [3,6].

Dynamic strain ageing and the PLC effect have been the subjects of numerous experimental and theoretical studies. In the past decade, numerical modeling with the finite element (FE) method has also been used to investigate the PLC effect and related phenomena. These studies have been aimed at representing the spatio-temporal evolution of the local mechanical variables using

appropriate constitutive laws. McCormick and Ling [7] proposed a model derived from the approach proposed by McCormick [6], Estrin and McCormick [8] and McCormick and Estrin [9] to simulate the PLC effect. Typical characteristics of the PLC effect, such as PLC instabilities and critical plastic strain, were correctly predicted with this model. Zhang et al. [10] adapted the McCormick and Ling [7] model, an elasto-viscoplastic constitutive law accounting for DSA through a new internal variable, the ageing time t_a and a hardening term. The morphology of PLC bands in Al–Mg–Si alloys was then studied via FE analysis using this model. Kok et al. [11,12] used a polycrystal plasticity model embedded in a FE framework to study the PLC effect in constant cross head velocity controlled tension tests. These authors used a constitutive law based on the Zhang et al. [10] model and introduced the model into a law of crystalline plasticity. Graff et al. [13,14] reformulated the constitutive model of Zhang et al. [10] through the introduction of a thermally activated elasto-viscoplastic law. This formulation was used by Belotteau et al. [15] to predict strain ageing (both static and dynamic) of a C–Mn steel over a large range of temperatures and strain rates. Mazière et al. [16] used the same constitutive model to simulate round smooth and notched specimens of a Ni based superalloy. Benallal et al. [17] used a phenomenological elastic–viscoplastic model based on [1] to study the PLC effect in tension tests with smooth axisymmetric specimens at different strain rates and with U-notched axisymmetric specimens. The experimental results,

* Corresponding author at: Université Paris-Sud 11, ICMMO/LEMHE CNRS UMR 8182, bat 410, 91405 Orsay cedex, France. Tel.: +33 1 69 15 31 97; fax: +33 1 69 15 48 19.
    E-mail address: clotilde.berdin@u-psud.fr (C. Berdin).

presented in a previous paper [18], were correctly predicted by the approach proposed in [17]. For example, the authors used different strain hardening laws for different strain rates to simulate negative strain rate sensitivity and were able to predict strain localization bands (PLC bands) using this model. Hopperstad et al. [19] used an anisotropic elastic–viscoplastic model including the McCormick model [6,10,20] for DSA. One can find an exhaustive critical review of existing numerical models which predict DSA and PLC effects in Rizzi and Hahner [21]. In addition, PLC effects in notched and cracked specimens were numerically investigated by Graff et al. [13,14] and Belotteau et al. [15] with 2D models. Recently, a 3D model of a notched CT specimen was used to study the strain localization stemming from static ageing including residual stress and plastic strain obtained by preloading in compression [22].

DSA is characterized by an increase in flow stress and ultimate tensile strength but also by a drop in fracture toughness [15,23–25]. However, Srinivas et al. [26,27] found the opposite effect of DSA on fracture toughness in a pure Armco Iron. The authors attributed this behavior to the absence of inclusions in pure iron which modifies the underlying ductile fracture mechanisms in the presence of DSA. Carbon–manganese steels, used for the secondary systems (feed water line and steam line) of nuclear pressurized water reactors, are sensitive to DSA at in-service temperatures (around 200 °C) [15,24]. Therefore, the design of these components requires the prediction of fracture toughness of these steels in the presence of DSA.

Amar and Pineau [28] and Wagner et al. [24] modelled the ductile fracture of such C–Mn steels in the presence of DSA. They used an elastic–plastic constitutive law ignoring the DSA effect. To predict the drop in fracture toughness, they applied the Rice and Tracey criterion [29]. So, a critical void growth ratio was identified at each temperature on notched tensile tests results. The results showed a variation in critical void growth ratio, which, however, was not evidenced on fracture surface [24]. Indeed, DSA can modify the local mechanical variables, especially when strain rate sensitivity is negative: strain localizations occur even in notched specimens that could induce a modification of the damage kinetics rather than a modification of the critical value.

Thus, the objective of the present study is to model the mechanical behaviour with an elasto-viscoplastic constitutive law which accounts for DSA and to predict, using a local approach, the fracture of a C–Mn steel in the DSA domain particularly at 200 °C. Consequently, the tensile behaviour is studied and modeled using a model derived from Kubin, McCormick, Estrin's works [3,6]. The fracture behavior of one C–Mn steel is characterized using notched tensile and precracked tests. Finite element simulations of fracture tests are performed taking DSA into account. These simulations are carried out in 2D but also in full 3D. Finally, the Rice and Tracey [29] criterion is applied to predict the fracture in the presence of DSA.

2. Experimental tests

2.1. Tensile tests

The material studied is a carbon manganese steel which was used by Belotteau et al. [15]. Mechanical behavior of the material was characterized by fourteen tensile tests performed on round tensile specimens (36 mm gage length, 6 mm diameter) at seven temperatures over the temperature range (20–350 °C) and at two strain rates: $10^{-2} s^{-1}$ and $10^{-4} s^{-1}$. Additional tests at two other strain rates were performed: $10^{-3} s^{-1}$ and $10^{-5} s^{-1}$ in order to improve the accuracy of the constitutive model [30] presented below. The PLC effect occurred in the temperature range of 150–300 °C, depending on the strain rate. Table 1 shows the per cent uniform elongation (A_u) for round tensile specimens tested at one of the prescribed strain rates ($10^{-3} s^{-1}$) for different temperatures.
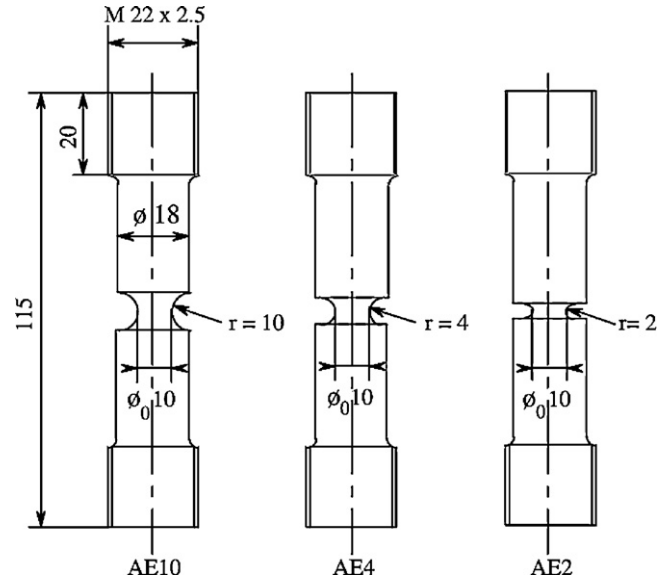
Fig. 1. Round notched specimens (all dimensions are in mm).

There is a minimum in the uniform elongation around 200 °C. The decrease of ductility is correlated with DSA [15,23–25]. The uniform elongation was a minimum at 200 °C for the strain rate of $10^{-4} s^{-1}$ and at 250 °C for the strain rate of $10^{-2} s^{-1}$ [15]. This behavior is expected since the DSA temperature domain depends on the strain rates; the DSA temperature domain moves to higher temperatures if strain rates increase and vice versa [31].

According to Kang et al. [32], PLC bands provide an additional local strain that enables the Considère condition to be reached locally before it is reached over the whole specimen. This may explain the reduced ductility of tensile specimens in the DSA temperature domain. Indeed, Hosford and Caddell [33] showed that in uniaxial tension, the cross-section inhomogeneity has an important influence on the necking strain. A PLC band may contain 1.4% plastic strain [34] which creates a local cross-section inhomogeneity thus reducing the necking strain. Wang et al. [30] predicted necking within a PLC band on round smooth specimens. Fracture under tension is thus essentially a strain localization problem, because ductile damage occurs after necking. So, tensile elongation does not depend on usual ductile fracture mechanisms. Fracture tests with stress triaxiality ratio promoting ductile damage were then conducted.

2.2. Fracture tests

Tests on round notched specimens were carried out over the same temperature range. The minimum diameter Φ_0 in the notch section was 10 mm for all samples, but the root notch radius r varied from 2 mm (AE2), 4 mm (AE4) and up to 10 mm (AE10) (Fig. 1). Thus, the stress triaxiality ratio, important for ductile fracture, varies between 0.8 and 1.2. To obtain the PLC effect in these tests, strain rates in the range of 10^{-4}-$10^{-3} s^{-1}$ have to be reached in the minimum cross-section. Preliminary FE computations allowed us to calculate the crosshead velocity of the testing machine to obtain these strain rates.

During the tensile tests, the variations of the load P versus diameter Φ, measured at the minimum section, were recorded. From these values, the mean stress $\bar{\sigma} = 4P/\pi\Phi_0^2$ and the mean strain $\bar{\varepsilon} = 2 \ln(\Phi_0/\Phi)$ were calculated. The mean stress and strain at failure ($\bar{\sigma}_R$ and $\bar{\varepsilon}_R$ respectively) were determined ($\bar{\sigma}_R$ from final diameter Φ_R measured on broken specimens). The results showed that at 200 °C, the PLC effect occurred in the form of serrations

Table 1
Uniform elongation (Au) for round smooth specimens tested at 10^{-3} s^{-1}.

Temperature (°C)	20	100	150	200	250	300	350
Au (%)	20	19.8	19.5	11.8	14.1	15.1	16.1

on the global curve: so, jerky flow behavior is observed not only on smooth tensile specimens, but also on notched specimens. At 200 °C, jerky flow is observed for all geometries.

Table 2 shows the fracture strain $\bar{\varepsilon}_R$ variation with temperature for specimens AE2, AE4 and AE10 and a sharp drop of the fracture strain $\bar{\varepsilon}_R$ is seen in contrast to the usual case, in which the fracture strain is expected to increase with temperature as seen for temperatures above 250 °C.

Tearing tests on CT specimens were carried out over the same temperature range as for the round notched specimens. The specimens used are side-grooved CT25 with an over-all thickness of 25 mm and a reduced thickness of 20 mm at the side grooves. The specimens were fatigue pre-cracked for 1,330,000 cycles at a maximum load of 14,000 N to a pre-crack length of 5 mm corresponding to an over-all initial crack length of 30 mm. At the end of fatigue pre-cracking, the stress intensity factor was $K_I = 20$ MPa$\sqrt{m}$. To calculate the tearing resistance, the specimen unloading compliance method was applied: crack growth was estimated from the unloading compliance at various crack opening displacements (COD). The compliance was calculated assuming a straight crack front under plane strain constraint. The tests were conducted at a prescribed crack opening displacement rate of 0.4 mm/min using a crack clip gauge and stopped when the COD reached 5 mm.

Fig. 2 shows the resistance to ductile fracture for CT specimens as a function of temperature. There was a sharp drop of the initiation fracture toughness, $J_{0.2}$ and of the tearing modulus, dJ/da between 150 and 250 °C due to the DSA effect, as was also observed by Amar and Pineau [28] and Wagner et al. [24] on other C–Mn steels. The reductions of the fracture toughness and tearing modulus from 20 °C to 200 °C were about 60%. Finally, experimental results from notched tensile and CT specimens obtained by Wagner et al. [24] were in agreement with the present results except that the ductility and fracture toughness of the current C–Mn steel was higher.

2.3. Fractographic analysis

To understand the mechanisms of fracture in the presence of DSA, fractographic analyses by SEM (Scanning Electron Microscopy) of broken specimens were carried out. On the fracture surface of AE specimen, no special dimple features were found

Fig. 2. Evolution of the toughness for CT specimens.

either in the absence or presence of the PLC effect in agreement with Wagner et al. [24] and Bréchet and Louchet [35]. Other authors [28,36,37] have reported shallower dimples associated with DSA, but these observations were not quantified.

Fig. 3 shows the fractographic analysis on the surfaces of the CT specimens tested at 20 °C (without DSA) and 200 °C (with DSA). The voids are rather spherical and regular with different sizes. The smaller voids were attributed to carbide fracture in pearlite whereas the larger ones were related to the MnS inclusions. Special local flat regions (Fig. 3b) were seen on the specimen fractured at 200 °C: these regions appear to be sheared. However, these areas were rare and not representative of the global fracture surface of the specimen tested at 200 °C. Similar flat regions were also seen by Gupta et al. [38]. These regions could be due to the presence of strain localizations at the crack tip associated to the PLC effect, or to small unstable crack extensions due to local softening as reported by Marshall et al. [39]. However, these infrequent features do not explain the relationship between the DSA effect and the loss of toughness. Mechanical modeling of strain localization was carried out in order to gain further insight into the relationship between DSA and ductile fracture as described below.

3. Numerical modeling

3.1. Constitutive model

In order to model the PLC phenomenon, the KEMC (Kubin–Estrin–McCormick) strain ageing model was invoked. This model incorporates elasto-viscoplastic behavior and thermal activation and was derived from earlier models proposed by Kubin and Estrin [3] and McCormick [6]; it allows the prediction of both types of strain ageing: static strain ageing (SSA) (Lüders effect) and DSA (PLC effect). It was first proposed by Zhang et al. [10] and adapted by Graff et al. [13]. The yield function f is based on the von Mises criterion with isotropic hardening:

$$f(\underset{\sim}{\sigma}, R, R_a) = J_2(\underset{\sim}{\sigma}) - R - R_a$$
$$R(p) = Q(1 - \exp(-bp)) + Hp \tag{1}$$

where Q, b, H are the strain hardening parameters and p is the cumulative equivalent plastic strain. The term $J_2(\underset{\sim}{\sigma})$ represents the second invariant of the deviatoric stress tensor and R is the isotropic strain hardening. Of particular interest in the KEMC model is the introduction of the term R_a which represents the overhardening due to strain ageing:

$$R_a(t_a, p) = P_1 C_s(t_a, p) \tag{2}$$

where C_s defines the relative concentration of solute atoms pinning the mobile dislocations. The parameter P_1 represents the maximal stress drop magnitude from a fully pinned state to a fully unpinned state. The solute atoms concentration depends on the ageing time t_a where higher values of t_a induce stronger overhardening. The variable p is the cumulative equivalent plastic strain:

$$\dot{p} = \sqrt{\frac{2}{3}\dot{\varepsilon}^p : \dot{\varepsilon}^p} \quad \dot{\varepsilon}^p = \dot{p}\frac{3}{2}\frac{\underset{\sim}{\sigma}^{dev}}{J_2(\underset{\sim}{\sigma})} \quad \dot{p} = \dot{\varepsilon}_0 \exp\left(-\frac{E_a}{k_B T}\right)$$
$$\sinh\left(\frac{\text{Max}(0, f(\underset{\sim}{\sigma}, R, R_a))}{k_B T}\right) \tag{3}$$

where ε^p is the plastic strain tensor, $\dot{\varepsilon}_0$, E_a, V_a, k_B, T are the strain rate threshold, the energy and volume of activation of the
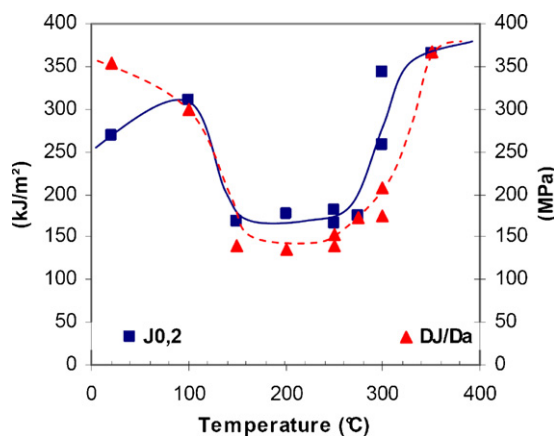
Table 2
Evolution of the strain to fracture for round notched specimens.

Temperature (°C)	20	100	125	150	200	250	300	350
AE2	0.543				0.421	0.368		0.474
AE4	0.648	0.580	0.528	0.414	0.404	0.327	0.447	0.528
AE10	0.713				0.441	0.430		0.473

dislocation mobility, the Boltzmann constant and the absolute temperature respectively.

The mean concentration of solute atoms depends on the parameters P_2, α and n:

$$C_s(p, t_a) = C_m(1 - \exp(-P_2 p^\alpha t_a^n)) \qquad (4)$$

The relative solute concentration evolves to a saturation value C_m when the ageing time t_a tends to infinity. The evolution law of the ageing time depends on the plastic strain rate through a parameter ω which represents the strain increment produced when all arrested dislocations overcome local obstacles and advance to the next pinned configuration (Eq. (5)):

$$\dot{t}_a = 1 - \frac{\dot{p}}{\omega} t_a \quad t_a(t = 0) = t_{a0} \qquad (5)$$

The initial time t_{a0} is related to the presence of static ageing and a large value allows simulating the Lüders peak and plateau.

The KEMC model was implemented in FE software [13,16]. The procedure for the parameter identification is explained in detail in [15]. However, some parameters were modified in order to better simulate the serrations and the geometrical features of PLC bands [30]. Here, only the results obtained at 20 °C and at 200 °C are presented and the parameters at these temperatures are provided in Table 3. The simulations were performed with finite strain formulation using the corotational frame of reference [16]. A full implicit resolution solver is used for the global equations. Local integration is solved by the Runge-Kutta method. Since the serrations have to be captured, the time increment is usually very small making the

computation time be very large (up to 60,000 increments currently used [15]).

3.2. Smooth tensile specimens

The tests on smooth tensile specimens were first simulated in 2D plane stress in order to minimize computation time. Eight node quadratic elements with reduced integration were employed. Fig. 4 shows a comparison of numerical and experimental tensile curves for two different temperatures at 10^{-3} s^{-1}. As can be seen, the KEMC model simulates both strain ageing phenomena: SSA (Lüders stress peak and plateau and Lüders bands [40]) and DSA (serrated flow and PLC bands). It should be noted that the simulated Lüders plateau is lower than the experimental one. Indeed it is difficult to correctly simulate both static and dynamic strain ageing with this model as previously discussed [15].

3.3. Round notched specimens

Round notched specimens were simulated using the KEMC model with the parameters identified in the previous section. 2D-Axisymmetric and full 3D computations were performed (Fig. 5). Generally, tensile tests on round notched specimens were modeled with a 2D axisymmetric model and planar symmetry: half-section is then modeled. However, in the presence of DSA effect, strain localization bands could occur and these bands present probably neither axisymmetry nor planar symmetry. Indeed, Graff et al. [13] showed, by in situ observations on polished surfaces of the specimens, that PLC bands on U-notched plate tensile specimens were
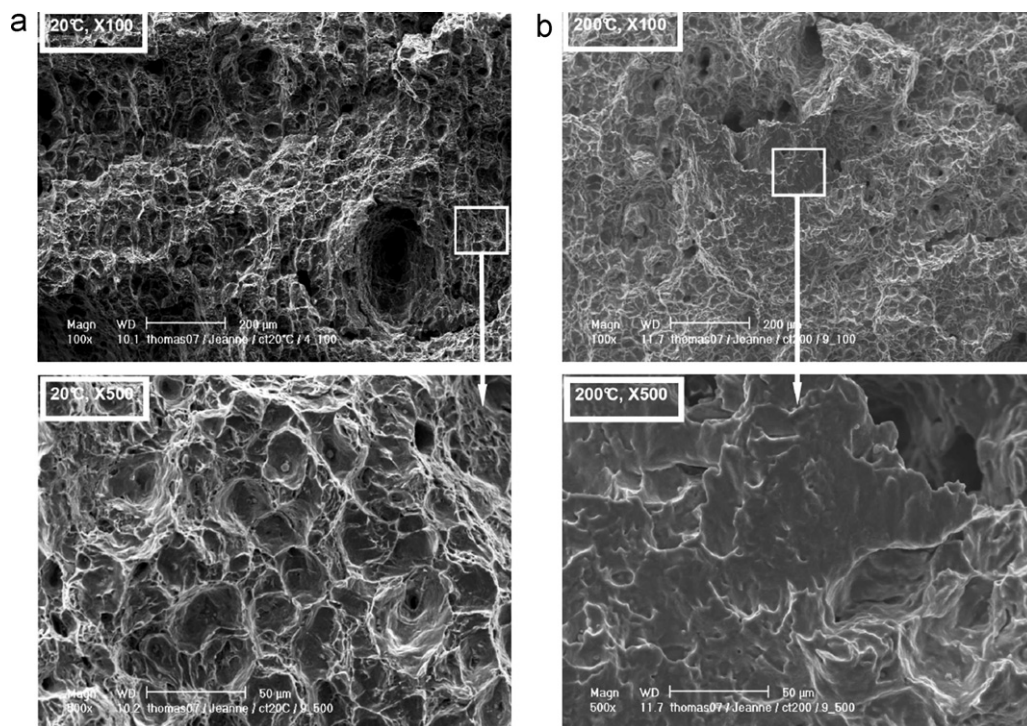

Fig. 3. Fractographic analysis of the fracture surfaces for CT specimens (a) 20 °C and (b) 200 °C: flat zones were observed at 200 °C.
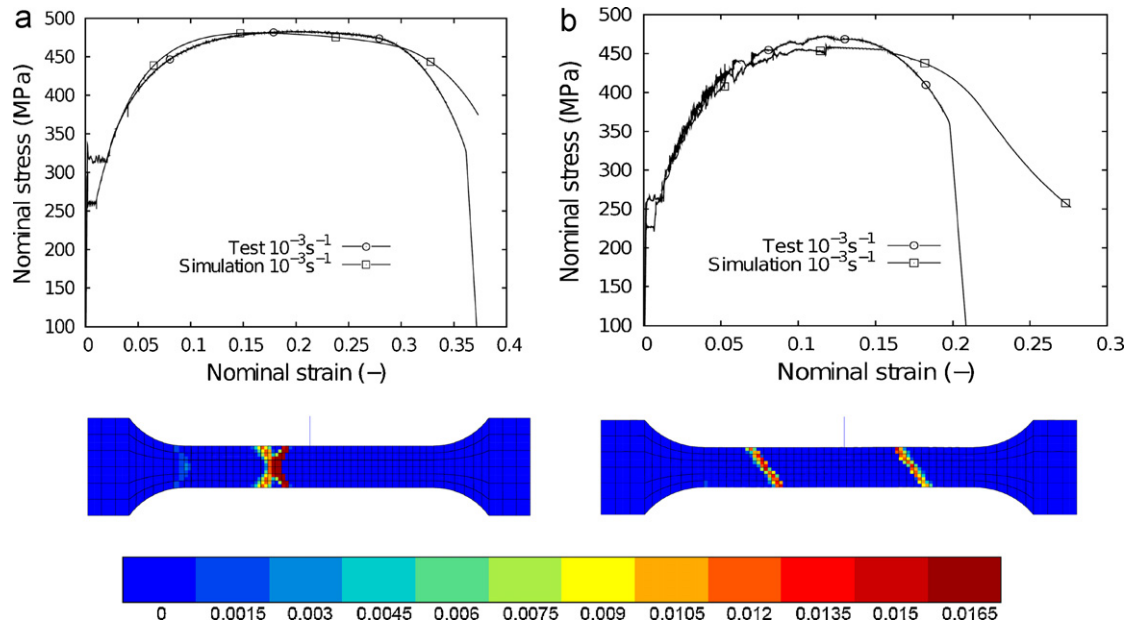
Fig. 4. Numerical and experimental tensile curves at 20 °C (a) and at 200 °C (b) at 10^{-3} s^{-1} and the corresponding strain localization bands (field of plastic strain rate).

not symmetric. Therefore, full 3D computations are necessary to correctly predict the DSA effect. The elements used were eight nodes quadratic elements with reduced integration for 2D simulations and twenty nodes quadratic brick elements with reduced integration for 3D simulations. The boundary conditions (Fig. 5) were:

1) 2D simulations: displacement equal to zero on the axis of the specimen in direction 1, displacement equal to zero on the minimum section in direction 2, and displacement rate on the upper surface in direction 2 was prescribed with details as discussed in the next paragraph.
2) 3D simulations: displacement equal to zero on the bottom surface in direction 2, displacement of one node on the bottom surface equal to zero in directions 1 and 3, displacement of the second node on the bottom surface equal to zero in direction 1 and displacement rate prescribed on the top surface in direction 2 as in 2D simulations.

Particular attention had to be paid to the prescribed displacement rate at the top of the mesh. Indeed, the actual condition in the experiment was a constant prescribed crosshead speed. This condition is not identical to a constant displacement rate at the head of the specimen (i.e. top of the mesh). The testing machine

stiffness (including the grip system) modifies the displacement rate at the head of the specimen. The non-linear behavior of the specimen induces a variation of this displacement rate versus time whereas crosshead speed remains constant. Since for the DSA phenomenon, loading rate is a major concern, the displacement rate at the top of the mesh was imposed so as to obtain the experimentally-measured diameter versus time. This resulted in using three different displacement rates increasing with time (the prescribed displacement is represented in Fig. 9 by the curve entitled "node 2 without spring"). In a second step, the machine stiffness was modeled as explained in the next section.

Fig. 6 shows the results obtained from simulations and experimental for AE4 at 200 °C. Two models were used for the simulations. One is the KEMC model and the other one is a standard elasto-plastic (EP) model which does not account for strain ageing and for which the parameters were obtained from the experimental curve of the round smooth specimen tested at 200 °C and 10^{-4} s^{-1}. The results show that the global behaviors predicted by 2D and 3D computations with the KEMC model are identical: the tensile curves are superposed. However, it is also noted that the magnitude of the simulated PLC serrations are less pronounced than for the experimental curve. This is attributed to the simplified boundary conditions as discussed later in this section. The curve obtained with the EP model in 3D gives a correct simulation of the force.
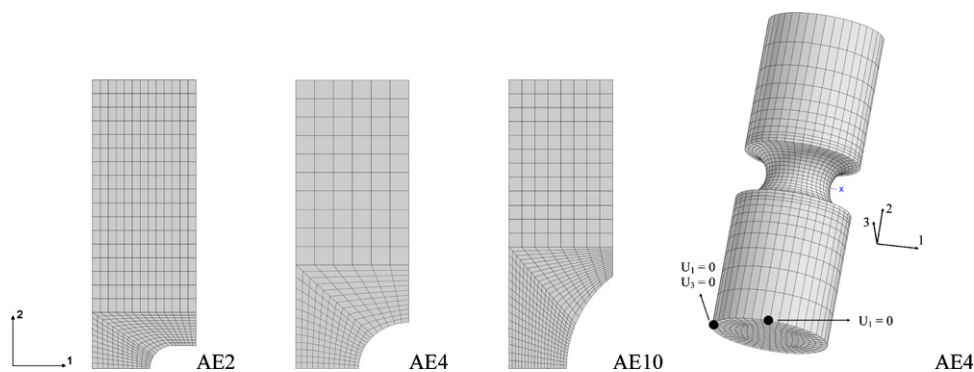

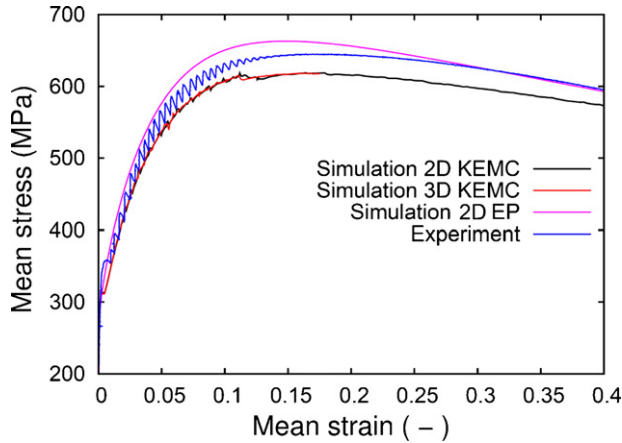**Fig. 5.** Meshes of axisymmetric notched specimens.

Fig. 6. Experimental and numerical curves at 200 °C: test results as well as 2D and 3D simulations for AE4.

Fig. 7 shows contour values of equivalent plastic strain rate obtained from 3D computation of AE4 at 200 °C at mean strains of 5% and 5.4%. Multiple bands develop inside the notch and are propagating. These bands occasionally extend beyond the notch region. In addition, the PLC bands on the 3D computation were not axisymmetric.

Observations of strain localization were performed by an optical technique on a mirror polished surface of the large section part of the specimen. Since strain localization can be observed in such a way only at room temperature, we looked for the Lüders bands after a tensile test interrupted during the Lüders plateau. Strain bands appear with a lattice pattern (Fig. 8). It is worth noting that the pattern observed corresponds to the pattern simulated by the FE method. Indeed, it is strain localization of DSA that is presented, but the main difference between both types of localization is the strain magnitude within the bands. Fig. 8 represents contour values of the

equivalent plastic strain of simulation of the AE4 tested at 200 °C at 5% of mean strain for the two models: KEMC and EP model. Comparing the observation and the 3D-model using the KEMC constitutive law, we can conclude that the KEMC model accurately represents strain localization. Consequently, to correctly predict PLC bands on round notched specimens, 3D computations must be performed.

The boundary condition related to the prescribed displacement was modified to directly take into account the influence of the testing machine stiffness on the PLC serrations. The AE2 and AE4 specimens were simulated taking into account the testing machine stiffness by means of a layer of purely elastic elements added at the top of the meshes (Fig. 10a). These elastic elements represent the spring simulating the testing machine stiffness. Considering the testing machine and the specimen to be two elastic springs in series, the testing machine stiffness is:

$$K_m = \frac{K_t K_{sp}}{K_{sp} - K_t} \tag{6}$$

with K_t the total stiffness obtained by the ratio of the load and the crosshead displacement measured experimentally in the linear domain of behavior, and K_{sp}, the elastic stiffness of the specimen computed by finite element method (in the modeling, plane symmetry imposes to take the double of K_{sp}). The machine stiffness calculated for AE2 and of AE4 is respectively 54,878 kN/m and 55,757 kN/m. Since the global curve is not sensitive to the 2D or 3D model, 2D computations were carried out to reduce computational time. The Fig. 9 shows the constant prescribed displacement imposed to node 1 (see Fig. 10 for the definition of the nodes 1 and 2) and the resulting displacement at node 2 that varies step by step when strain localizations occur; it should be noted that this displacement fits very well the displacement prescribed at node 2 in the preliminary step of AE modeling and defined in order to recover the diameter variation of the specimen.

Fig. 10b shows simulated and experimental curves for AE2 and AE4 taking into account the testing machine stiffness. Incorporating machine stiffness into the model resulted in simulated PLC
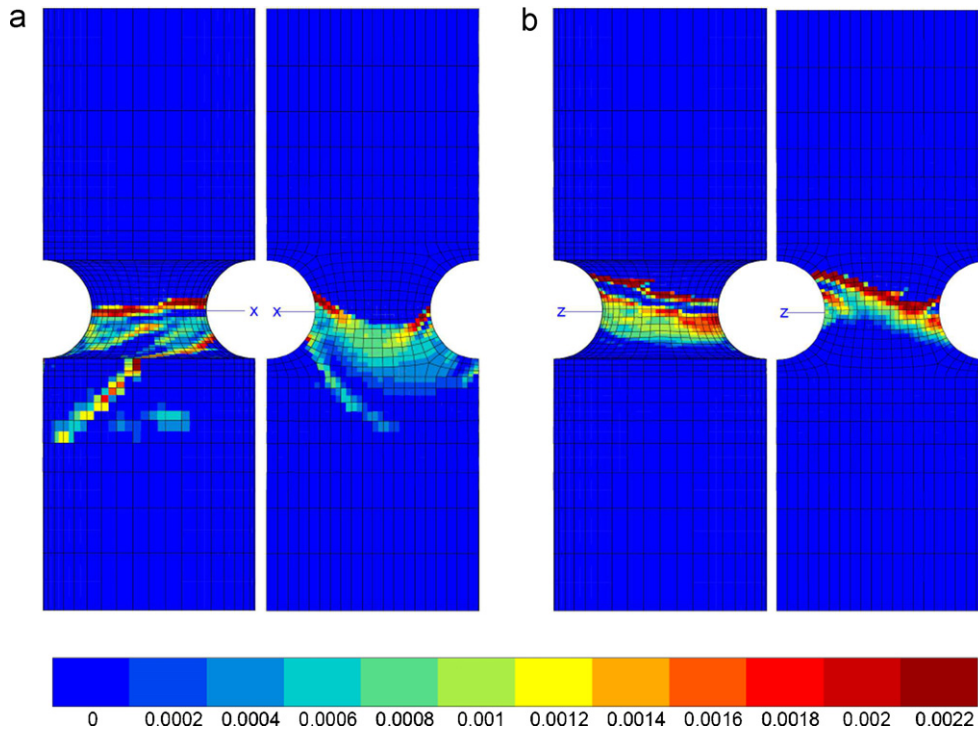

Fig. 7. Contour values of equivalent plastic strain rate ($\dot{p}$) for AE4. 3D computation using KEMC model at 200 °C for (a) 5% and (b) 5.4% mean strain: exterior surface (left) and axial section (right).
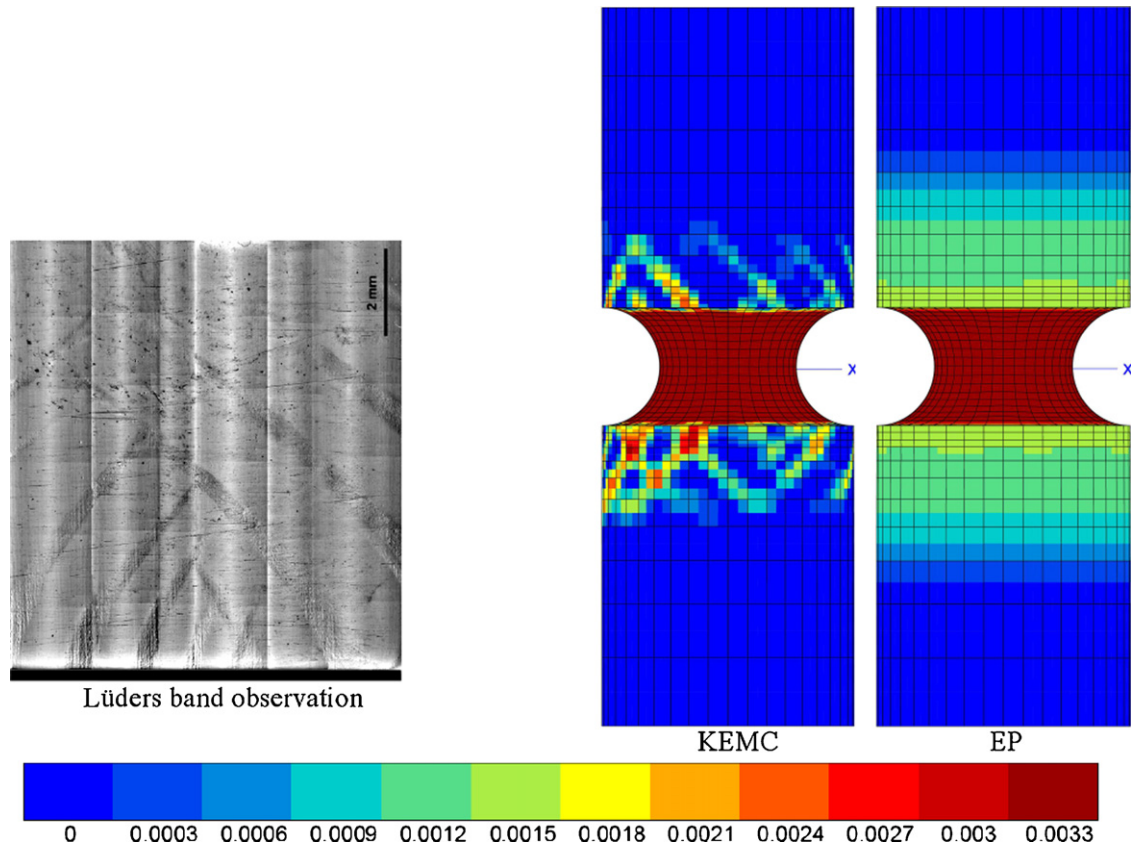
Fig. 8. Observation of the Lüders bands on specimen NT4 ahead of the notch (left), contour values of cumulative equivalent plastic strain for AE4 from 3D computations using KEMC model and EP model at 200 °C at 5% of mean strain (right).

serrations which were much closer to the experimental curves. The amplitude of PLC serrations is larger and the PLC serrations are more frequent than in the previous simulations. The larger serrations are explained by the release of elastic energy stored in the spring when strain rate localization bands form in the notch zone: since the load decreases, the displacement of the spring (*i.e.* the testing machine) decreases too, inducing a rapid increase displacement at the head of the specimen in order to reach the constant crosshead speed value that is prescribed. The local strain rate increases in the neck and a stronger PLC effect is observed. Nevertheless, it should be noted that the result could be a weaker PLC effect, if the temperature and strain

rate domain is such that a higher strain rate is outside the PLC domain.

It is also noted that the amplitude of the PLC serrations is overestimated by the simulations. This may be explained by the fact that the maximal stress drop magnitude driven by the parameter P_1 was too high. Nevertheless, it must be pointed out that such serrations were observed on experimental curves for the same type of specimens on another C–Mn steel by Wagner et al. [24]. It is worth noting that the shape of the serrations is correctly predicted. However, in contrast to the experimental results, the serrations do not stop after the maximum load indicating that the parameters controlling the solute atom concentration have to be adjusted.

These results indicated that machine stiffness should be taken into account for the identification of strain ageing parameters. This is a subtle issue that should be considered in the future because it depends on the relative stiffness between specimen and testing machine.

3.4. CT specimens

CT specimens were also simulated with the same parameters as the two preceding cases using the KEMC model. The CT specimens were firstly simulated by 2D computations since the cost of a full 3D computation is very high due to the PLC strain localizations. Full 3D computations were then carried out in order to show the geometry effect on the PLC band characteristics as was done for the notched round specimens. 2D simulations were conducted for plane stress and plane strain for later comparison with the 3D results. For saving computation time, only one half of the CT specimen was computed, even though it is known that the strain localization modes break the symmetry of specimen geometry. The element types were exactly the same as those used for the round notched specimens except

Fig. 9. Displacement of node 1 and node 2 (see Fig. 10) without or with spring.

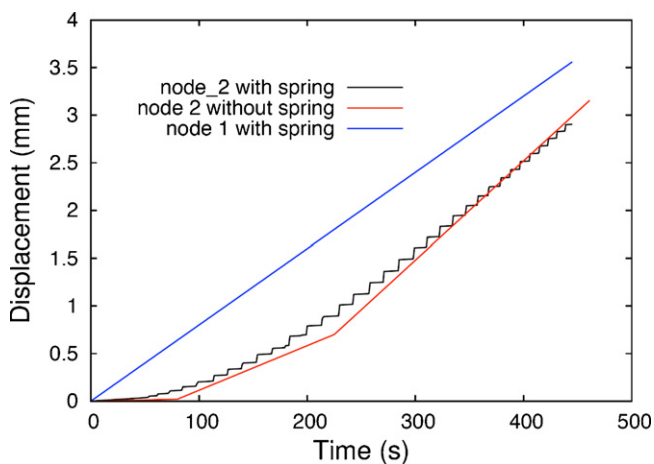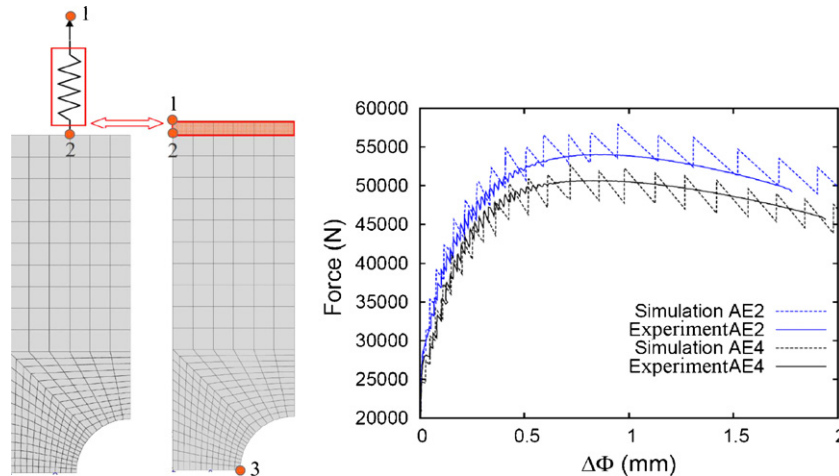**Fig. 10.** (a) Mesh of AE4 with a layer of elastic elements equivalent to a spring with the same stiffness as the testing machine; and (b) simulation and experimental curves for AE2 and AE4 taking into account the testing machine stiffness at 200 °C.

that the 2D elements for CT specimens were for plane stress and plane strain state instead of for axisymmetric elements.

Fig. 11 shows the 2D mesh and the loading conditions for CT specimens. Since the machine stiffness was not taken into account in determining the material parameters, simulations were done ignoring the effect of machine stiffness. The speed prescribed to the pin loading is 0.4 mm/mn corresponding to the COD prescribed speed which was controlled by the clip gage. To simulate the experimental load, a group of elements was added to the loading hole. These elements are purely elastic with a much higher Young's modulus than the actual material, so that the elastic strain of the pin can be neglected. The loading was then applied to the tip of the elastic zone. The displacement of the tip is fixed in the direction 1 ($U_1 = 0$). Symmetric conditions were imposed on the ligament. The COD was measured at the same location as in experiments. The zone enclosed in the red box was meshed with elements of 200 μm since two types of strain localization are present in this zone: classic strain localization near the crack tip and strain localization due to the DSA effect. A sufficiently fine mesh can account for both types of strain localization. Simulations were carried out for the specimen tested at 200 °C since DSA manifested its maximum effect at this temperature: the toughness takes its minimum value.

Fig. 12a shows the field of equivalent plastic strain rate and Fig. 12b shows the cumulative equivalent plastic strain for plane stress (left) and plane strain (right) conditions at a COD of 0.73 mm.
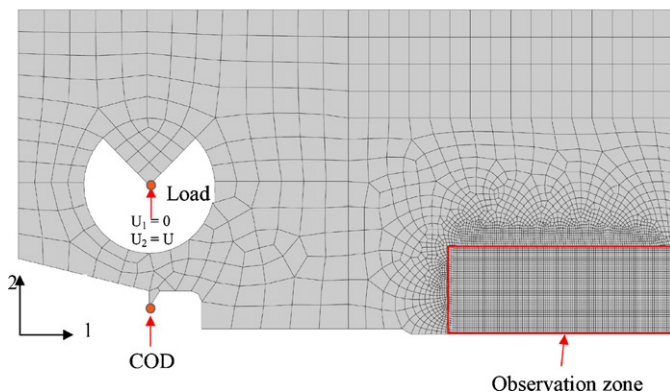
Fig. 12a shows that, in plane stress, the PLC bands are numerous, very short and scattered near the crack tip. In plane strain, the PLC bands are much less numerous and they are much longer than those in plane stress. In Fig. 12b, it can be seen that the plastic zones are more localized compared to the classical case, i.e. with an elastic–plastic behavior [15]. In plane stress, the strain localization bands are parallel to the crack plane and similar to those observed near the notch tip of an aluminum alloy specimen by Delafosse et al. [41]. In plane strain, the plastic zone near the crack tip is localized into multiple strain bands. These strain localization bands tend to extend to the back of the specimen.

Two full 3D computations were carried out on a quarter of the whole CT25 specimen (Fig. 13) tested at 200 °C: one using the KEMC model and the other using the elastic–plastic model already presented for notched specimens. The side groove was also modeled to get a mechanical state as close as possible to the experimental situation. The loading conditions were the same as for the 2D simulations. Around the crack tip, a regular 500 μm mesh was used which was coarser than in 2D simulations owing to the increased computational time.

Fig. 14 shows the equivalent plastic strain rate at a COD of 0.7 mm for the 3D simulation with the KEMC model at 200 °C. As was the case for 2D plane strain, the PLC bands were much less numerous than those observed in 2D plane stress.

Fig. 15 shows the equivalent plastic strain at the COD of 0.7 mm for the 3D simulation with the KEMC model at 200 °C. Similar to the 2D plane strain case, the plastic zones exhibited multiple strain localization bands. These bands were also divided into two groups: one initiated from the crack tip and the other from the side groove. It is noted that the bands on the symmetry plane share the same characteristics as those simulated in 2D plane strain whereas those on the free side were less numerous and less pronounced because the material on the free side had less plastic deformation. Fig. 16 shows the equivalent plastic strain at a COD of 0.7 mm for the 3D simulation using the elastic–plastic model at 200 °C. Compared to the KEMC model, globally, the plastic zones are of the same dimension. However, the plastic zones are much less localized than those simulated with the KEMC model.

To visualize the PLC strain localization bands within the specimen, a transverse section about 5 mm from the crack tip (the length of the ligament is 20 mm) was examined (Fig. 17). For the equivalent plastic strain, the left side is the symmetry plane and the right is the free side. It is noted that the plastic zone is in the form of a half

Fig. 11. 2D mesh of CT specimen.
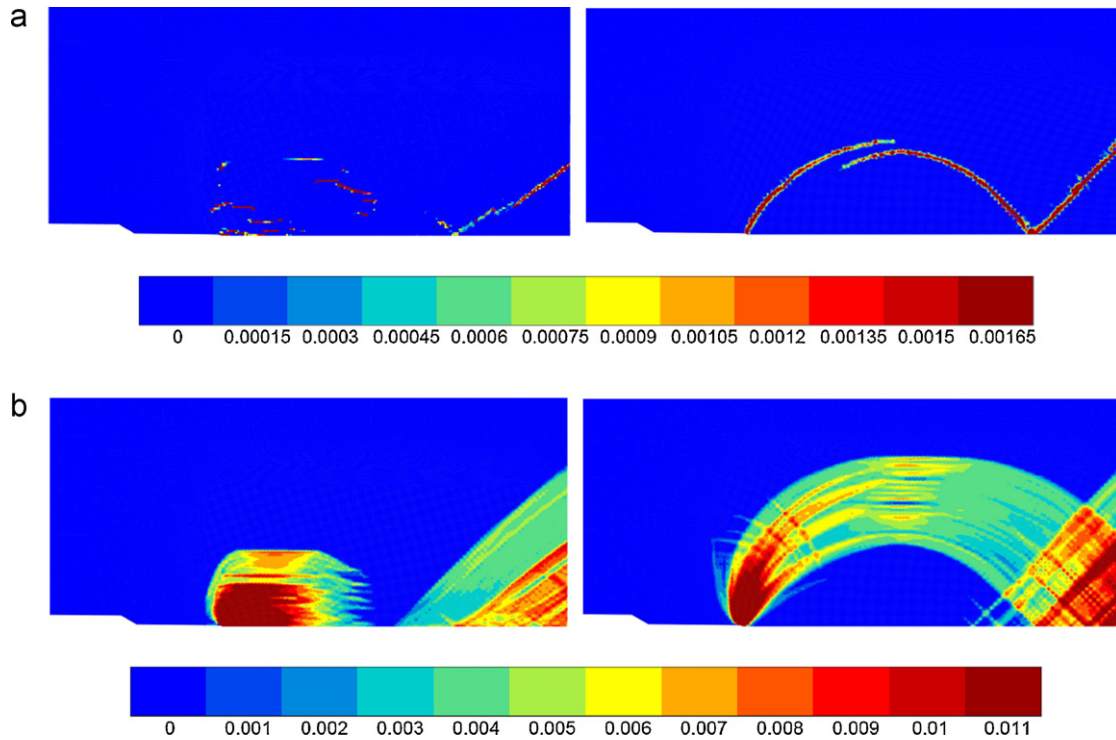
Fig. 12. Simulation results at a COD of 0.73 mm for plane stress (left) and plane strain (right): (a) field of equivalent plastic strain rate and (b) field of equivalent plastic strain.
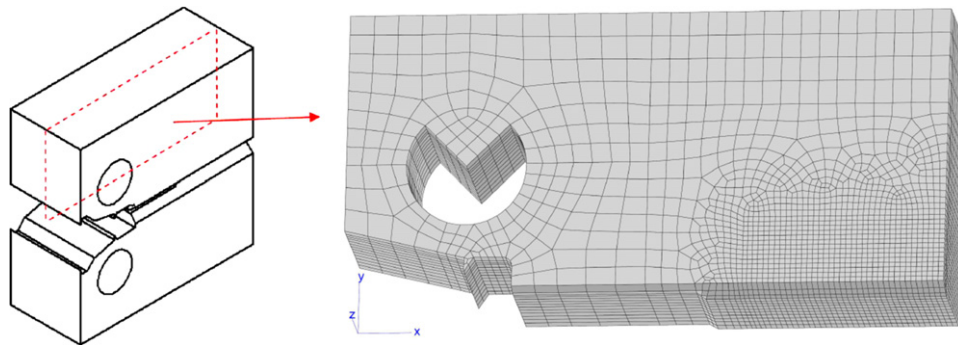
Fig. 13. Mesh of a quarter of a whole CT25 specimen.

arc which initiated from the bottom of the groove in the transverse direction. Two groups of PLC bands can be seen:

1) Bands initiated from the crack tip. These bands cross the whole specimen in the longitudinal direction (crack propagation direction) (Fig. 15).

2) Bands initiated from the groove. These bands cross the geometry in the thickness direction.

These two groups of strain localization bands interfere. Nevertheless, globally, the geometry remains in a quasi-plane strain state for ligament as it will be confirmed by the COD/force curves.
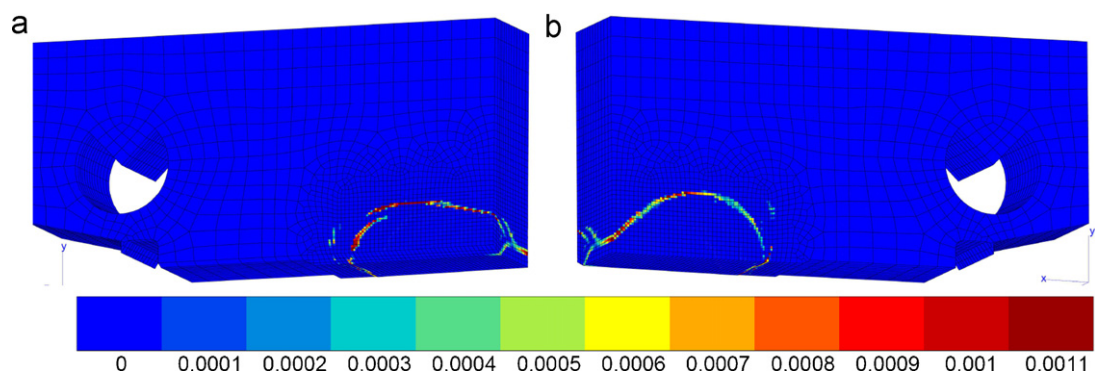
Fig. 14. Field of equivalent plastic strain rate at a COD of 0.7 mm for the 3D simulation using the KEMC model at 200 °C: (a) grooved side; and (b) symmetric plane side.
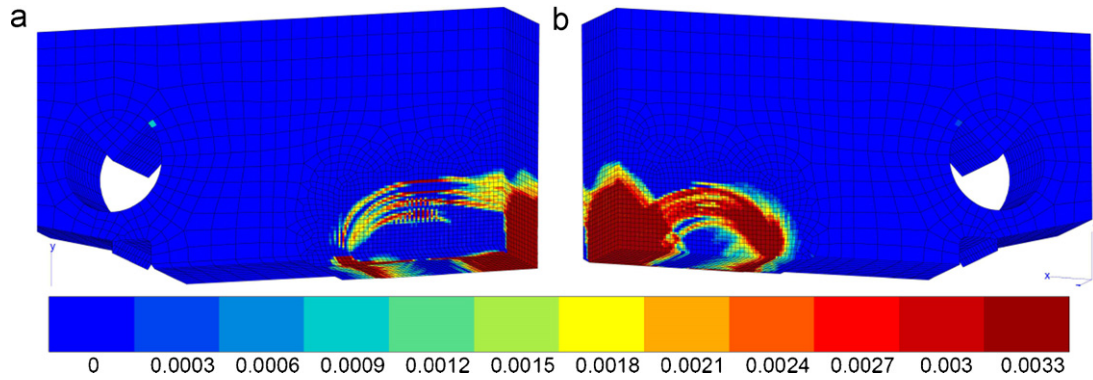
Fig. 15. Cumulative equivalent plastic strain at a COD of 0.7 mm for the 3D simulation using the KEMC model at 200 °C: (a) grooved side; and (b) symmetry plane side.
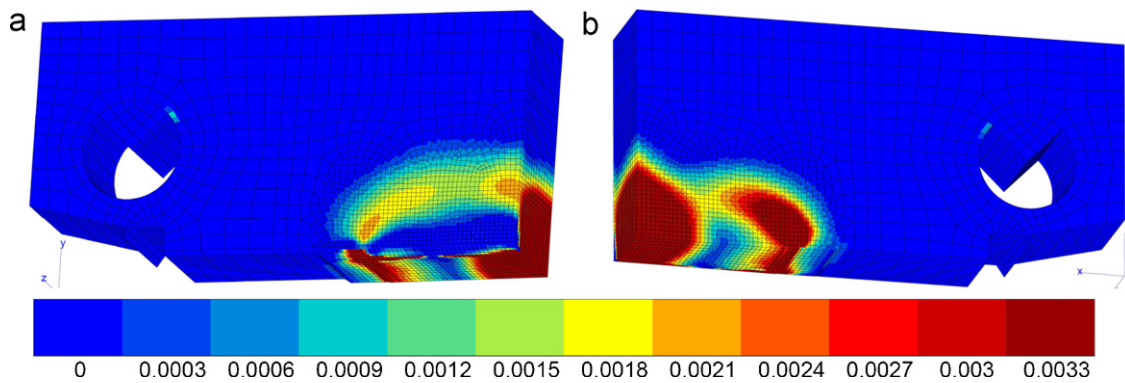
Fig. 16. Cumulative equivalent plastic strain at a COD of 0.7 mm for a 3D simulation using the elastic–plastic model at 200 °C: (a) grooved side; and (b) symmetry plane.

The 3D simulation COD/force curve was compared to those obtained from 2D simulations and to the experimental one (Fig. 18). It must be pointed out that the simulations were carried out under monotonic loading and without crack propagation. Therefore, there is no unloading line on the simulation curves and the simulated curves deviate from the experimental curve at 1.5 mm COD because of the onset of ductile tearing. Nonetheless, serrations are observed on the simulation curves which are related to the PLC effect in agreement with experiment [15]. The amplitudes of the PLC serrations obtained from simulation are higher than those seen on the experimental curve. This may be due to an over estimate of the parameter P_1. Examination of the results of the simulations shows that the plane strain 3D simulation gave the best prediction of the experimental curve. PLC serrations were also observed for the 3D simulation curve; their amplitude is lower than that of the plane strain curve and thus would appear to be more realistic. It is noted that the 3D simulation using the EP model yields results which are very close to those obtained from the KEMC 3D model even though the corresponding local strain fields are different.
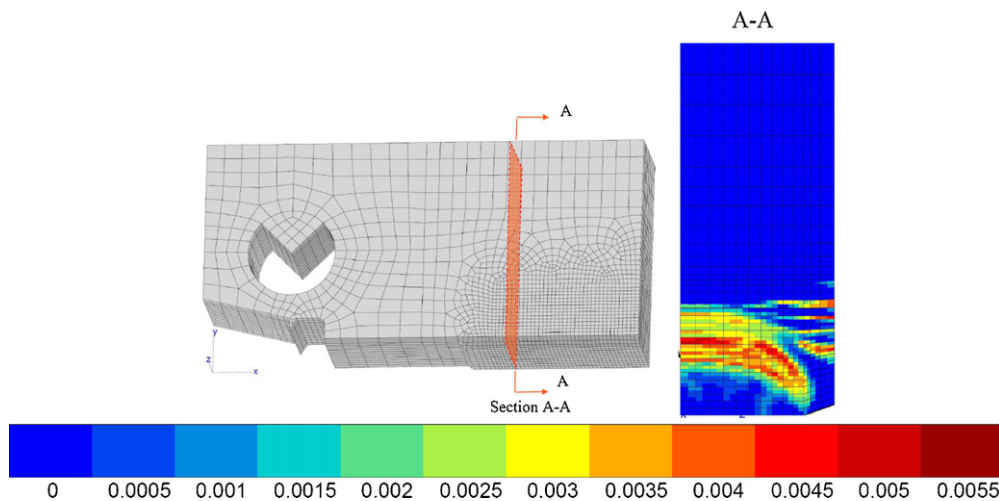
Fig. 17. Contours of cumulative equivalent plastic strain using the KEMC model at a COD of 0.8 mm: transverse section behind the crack tip.

Table 3
Parameters determined at 20 °C and at 200 °C.

Temperature (°C)	E (GPa)	N	R_0 (MPa)	Q (MPa)	b	H (MPa)	$\dot{\varepsilon}_0$ (s^{-1})	E_0 (eV)	V_a (b^3)	n	P_1 (MPa)	t_{a0} (s)	P_2 (s^{-n})	ω	α
20	210	0.3	197	312	25.2	360	1×10^{-3}	0.0022	83	0.66	94	5,000,000	0.01	0.0002	0.26
200	198	0.3	176	287	29.3	360	1×10^{-3}	0.0022	121	0.66	83	100	0.85	0.0002	0.17
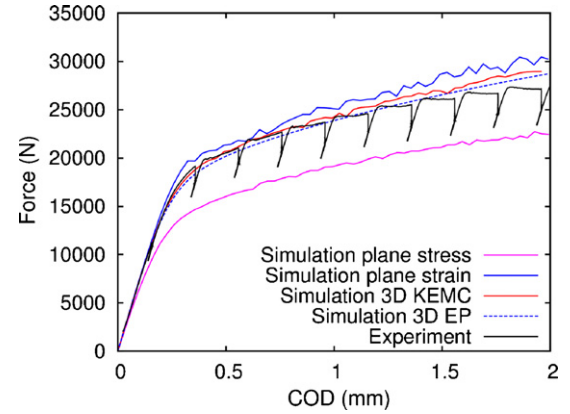
Fig. 18. Experimental and numerical force/COD curves for CT25 tested at 200 °C.

4. Ductile fracture prediction

4.1. Identification of the fracture criterion

The objective of the fracture specimen geometry modeling (notched and CT specimen) was to obtain correct mechanical fields in order to use the local approach for fracture prediction. It should be recalled that at 200 °C the ductility is lower than at room temperature. Since ductile fracture mechanisms were observed on fracture surfaces, the Rice and Tracey model was used to predict the fracture of notched specimens. The void growth ratio is computed at each point of the specimen from the Rice and Tracey damage law [29]:

$$\frac{\dot{R}}{R} = 0.238 \exp\left(\frac{3}{2}\frac{\sigma_m}{\sigma_{eq}}\right)\dot{p} \quad R(0) = R_0 \tag{7}$$

where R is the current void radius; R_0 is the initial void radius; $\dot{p}$ is the equivalent plastic strain rate; σ_m is the hydrostatic stress; σ_{eq} is the von Mises equivalent stress. Fracture is assumed to occur when the void growth ratio reaches a critical value $(R/R_0)_c$. This critical value must be determined from experiment in order to predict strain to fracture measured in experiments.

In the present study, Eq. (7) was assumed to be independent of temperature since the fractographic analysis did not show any features on the fracture surfaces uniquely associated with the DSA domain. Determination of the parameter calibration was performed at 20 °C via 2D simulations of specimen AE4. Indeed, 2D simulations proved to be sufficient for that purpose as discussed later. Fig. 19 shows the stress triaxiality ratio σ_m/σ_{eq} and the damage variable R/R_0 computed at the Gauss point that is near the specimen center versus the change in diameter at the notch section; the center of the section is the location of the largest value of the damage variable over a large variation of the diameter, and is thus the location of ductile fracture initiation. As seen in Fig. 19, the damage variable continuously increases for the KEMC model, even though there are oscillations of the local mechanical variables due to strain localizations. Indeed, the integration over time (see Eq. (7)) masks the time variations. Therefore, the damage variable assessment does not depend on symmetry, and the 2D model adequately captures the damage level, although the current variables have not the same values in the 2D and 3D computations as previously discussed. The criterion is calibrated at 20 °C in order to get the strain at fracture. The mean value obtained using the results from specimens AE4 and AE2 was $(R/R_0)_C = 2.25$.

4.2. Prediction of ductile fracture

Simulations of the notched tensile specimen AE4 were performed at each temperature, with appropriate parameter sets at
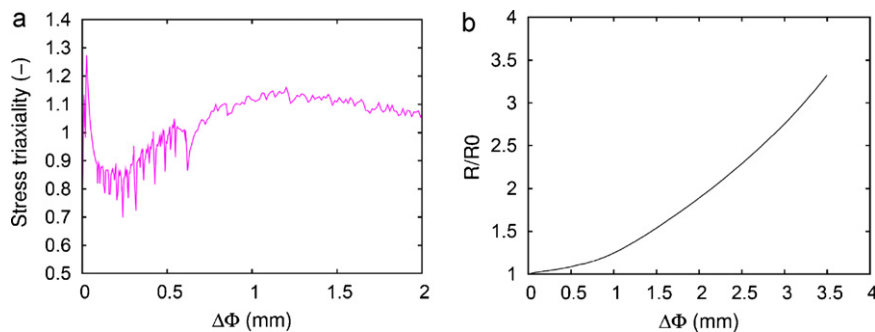
Fig. 19. Evolution of mechanical variables in the element at the center of the AE4 notched specimen; (a) stress triaxiality ratio, and (b) damage variable.

each temperature of the KEMC model. The parameter sets were not determined at each temperature. Instead the calibration procedure involved assumptions concerning the temperature dependence of each parameter as detailed elsewhere [15]. For the sake of simplicity, the results are not reproduced here and do not affect subsequent discussion. Nevertheless, it should be noted that simulation of the AE4 specimen tests underestimates the maximum load by 10% at 150 °C and 250 °C, by 5% at 300 °C, while more precise simulations are obtained for the other temperatures. These slight discrepancies underline the difficulty in predicting the correct strain rate sensitivity for DSA sensitive materials over a wide range of temperature.

Predictions of ductile fracture for AE4 were made for different temperatures (Fig. 20). As can be seen, a decrease in ductility was observed in the DSA domain in agreement with experiment. Nevertheless, the predicted magnitude of the ductility drop was less than observed experimentally. Thus, even using a model which takes the DSA effect into account, the prediction of the ductility loss at the temperature where DSA reaches its maximum effect is underestimated.

This shortcoming implies that the damage model has to be revisited. Amar and Pineau [28] and Wagner et al. [24] used the same damage model computed from an elastic–plastic constitutive law, but they assumed that the criterion was in fact temperature dependent. However they did not justify this hypothesis, and we did not observe such behavior in this study. Improved prediction of ductility loss in the negative strain rate sensitivity regime could be gained by performing micromechanical computations: particular strain hardening and strain localizations could accelerate the void growth. It should be noted that a particular attention must be paid on large strain behavior because the fracture of the AE4 specimen occurred at a local strain about 60%.
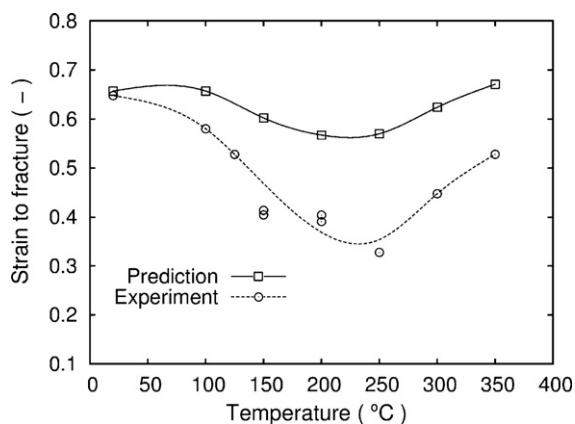
Fig. 20. Prediction of strain to fracture for AE4 from 20 °C to 350 °C.

5. Conclusions

In this study, dynamic strain ageing and its relation to ductile fracture of a C–Mn steel were studied via experimental and numerical methods.

Dynamic strain ageing was evidenced between 100 °C and 300 °C depending on the strain rate along with a decrease of the uniform elongation around 200 °C. The decreased ductility was related to the plasticity in presence of DSA which reduces the necking strain [32,33] and consequently the fracture strain. This phenomenon does not involve the relation between DSA and ductile fracture mechanisms, void nucleation, growth and coalescence.

Fracture tests were carried out on round notched and precracked specimens (CT25). A sharp drop in the fracture strain and of the fracture toughness was observed between 150 and 250 °C, a temperature range where the PLC effect was seen. Fractographic analyses by SEM did not show any feature associated with the PLC effect.

To model the fracture tests and obtain correct mechanical results in the fracture specimen, a thermally activated elasto-viscoplastic model, the KEMC (Kubin–Estrin–McCormick) strain ageing model, was used. The parameters of the KEMC model were developed between 20 °C and 350 °C from a previous work [15] and from additional results.

2D-axisymmetric and full 3D computations were then performed on round notched specimens. The results show that the global behaviors predicted by the 2D and 3D computations with the KEMC model were identical. It was noted that PLC bands in 3D computations were not symmetric. Consequently, to correctly predict PLC bands on round notched specimens, 3D computations were necessary, but were otherwise not needed to obtain the global behavior.

Fracture tests on side grooved CT specimens were also simulated. The 2D plane strain simulation was very close to the 3D simulation because of the side groove. The plastic zone had a complex spatial form due to two groups of strain bands: one coming from the crack tip and one coming from the notch of the groove. Global curves showed that PLC serrations, which were observed experimentally [15] were simulated. The global behavior of the specimen was well predicted. Since there is a high strain rate gradient in this specimen, it means that the strain rate sensitivity of the material is accurately taken into account by the KEMC model at this temperature.

The simulations with KEMC model were compared to those obtained using a standard EP model. This model accounts for the apparent strain hardening obtained from the tensile curve at 200 °C and 10^{-4} s^{-1} but which does not account for strain ageing. The global curves are reasonably predicted for the notched tensile specimen and more accurately predicted for the CT specimen at 200 °C. Indeed, this result depends on the strain rate sensitivity of the

material and on the strain rate gradient in the specimen. Thus, a prediction of mechanical behaviour of a component made for a strain ageing sensitive material with a standard elastic–plastic model is not recommended. For example, concerning the plastic zone, the lattice pattern observed on a notched specimen could not be reproduced with the plastic model. In the CT specimen, the plastic zones simulated using the KEMC model are more localized, but the plastic zone sizes are not so different.

The influence of testing machine stiffness and actual boundary conditions on PLC occurrence was assessed for the round notched specimen. The PLC serrations predicted taking testing machine stiffness into account were closer to those seen on the experimental curves. The overestimate of the PLC serrations amplitude may be explained by a too high maximal stress drop magnitude driven by the parameter P_1. Contrary to the experimental results, the serrations did not stop after the maximum load; the parameters associated with the solute atoms concentration and controlling the strain influence on free solute atoms need to be adjusted. These results indicated that machine stiffness should be taken into account for in any determination of strain ageing parameters.

Using the results obtained by the FE simulations of AE4 specimens, ductile fracture was predicted using the Rice and Tracey damage law. Based on fractographic analysis, it was assumed that the fracture criterion was independent of temperature. The ductility loss observed in the DSA domain was predicted but the magnitude was less than that obtained from experiment. Therefore, even with a model which takes the DSA effect into account for computation of mechanical parameters, the prediction of the ductility loss in the intermediate temperatures, where DSA reached its maximum effect, was still underestimated. It should be noted that the damage variable is not sensitive to the PLC effect, because it is based on the time integration of mechanical variables that masks their complex evolution. Other authors [24,28] assumed that the criterion was dependent on temperature without justifying this hypothesis. Improved prediction of ductility loss in the DSA regime could be gained by performing micromechanical computations on unit cells. Micromechanical details of strain hardening and strain localization could result in accelerated void growth.

References

[1] P. Penning, Acta Metall. 20 (1972) 1169.
[2] A. Van den Beukel, Phys. Status Solidi (A) 30 (1975) 197.
[3] L.P. Kubin, Y. Estrin, Acta Metall. 33 (1985) 397–407.
[4] K. Chihab, Y. Estrin, L.P. Kubin, J. Vergnol, Scripta Metall. 21 (1987) 203.
[5] R. Shabadi, S. Kumar, H.J. Roven, E.S. Dwarakadasa, Mater. Sci. Eng. A 364 (2004) 140.
[6] P.G. McCormick, Acta metall. 36 (1988) 3061–3067.
[7] P.G. McCormick, C.P. Ling, Acta Met. Mater. 43 (1995) 1969–1977.
[8] Y. Estrin, P.G. McCormick, Acta Met. Mater. 39 (1991) 2977–2983.
[9] P.G. McCormick, Y. Estrin, in: T.C.<ET-AL.> Lowe (Ed.), Modeling the Deformation of Crystalline Solids, TMS, Warrendale, PA, 1991, p. 293.
[10] S. Zhang, P.G. McCormick, Y. Estrin, Acta Mater. 49 (2001) 1087–1094.
[11] S. Kok, A.J. Beaudoin, D.A. Tortorelli, M. Lebyodkin, Modell. Simul. Mater. Sci. Eng. 10 (2002) 745–763.
[12] S. Kok, A.J. Beaudoin, D.A. Tortorelli, M. Lebyodkin, L. Kubin, C. Fressengeas, J. Phys. IV 105 (2003) 191–197.
[13] S. Graff, S. Forest, J.-L. Strudel, C. Prioul, P. Pilvin, J.-L. Béchade, Mater. Sci. Eng. A 387–389 (2004) 181–185.
[14] S. Graff, S. Forest, J.-L. Strudel, C. Prioul, P. Pilvin, J.-L. Béchade, Scripta Mater. 52 (2005) 1181–1186.
[15] J. Belotteau, C. Berdin, S. Forest, A. Parrot, C. Prioul, Mater. Sci. Eng. A 526 (2009) 156–165.
[16] M. Mazière, J. Besson, S. Forest, B. Tanguy, H. Chalons, F. Vogel, Comput. Methods Appl. Mech. Eng. 199 (2010) 734–754.
[17] A. Benallal, T. Berstad, T. Børvik, A.H. Clausen, O.S. Hopperstad, Eur. J. Mech. A/Solids 25 (2006) 397–424.
[18] A.H. Clausen, T. Børvik, O.S. Hopperstad, A. Benallal, Mater. Sci. Eng. A 364 (2004) 260–272.
[19] O.S. Hopperstad, T. Børvik, T. Berstad, O.-G. Lademo, A. Benallal, Modell. Simul. Mater. Sci. Eng. 15 (2007) 747–772.
[20] S.D.J. Mesarovic, J. Mech. Phys. Solids 43 (1995) 671–700.
[21] E. Rizzi, P. Hähner, Int. J. Plast. 20 (2004) 121–165.
[22] M.R. Wenman, P.R. Chard-Tuckey, Int. J. Plast. 26 (2010) 1013–1028.
[23] D. Wagner, J.C. Moreno, C. Prioul, J. Nucl. Mater. 252 (1998) 257–265.
[24] D. Wagner, J.C. Moreno, C. Prioul, J.M. Frund, B. Houssin, J. Nucl. Mater. 300 (2002) 178–191.
[25] K.C. Kim, J.T. Kim, J.I. Suk, U.H. Sung, H.K. Kwon, Nucl. Eng. Des. 228 (2004) 151–159.
[26] M. Srinivas, G. Malakondaiah, P. RamaRao, Acta Metall. Mater. 41 (4) (1993) 1301.
[27] M. Srinivas, S.V. Kamat, P. Rama Rao, Mater. Sci. Eng. A 443 (2007) 132–141.
[28] E. Amar, A. Pineau, Eng. Frac. Mech. 22 (1985) 1061–1071.
[29] J.R. Rice, D.M. Tracey, J. Mech. Phys. Sol. 17 (1969) 201.
[30] H.D. Wang, C. Berdin, M. Mazière, S. Forest, C. Prioul, A. Parrot, P. Le-Delliou, Scripta Mater. 64 (2011) 430–433.
[31] L.P. Kubin, Y. Estrin, J. Phys. III 1 (1991) 929–943.
[32] J. Kang, D.S. Wilkinson, M. Jain, J.D. Embury, A.J. Beaudoin, S. Kim, R. Mishira, A.K. Sachdev, Acta Mater. 54 (2006) 209–218.
[33] W.F. Hosford, R.M. Caddell, Metal Forming-mechanics and Metallurgy, Prentice-Hall International, Inc., 1983, 74.
[34] N. Ranc, D. Wagner, Mater. Sci. Eng. A 394 (2005) 87–95.
[35] Y. Bréchet, F. Louchet, Acta Metall. 41 (1993) 783.
[36] J.H. Yoon, B.S. Lee, Y.J. Oh, J.H. Hong, Int. J. Pres. Ves. Pip. 76 (1999) 663–670.
[37] S. Xu, X.Q. Wu, E.H. Han, W. Ke, J. Mater. Sci. 44 (2009) 2882–2889.
[38] C. Gupta, J.K. Chakravartty, S.L. Wadekar, S. Banerjee, Scripta Mater. 55 (2006) 1091–1094.
[39] C.W. Marschall, M.P. Landow, G.M. Wilkowski, ASTM STP 1074 (1990) 339–360.
[40] J. Zhang, Y. Jiang, Int. J. Plast. 21 (2005) 651–670.
[41] D. Delafosse, G. Lapasset, L.P. Kubin, Scripta Metall. Mater. 29 (1993) 1379–1384.

6 Ten projects for the next ten years

The strain ageing phenomena have been a source of activity for scientists for more than one century. In this last section are proposed 10 axis of research on the subject. This list is clearly not exhaustive and one could bet that strain ageing is such a surprising phenomenon that many others fascinating subjects will appear in the future.

6.1 Limits and potential improvments of the KEMC model

I. Strain ageing and very low strain rates – relaxation and creep arrest

Strain ageing phenomena like Lüders band and the Portevin - Le Chatelier effect are generally investigated in the usual global strain rate range of quasi-static tensile tests i.e. between 10^{-5}s^{-1} and 10^{-1}s^{-1}. Experiments at higher strain rates can be made using high velocity tensile machines or Hopkinson bars. However the stress vs. strain curves are serrated by nature and only the average stress level is generally available from this kind of experiments. On the other side of strain rate scale, creep and relaxation tests are on the contrary rather easy to carry out and very relevant for the understanding and the modelling of strain ageing phenomena.

In a PhD thesis on zirconium alloy Zr702 [105], C.Pujol has shown the strong influence of strain ageing on the creep behaviour of this alloy. For high creep stress levels, the creep response is rather usual showing a primary, secondary, and ternary phases up to failure. But below a given stress level, the creep stops after the primary stage, the creep strain rate tending to 0. This creep bifurcation can be seen on the strain rate vs. strain plot presented on figure 76(top) between 190 and 195 MPa. It is clearly a manifestation of strain ageing through the negativity of the strain rate sensitivity at relatively low strain rates and the non convexity of the stress surface in the strain and strain rate space (see figure 46).

The KEMC model can be identified in order to reproduce this creep bifurcation, like on figure 76(bottom). This kind of experimental results are even a very valuable source of information at low strain rate for the calibration of material parameters, in addition to usual tensile experiments carried out at higher strain rates.

Relaxation experiments were also carried out in the PhD thesis of C.Pujol. An influence of strain ageing was reported by the author comparing experiments at 20°C and 200°C. At 20°C, the relaxation process is still effective after 100 hours of experiment, very probably because of the static recovery phenomenon (time driven annihilation of dislocations). At 200°C, this process which should be more present since thermally activated is on the contrary restrained and relaxation is almost arrested after 100 hours. This is probably due to the influence of solute atoms that block the static recovery phenomenon by pinning mobile dislocations. Contrary to creep, an improvement of the KEMC model would be required to account for such an interaction, in the same spirit as the dislocation density based model proposed on section 3.2.

Some very similar results have been found in Titanium alloy Ti6242 in the PhD thesis of H.Jousset [170]. The results are even more interesting since creep and creep-fatigue experiments have been carried out for different temperatures within and without the strain ageing domain. Pure creep tests at low stress level show creep arrest like in the case of Zr702. On the contrary a combined creep-fatigue experiment carried out at the same stress level but adding regular unloading/reloading stages can lead to failure of the specimen. In this case the KEMC model also shows some strong limits since a coupling between strain ageing, isotropic and kinematic
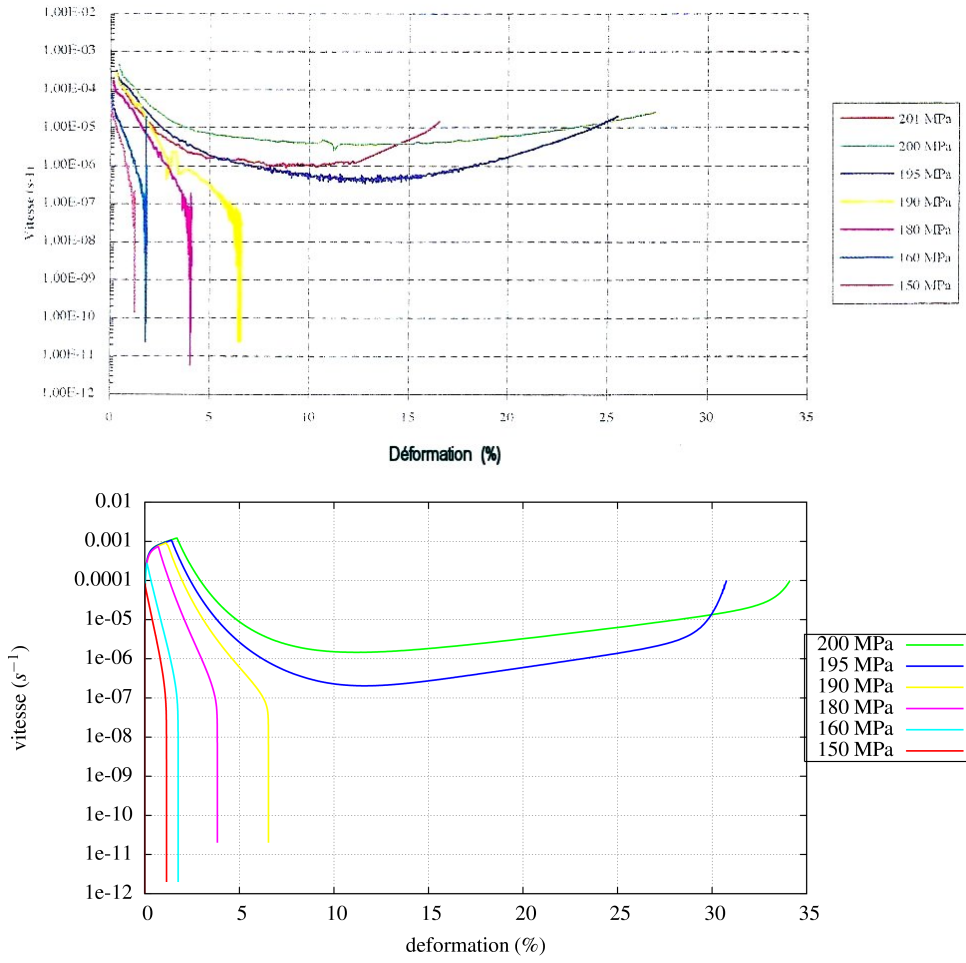
FIGURE 76 – (top) Experimental creep behaviour at 200°C for zirconium alloy Zr702, taken in transverse direction of rolling in the logarithm of creep rate versus strain curve taken form the PhD thesis of C.Pujol [105]. (bottom) Corresponding finite element simulation carried out after a precise identification of the KEMC model in order to reproduce the creep bifurcation between 190 and 195 MPa.

hardening should be introduced. However the conclusion of this section is that creep, relaxation, and combined creep-fatigue or relaxation-fatigue experiments are essential in addition to usual monotonic tensile tests for a complete understanding and modelling of strain ageing in metallic alloys.

II. Multiscale approach of strain ageing for a complete strain-time-temperature-concentration representative model

The KEMC model has been built based on some physical mechanisms at the dislocation level identified between 1950 and 1980 by A.H.Cottrell, J.Friedel, P.G.McCormick, and A. van den Beukel (see section 2 for more details). The model is then by nature multi-scale since the stress required to move a single dislocation and the stress needed to deform a macroscopic specimen are influenced in a similar way by strain level, strain rate, and temperature. However, the initial physical theories at the microscopic level contains a lot of approximation and can then only provide qualitative informations for the macroscopic level.

The development of modelling and simulations at small scales like ab initio, molecular dynamic, and discrete dislocation dynamic calculations could provide some more quantitative results that can be used at the macroscopic level. In particular the influence of temperature, strain, strain rate, and solute concentration on parameters P_1, n, t_0, and w of the KEMC model should be predefined by such low scale simulations, and then adjusted on macroscopic experiments. The differences between strain ageing due to substitutional atoms and interstitial ones could also be highlighted by such simulations. The final objective could be to obtain for each base metal a unified model for strain ageing suitable for all temperatures, all strain level, all strain rates, and all solute concentration value. A validation of such a model could be obtain by testing its ability to correctly reproduce the evolution of the critical plastic strain as a function of all these parameters, as it can be seen on figure 77 extracted from recent experimental studies on Al-Mg alloys ([216, 227]).
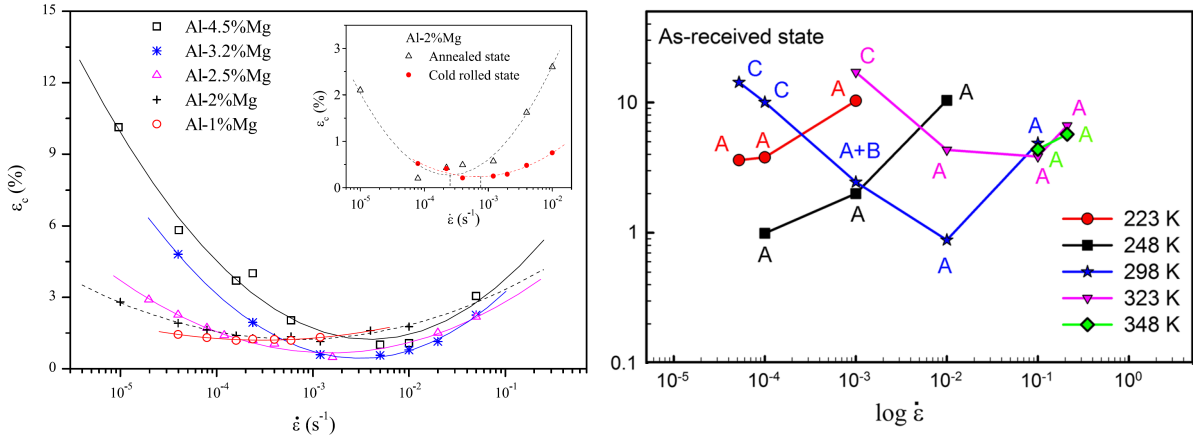
FIGURE 77 – (left) Evolution of the critical plastic strain as a function of strain rate and solute concentration in an Al-Mg alloy [216]. (right) Evolution of the critical plastic strain as a function of strain rate and temperature in an Al-Mg alloy [227]. The influence of micro-structure is also investigated in this latter article.

III. Relation between strain ageing, strain localisation, and ductile failure

Clarifying the links between strain localisation and ductile failure of metallic materials is a very topical challenge that has induced many recent experimental and numerical studies. The question of the responsibility of failure between the mechanic (strain localization) and the material (ductile damage) is a very difficult and interesting topic that is besides very probably dependant on the investigated metallic material. In the case of alloys showing strain ageing phenomena, the problem is even more complex since a competition takes place between propagating strain localisation bands, the non propagating necking like one, and ductile damage.

It is well known the ductility of tensile smooth, notched, and cracked specimens is reduced in the domain where PLC effect is present. Another very relevant and obvious influence of the Portevin - Le Chatelier effect on failure has been reported in 2007 in the PhD thesis of M.Maziere in a Nickel based super alloy [159], and in 2011 in a C-Mn steel by H.Wang [196]. In both cases it was observed that the (ductile) failure of axi-symmetrical smooth tensile specimens was flat with a small cup-cone outside the PLC domain and fully slant inside it. These observations are summarized on figure 78.

Modelling this influence of PLC effect on the ductile failure of tensile specimens is from our
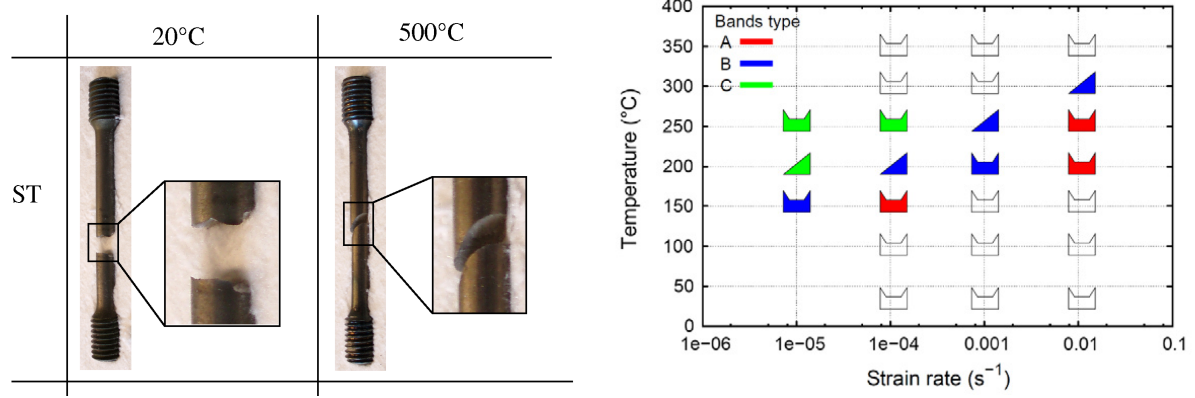
FIGURE 78 – (left) Difference in the failure mode of axi-symmetrical smooth tensile specimens made of nickel based superalloy outside (20°C) and inside (500°C) the PLC domain. (right) Almost the same observation made on a C-Mn steel by H.Wang [196].

point of view an original and relevant approach to understand the rôle of damage and strain localisation in the final failure of specimens. A complete model coupling plasticity, damage, and strain ageing should be proposed and calibrated in order to model the difference in strain to failure and failure modes observed inside and outside the PLC domain. A recent attempt has been made to introduce in this way the strain ageing contribution in a ductile damage model [224]. However, the coupling between plasticity, damage, and strain ageing makes it rather difficult to identify the numerous parameters and some specific experiments will probably have to be proposed in the future to overcome this problem.

IV. PLC and fatigue, PLC and multi-axial loadings

The Portevin - Le Chatelier effect has been reported under cycling loading conditions in various material like cobalt based super-alloys [112, 129, 206, 221], nickel based super-alloys [108], steels [132, 133, 210], aluminium alloys [80], and copper alloys [36, 89]. The observations are almost always the same : in a given range of temperature and/or strain rate and/or strain amplitude, the serrations appears after a given number of cycle together with a strong isotropic cyclic hardening and a decrease in life length of specimens. However, up to recently the full stress vs. strain curves were not recorder during most of the fatigue experiments and consequently many evidences of Portevin - Le Chatelier effect under such conditions have been missed in the past.

The problem of the command of fatigue experiments in presence of visco-plastic instabilities is also crucial. Usually fatigue tests with relatively small amplitudes are controlled using an extensometer whose gauge length can be smaller than the whole gauge length of the specimen. When the deformation is homogeneous it is a good solution to prescribe accurately the desired strain amplitude to the specimen. But when PLC effect occurs together with strain localisation it can have disastrous effect on the control of the experiment especially if the bands propagates outside the extensometer gauge length. There is consequently an interesting challenge to carry out precise and accurately controlled fatigue experiment in presence of the Portevin - Le Chatelier effect for different temperature, strain rates, and strain amplitudes, and to evaluate its influence on the life length of the specimens. The ability of the modified KEMC model to correctly reproduce these experiments should also be tested.

In the same spirit, the Portevin - Le Chatelier effect should be investigated more frequently under multi-axial stress states. All the experiment proposed up to now are based on uniaxial

152

smooth tension (monotonic, cyclic, creep, relaxation), usually along one single direction [16]. PLC effect has however also been reported under torsion or shear [207, 213], and for non uniform stress states like in notched and crack specimens [192, 202]. Such experiments can be used as very suitable validation examples to test the identification of the model. Finally it would be very valuable to find which specific experiments coupling all the aspect presented in this section (tension, creep, relaxation, cyclic, notch, crack, shear, ...) would be the more adequate to evaluate rapidly as many material parameters as possible.

6.2 Towards fast, representative, and reliable finite element simulations of strain ageing

V. Stabilization of the model, elimination of serrations for fast simulations

One of the main difficulty while simulating the Portevin - Le Chatelier effect with finite element simulations is the duration of the computations. Because of the propagation of the plastic strain localisation bands, the time step remains continuously very small, at least once the PLC effect occurs. When some fast approximate simulations are required, the strain ageing term is generally omitted by prescribing $P_1 = 0$, however the negative strain rate sensitivity is lost in the same time. It would be convenient to be able to run finite element simulations accounting for the negative strain rate sensitivity but without serrations and band propagation for two reasons :
  — to get rapidly some approximate evaluations of the stress components during finite element simulations on structures in the PLC domain, the stress level calculated being as closed as possible to the one calculated with the complete model.
  — to dissociate the influence of negative strain rate sensitivity and of strain localisation for example during study on the influence of PLC effect on ductile failure, by comparing the results given by the approximate and the complete model.

A solution to postpone the serrations during tensile simulation by modifying the evolution equation for the ageing time t_a has been proposed recently by F.Zhang [203]. Their solution is to slow done the transient evolution of the ageing time t_a with an additional parameter fixed in advance. We think that this modification is not the most adequate one to fulfil the objectives presented just above, and that a more clever modification of the model could be proposed. Using the prediction of the critical strain based on the stability analysis of section 4 the modification of the evolution equation of t_a could be tuned in order to remain continuously at the border of the unstable domain. The model would then be in a given sense the stable model the closest to the unmodified one. This idea could be implemented and tested for different materials and specimens.

VI. Rôle of the machine stiffness

The influence of the machine stiffness on the Portevin - Le Chatelier effect has been reported from the very early articles of the 60's. It appears also as an important parameter in the theoretical studies of P.Penning [50] and S.Mesarovic [107]. However this stiffness is usually not accounted for in the finite element simulations and a perfectly rigid machine is assumed (or a perfectly soft one for simulations at a constant stress rate). It has be showed in an article by H.Wang

---

16. In some cases even under simple tensile loadings, the anisotropy of the material and of the PLC effect would required some advanced version of the KEMC model.

in 2012 [202] that even a rather rigid machine with a stiffness identified on the experimental data (basically on the difference between extensometer and cross-head displacement measures) can modify significantly the results of the simulations. A exhaustive study on the influence of the machine stiffness on the main characteristics of serrations should be carried out based on the post-critical analysis presented on section 4.3.

To get further, the tensile machine should even be considered itself as a dynamic system whose response is dependant on the velocity of the solicitation. A complete coupling between the dynamic response of the machine and of the specimen could be accounted for in the simulation and compared with the usual assumption of a perfectly rigid machine.

VII. Regularisation of models, experimental evaluation of material internal length

As discussed in sections 4.2 and 4.3, the question of mesh sensitivity of finite element simulations in the presence of serrations and strain localisation is not completely solved. It seems that in the worth case i.e. 2D plane stress, a weak positive strain rate sensitivity outside of the PLC domain, and elements aligned along preferential localisation angle, some characteristics of the strain ageing localisation bands are highly mesh sensitive. Many parameters may limit this mesh sensitivity like geometric effect via 3D simulations, positive strain rate sensitivity, and free randomly oriented meshes. However all these methods are not effective in all the cases. For example the geometric regularization is non-effective for shearing tests, and the positiveness of strain rate sensitivity is a material characteristic that should not be artificially increased.

The introduction of an internal length – for example through an additive gradient term – in the KEMC model is probably the only solution that guarantee mesh insensitive simulations in any cases. The gradient term is taken on the cumulated plastic strain, on its rate, or on the whole inelastic strain tensor. One main challenge is then the identification of the internal length that required very precise and reliable full field experimental measures of the strain. The digital image correlation is probably the perfect tool for that, but it should be used very carefully in order not to identified unrealistic value for the internal length. An interesting project would be to identify this internal length for different experimental conditions (specimen size and shape, grain size, prescribed global strain rate,...) and to conclude on the physical meaning of this latter.

6.3   Modeling strain-ageing like phenomena in advanced materials

VIII. Strain ageing in advanced high strength steels

Serrated yielding has been observed recently in many austenitic stainless steels [151, 165, 182, 186, 197, 219]. All these steels belong to the family of advanced high strength steels (AHSS) and are called TRIP steels (transformation induce plasticity), TWIP steels (twinning induce plasticity), or 3rd generation steels that couple both effects. The particularity of these steels is that negative strain rate sensitivity and serrated yielding occurs at room temperature, contrary to ferritic steels for which it is observed at intermediate temperature (i.e. around 200°C). Contrary to what is sometimes mentioned in article reporting this phenomenon, the usual strain ageing mechanisms (interaction between dislocations and carbon atoms) can not be responsible for serrated yielding at this temperature since the diffusion coefficient of carbon is very too low. Serrated yielding is more probably due to some more complex interactions of dislocation core with twins (for TWIP steels), or new martensitic phase (for TRIP steel). However since the macroscopic manifestations in these steels look very similar to the usual PLC effect, it could probably be modelled using a modified version of the KEMC model. An interesting project

would be to study in details this phenomena on one of these particular steels with the following steps :

— Observation and quantification of serrated yielding (statistical analysis) and strain localisation (spatio-temporal diagrams via DIC) during tensile experiments.
— Evidence of the physical mechanism responsible for strain ageing using interrupted tests and micro-structural observations.
— Modification of the KEMC model to account for the specificity of strain-ageing like phenomenon is these steels.
— Calibration of the model and finite element simulation of serrated yielding, investigations on the influence on failure of specimens.
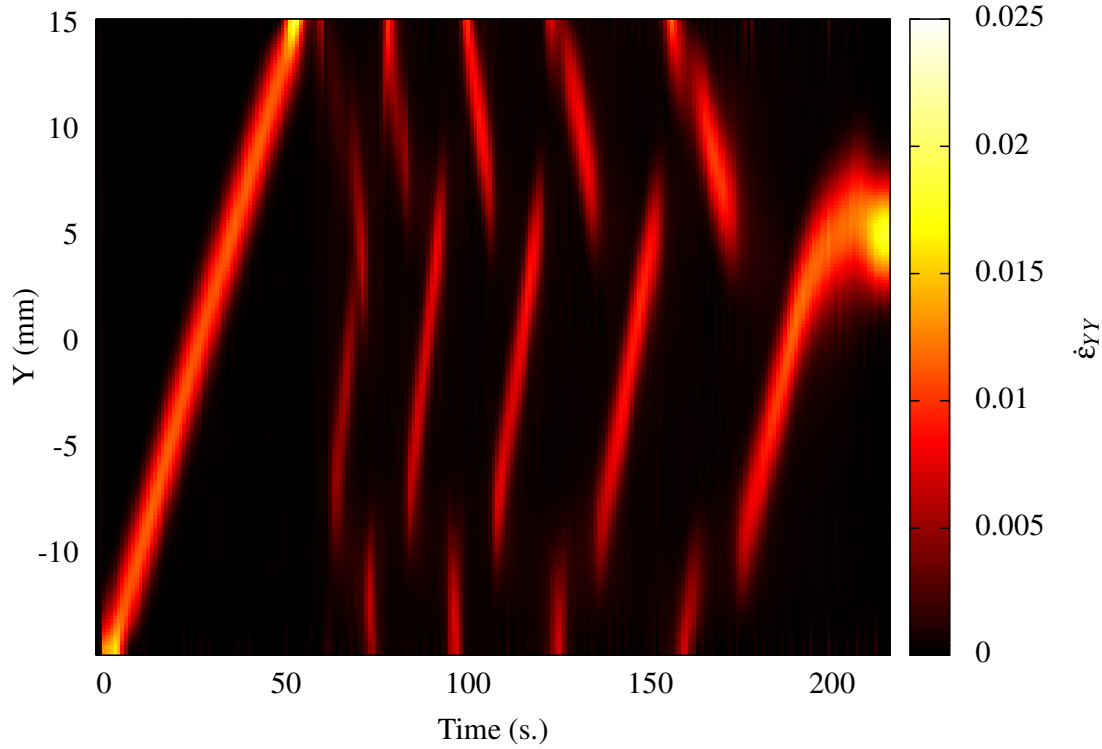
FIGURE 79 – Experimental (DIC) spatio-temporal diagram showing strain localisation in a 3rd generation advanced high strength steels. The three types of strain localisations are present in this case : Lüders single propagating band (left), PLC like repetitive propagating bands (middle), and final necking (right).

IX. Strain ageing in heterogeneous materials

Metal matrix composites are designed by introducing in a metal matrix some ceramic microparticles. In the case of aluminium alloy reinforced by Al_2O_3 particles, serrated yielding has been observed for low volume fraction (2% to 10%) of particles [130, 155, 169], but also for rather high volume fractions (up to 60%) [134]. The addition of particles in the metallic alloy influences its mechanical response in terms of average stress level and ductility, but also the characteristics of serrated yielding (critical plastic strain, shape of serrations,...). The size, the shape, and the volume fraction of composites seems to influence the PLC effect in such materials and it would consequently be useful to use numerical tools to design some composites where serrated yielding,

155

is postponed, limited, or even suppressed. Following the example of figure 80 a large number of finite element simulations could then be launched playing with different parameters like particle shape, spacing, size and volume fraction. The post-critical analysis tools of section 4.3 should then be used and some advices on the design of such composites should be provided.
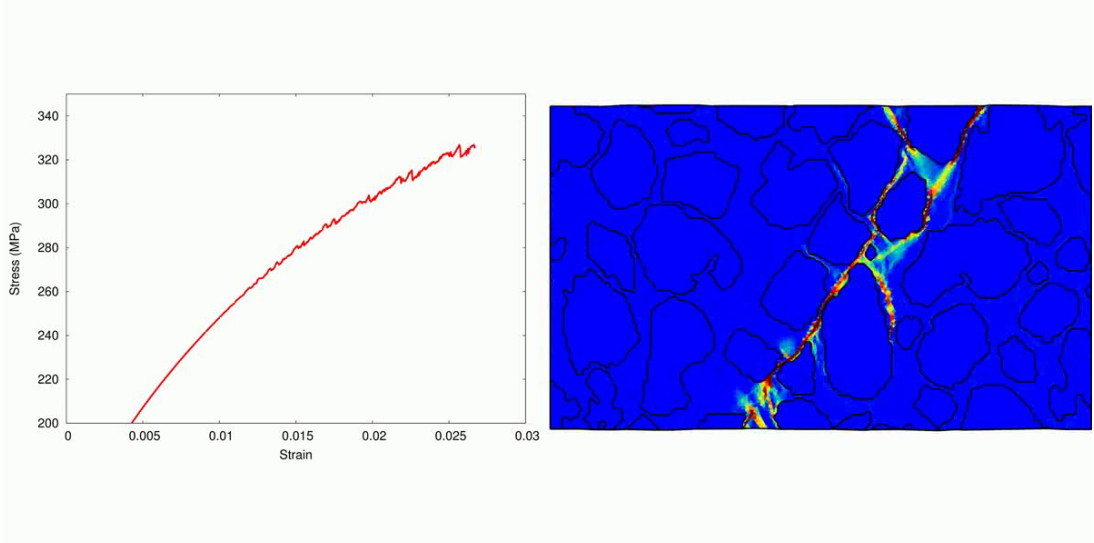
FIGURE 80 – Finite element simulation of the propagation of a PLC band in a metal matrix composite with a high volume fraction of particles ($\sim 60\%$). The band pass through the particles.

X. Serrated yielding at very low temperature, spatio-temporal elasto-visco-plastic instabilities in non crystalline materials

Low temperature ($4K$) serrated yielding as been reported in Aluminium alloy in 1981 by Y.Estrin [65] and summarized some years latter by Pustovalov [173]). This kind of visco-plastic instabilities look very similar to PLC effect. Serrated yielding seems however to be due in this case to thermo-mechanical coupling effects, based on the heat generation associated with plastic events that may gives rise to material softening. Even if the experimental results are hard to obtain because of the difficulty to work at such low temperatures, the subject is very interesting and should be investigated with more details for a better understanding of elementary plasticity mechanisms.

Serrated yielding has been observed in 2009 by G.Wang [185] in some bulk metallic glasses during compression experiments at room temperature. The serrations look very similar to PLC C-type ones even if the physical origin is totally different compared with strain ageing. In the case of metallic glasses (amorphous materials), it seems that serrated yielding is due to generation and propagation of shear bands over short distances. However since these kind of materials are rather new, the phenomenon is not very well understood and some complementary experimental and theoretical studies should be engaged.

Finally, an analogy is made for years between the PLC effect and earth quakes (see for example E.N.Andrade in 1910 [19]). It is then logical to compare more in details the similarities and differences between both phenomena, from their physical origin at low scale level, up to their macroscopic manifestations. This is especially justified since one of the most common mechanical

model used for earth quakes simulations is very similar to the KEMC model. This latter called the "rate and state model" (see the articles of H.Perfettini [160] and A.Ruina [69] for more details) is based on an internal variable θ whose evolution equation is the following :

$$\frac{d\theta}{dt} = 1 - \frac{V\theta}{d_c} \tag{130}$$

where V is a slip velocity and d_c a characteristic distance for the unstable event. This state variable θ is then introduced via a logarithmic term in the frictional stress and is at the origin of intermittent and heterogeneous slip. It appears clearly that this model is then very similar to the KEMC one and to the evolution of the ageing time t_a. It would consequently be very interesting to organize some collaborations between both scientific community in order to exchange experiences about this fascinating family of instabilities.

7 References

[1] M. Coulomb. Recherche théorique et expérimentale sur la force de torsion et sur l'élasticité des fils de métal. *Mémoire de l'Académie Royale des Sciences*, pages 229–269, 1784.

[2] G. Rennie. Account of experiments made on the strength of materials. *Phil. Trans. R. Soc. Lond.*, 108 :118–136, 1818.

[3] A. Duleau. *Essai théorique et expérimental sur la résistance du fer forgé*. Courcier, Paris, 1820.

[4] J. Leslie. *Element of natural philosophy*. Edinburgh, 1823.

[5] T. Tredgold. Experiments on the elasticity and strength of hard and soft steel. *Phil. Trans. R. Soc. Lond.*, 114 :354–359, 1824.

[6] A. Seguin. *Des ponts en fils de fer*. Bachelier, Paris, 1826.

[7] F.J. von Gerstner. *Handbuch der Mechanik - erster Band : Mechanik Fester Körper*. Johann Spurny, Prag., 1831.

[8] F. Savart. Recherche sur les vibrations longitudinales. *Annales de Chimie et de Physique*, T65 :337–402, 1837.

[9] M.A. Masson. Sur l'élasticité des corps solides. *Annales de Chimie et de Physique*, SER3-T3 :451–462, 1841.

[10] J. V. Poncelet. *Introduction à la mécanique industrielle physique ou expérimentale*. Thiel, Metz, 1841.

[11] G. Piobert, I. Didion, and A. Morin. Expérience sur la pénétration des projectiles dans le fer forgé. *Mémoire de l'Artillerie*, pages 501–537, 1842.

[12] M.G. Wertheim. Recherches sur l'élasticité. *Annales de Chimie et de Physique*, Série 3 – Tome 12 :385–454, 1844.

[13] W. Lüders. Über die äusserung der elasticität an stahlartigen eisenstäben und stahlstäben, und über eine beim biegen solcher stäbe beobachtete molecularbewegung. *Dinglers Polytech*, J5 :18–22, 1860.

[14] A. Morin. *Résistance des Matériaux - Tome 1*. Paris, 1862.

[15] D. Adamson. On the mechanical and other properties of iron and mild steel. *Journal of Iron and Steel Institute*, 2 :383–403, 1878.

[16] L. Hartmann. *Distribution des déformations dans les métaux soumis à des efforts*. Berger Levrault, Paris, 1896.

[17] F.R.S. Trouton and A.O. Rankine. On the stretching and torsion of a lead wire beyond the elastic limit. *Philosophical magazine*, 8 :538–556, 1904.

[18] A. Le Chatelier. Influence du temps et de la température sur les essais au choc. *Revue de métallurgie*, 6 :914–917, 1909.

[19] E.N.D. Andrade. On the viscous flow in metals, and allied phenomena. *Proceedings of the Royal Society of London Series A-Containing Papers of a Mathematical and Physical Character*, 84 :1–12, 1910.

[20] W. Rosenhain and L. Archbutt. Tenth report to the alloys research committee : on the alloys of aluminium and zinc. *Proceedings of the Institution of Mechanical Engineers*, 1-2 :318–445, 1912.

[21] A. Portevin and F. Le Chatelier. Sur le phénomène observé lors de l'essai de traction d'alliages en cours de transformation. *Comptes Rendus de l'Academie des Sciences*, 176 :507–510, 1923.

[22] M.J. Manjoine. Influence of rate of strain and temperature on yield stresses of mild steel. *Journal of Applied Mechanics*, 11 :211–218, 1944.

[23] A.H. Cottrell and B.A. Bilby. Dislocation theory of yielding and strain ageing of iron. *Proc. Phys. Soc.*, A62 :49–62, 1949.

[24] A.W. Sleeswyk. Slow strain-hardening of ingot iron. *Acta Metallurgica*, 6 :598–603, 1958.

[25] T.C. Lindley and R.E. Smallman. The plastic deformation of polycrystalline vanadium at low temperatures. *Acta Metallurgica*, 11 :361–371, 1963.

[26] B. Russell. Repeated yielding in tin bronze alloys. *Philosophical magazine*, 8 :615–630, 1963.

[27] J. Friedel. *Dislocations*, chapter 16, pages 405–414. Oxford, 1964.

[28] B.A. Wilcox and G.C. Smith. The portevin - le chatelier effect in hydrogen charged nickel. *Acta Metallurgica*, 12 :371–376, 1964.

[29] J.D. Baird and A. Jamieson. Effects of manganese and nitrogen on tensile properties of iron in range 20-600 degrees c. *Journal of the Iron and Steel Institute*, 204 :793–803, 1966.

[30] J.S. Blakemore and E.O. Hall. Blue-brittle behaviour of mild steel. *Journal of the Iron and Steel Institute*, 204 :817–820, 1966.

[31] B.J. Brindley and J.T. Barnby. Dynamic strain ageing in mild steel. *Acta Metallurgica*, 14 :1765 – 1780, 1966.

[32] A.T. Thomas. The tensile deformation behaviour of an aluminium-magnesium alloy. *Acta Metallurgica*, 14 :1363 – 1374, 1966.

[33] B.A. Wilcox and A.R. Rosenfield. On serrated yielding and negative strain-rate sensitivity. *Materials Science and Engineering*, 1 :201–205, 1966.

[34] S.R. Bodner and A. Rosen. Discontinuous yielding of commercially-pure aluminium. *J. Mech. Phys. Solids*, 15 :63–77, 1967.

[35] D.J. Dingley and D. McLean. Components of the flow stress of iron. *Acta Metallurgica*, 15 :885–901, 1967.

[36] R.K. Ham and D. Jaffrey. Dislocation multiplication, vacancy accumulation, and the onset of jerky flow during forward and reverse strain in cu-3.2 at% sn. *Philosophical magazine*, 15 :247–256, 1967.

[37] A. Rosen and S.R. Bodner. The influence of strain rate and strain ageing on the flow stress of commercially-pure aluminium. *J. Mech. Phys. Solids*, 15 :47–62, 1967.

[38] N.G. Turner and W.T. Roberts. Dynamic strain ageing in titanium. *Journal of the Less Common Metals*, 16 :37 – 44, 1968.

[39] B.J. Brindley and P.J. Worthington. Serrated yielding in aluminium-3% magnesium. *Acta Metallurgica*, 17 :1357 – 1361, 1969.

[40] A.J.R. Soler-Gomez and W.J.M. Tegart. Serrated flow in gold-indium alloys. *Philosophical magazine*, 20 :495–509, 1969.

[41] B.J. Brindley. The effect of dynamic strain-ageing on the ductile fracture process in mild steel. *Acta Metallurgica*, 18 :325 – 329, 1970.

[42] M.J. Roberts and W.S. Owen. Unstable flow in martensite and ferrite. *Metallurgical Transactions*, 1 :3203–3213, 1970.

[43] I.E. Dolzhenkov. The nature of blue brittleness of steel. *Metallovedenie i Termicheskaya Obrabotka Metallov*, 3 :pp. 42–47, 1971.

[44] P.G. McCormick. Portevin-le chatelier effect in an al-mg-si alloy. *Acta Metallurgica*, 19 :463–471, 1971.

[45] A. Wijler and J.S. Vanwestrum. Serrated yielding and inhomogeneous deformation in Au (14 at% Cu). *Scripta Metallurgica*, 5 :159–163, 1971.

[46] A. Wijler and J.S. Vanwestrum. Strain rate experiments and portevin le chatelier effect in au (14 at% cu). *Scripta Metallurgica*, 5 :531–535, 1971.

[47] A.M. Garde, A.T. Santhanam, and R.E. Reed-Hill. The significance of dynamic strain aging in titanium. *Acta Metallurgica*, 20 :215 – 220, 1972.

[48] J. Guillot and J. Grilhe. Phenomene portevin-le chatelier dans les alliages al-mg a hautes temperatures, en fonction de la concentration. *Acta Metallurgica*, 20 :291 – 295, 1972.

[49] P.G. McCormick. Inverse portevin-le chatelier effect in an Al-Mg-Si alloy. *Scripta Metallurgica*, 6 :165–169, 1972.

[50] P. Penning. Mathematics of the Portevin-Le Chatelier effect. *Acta Materialia*, 20 :1169–1175, 1972.

[51] H.M. Tensi, H. Borchers, and P. Dropmann. Portevin-le chatelier effect in aluminum-magnesium single-crystals. *Acta Metallurgica*, 20 :87–93, 1972.

[52] A. Wijler, J.S. Vanwestrum, and A. VanDenBeukel. New type of stress-strain curve and portevin-le chatelier effect in Au (14 at% Cu). *Acta Metallurgica*, 20 :355–362, 1972.

[53] W.C. Leslie, L.J. Cuddy, and R.J. Sober. Serrated yielding and flow in substitutional solid solutions of alpha iron. In *ICSMA3, Vol. 1, Cambridge*, 1973.

[54] W. Räuchle, O. Vöhringer, and E. Macherauch. Der portevin-le chatelier-effekt bei alpha-kupfer-zinn-legierungen. *Materials Science and Engineering*, 12 :147 – 161, 1973.

[55] S.H. van den Brink and P.G. McCormick. The ageing time for serrated yielding in a au-cu alloy. *Scripta Metallurgica*, 8 :1251 – 1254, 1974.

[56] A. Wijler, M.M. Vrijhoef, and A. Vandenbeukel. Onset of serrated yielding in Au-Cu alloys. *Acta Metallurgica*, 22 :13–19, 1974.

[57] A. van den Beukel. Theory of the effect of dynamic strain ageing on mechanical properties. *Physica Status Solidi*, 30 :197–206, 1975.

[58] S.H. van den Brink, A. van den Beukel, and P.G. McCormick. Strain rate sensitivity and portevin-le chatelier effect in au-cu alloys. *Physica Status Solidi A-Applied Research*, 30 :469–477, 1975.

[59] J.R.G. da Silva and R.B. McLellan. Diffusion of carbon and nitrogen in b.c.c. iron. *Materials Science and Engeneering*, 26 :83 – 87, 1976.

[60] H. Fujita and T. Tabata. Discontinuous deformation in al-mg alloys under various conditions. *Acta Metallurgica*, 25 :793 – 800, 1977.

[61] P.G. McCormick. Strain rate sensitivity prior to the onset of serrated yielding in a pressurized low carbon steel. *Scripta Metallurgica*, 12 :197 – 200, 1978.

[62] H.J. Harun and P.G. McCormick. Effect of precipitation hardening on strain rate sensitivity and yield behaviour in an al-mg-si alloy. *Acta Metallurgica*, 27 :155 – 159, 1979.

[63] R.A. Mulford and U.F. Kocks. New observations on the mechanisms of dynamic strain aging and of jerky flow. *Acta Metallurgica*, 27 :1125 – 1134, 1979.

[64] N. Itoh, M. Ogaya, S. Ishiyama, T. Matsushita, Y. Hayashi, and M. Koike. The press formability of commercial pure titanium art warm working temperature. In *Science and Technology : proceedings of the Fourth International Conference on Titanium*, 1980.

[65] Y. Estrin and K. Tangri. Thermal mechanism of the anomalous temperature dependence of the flow stress. *Scripta Metallurgica*, 15 :1323 – 1328, 1981.

[66] N. Louat. On the theory of the portevin-le chatelier effect. *Scripta Metallurgica*, 15 :1167–1170, 1981.

[67] E. Pink and A. Grinberg. Serrated flow in a ferritic stainless steel. *Materials Science and Engineering*, 51 :1 – 8, 1981.

[68] R.W. Hayes. On a proposed theory for the disappearance of serrated flow in f.c.c. ni alloys. *Acta Metallurgica*, 31 :365 – 371, 1983.

[69] A. Ruina. Slip instability and state variable friction laws. *Journal of Geophysical Research*, 88 :359–370, 1983.

[70] A. van den Beukel, J. Blonk, and G.H. van Haastert. The strain dependence of static strain aging in a gold-copper alloy. *Acta Metallurgica*, 31 :69 – 75, 1983.

[71] G. H. van Haastert and A. van den Beukel. Static and dynamic strain aging in a ni(c) solid solution. *Physica Status Solidi*, 76 :609–614, 1983.

[72] G.G. Saha, P.G. McCormick, and P. Rama Rao. Portevin-le chatelier effect in an al-mn alloy i : Serration characteristics. *Materials Science and Engineering*, 62 :187 – 196, 1984.

[73] G.G. Saha, P.G. McCormick, and P. Rama Rao. Portevin-le chatelier effect in an al-mn alloy ii : Yield transition and strain rate sensitivity measurements. *Materials Science and Engineering*, 62 :197 – 203, 1984.

[74] J.-L. Strudel. Interactions between dislocations and impurities. In *Japan-France seminar on fundamental aspects of mechanical properties and microstructure evolution of stainless steels at high temperature*, pages 169–180. Tokyo, 1984.

[75] U.F. Kocks, R.E. Cook, and R.A. Mulford. Strain aging and strain hardening in ni-c alloys. *Acta Metallurgica*, 33 :623 – 638, 1985.

[76] L. P. Kubin and Y. Estrin. The Portevin-Le Chatelier effect in deformation with constant stress rate. *Acta Metallurgica*, 33 :397–407, 1985.

[77] R.B. Schwarz and L.L. Funk. Kinetics of the portevin-le chatelier effect in al 6061 alloy. *Acta Metallurgica*, 33 :295 – 307, 1985.

[78] Y. Estrin and L.P. Kubin. Local strain-hardening and nonuniformity of plastic-deformation. *Acta Metallurgica*, 34 :2455–2464, 1986.

[79] K. Chihab, Y. Estrin, L.P. Kubin, and J. Vergnol. The kinetics of the portevin-le chatelier bands in an al-5at%mg alloy. *Scripta Metallurgica*, 21 :203 – 208, 1987.

[80] J.M. Gentzbittel and R. Fougeres. The phenomenon of stress instabilities in cyclic deformation of Al-Li alloys. *Scripta Metallurgica*, 21 :1411–1416, 1987.

[81] H. Dybiec. The strain rate sensitivity during serrated yielding. *Scripta Metallurgica*, 22 :595–599, 1988.

[82] Y. Estrin and L.P. Kubin. Plastic instabilities : Classification and physical mechanisms. *Res Mechanica*, 23 :197–221, 1988.

[83] L.P. Kubin, K. Chihab, and Y. Estrin. The rate dependence of the portevin-le chatelier effect. *Acta Metallurgica*, 36 :2707 – 2718, 1988.

[84] L.P. Kubin and Y. Estrin. Strain Nonuniformities and Plastic Instabilities. *Revue de Physique Appliquee*, 23 :573–583, 1988.

[85] P.G. McCormick. Theory of flow localization due to dynamic strain ageing. *Acta Metallurgica*, 36 :3061–3067, 1988.

[86] Y. Estrin and L.P. Kubin. Collective dislocation behaviour in dilute alloys and the portevin - le chatelier effect. *Journal of the Mechanical Behavior of Materials*, 2 :255–292, 1989.

[87] L.P. Kubin and Y. Estrin. The strain rate sensitivity during serrated yielding - comment. *Scripta Metallurgica*, 23 :815–817, 1989.

[88] P.G. McCormick and Y. Estrin. Transient flow behavior associated with dynamic strain aging. *Scripta Metallurgica*, 23 :1231–1234, 1989.

[89] S.I. Hong and C. Laird. Cyclic deformation-behavior of cu-16 at%-al single-crystals : 1.strain burst behavior. *Materials Science and Engineering A*, 124 :183–201, 1990.

[90] L.P. Kubin and Y. Estrin. Evolution of dislocation densities and the critical conditions for the portevin-le chatelier effect. *Acta Metallurgica et Materialia*, 38 :697 – 708, 1990.

[91] H. Dybiec and M.C. Chaturvedi. Serrated yielding in inconel 718. *Archives of Metallurgy*, 36 :341–352, 1991.

[92] M. Fellner, M. Hamersky, and E. Pink. A comparison of the Portevin - Le Chatelier effect in constant-strain-rate and constant-stress-rate tests. *Materials Science and Engineering A*, 136 :157–161, 1991.

[93] L.P. Kubin and Y. Estrin. Dynamic Strain Aging and the Mechanical Response of Alloys. *Journal de Physique III*, 1 :929–943, 1991.

[94] F. Springer and C. Schwink. Quantitative investigations on dynamic strain aging in polycrystalline Cu-Mn alloys. *Scripta Metallurgica et Materialia*, 25 :2739–2744, 1991.

[95] P. Gomiero, Y. Brechet, F. Louchet, A. Tourabi, and B. Wack. Microstructure and mechanical properties of a Al-Li alloy - iii. quantitative analysis relation to toughness in Al-Li, Al-Cu-Li and Al-Li-Cu-Mg (2091) alloys. *Acta Metallurgica et Materialia*, 40 :863–871, 1992.

[96] L.P. Kubin, Y. Estrin, and C. Perrier. On static strain ageing. *Acta Metallurgica et Materialia*, 40 :1037 – 1044, 1992.

[97] J.M. Robinson and M.P. Shaw. The influence of specimen geometry on the portevin-lechatelier effect in an Al-Mg alloy. *Materials Science and Engineering A*, 159 :159–165, 1992.

[98] J. Balik and P. Lukac. Portevin-le chatelier instabilities in al-3 mg conditioned by strain-rate and strain. *Acta Metallurgica et Materialia*, 41 :1447–1454, 1993.

[99] D. Delafosse, G. Lapasset, and L.P. Kubin. Dynamic strain ageing and crack propagation in the 2091 al-li alloy. *Scripta Metallurgica et Materialia*, 29 :1379 – 1384, 1993.

[100] C.P. Ling and P.G. McCormick. The effect of temperature on strain-rate sensitivity in an Al-Mg-Si alloy. *Acta Metallurgica et Materialia*, 41 :3127–3131, 1993.

[101] C.P. Ling, P.G. McCormick, and Y. Estrin. A load perturbation method of examining dynamic strain-aging. *Acta Metallurgica et Materialia*, 41 :3323–3330, 1993.

[102] P.G. McCormick, S. Venkadesan, and C.P. Ling. Propagative instabilities - an experimental view. *Scripta Metallurgica et Materialia*, 29 :1159–1164, 1993.

[103] D. Park and J.G. Morris. The portevin-le chatelier effect in an Al-Mn-Mg alloy. *Scripta Metallurgica et Materialia*, 29 :365–369, 1993.

[104] M. Srinivas, G. Malakondaiah, and P.R. Rao. Fracture-toughness of fcc nickel and strain aging bcc iron in the temperature-range 77-773k. *Acta Metallurgica et Materialia*, 41 :1301–1312, 1993.

[105] C. Pujol. *Etude des mecanismes de deformation en traction et fluage du zircomium alpha entre 20°C et 300°c.* PhD thesis, Mines Paris - ParisTech, 1994.

[106] J.M. Robinson and M.P. Shaw. Observations on deformation characteristics and micro-structure in an al-mg alloy during serrated flow. *Materials Science and Engineering : A*, 174 :1 – 7, 1994.

[107] S. Mesarovic. Dynamic strain aging and plastic instabilities. *J. Mech. Phys. Solids*, 43 :671–700, 1995.

[108] K.B.S. Rao, S. Kalluri, G.R. Halford, and M.A. McGaw. Serrated flow and deformation substructure at room temperature in inconel 718 superalloy during strain controlled fatigue. *Scripta Metallurgica et Materialia*, 32 :493–498, 1995.

[109] M. Lebyodkin, Y. Brechet, Y. Estrin, and L. Kubin. Statistical behaviour and strain localization patterns in the portevin-le chatelier effect. *Acta Materialia*, 44 :4531 – 4541, 1996.

[110] D. Wagner, J.C. Moreno, and C. Prioul. Influence of post weld heat treatment on the dynamic strain aging of C-Mn steels. *Journal de Physique IV*, 6 :159–162, 1996.

[111] P. Hähner. On the critical conditions of the portevin-le chatelier effect. *Acta Materialia*, 45 :3695 – 3707, 1997.

[112] K.B.S. Rao, M.G. Castelli, G.P. Allen, and J.R. Ellis. A critical assessment of the mechanistic aspect in Haynes 188 during low-cycle fatigue in the range 25C to 1000C. *Metallurgical and Materials Transactions A*, 28A :347–361, 1997.

[113] M. Zaiser and P. Hahner. Oscillatory modes of plastic deformation : Theoretical concepts. *Physica Status Solidi B-Basic Research*, 199 :267–330, 1997.

[114] I. Choi, S. Jin, and S. Kang. Effects of microstructure and alloy contents on the lüders line formation in al-mg alloys. *Scripta Materialia*, 38 :887 – 892, 1998.

[115] D. Wagner, J.C. Moreno, and C. Prioul. Dynamic strain aging sensitivity of heat affected zones in C-Mn steels. *Journal of Nuclear Materials*, 252 :257–265, 1998.

[116] G. d'Anna and F. Nori. Critical dynamics of burst instabilities in the portevin - le chatelier effect. *Physical Review Letters*, 85 :4096–4099, 2000.

[117] S.V. Franklin, F. Mertens, and M. Marder. Portevin - le chatelier effect. *Phys. Rev. E*, 62 :8195–8206, 2000.

[118] Zs. Kovacs, J. Lendvai, and G. Vörös. Localized deformation bands in Portevin - Le Chatelier plastic instabilities at a constant stress rate. *Materials Science and Engineering A*, 279 :179–184, 2000.

[119] M. Lebyodkin, L. Dunin-Barkowskii, Y. Brechet, Y. Estrin, and L.P. Kubin. Spatio-temporal dynamics of the Portevin-le Chatelier effect : Experiment and modelling. *Acta Materialia*, 48 :2529–2541, 2000.

[120] L. Fournier, D. Delafosse, and T. Magnin. Oxidation induced intergranular cracking and Portevin - Le Chatelier effect in nickel base superalloy 718. *Materials Science and Engineering A*, 316 :166–173, 2001.

[121] C.L. Hale, W.S. Rollings, and M.L. Weaver. Activation energy calculations for discontinuous yielding in inconel 718spf. *Materials Science and Engineering : A*, 300 :153 – 164, 2001.

[122] S. Zhang, P.G. McCormick, and Y. Estrin. The morphology of Portevin- le Chatelier bands : finite element simulation for Al-Mg-Si. *Acta Materialia*, 49 :1087–1094, 2001.

[123] F. Chmelik, A. Ziegenbein, H. Neuhäuser, and P. Lukac. Investigating Portevin - Le Chatelier effect by the acoustic emission and laser extensometry techniques. *Materials Science and Engineering A*, 324 :200–207, 2002.

[124] D. Wagner, J.C. Moreno, C. Prioul, J.M. Frund, and B. Houssin. Influence of dynamic strain aging on the ductile tearing of C-Mn steels : modelling by a local approach method. *Journal of Nuclear Materials*, 300 :178–191, 2002.

[125] A. Benallal, T. Borvik, A. Clausen, and O. Hopperstad. Dynamic strain aging, negative strain-rate sensitivity and related instabilities. *Technische Mechanik*, 23 :160–166, 2003.

[126] M. Cieslar, C. Fressengeas, A. Karimi, and J.-L. Martin. Portevin-Le Chatelier effect in biaxially strained Al-Fe-Si foils. *Scripta Materialia*, 48 :1105–1110, 2003.

[127] F.B. Klose, A. Ziegenbein, H. Weidenmüller, and P. Hähner. Portevin - le chatelier effect in strain and stress controlled tensile tests. *Computational Materials Science*, 26 :80–86, 2003.

[128] S. Kok, M.S. Bharathi, A.J. Beaudoin, C. Fressengeas, G. Ananthakrishna, L.P. Kubin, and M. Lebyodkin. Spatial coupling in jerky flow using polycrystal plasticity. *Acta Materialia*, 51 :3651–3662, 2003.

[129] L.J. Chen, P.K. Liaw, H. Wang, Y.H. He, R.L. McDaniels, L. Jiang, B. Yang, and D.L. Klarstrom. Cyclic deformation behavior of HAYNES (R) HR-120 (R) superalloy under low-cycle fatigue loading. *Mechanics of Materials*, 36 :85–98, 2004.

[130] Y. Estrin and M.A. Lebyodkin. The influence of dispersion particles on the Portevin-Le Chatelier effect : from average particle characteristics to particle arrangement. *Materials Science and Engineering A*, 387 :195–198, 2004. 13th International Conference on the Strength of Materials (ICSMA 13), Budapest, HUNGARY, AUG, 2003.

[131] S. Graff, S. Forest, J.-L. Strudel, C. Prioul, P. Pilvin, and J.-L. Béchade. Strain localization phenomena associated with static and dynamic strain ageing in notched specimen :experiments and finite element simulations. *Materials Science and Engineering A*, 387 :181–185, 2004.

[132] S.G. Hong and S.B. Lee. Dynamic strain aging under tensile and LCF loading conditions, and their comparison in cold worked 316L stainless steel. *Journal of Nuclear Materials*, 328 :232–242, 2004.

[133] S.G. Hong and S.B. Lee. The tensile and low-cycle fatigue behavior of cold worked 316L stainless steel : influence of dynamic strain aging. *International Journal of Fatigue*, 26 :899–910, 2004.

[134] A. Miserez and A.. Mortensen. Fracture of aluminium reinforced with densely packed ceramic particles : influence of matrix hardening. *Acta Materialia*, 52 :5331–5345, 2004.

[135] R. Shabadi, S. Kumar, H.J. Roven, and E.S. Dwarakadasa. Characterisation of PLC band parameters using laser speckle technique. *Materials Science and Engineering A*, 364 :140–150, 2004.

[136] R. Shabadi, S. Kumar, H.J. Roven, and E.S. Dwarakadasa. Effect of specimen condition, orientation and alloy composition on PLC band parameters. *Materials Science and Engineering A*, 382 :203–208, 2004.

[137] N.Q. Chinh, G. Horvath, Z. Kovacs, A. Juhasz, G. Berces, and J. Lendvai. Kinematic and dynamic characterization of plastic instabilities occurring in nano- and microindentation tests. *Materials Science and Engineering A*, 409 :100–107, 2005. Symposium on Micromechanics of Advanced Materials held in Honour of James C M Lis 80th Birthday held at the TMS 2004 Annual Meeting, San Francisco, CA, NOV, 2004.

[138] X. Duan, M. Jain, D. Metzger, J. Kang, D.S. Wilkinson, and J.D. Embury. Prediction of shear localization during large deformation of a continuous cast Al-Mg sheet. *Materials Science and Engineering A*, 394 :192–203, 2005.

[139] C. Fressengeas, A.J. Beaudoin, M. Lebyodkin, L.P. Kubin, and Y. Estrin. Dynamic strain aging : a coupled dislocation-solute dynamic model. *Materials Science and Engineering A*, 51 :226–230, 2005.

[140] S. Graff, S. Forest, J.-L. Strudel, C. Prioul, P. Pilvin, and J.-L. Béchade. Finite element simulations of dynamic strain ageing effects at v-notches and crack tips. *Scripta Materialia*, 52 :1181–1186, 2005.

[141] M.A. Lebyodkin and Y. Estrin. Multifractal analysis of the Portevin-Le Chatelier effect : General approach and application to AlMg and AlMg/Al2O3 alloys. *Acta Materialia*, 53 :3403–3413, 2005.

[142] H. Louche, P. Vacher, and R. Arrieux. Thermal observations associated with the Portevin-le Chatelier effect in an al-mg alloy. *Materials Science and Engineering A*, 404 :188–196, 2005.

[143] R.C. Picu, G. Vincze, F. Ozturk, J.J. Gracio, F. Barlat, and A.M. Maniatty. Strain rate sensitivity of the commercial aluminum alloy AA5182-O. *Materials Science and Engineering A*, 390 :334–343, 2005.

[144] N. Ranc and D. Wagner. Some aspect of Portevin-Le Chatelier plastic instabilities investigated by infrared pyrometry. *Materials Science and Engineering A*, 394 :87–95, 2005.

[145] H. Ait-Amokhtar, S. Boudrahem, and C. Fressengeas. Spatiotemporal aspects of jerky flow in al-mg alloys, in relation with the mg content. *Scripta Materialia*, 54 :2113–2118, 2006.

[146] H. Ait-Amokhtar, P. Vacher, and S. Boudrahem. Kinematics fields and spatial activity of Portevin-Le Chatelier bands using the digital image correlation method. *Acta Materialia*, 54 :4365–4371, 2006.

[147] A. Benallal, T. Berstad, T. Borvik, A.H. Clausen, and O.S. Hopperstad. Dynamic strain aging and related instabilities : experimental, theoretical and numerical aspects. *European Journal of Mechanics - A/Solids*, 25 :397 – 424, 2006.

[148] G. Besnard, F. Hild, and S. Roux. "Finite-Element" displacement fields analysis from digital images : Application to portevin-le chatelier bands. *Experimental Mechanics*, 46 :789–803, 2006.

[149] O.S. Hopperstad, T. Borvik, T. Berstad, and A. Benallal. Finite element simulations of the Portevin - Le Chatelier effect in aluminium alloy. *Journal de Physique IV*, 134 :435–441, 2006.

[150] J. Kang, D.S. Wilkinson, M. Jain, J.D. Embury, A.J. Beaudoin, S. Kim, R. Mishira, and A.K. Sachdev. On the sequence of inhomogeneous deformation processes occurring during tensile deformation of strip cast AA5754. *Acta Materialia*, 54 :209–218, 2006.

[151] L. Chen, H.-S. Kim, S.-K. Kim, and B.C. De Cooman. Localized deformation due to Portevin-LeChatelier effect in 18Mn-0.6C TWIP austenitic steel. *ISIJ International*, 47 :1804–1812, 2007.

[152] F. Chmelik, F.B. Klose, H. Dierke, J. Sach, H. Neuhäuser, and P. Lukac. Investigating Portevin - Le Chatelier effect in strain rate and stress rate controlled tests by the acoustic emission and laser extensometry techniques. *Materials Science and Engineering A*, 426 :52–60, 2007.

[153] K. Darowicki and J. Orlikowski. Impedance analysis of Portevin-Le Chatelier effect on aluminium alloy. *Electrochimica Acta*, 52 :4043–4052, 2007.

[154] K. Darowicki, J. Orlikowski, A. Zielinski, and W. Jurczak. Quadratic Cohen representations in spectral analysis of serration process in Al-Mg alloys. *Computational Materials Science*, 39 :880–886, 2007.

[155] H. Dierke, F. Krawehl, S. Graff, S. Forest, J. Sach, and H. Neuhäuser. Portevin - Le Chatelier effect in Al-Mg alloys : Influence of obstacles - experiments and modelling. *Computational Materials Science*, 39 :106–112, 2007.

[156] H. Halim, D.S. Wilkinson, and M. Niewczas. The Portevin - Le Chatelier (PLC) effect and shear band formation in an aa5754 alloy. *Acta Materialia*, 55 :4151–4160, 2007.

[157] O.S. Hopperstad, T. Borvik, T. Berstad, 0.G. Lademo, and A. Benallal. A numerical study on the influence of the Portevin - Le Chatelier effect on necking in an aluminium alloy. *Model. Simul. Mater. Sci. Eng.*, 15 :747–772, 2007.

[158] H. Jiang, Q. Zhang, X. Chen, Z. Chen, Z. Jiang, X. Wu, and J. Fan. Three types of Portevin - Le Chatelier effect : Experiment and modelling. *Acta Materialia*, 55 :2219–2228, 2007.

[159] M. Mazière. *Overspeed burst of turboengine disks.* PhD thesis, Mines Paris - ParisTech, 2007.

[160] H. Perfettini and J.-P. Avouac. Modeling afterslip and aftershocks following the 1992 Landers earthquake. *Journal of Geophysical Research-Solid Earth*, 112, 2007.

[161] A. Sarkar, A. Chatterjee, P. Barat, and P. Mukherjee. Comparative study of the Portevin-Le Chatelier effect in interstitial and substitutional alloy. *Materials Science and Engineering A*, 459 :361–365, 2007.

[162] M. Srinivas, S. V. Kamat, and P. Rama Rao. Influence of dynamic strain ageing on mixed mode I/III fracture toughness of Armco iron. *Materials Science and Engineering A*, 443 :132–141, 2007.

[163] G.F. Xiang, Q.C. Zhang, H.W. Liu, X.P. Wu, and X.Y. Ju. Time-resolved deformation measurements of the Portevin-Le Chatelier bands. *Scripta Materialia*, 56 :721–724, 2007.

[164] H. Ait-Amokhtar, C. Fressengeas, and S. Boudrahem. The dynamics of Portevin-Le Chatelier bands in an Al-Mg alloy from infrared thermography. *Materials Science and Engineering A*, 488 :540–546, 2008.

[165] S. Allain, P. Cugy, C. Scott, J.-P. Chateau, A. Rusinek, and A. Deschamps. The influence of plastic instabilities on the mechanical properties of a high-manganese austenitic FeMnC steel. *International Journal of Materials Research*, 99 :734–738, 2008.

[166] A. Benallal, T. Berstad, T. Borvik, O.S. Hopperstad, I. Koutiri, and R. Nogueira de Codes. An experimental and numerical investigation of AA5083 aluminium alloy in presence of the Portevin-Le Chatelier effect. *International Journal of Plasticity*, 24 :1916–1945, 2008.

[167] A. Chatterjee, A. Sakar, S. Bhattacharya, P. Mukherjee, N. Gayathri, and P. Barat. Markov property of continuous dislocation band propagation. *Physics Letters*, 372 :4016–4020, 2008.

[168] V. Garat, J.M. Cloue, D. Poquillon, and E. Andrieu. Influence of Portevin-Le Chatelier effect on rupture mode of alloy 718 specimens. *Journal of Nuclear Materials*, 375 :95–101, 2008.

[169] S. Graff, H. Dierke, S. Forest, H. Neuhäuser, and J.-L. Strudel. Finite element simulations of the Portevin - Le Chatelier effect in metal-matrix composites. *Philosophical magazine*, 88 :3389–3414, 2008.

[170] H. Jousset. *Viscoplasticité et microstructures d'un alliage de titane : effets de la température et de la vitesse de sollicitation.* PhD thesis, Mines Paris - ParisTech, 2008.

[171] T.A. Lebedkina and M.A. Lebyodkin. Effect of deformation geometry on the intermittent plastic flow associated with the portevin-le chatelier effect. *Acta Materialia*, 56 :5567–5574, 2008.

[172] M. Mazière, J. Besson, S. Forest, B. Tanguy, H. Chalons, and F. Vogel. Numerical modelling of the Portevin-Le Chatelier effect. *European Journal of Computational Mechanics*, 17 :761–772, 2008.

[173] V.V. Pustovalov. Serrated deformation of metals and alloys at low temperatures (Review). *Low Temperature Physics*, 34 :683–723, 2008.

[174] N. Ranc and D. Wagner. Experimental study by prometry of Portevin-Le Chatelier plastic instabilities–type a to type b transition. *Materials Science and Engineering A*, 474 :188–196, 2008.

[175] A.K. Roy, J. Pal, and C. Mukhopadhyay. Dynamic strain ageing of an austenitic superalloy - temperature and strain rate effects. *Materials Science and Engineering : A*, 474 :363 – 370, 2008.

[176] A. Sarkar, L. Charles, Jr. Webber, P. Barat, and P. Mukherjee. Recurrence analysis of the portevin-le chatelier effect. *Physics Letters*, 372 :1101–1105, 2008.

[177] R. Sharghi-Moshtaghin and S. Asgari. The characteristics of serrated flow in superalloy {IN738LC}. *Materials Science and Engineering : A*, 486 :376 – 380, 2008.

[178] J. Belotteau, C. Berdin, S. Forest, A. Parrot, and C. Prioul. Mechanical behavior and crack tip plasticity of a strain aging sensitive steel. *Materials Science and Engineering : A*, 526 :156–165, 2009.

[179] T. Böhlke, G. Bondar, Y. Estrin, and M.A. Lebyodkin. Geometrically non-linear modeling of the portevin-le chatelier effect. *Computational Materials Science*, 44 :1076 – 1088, 2009.

[180] L. Casarotto, H. Dierke, R. Tutsch, and H. Neuhaeuser. On nucleation and propagation of PLC bands in an Al-3Mg alloy. *Materials Science and Engineering A*, 527 :132–140, 2009.

[181] C.-M. Kuo, C.-H. Tso, and C.-H. Lin. Plastic instability of Al-Mg alloys during stress rate change test. *Materials Science and Engineering A*, 519 :32–37, 2009.

[182] T.A. Lebedkina, M.A. Lebyodkin, J.-P. Chateau, A. Jacques, and S. Allain. On the mechanism of unstable plastic flow in an austenitic femnc twip steel. *Materials Science and Engineering : A*, 519 :147–154, 2009.

[183] R.J. McDonald, C. Efstathiou, and P. Kurath. The Wavelike Plastic Deformation of Single Crystal Copper. *Journal of Engineering Materials and Technology - Transactions of the ASME*, 131, 2009.

[184] S. Varadhan, A.J. Beaudoin, and C. Fressengeas. Lattice incompatibility and strain-aging in single crystals. *J. Mech. Phys. Solids*, 57 :1733–1748, 2009.

[185] G. Wang, K.C. Chan, L. Xia, P. Yu, J. Shen, and W.H. Wang. Self-organized intermittent plastic flow in bulk metallic glasses. *Acta Materialia*, 57 :6146 – 6155, 2009.

[186] P.D. Zavattieri, V. Savic, L. G. Hector, J.R. Fekete, W. Tong, and Y. Xuan. Spatio-temporal characteristics of the Portevin-Le Chatelier effect in austenitic steel with twinning induced plasticity. *International Journal of Plasticity*, 25 :2298–2330, 2009.

[187] H. Ait-Amokhtar and C. Fressengeas. Crossover from continuous to discontinuous propagation in the Portevin-Le Chatelier effect. *Acta Materialia*, 58 :1342–1349, 2010.

[188] T. Li, Y. Liu, Z. Cao, D. Jiang, and L. Cheng. The tensile properties and high cyclic fatigue characteristics of Mg-5Li-3Al-1.5Zn-2RE alloy. *Materials Science and Engineering A*, 527 :7808–7811, 2010.

[189] M. Mazière, J. Besson, S. Forest, B. Tanguy, H. Chalons, and F. Vogel. Numerical aspects in the finite element simulation of the Portevin-Le Chatelier effect. *Comput. Methods Appl. Mech. Engrg.*, 199 :734–754, 2010.

[190] A. Benallal, T. Berstad, T. Borvik, R. Nogueira des Codes, and O. S. Hopperstad. Computational aspects in presence of negative strain-rate sensitivity with application to aluminium alloys exhibiting the Portevin-Le Chatelier effect. *Model. Simul. Mater. Sci. Eng.*, 19, 2011.

[191] C. Y. Cui, Y. F. Gu, Y. Yuan, and H. Harada. Dynamic strain aging in a new Ni-Co base superalloy. *Scripta Materialia*, 64 :502–505, 2011.

[192] R.N. De Codes and A. Benallal. Influence of specimen geometry on the portevin-le chatelier effect due to dynamic strain aging for the aa5083-h116 aluminum alloy. *Journal of Mechanics of Materials and Structures*, 6 :951–968, 2011. 11th Pan-American Congress of Applied Mechanics (PACAM)/48th Meeting of the Society-for-Natural-Philosophy (SNP), Foz do Iguacu, BRAZIL, JAN 04-08, 2010.

[193] R.N. De Codes, O.S. Hopperstad, O. Engler, O.-G. Lademo, J.D. Embury, and A. Benallal. Spatial and Temporal Characteristics of Propagating Deformation Bands in AA5182 Alloy at Room Temperature. *Metallurgical and Materials Transactions A*, 42A :3358–3369, 2011.

[194] S.H. Fu, Q.C. Zhang, Q. Hu, M. Gong, P.T. Cao, and H.W. Liu. The influence of temperature on the PLC effect in Al-Mg alloy. *Science China-technological Sciences*, 54 :1389–1393, 2011.

[195] C. Li, C.N. Xu, Y. Imai, and N. Bu. Real-Time Visualisation of the Portevin-Le Chatelier Effect With Mechanoluminescent-Sensing Film. *Strain*, 47 :483–488, 2011.

[196] H.D. Wang, C. Berdin, M. Mazière, S. Forest, C. Prioul, A. Parrot, and P. Le-Delliou. Portevin-Le Chatelier (PLC) instabilities and slant fracture in C-Mn steel round tensile specimens. *Scripta Materialia*, 64 :430–433, 2011.

[197] R. Larsson and L. Nilsson. On the modelling of strain ageing in a metastable austenitic stainless steel. *Journal of Materials Processing Technology*, 212 :46–58, 2012.

[198] A. Marais, M. Mazière, S. Forest, A. Parrot, and P. Le Delliou. Identification of a strain-aging model accounting for Lüders behavior in a C-Mn steel. *Philosophical Magazine*, 92 :3589–3617, 2012.

[199] M. Mazière and H. Dierke. Investigations on the portevin le chatelier critical strain in an aluminum alloy. *Computational Materials Science*, 52 :68 – 72, 2012.

[200] T. Sakthivel, K. Laha, M. Nandagopal, K.S. Chandravathi, P. Parameswaran, S. Panneer Selvi, M.D. Mathew, and S.K. Mannan. Effect of temperature and strain rate on serrated flow behaviour of hastelloy x. *Materials Science and Engineering : A*, 534 :580 – 587, 2012.

[201] B. Ter-Ovanessian, D. Poquillon, J.-M. Cloue, and E. Andrieu. Influence of local mechanical loading paths on the oxidation assisted crack initiation of alloy 718. *Materials Science and Engineering A*, 533 :43–49, 2012.

[202] H.D. Wang, C. Berdin, M. Mazière, S. Forest, C. Prioul, A. Parrot, and P. Le-Delliou. Experimental and numerical study of dynamic strain ageing and its relation to ductile fracture of a c-mn steel. *Materials Science and Engineering A*, 547 :19–31, 2012.

[203] F. Zhang, A.F. Bower, and W.A. Curtin. The influence of serrated flow on necking in tensile specimens. *Acta Materialia*, 60 :43–50, 2012.

[204] L. Ziani, S. Boudrahem, H. Ait-Amokhtar, M. Mehenni, and B. Kedjar. Unstable plastic flow in the Al-2%Mg alloy, effect of annealing process. *Materials Science and Engineering A*, 536 :239–243, 2012.

[205] C. Berdin and H. Wang. Local approach to ductile fracture and dynamic strain aging. *International Journal of Fracture*, 182 :39–51, 2013.

[206] J.-L. Chaboche, A. Gaubert, P. Kanouté, A. Longuet, F. Azzouz, and M. Mazière. Viscoplastic constitutive equations of combustion chamber materials including cyclic hardening and dynamic strain aging. *International Journal of Plasticity*, 46 :1 – 22, 2013.

[207] J. Coer, P.Y. Manach, H. Laurent, M.C. Oliveira, and L.F. Menezes. Piobert-Luders plateau and Portevin-Le Chatelier effect in an Al-Mg alloy in simple shear. *Mechanics Research Communications*, 48 :1–7, 2013.

[208] G. Saada and T. Kruml. Removal of plastic instabilities by reversal of the applied stress. *Philosophical Magazine*, 93 :256–271, 2013.

[209] D. Colas, E. Finot, S. Flouriot, S. Forest, M. Mazière, and T. Paris. Investigation and modeling of the anomalous yield point phenomenon in pure tantalum. *Materials Science and Engineering : A*, 615 :283 – 295, 2014.

[210] Z.Y. Huang, J.-L. Chaboche, Q.Y. Wang, D. Wagner, and C. Bathias. Effect of dynamic strain aging on isotropic hardening in low cycle fatigue for carbon manganese steel. *Materials Science and Engineering A*, 589 :34–40, 2014.

[211] P. Maj, J. Zdunek, M. Gizynski, J. Mizera, and K. J. Kurzydlowski. Statistical analysis of the Portevin-Le Chatelier effect in Inconel 718 at high temperature. *Materials Science and Engineering A*, 619 :158–164, 2014.

[212] P. Maj, J. Zdunek, J. Mizera, and K. J. Kurzydlowski. The effect of a notch on the Portevin-Le Chatelier phenomena in an Al-3Mg model alloy. *Materials Characterization*, 96 :46–53, 2014.

[213] P.Y. Manach, S. Thuillier, J.W. Yoon, J. Coer, and H. Laurent. Kinematics of Portevin-Le Chatelier bands in simple shear. *International Journal of Plasticity*, 58 :66–83, 2014.

[214] B. Max, B. Viguier, E. Andrieu, and J.-M. Cloue. A Re-examination of the Portevin-Le Chatelier Effect in Alloy 718 in Connection with Oxidation-Assisted Intergranular Cracking. *Metallurgical and Materials Transactions A*, 45A :5431–5441, 2014.

[215] J. Min, Jr.L.G. Hector, J. Lin, J.T. Carter, and A.K. Sachdev. Spatio-temporal characteristics of propagative plastic instabilities in a rare earth containing magnesium alloy. *International Journal of Plasticity*, 57 :52–76, 2014.

[216] H. Ait-Amokhtar, C. Fressengeas, and K. Bouabdallah. On the effects of the mg content on the critical strain for the jerky flow of al-mg alloys. *Materials Science and Engineering : A*, 631 :209 – 213, 2015.

[217] Y. Cai, C. Tian, S. Fu, G. Han, C. Cui, and Q. Zhang. Influence of gamma ' precipitates on Portevin-Le Chatelier effect of NI-based superalloys. *Materials Science and Engineering A*, 638 :314–321, 2015.

[218] B. Klusemann, G. Fischer, T. Boehlke, and B. Svendsen. Thermomechanical characterization of Portevin-Le Chatelier bands in AlMg3 (AA5754) and modeling based on a modified Estrin-McCormick approach. *International Journal of Plasticity*, 67 :192–216, 2015.

[219] J. Lorthios, M. Mazière, X. Lemoine, P. Cugy, J. Besson, and A.-F. Gourgues-Lorenzon. Fracture behaviour of a fe-22mn-0.6c-0.2v austenitic {TWIP} steel. *International Journal of Mechanical Sciences*, 101 - 102 :99 – 113, 2015.

[220] A. Marais, M. Mazière, S. Forest, A. Parrot, and P. Le Delliou. Influence of static strain aging on the cleavage fracture of a c-mn steel. *Engineering Fracture Mechanics*, 141 :95 – 110, 2015.

[221] M. Mazière and Q. Pujol d d'Andrebo. Portevin - le chatelier effect under cyclic loading : experimental and numerical investigations. *Philosophical magazine*, 2015.

[222] M. Mazière and S. Forest. Strain gradient plasticity modeling and finite element simulation of lüders band formation and propagation. *Continuum Mechanics and Thermodynamics*, 27 :83–104, 2015.

[223] H. Ovri and E.T. Lilleodden. New insights into plastic instability in precipitation strengthened al-li alloys. *Acta Materialia*, 89 :88 – 97, 2015.

[224] G. Rousselier and S. Quilici. Combining porous plasticity with coulomb and portevin-le chatelier models for ductile fracture analyses. *International Journal of Plasticity*, 69 :118 – 133, 2015.

[225] P. Verma, G.S; Rao, P. Chellapandi, G.S. Mahobia, K. Chattopadhyay, N.C.S. Srinivas, and V. Singh. Dynamic strain ageing, deformation, and fracture behavior of modified 9Cr-1Mo steel. *Materials Science and Engineering A*, 621 :39–51, 2015.

[226] D. Delpueyo, X. Balandraud, and M. Grédiac. Calorimetric signature of the portevin - le chatelier effect in an aluminum alloy from infrared thermography measurements and heat source reconstruction. *Materials Science and Engineering : A*, 651 :135 – 145, 2016.

[227] A. Mogucheva, D. Yuzbekova, R. Kaibyshev, T. Lebedkina, and M. Lebyodkin. Effect of grain refinement on jerky flow in an al-mg-sc alloy. *Metallurgical and Materials Transactions A*, 47 :2093–2106, 2016.

8 Lists of articles sorted by thema

8.1 Experimental evidences of the PLC effect in aluminium alloys

— DIC : Digital Image Correlation
— DIT : Digital Image Thermography
— OLE : Other Laser Extensometry
— GS : Different Grain Size
— MMC : Metal Matrix Composite
— Shear : Shear experiments
— CSR : Experiment at a constant stress rate
— Foils : Very thin foils
— Cyclic : Cyclic experiments
— SC : Single Crystal
— LowTemp : Experiment at very low temperature
— AE : Acoustic Emission Measures

Ref.	Authors	Year	Material	Remarks
[158]	Jiang H.; Zhang Q.; Chen X.; Chen Z.; Jiang Z.; Wu X.; Fan J.	2007	AA2017	OLE
[163]	Xiang G.F.; Zhang Q.C.; Liu H.W.; Wu X.P.; Ju X.Y.	2007	AA2017	OLE
[179]	Böhlke T.; Bondar G.; Estrin Y.; Lebyodkin M.A.	2009	AA2024	
[99]	Delafosse D.; Lapasset G.; Kubin L.P.	1993	AA2091	
[223]	Ovri H.; Lilleodden E.T.	2015	AA2198	
[136]	Shabadi R.; Kumar S.; Roven H.J.; Dwarakadasa E.S.	2004	AA2219	OLE
[148]	Besnard G.; Hild F.; Roux S.	2006	AA5005	DIC
[227]	Mogucheva A.; Yuzbekova D.; Kaibyshev R.; Lebedkina T.; Lebyodkin M.	2016	AA5024	GS
[154]	Darowicki K.; Orlikowski J.; Zielinski A.; Jurczak W.	2007	AA5052	
[195]	Li C.; Xu C.N.; Imai Y.; Bu N.	2011	AA5052	OLE
[226]	Delpueyo D.; Balandraud X.; Grédiac M.	2016	AA5062	DIT
[135]	Shabadi R.; Kumar S.; Roven H.J.; Dwarakadasa E.S.	2004	AA5082 AA7020	OLE
[125]	Benallal A.; Borvik T.; Clausen A.; Hopperstad O.	2003	AA5083	
[147]	Benallal A.; Berstad T.; Borvik T.; Clausen A.H.; Hopperstad O.S.	2006	AA5083	

173

Ref.	Authors	Year	Material	Remarks
[149]	Hopperstad O.S. ; Borvik T. ; Berstad T. ; Benallal A.	2006	AA5083	
[157]	Hopperstad O.S. ; Borvik T. ; Berstad T. ; Lademo 0.G. ; Benallal A.	2007	AA5083	
[166]	Benallal A. ; Berstad T. ; Borvik T. ; Hopperstad O.S. ; Koutiri I. ; Nogueira de Codes R.	2008	AA5083	DIC
[192]	De Codes R.N. ; Benallal A.	2011	AA5083	DIC DIT
[106]	Robinson J.M. ; Shaw M.P.	1994	AA5182	
[143]	Picu R.C. ; Vincze G. ; Ozturk F. ; Gracio J.J. ; Barlat F. ; Maniatty A.M.	2005	AA5182	
[193]	De Codes R.N. ; Hopperstad O.S. ; Engler O. ; Lademo O.-G. ; Embury J.D. ; Benallal A.	2011	AA5182	DIC DIT
[153]	Darowicki K. ; Orlikowski J.	2007	AA5251	
[150]	Kang J. ; Wilkinson D.S. ; Jain M. ; Embury J.D. ; Beaudoin A.J. ; Kim S. ; Mishira R. ; Sachdev A.K.	2006	AA5754	DIC
[155]	"Dierke H. ; Krawehl F. ; Graff S. ; Forest S. ; Sach J. ; Neuḧauser H."	2007	AA5754	MMC
[156]	Halim H. ; Wilkinson D.S. ; Niewczas M.	2007	AA5754	DIC
[199]	Mazière M. ; Dierke H.	2012	AA5754	
[207]	Coer J. ; Manach P.Y. ; Laurent H. ; Oliveira M.C. ; Menezes L.F.	2013	AA5754	DIC Shear
[213]	Manach P.Y. ; Thuillier S. ; Yoon J.W. ; Coer J. ; Laurent H.	2014	AA5754	Shear
[218]	Klusemann B. ; Fischer G. ; Boehlke T. ; Svendsen B.	2015	AA5754	DIT
[77]	Schwarz R.B. ; Funk L.L.	1985	AA6061	
[169]	"Graff S. ; Dierke H. ; Forest S. ; Neuḧauser H. ; Strudel J.-L."	2008	AA7574	MMC
[34]	Bodner S.R. ; Rosen A.	1967	Al	CSR
[37]	Rosen A. ; Bodner S.R.	1967	Al	
[131]	Graff S. ; Forest S. ; Strudel J.-L. ; Prioul C. ; Pilvin P. ; Béchade J.-L.	2004	Al-Cu	
[134]	Miserez A. ; Mortensen A..	2004	Al-Cu	MMC
[144]	Ranc N. ; Wagner D.	2005	Al-Cu	DIT
[174]	Ranc N. ; Wagner D.	2008	Al-Cu	DIT
[140]	Graff S. ; Forest S. ; Strudel J.-L. ; Prioul C. ; Pilvin P. ; Béchade J.-L.	2005	Al-Cu Al-Li	
[21]	Portevin A. ; Le Chatelier F.	1923	Al-CuMgMn	

Ref.	Authors	Year	Material	Remarks
[126]	Cieslar M.; Fressengeas C.; Karimi A.; Martin J.-L.	2003	Al-FeSi	Foils
[80]	Gentzbittel J.M.; Fougeres R.	1987	Al-Li	Cyclic
[95]	Gomiero P.; Brechet Y.; Louchet F.; Tourabi A.; Wack B.	1992	Al-Li Al-CuMg Al-LiCuMgZr	
[32]	Thomas A.T.	1966	Al-Mg	GS
[39]	Brindley B.J.; Worthington P.J.	1969	Al-Mg	GS SC
[48]	Guillot J.; Grilhe J.	1972	Al-Mg	
[51]	Tensi H.M.; Borchers H.; Dropmann P.	1972	Al-Mg	SC
[60]	Fujita H.; Tabata T.	1977	Al-Mg	SC
[65]	Estrin Y.; Tangri K.	1981	Al-Mg	LowTemp
[76]	Kubin L. P.; Estrin Y.	1985	Al-Mg	
[79]	Chihab K.; Estrin Y.; Kubin L.P.; Vergnol J.	1987	Al-Mg	
[88]	McCormick P.G.; Estrin Y.	1989	Al-Mg	
[97]	Robinson J.M.; Shaw M.P.	1992	Al-Mg	
[98]	Balik J.; Lukac P.	1993	Al-Mg	
[109]	Lebyodkin M.; Brechet Y.; Estrin Y.; Kubin L.	1996	Al-Mg	
[114]	Choi I.; Jin S.; Kang S.	1998	Al-Mg	
[116]	d'Anna G.; Nori F.	2000	Al-Mg	
[118]	Kovacs Zs.; Lendvai J.; Vörös G.	2000	Al-Mg	CSR
[119]	Lebyodkin M.; Dunin-Barkowskii L.; Brechet Y.; Estrin Y.; Kubin L.P.	2000	Al-Mg	
[123]	"Chmelik F.; Ziegenbein A.; Neuh¨auser H.; Lukac P."	2002	Al-Mg	AE OLE
[130]	Estrin Y.; Lebyodkin M.A.	2004	Al-Mg	MMC
[138]	Duan X.; Jain M.; Metzger D.; Kang J.; Wilkinson D.S.; Embury J.D.	2005	Al-Mg	
[141]	Lebyodkin M.A.; Estrin Y.	2005	Al-Mg	MMC
[142]	Louche H.; Vacher P.; Arrieux R.	2005	Al-Mg	DIT
[145]	Ait-Amokhtar H.; Boudrahem S.; Fressengeas C.	2006	Al-Mg	OLE
[146]	Ait-Amokhtar H.; Vacher P.; Boudrahem S.	2006	Al-Mg	DIC
[152]	"Chmelik F.; Klose F.B.; Dierke H.; Sach J.; Neuh¨auser H.; Lukac P."	2007	Al-Mg	AE OLE
[164]	Ait-Amokhtar H.; Fressengeas C.; Boudrahem S.	2008	Al-Mg	DIT
[167]	Chatterjee A.; Sakar A.; Bhattacharya S.; Mukherjee P.; Gayathri N.; Barat P.	2008	Al-Mg	
[171]	Lebedkina T.A.; Lebyodkin M.A.	2008	Al-Mg	

Ref.	Authors	Year	Material	Remarks
[176]	Sarkar A.; Charles L.; Webber Jr.; Barat P.; Mukherjee P.	2008	Al-Mg	
[180]	Casarotto L.; Dierke H.; Tutsch R.; Neuhaeuser H.	2009	Al-Mg	OLE DIC
[181]	Kuo C.-M.; Tso C.-H.; Lin C.-H.	2009	Al-Mg	CSR
[187]	Ait-Amokhtar H.; Fressengeas C.	2010	Al-Mg	DIC DIT
[194]	Fu S.H.; Zhang Q.C.; Hu Q.; Gong M.; Cao P.T.; Liu H.W.	2011	Al-Mg	
[204]	Ziani L.; Boudrahem S.; Ait-Amokhtar H.; Mehenni M.; Kedjar B.	2012	Al-Mg	
[208]	Saada G.; Kruml T.	2013	Al-Mg	Cyclic
[212]	Maj P.; Zdunek J.; Mizera J.; Kurzydlowski K. J.	2014	Al-Mg	
[216]	Ait-Amokhtar H.; Fressengeas C.; Bouabdallah K.	2015	Al-Mg	
[137]	Chinh N.Q.; Horvath G.; Kovacs Z.; Juhasz A.; Berces G.; Lendvai J.	2005	Al-Mg Al-Cu	Indentation
[33]	Wilcox B.A.; Rosenfield A.R.	1966	Al-Mg Fe-Si Ti	
[63]	Mulford R.A.; Kocks U.F.	1979	Al-Mg Ni(Inco600)	
[62]	Harun H.J.; McCormick P.G.	1979	Al-Mg-Si	
[44]	McCormick P.G.	1971	Al-MgSi	
[49]	McCormick P.G.	1972	Al-MgSi	
[100]	Ling C.P.; McCormick P.G.	1993	Al-MgSi	
[101]	Ling C.P.; McCormick P.G.; Estrin Y.	1993	Al-MgSi	CSR
[102]	McCormick P.G.; Venkadesan S.; Ling C.P.	1993	Al-MgSi	
[73]	Saha G.G.; McCormick P.G.; Rao P. Rama	1984	Al-Mn-Mg	
[72]	Saha G.G.; McCormick P.G.; Rao P. Rama	1984	Al-Mn-Mg	
[103]	Park D.; Morris J.G.	1993	Al-MnMg	
[20]	Rosenhain W.; Archbutt L.	1912	Al-Zn	
[92]	Fellner M.; Hamersky M.; Pink E.	1991	Al-ZnMg Al-Mg	CSR

8.2   Experimental evidences of the PLC effect in other metallic alloys

Ref.	Authors	Year	Material	Remarks
[46]	Wijler A.; Vanwestrum J.S.	1971	Au-Cu	
[45]	Wijler A.; Vanwestrum J.S.	1971	Au-Cu	

Ref.	Authors	Year	Material	Remarks
[52]	Wijler A.; Vanwestrum J.S.; Van-DenBeukel A.	1972	Au-Cu	
[55]	van den Brink S.H.; McCormick P.G.	1974	Au-Cu	
[56]	Wijler A.; Vrijhoef M.M.; Van-denbeukel A.	1974	Au-Cu	
[58]	van den Brink S.H.; van den Beu-kel A.; McCormick P.G.	1975	Au-Cu	
[70]	van den Beukel A.; Blonk J.; van Haastert G.H.	1983	Au-Cu	
[40]	Soler-Gomez A.J.R.; Tegart W.J.M.	1969	Au-In	
[129]	Chen L.J.; Liaw P.K.; Wang H.; He Y.H.; McDaniels R.L.; Jiang L.; Yang B.; Klarstrom D.L.	2004	Co (Haynes120)	Cyclic
[112]	Rao K.B.S.; Castelli M.G.; Allen G.P.; Ellis J.R.	1997	Co (Haynes188)	Cyclic
[206]	Chaboche J.-L.; Gaubert A.; Ka-nouté P.; Longuet A.; Azzouz F.; Mazière M.	2013	Co (Haynes188)	Cyclic
[221]	Mazière M.; d d'Andrebo Q. Pu-jol	2015	Co (Haynes188)	Cyclic
[8]	Savart F.	1837	Cu	
[9]	Masson M.A.	1841	Cu	
[19]	Andrade E.N.D.	1910	Cu	
[183]	McDonald R.J.; Efstathiou C.; Kurath P.	2009	Cu	SC
[89]	Hong S.I.; Laird C.	1990	Cu-Al	Cyclic SC
[127]	Klose F.B.; Ziegenbein A.; Wei-denmüller H.; Hähner P.	2003	Cu-Al	CSR OLE
[94]	Springer F.; Schwink C.	1991	Cu-Mn	
[26]	Russell B.	1963	Cu-Sn	
[36]	Ham R.K.; Jaffrey D.	1967	Cu-Sn	Cyclic
[54]	Räuchle W.; Vöhringer O.; Ma-cherauch E.	1973	Cu-Sn	
[81]	Dybiec H.	1988	Cu-Zn	
[6]	Seguin A.	1826	Fe	
[12]	Wertheim M.G.	1844	Fe	
[35]	Dingley D.J.; McLean D.	1967	Fe	
[18]	Le Chatelier A.	1909	Fe (mild steel)	
[22]	Manjoine M.J.	1944	Fe (mild steel)	
[30]	Blakemore J.S.; Hall E.O.	1966	Fe (mild steel)	
[31]	Brindley B.J.; Barnby J.T.	1966	Fe (mild steel)	GS
[41]	Brindley B.J.	1970	Fe (mild steel)	
[67]	Pink E.; Grinberg A.	1981	Fe (stainless steel)	
[74]	Strudel J.-L.	1984	Fe (stainless steel)	CSR

Ref.	Authors	Year	Material	Remarks
[132]	Hong S.G.; Lee S.B.	2004	Fe (stainless steel)	Cyclic
[133]	Hong S.G.; Lee S.B.	2004	Fe (stainless steel)	Cyclic
[197]	Larsson R.; Nilsson L.	2012	Fe (TRIP steel)	
[151]	Chen L.; Kim H.-S.; Kim S.-K.; De Cooman B.C.	2007	Fe (TWIP steel)	DIT
[165]	Allain S.; Cugy P.; Scott C.; Chateau J.-P.; Rusinek A.; Deschamps A.	2008	Fe (TWIP steel)	DIC DIT
[182]	Lebedkina T.A.; Lebyodkin M.A.; Chateau J.-P.; Jacques A.; Allain S.	2009	Fe (TWIP steel)	OLE
[186]	Zavattieri P.D.; Savic V.; Hector L. G.; Fekete J.R.; Tong W.; Xuan Y.	2009	Fe (TWIP steel)	DIC
[219]	Lorthios J.; Mazière M.; Lemoine X.; Cugy P.; Besson J.; Gourgues-Lorenzon A.-F.	2015	Fe (TWIP steel)	
[24]	Sleeswyk A.W.	1958	Fe armco	
[104]	Srinivas M.; Malakondaiah G.; Rao P.R.	1993	Fe armco	
[162]	Srinivas M.; Kamat S. V.; Rao P. Rama	2007	Fe armco	
[10]	Poncelet J. V.	1841	Fe Cu-Zn	
[43]	Dolzhenkov I.E.	1971	Fe-C	
[61]	McCormick P.G.	1978	Fe-C	
[42]	Roberts M.J.; Owen W.S.	1970	Fe-C Fe-NiC	
[110]	Wagner D.; Moreno J.C.; Prioul C.	1996	Fe-CMn	
[115]	Wagner D.; Moreno J.C.; Prioul C.	1998	Fe-CMn	
[124]	Wagner D.; Moreno J.C.; Prioul C.; Frund J.M.; Houssin B.	2002	Fe-CMn	
[178]	Belotteau J.; Berdin C.; Forest S.; Parrot A.; Prioul C.	2009	Fe-CMn	
[196]	Wang H.D.; Berdin C.; Mazière M.; Forest S.; Prioul C.; Parrot A.; Le-Delliou P.	2011	Fe-CMn	
[202]	Wang H.D.; Berdin C.; Mazière M.; Forest S.; Prioul C.; Parrot A.; Le-Delliou P.	2012	Fe-CMn	
[205]	Berdin C.; Wang H.	2013	Fe-CMn	
[161]	Sarkar A.; Chatterjee A.; Barat P.; Mukherjee P.	2007	Fe-CMn Al-Mg	

Ref.	Authors	Year	Material	Remarks
[225]	Verma P.; Rao G.S;.; Chellapandi P.; Mahobia G.S.; Chattopadhyay K.; Srinivas N.C.S.; Singh V.	2015	Fe-CrMo	
[29]	Baird J.D.; Jamieson A.	1966	Fe-Mn	
[210]	Huang Z.Y.; Chaboche J.-L.; Wang Q.Y.; Wagner D.; Bathias C.	2014	Fe-Mn	Cyclic
[53]	Leslie W.C.; Cuddy L.J.; Sober R.J.	1973	Fe-Ni Fe-Pt Fe-Re Fe-Rh Fe-Mn Fe-Al Fe-Mo Fe-Ti	
[188]	Li T.; Liu Y.; Cao Z.; Jiang D.; Cheng L.	2010	Mg-LiAlZnRe	
[215]	Min J.; Hector Jr.L.G.; Lin J.; Carter J.T.; Sachdev A.K.	2014	Mg-ZnNdZr	DIC
[71]	van Haastert G. H.; van den Beukel A.	1983	Ni	
[75]	Kocks U.F.; Cook R.E.; Mulford R.A.	1985	Ni	Compression
[175]	Roy A.K.; Pal J.; Mukhopadhyay C.	2008	Ni (C-276)	
[200]	Sakthivel T.; Laha K.; Nandagopal M.; Chandravathi K.S.; Parameswaran P.; Selvi S. Panneer; Mathew M.D.; Mannan S.K.	2012	Ni (Hastelloy X)	
[68]	Hayes R.W.	1983	Ni (Inconel718 and 600)	
[91]	Dybiec H.; Chaturvedi M.C.	1991	Ni (Inconel718)	
[108]	Rao K.B.S.; Kalluri S.; Halford G.R.; McGaw M.A.	1995	Ni (Inconel718)	Cyclic
[120]	Fournier L.; Delafosse D.; Magnin T.	2001	Ni (Inconel718)	
[121]	Hale C.L.; Rollings W.S.; Weaver M.L.	2001	Ni (Inconel718)	
[168]	Garat V.; Cloue J.M.; Poquillon D.; Andrieu E.	2008	Ni (Inconel718)	
[201]	Ter-Ovanessian B.; Poquillon D.; Cloue J.-M.; Andrieu E.	2012	Ni (Inconel718)	
[211]	Maj P.; Zdunek J.; Gizynski M.; Mizera J.; Kurzydlowski K. J.	2014	Ni (Inconel718)	
[214]	Max B.; Viguier B.; Andrieu E.; Cloue J.-M.	2014	Ni (Inconel718)	
[177]	Sharghi-Moshtaghin R.; Asgari S.	2008	Ni (Inconel738)	

Ref.	Authors	Year	Material	Remarks
[105]	Pujol C.	1994	Ni (Udimet720)	
[159]	Mazière M.	2007	Ni (Udimet720)	
[170]	Jousset H.	2008	Ni (Udimet720)	
[172]	Mazière M. ; Besson J. ; Forest S. ; Tanguy B. ; Chalons H. ; Vogel F.	2008	Ni (Udimet720)	
[217]	Cai Y. ; Tian C. ; Fu S. ; Han G. ; Cui C. ; Zhang Q.	2015	Ni- ?	
[191]	Cui C. Y. ; Gu Y. F. ; Yuan Y. ; Harada H.	2011	Ni-Co	
[28]	Wilcox B.A. ; Smith G.C.	1964	Ni-H	
[38]	Turner N.G. ; Roberts W.T.	1968	Ti	
[47]	Garde A.M. ; Santhanam A.T. ; Reed-Hill R.E.	1972	Ti	
[64]	Itoh N. ; Ogaya M. ; Ishiyama S. ; Matsushita T. ; Hayashi Y. ; Koike M.	1980	Ti	
[25]	Lindley T.C. ; Smallman R.E.	1963	V	

8.3 Finite element modelling of the Portevin - Le Chatelier effect

— ST : Smooth Tensile Specimens (flat or axisymmetric)
— NT-U : U-Notched Tensile Specimens
— NT-V : V-Notched Tensile Specimens
— CT : Compact Tensile Specimens
— 2D : 2D Plane Stress Simulations
— 2D : 2D Axisymmetric Simulations
— 3D : 3D Simulations
— MS : Investigations on Mesh Size
— HM : Heterogeneous materials
— CP : Crystal Plasticity Modified Model

Ref.	Authors	Year	Material	Remarks
[122]	Zhang S. ; Mccormick P.G. ; Estrin Y.	2001	Al-Mg-Si	ST 3D MS
[128]	Kok S. ; Bharathi M.S. ; Beaudoin A.J. ; Fressengeas C. ; Ananthakrishna G. ; Kubin L.P. ; Lebyodkin M.	2003	AL-Mg	ST 3D CP
[131]	Graff S. ; Forest S. ; Strudel J.-L. ; Prioul C. ; Pilvin P. ; Béchade J.-L.	2004	Al-Cu	NT-U 2D
[140]	Graff S. ; Forest S. ; Strudel J.-L. ; Prioul C. ; Pilvin P. ; Béchade J.-L.	2005	Al-Cu Al-Li	NT-V CT 2D

Ref.	Authors	Year	Material	Remarks
[147]	Benallal A.; Berstad T.; Borvik T.; Clausen A.H.; Hopperstad O.S.	2006	AA5083	ST NT-U 2D-AXI MS
[149]	Hopperstad O.S.; Borvik T.; Berstad T.; Benallal A.	2006	AA5083	ST 3D
[155]	"Dierke H.; Krawehl F.; Graff S.; Forest S.; Sach J.; Neuḧauser H."	2007	AA5754	ST 2D HM
[157]	Hopperstad O.S.; Borvik T.; Berstad T.; Lademo 0.G.; Benallal A.	2007	AA5083	ST 2D
[166]	Benallal A.; Berstad T.; Borvik T.; Hopperstad O.S.; Koutiri I.; Nogueira de Codes R.	2008	AA5083	ST NT-U 3D
[169]	"Graff S.; Dierke H.; Forest S.; Neuḧauser H.; Strudel J-L."	2008	AA7574	ST Shear 2D HM
[172]	Mazière M.; Besson J.; Forest S.; Tanguy B.; Chalons H.; Vogel F.	2008	Ni (Udimet720)	ST 2D
[178]	Belotteau J.; Berdin C.; Forest S.; Parrot A.; Prioul C.	2009	Fe-CMn	ST CT 2D
[179]	Böhlke T.; Bondar G.; Estrin Y.; Lebyodkin M.A.	2009	AA2024	ST 3D Structure
[180]	Casarotto L.; Dierke H.; Tutsch R.; Neuhaeuser H.	2009	Al-Mg	ST 2D
[184]	Varadhan S.; Beaudoin A.J.; Fressengeas C.	2009	Al-Mg	ST 3D CP
[189]	Mazière M.; Besson J.; Forest S.; Tanguy B.; Chalons H.; Vogel F.	2010	Ni (Udimet720)	ST NT-U 3D MS
[196]	Wang H. D.; Berdin C.; Mazière M.; Forest S.; Prioul C.; Parrot A.; Le-Delliou P.	2011	Fe-CMn	ST 3D
[197]	Larsson Rikard; Nilsson Larsgunnar	2012	Fe (TRIP steel)	ST DP Shear 2D
[199]	Mazière M.; Dierke H.	2012	AA5754	ST 2D
[202]	Wang H.D.; Berdin C.; Mazière M.; Forest S.; Prioul C.; Parrot A.; Le-Delliou P.	2012	Fe-CMn	ST NT-U CT 3D
[203]	Zhang F.; Bower A. F.; Curtin W. A.	2012	AA5083	ST 3D
[213]	Manach P. Y.; Thuillier S.; Yoon J. W.; Coer J.; Laurent H.	2014	AA5754	Shear 3D
[218]	Klusemann Benjamin; Fischer Gottfried; Boehlke Thomas; Svendsen Bob	2015	AA5754	ST 3D MS
[221]	Mazière M.; d'Andrebo Q. Pujod	2015	Co (Haynes188)	ST 2D Cyclic